THE EFFECT OF SLEEP AND CIRCADIAN RHYTHMS ON DYNAMIC BRAIN NETWORKS

by

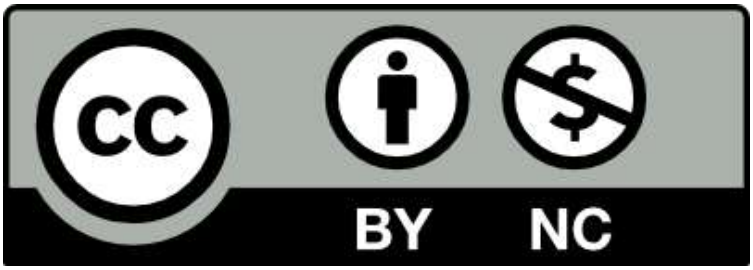
SOPHIE LAUREN MASON

A thesis submitted to
The University of Birmingham
for the degree of
DOCTOR OF PHILOSOPHY

School of Mathematics
College of Engineering and Physical Sciences
The University of Birmingham
July 2023

UNIVERSITY OF BIRMINGHAM

University of Birmingham Research Archive
e-theses repository



This unpublished thesis/dissertation is under a Creative Commons Attribution-NonCommercial 4.0 International (CC BY-NC 4.0) licence.

You are free to:

Share — copy and redistribute the material in any medium or format

Adapt — remix, transform, and build upon the material

The licensor cannot revoke these freedoms as long as you follow the license terms.

Under the following terms:



Attribution — You must give appropriate credit, provide a link to the license, and indicate if changes were made. You may do so in any reasonable manner, but not in any way that suggests the licensor endorses you or your use.



NonCommercial — You may not use the material for commercial purposes.

No additional restrictions — You may not apply legal terms or technological measures that legally restrict others from doing anything the license permits.

Notices:

You do not have to comply with the license for elements of the material in the public domain or where your use is permitted by an applicable exception or limitation.

No warranties are given. The license may not give you all of the permissions necessary for your intended use. For example, other rights such as publicity, privacy, or moral rights may limit how you use the material.

Unless otherwise stated, any material in this thesis/dissertation that is cited to a third-party source is not included in the terms of this licence. Please refer to the original source(s) for licencing conditions of any quotes, images or other material cited to a third party.

Abstract

The daily oscillations of sleep, fatigue, and performance tightly interconnect and dominate almost all aspects of life. However, unique to humans, our 24 h world is causing us to routinely ignore our circadian clock, resulting in people being increasingly at odds with their biological drive for sleep. This misalignment between our endogenous drive to sleep and daily commitments increasingly restricts sleep timing, which can lead to increased time awake, sleep debt and higher levels of fatigue. The resultant effect on our body and in particular our brain is a key research area in chronobiology as well as sleep and circadian research. Network analysis is a key tool in understanding the complex macroscale interactions in the brain. Therefore, this thesis will investigate the effect of chronotype on functional brain networks derived from fMRI through classification pipelines and show evidence of differentiable information between the functional networks of extreme chronotypes. Also, this thesis will investigate features of functional networks which are associated with resilience to sleep deprivation. In particular, this thesis will highlight the association between the mean node strength of functional networks, calculated from a baseline EEG acquisition before sleep deprivation has occurred, with the effect of sleep deprivation as measured using psychomotor vigilance tests.

Acknowledgements

I would like to thank my supervisors Professor John Terry, Professor Andrew Bagshaw, Dr Leandro Junges and Dr Wessel Woldman for their continual guidance and support over the past four years. I am truly grateful for all of the time and energy you have invested in our meetings and the countless amount of proofreading and feedback you provided. Our conversations were always thought provoking and learning from each of you has helped me improve academically, professionally and personally. I am genuinely honoured to have completed my PhD under your supervision. I would also like to thank the School of Mathematics and the Alumni Scholarship, which funded my PhD research.

I would also like to thank my collaborators. Professor Clare Anderson thank you for providing access to the incredible dataset I analysed in Chapter 7. Our conversations were always incredibly insightful and were a continual source of inspiration for new avenues of research as well as motivation to carry on. Dr Elise Facer-Childs thank you for collecting the chronotype dataset (that Andy loves so much!) that started my journey into the world of circadian research. Dr Brunno de Campos thank you for your help with understanding coding and Tikhonov partial correlation.

To my friends and family thank you for your support, which was essential for completing this thesis. In particular, I would like to extend a thank you to my friend Rachel, my parents John and Vera and my partner Euan, thank you for loving me and believing in me, even when I doubted.

CONTENTS

1 Introduction **1**

1.1 Outline of Chapters 3

2 Literature Review **4**

2.1 Imaging Modalities 4

2.1.1 Structural, Functional and Effective Connectivity 5

2.1.2 fMRI 7

2.1.3 EEG 9

2.2 Chronobiology 11

2.2.1 Circadian Rhythms 11

2.2.2 Chronotypes 13

2.2.3 Wake Maintenance Zone 17

2.3 Sleep Deprivation 19

2.3.1 Sleep Debt and Social Jetlag 24

2.4 Introduction to Excitability 25

3 Introduction to Methods **28**

3.1 Analysis of Large-Scale Brain Networks 28

3.1.1 Functional Network Pipeline 28

3.1.2 Network-Based Statistic 45

3.2 Kuramoto Model 47

3.2.1 Order Parameter: R 56

3.3 Two Process Model 59
3.3.1 Extensions to the Two Process Model 62

4 Classification of Human Chronotype Based on fMRI Graph Theoretical Methods 68

4.1 Introduction 68
4.2 Methodology 69
4.2.1 Ethical Approval 70
4.2.2 Participants 70
4.2.3 Chronotype Labeling 72
4.2.4 fMRI Scanning Specifications 72
4.2.5 fMRI Preprocessing 73
4.2.6 Functional Network Construction 74
4.2.7 Thresholding and Binarization 82
4.2.8 Graph Metrics 82
4.2.9 Spatial Scales 83
4.2.10 Balancing Groups 83
4.2.11 The Classifier 83
4.2.12 Statistical Analysis 84
4.3 Results 84
4.3.1 Afternoon Scanning Session 85
4.3.2 Evening Scanning Session 92
4.3.3 Morning Scanning Session 98
4.4 Discussion 104

5 Classification of Human Chronotype Based on fMRI Network-Based Statistics 111

5.1 Introduction 111
5.2 Methodology 113

5.2.1 Network-Based Statistic . . . 113
5.2.2 NBS Threshold Selection . . . 114
5.2.3 The Classifier . . . 115
5.2.4 Varying the t-statistic Threshold . . . 116
5.2.5 Investigating the Stability of the Classifier . . . 118
5.2.6 Varying the Threshold for Significance . . . 119
5.3 Results . . . 120
5.3.1 Classifier Performance . . . 120
5.3.2 How the t-statistic Threshold Impacts Classifier Performance . . . 123
5.3.3 Investigating the Stability of the Classifier . . . 127
5.3.4 How the Significance Threshold Impacts Classifier Performance: Partial Datasets . . . 134
5.3.5 How the Significance Threshold Impacts Classifier Performance: Original Datasets . . . 135
5.4 Discussion . . . 138

6 Using the Kuramoto Model to Investigate the Link Between Network Structure, Excitability and Sleep Deprivation 148

6.1 Introduction . . . 148
6.2 Methodology . . . 150
6.2.1 Network Selection . . . 150
6.2.2 Selecting Kg and Kcc . . . 154
6.2.3 Kuramoto Model . . . 158
6.2.4 Simulating the Time-series . . . 159
6.2.5 Synchrony Measures . . . 160
6.2.6 Phase Locking Factor . . . 163
6.2.7 Graph Metrics . . . 164
6.2.8 Statistical Analysis . . . 165
6.3 Results . . . 165

6.3.1 Three Node Networks . . . 165
6.3.2 18 Node Networks: Mean Node Degree Three . . . 177
6.3.3 18 Node Networks: Mean Node Degree Four . . . 188
6.4 Discussion . . . 198

7 Using Functional Networks to Predict and Understand the Effect of Sleep Deprivation as Measured Using PVT 203

7.1 Introduction . . . 203
7.2 Methodology . . . 205
7.2.1 Ethical Approval . . . 205
7.2.2 Participants . . . 206
7.2.3 Dim Light Melatonin Onset Calculation . . . 207
7.2.4 Psychomotor Vigilance Test . . . 207
7.2.5 PVT Impairment and Performance . . . 208
7.2.6 EEG Acquisition . . . 209
7.2.7 EEG Preprocessing . . . 211
7.2.8 Epoch Selection . . . 212
7.2.9 Functional Network Construction . . . 212
7.2.10 Calculating Graph Metrics . . . 213
7.2.11 Kuramoto Model and Synchronisation Index . . . 214
7.2.12 Stability Analysis . . . 214
7.2.13 Statistical Analysis . . . 215
7.3 Results . . . 215
7.3.1 Predicting PVT Impairment Using Mean Node Strength . . . 215
7.3.2 Predicting PVT Impairment Using Trophic Incoherence . . . 218
7.3.3 Predicting PVT Impairment Using Synchronisation Index . . . 221
7.3.4 Trophic Incoherence Adds Value . . . 224
7.3.5 Stability . . . 226
7.3.6 Predicting PVT Impairment Using Stability . . . 232

7.3.7 Predicting PVT Performance Over the Constant Routine Protocol Using Mean Node Strength . . . 234
7.3.8 Predicting PVT Performance Over the Constant Routine Protocol Using Trophic Incoherence . . . 236
7.3.9 Predicting PVT Performance Over the Constant Routine Protocol Using Synchronisation Index . . . 239
7.3.10 Predicting PVT Performance Over the Constant Routine Protocol Using Stability . . . 241
7.4 Discussion . . . 243

8 Discussion **254**
8.1 NBS is an Important Alternative to Graph Metrics . . . 255
8.2 Susceptibility to Sleep Deprivation is Associated with FN Properties . . . 257
8.3 Future Research . . . 259
8.3.1 Greater Separation of Chronotype and Fatigue . . . 259
8.3.2 Additional Studies and the Inclusion of Extreme Chronotypes as Study Cohorts . . . 260
8.3.3 Circadian Strength Should Receive More Focus . . . 261
8.4 Concluding Remarks . . . 263

Appendix A: Kuramoto Derivation **265**
A.1 Mean-field Limit . . . 265
A.1.1 The Continuity Equation . . . 266
A.2 Deriving K_g . . . 269

Appendix B: Chapter 5 **273**
B.1 Main Steps of the Classifier . . . 273
B.2 NBS Predict . . . 275
B.3 Participant's Metadata . . . 277

Appendix C: Chapter 6 **278**

C.1 Examplar Simulated Time-series 278

C.2 Synchronisation Using N_c=1000 281

C.3 NSI calculated with 30 s 285

C.4 Scatterplots for P = 3 287

C.5 Consistency of Outliers 293

Appendix D: Chapter 7 **295**

D.1 Psychomotor Vigilance Test 295

D.1.1 Group Level 295

D.1.2 PVT Groups 295

D.2 Circadian Strength 298

D.2.1 Calculating Circadian Strength 298

D.2.2 Investigating Circadian Strength 298

D.3 Removal of Outliers 300

D.4 Figures for SI Impairment and Uncorrected p-values 309

D.5 Predicting Performance using Synchronisation Index 317

List of References **321**

LIST OF FIGURES

2.1 10-20 Electrode Placement 10

2.2 Yearly Pubmed Publications after searching “Wake Maintenance Zone” . . 18

3.1 Functional Network Flowchart 29

3.2 Undirected and Directed Functional Networks and Corresponding Adjacency Matrices 32

3.3 The Functional Network and Corresponding Adjacency Matrix for Weighted Network and Edge Reduction Techniques 34

3.4 Relationship Between Ground Truth and Simulated Functional Networks . 35

3.5 Trophic Incoherence Examples 43

3.6 Summary Pipeline for Network Based-Statistic 46

3.7 Example r Values for Kuramoto Oscillators with Different Phase Ranges . 49

3.8 Relationship Between the Order Parameter and the Coupling Strength for a Single Population 50

3.9 Multiscale Kuramoto Diagram 51

3.10 Three Node Kuramoto Simulation 54

3.11 Application of the Two Process Model 59

3.12 Sleep Deprivation Within the Two Process Model 63

3.13 Predicting Fatigue Using the Two Process Model 64

3.14 Predicting Fatigue Under Sleep Deprivation Using the Two Process Model 65

3.15 Predicting Performance Impairment for the Metro-North Train Crash . . . 66

4.1 Summary Pipeline for Graph Metric Classifier 71

4.2 Distribution of Extreme Chronotypes Within the Dataset 73
4.3 Finding argmin($f(\alpha)$) for Varying Ranges 79
4.4 Comparison of Tikhonov and Pearson's Correlation in a Common Cause Network 80
4.5 Simulated Toy Examples Varying α for Tikhonov Partial Correlation . . . 81
4.6 Results of Logistic Regression Classifier for the Afternoon Scan: Whole Network - Binarized 85
4.7 Distribution of Graph Metrics for the Afternoon Scan: Whole Network - Binarized 86
4.8 Results of Logistic Regression Classifier for the Afternoon Scan: mPFC - Binarized 87
4.9 Results of Logistic Regression Classifier for the Afternoon Scan: PCC - Binarized 87
4.10 Results of Logistic Regression Classifier for the Afternoon Scan: Whole Network - Positive Weighted 88
4.11 Scatterplots of Graph Metrics for the Afternoon Scan: Whole Network - Weighted 89
4.12 Results of Logistic Regression Classifier for the Afternoon Scan: mPFC - Positive Weighted 90
4.13 Results of Logistic Regression Classifier for the Afternoon Scan: PCC - Positive Weighted 90
4.14 Results of Logistic Regression Classifier for the Evening Scan: Whole Network - Binarized 92
4.15 Distribution of Graph Metrics for the Evening Scan: Whole Network - Binarized 93
4.16 Results of Logistic Regression Classifier for the Evening Scan: mPFC - Binarized 94

4.17 Results of Logistic Regression Classifier for the Evening Scan: PCC - Binarized . . . 94
4.18 Results of Logistic Regression Classifier for the Evening Scan: Whole Network - Positive Weighted . . . 95
4.19 Scatterplots of Graph Metrics for the Evening Scan: Whole Network - Weighted . . . 96
4.20 Results of Logistic Regression Classifier for the Evening Scan: mPFC - Positive Weighted . . . 96
4.21 Results of Logistic Regression Classifier for the Evening Scan: PCC - Positive Weighted . . . 97
4.22 Results of Logistic Regression Classifier for the Morning Scan: Whole Network - Binarized . . . 98
4.23 Distribution of Graph Metrics for the Morning Scan: Whole Network - Binarized . . . 99
4.24 Results of Logistic Regression Classifier for the Morning Scan: mPFC - Binarized . . . 100
4.25 Results of Logistic Regression Classifier for the Morning Scan: PCC - Binarized . . . 100
4.26 Results of Logistic Regression Classifier for the Morning Scan: Whole Network - Positive Weighted . . . 101
4.27 Scatterplots of Graph Metrics for the Morning Scan: Whole Network - Weighted . . . 102
4.28 Results of Logistic Regression Classifier for the Morning Scan: mPFC - Positive Weighted . . . 102
4.29 Results of Logistic Regression Classifier for the Morning Scan: PCC - Positive Weighted . . . 103

5.1 Summary Diagram Showing the NBS Classification Pipeline . . . 117
5.2 Classifier Performance as a Function of t-statistic Threshold . . . 124

5.3 Dysconnected Network Produced using NBS for the Afternoon Scanning Session using ECP<LCP and t-statistic Threshold 2.19 125
5.4 Dysconnected Network Produced using NBS for the Evening Scanning Session using ECP>LCP and t-statistic Threshold 1.692 126
5.5 Dysconnected Network Produced using NBS for the Morning Scanning Session using ECP<LCP and t-statistic Threshold 2.19 126
5.6 Dysconnected Network Produced using NBS for the Morning Scanning Session using ECP<LCP and t-statistic Threshold 2.79 127
5.7 Boxplots Showing the Accuracy When Removing Subjects and Varying Across Thresholds for Significance 135
5.8 Performance of the Classifier When Removing Subjects and Varying Across Thresholds for Significance 136
5.9 Performance of the Classifier When Varying Across Thresholds for Significance 137

6.1 Small World Index of Various Watts-Strogatz Networks for $\langle k \rangle = 3$ 153
6.2 Small World Index of Various Watts-Strogatz Networks for $\langle k \rangle = 4$ 154
6.3 Relationship Between K_{cc} and K_g for Selected Three Node Networks . . . 155
6.4 Possible Functions for the Drive Towards Sleep 157
6.5 Three Synchrony Measures 161
6.6 Scatterplot Comparing Mean Node Degree to Trophic Incoherence for Three Node Networks 166
6.7 Normalised Synchronisation Index for each Global Coupling Strength . . . 170
6.8 Normalised Node Strength Index for each Global Coupling Strength 172
6.9 Normalised R for each Global Coupling Strength 177
6.10 Scatterplot Comparing Small World Index to Trophic Incoherence for 18 Node Networks with Mean Node Degree 3 178
6.11 Scatterplots Showing the Relationship Between Trophic Incoherence and SI: Mean Node Degree Three 180

6.12 Scatterplots Showing the Relationship Between Small World Index and SI: Mean Node Degree Three . . . 181
6.13 Scatterplots Showing the Relationship Between Trophic Incoherence and NSI: Mean Node Degree Three . . . 183
6.14 Scatterplots Showing the Relationship Between Small World Index and NSI: Mean Node Degree Three . . . 184
6.15 Scatterplots Showing the Relationship Between Trophic Incoherence and R: Mean Node Degree Three . . . 186
6.16 Scatterplots Showing the Relationship Between Small World Index and R: Mean Node Degree Three . . . 187
6.17 Scatterplot Comparing Small World Index to Trophic Incoherence for 18 Node Networks: Mean Node Degree Four . . . 188
6.18 Scatterplots Showing the Relationship Between Trophic Incoherence and SI: Mean Node Degree Four . . . 190
6.19 Scatterplots Showing the Relationship Between Small World Index and SI: Mean Node Degree Four . . . 191
6.20 Scatterplots Showing the Relationship Between Trophic Incoherence and SI: Mean Node Degree Four . . . 193
6.21 Scatterplots Showing the Relationship Between Small World Index and SI: Mean Node Degree Four . . . 194
6.22 Scatterplots Showing the Relationship Between Trophic Incoherence and R: Mean Node Degree Four . . . 196
6.23 Scatterplots Showing the Relationship Between Small World Index and R: Mean Node Degree Four . . . 197

7.1 PVT Acquisitions Available . . . 208
7.2 EEG Acquisitions Available . . . 211
7.3 Scatterplot Relating PVT Impairment to Mean Node Strength for the First Acquisition After Awakening . . . 216

7.4 Scatterplot Relating PVT Impairment to Mean Node Strength for the Acquisition 11 Hours Before DLMO 217
7.5 Scatterplot Relating PVT Impairment to Trophic Incoherence for the First Acquisition After Awakening 219
7.6 Scatterplot Relating PVT Impairment to Trophic Incoherence 220
7.7 Scatterplot Relating PVT Impairment to SI for the First Acquisition After Awakening 222
7.8 Scatterplot Relating PVT Impairment to SI for the Acquisition 11 Hours Before DLMO 223
7.9 Scatterplot Relating PVT Impairment to Mean Node Strength and Trophic Incoherence for the First Acquisition After Awakening 225
7.10 Stability of Participant's Functional Networks 227
7.11 Stability of Participant's Functional Networks with Low and High Impairment 228
7.12 Individual Stability and Standard Deviation on PVT 230
7.13 Scatterplot Relating PVT Impairment to Stability for the First Acquisition After Awakening 232
7.14 Scatterplot Relating PVT Impairment to Stability for the Acquisition 11 Hours Before DLMO 233
7.15 Correlation Between Baseline Mean Node Strength for the First Acquisition and PVT Performance Over Time 234
7.16 Scatterplots Relating Mean Node Strength to Standard Deviation of RT for the First Acquisition 235
7.17 Correlation Between Baseline Mean Node Strength for the Acquisition 11 hours before DLMO and PVT Performance Over Time 236
7.18 Correlation Between Baseline Trophic Incoherence for the First Acquisition and PVT Performance Over Time 237
7.19 Correlation Between Baseline Trophic Incoherence for the Acquisition 11 hours before DLMO and PVT Performance Over Time 238

7.20 Colorplots Showing the Correlation Between the SI for the First Acquisition after Awakening and PVT Standard Deviation of RT 239
7.21 Colorplots Showing the Correlation Between the SI for the Acquisition 11 hours before DLMO and PVT Standard Deviation of RT 240
7.22 Correlations Between the SI for the First Acquisition and PVT Performance Over Time 240
7.23 Correlation Between Baseline Stability for the First Acquisition and PVT Performance Over Time 241
7.24 Correlation Between Baseline Stability for the Acquisition 11 hours before DLMO and PVT Performance Over Time 242

C.1 Time-series for N_1^3 Across the 19 Simulations 279
C.2 Time-series for N_9^3 Across the 19 Simulations 280
C.3 Scatterplot Comparing Mean Node Strength With SI for Three Node Networks 287
C.4 Scatterplot Comparing Trophic Incoherence With SI for Three Node Networks 288
C.5 Scatterplot Comparing Mean Node Strength With NSI for Three Node Networks 289
C.6 Scatterplot Comparing Trophic Incoherence With NSI for Three Node Networks 290
C.7 Scatterplot Comparing Mean Node Strength With R for Three Node Networks 291
C.8 Scatterplot Comparing Trophic Incoherence With R for Three Node Networks 292
C.9 Barchart Showing the Total Percentage Difference Between the Simulation and Linear Fit: Mean Degree Three 293
C.10 Barchart Showing the Total Percentage Difference Between the Simulation and Linear Fit: Mean Degree Four 294

D.1 Psychomotor Vigilance Test Performance 296
D.2 Psychomotor Vigilance Test Performance Split into Groups Based on High and Low Impairment 297
D.3 Scatterplot Relating PVT Impairment to SI Using Mean RT for the First Acquisition After Awakening 311
D.4 Scatterplot Relating PVT Impairment to SI Using Median RT for the First Acquisition After Awakening 312
D.5 Scatterplot Relating PVT Impairment to SI Using Percentage of Lapses for the First Acquisition After Awakening 313
D.6 Scatterplot Relating PVT Impairment to SI Using Mean RT for the Acquisition 11 Hours Before DLMO 314
D.7 Scatterplot Relating PVT Impairment to SI Using Median RT for the Acquisition 11 Hours Before DLMO 315
D.8 Scatterplot Relating PVT Impairment to SI Using Percentage of Lapses for the Acquisition 11 Hours Before DLMO 316
D.9 Colorplots Showing the Correlation Between the SI for the First Acquisition after Awakening and PVT Mean RT 317
D.10 Colorplots Showing the Correlation Between the SI for the Acquisition 11 hours before DLMO and PVT Mean RT 318
D.11 Colorplots Showing the Correlation Between the SI for the First Acquisition after Awakening and PVT Median RT 318
D.12 Colorplots Showing the Correlation Between the SI for the Acquisition 11 hours before DLMO and PVT Median RT 319
D.13 Colorplots Showing the Correlation Between the SI for the First Acquisition after Awakening and Percentage of Lapses 319
D.14 Colorplots Showing the Correlation Between the SI for the Acquisition 11 hours before DLMO and Percentage of Lapses 320

LIST OF TABLES

4.1 The Nodes, ICNs and MNI Coordinates used for 70 Functional Connectivity ROIs 75

4.2 The Optimum α Values for Various Subgroups of the Dataset 76

4.3 Results of SVM Classifier for the Afternoon Scan: Whole Network - Binarized 91

4.4 Results of SVM Classifier for the Evening Scan: Whole Network - Binarized 97

4.5 Results of SVM Classifier for the Morning Scan: Whole Network - Binarized 103

5.1 Table Showing the Breakdown of Classifications at each Step 121

5.2 The Labels Assigned by the Classifier for the Different Scanning Sessions and Contrasts 122

5.3 Table Showing Key Topological Features of Four dysconnected Networks . 125

5.4 Afternoon [ECP>LCP] Results: Partial Datasets 129

5.5 Afternoon [ECP<LCP] Results: Partial Datasets 129

5.6 Evening [ECP>LCP] Results: Partial Datasets 131

5.7 Evening [ECP<LCP] Results: Partial Datasets 131

5.8 Morning [ECP>LCP] Results: Partial Datasets 133

5.9 Morning [ECP<LCP] Results: Partial Datasets 133

5.10 Values of α which give the Highest Accuracy with the Accuracy Values given in Brackets 138

6.1 Three Node Adjacency Matrices 151

6.2 Correlating SI with Mean Node Degree and Trophic Incoherence 167

6.3 Correlating SI with Mean Node Degree and Trophic Incoherence - No Basal Node Networks 168
6.4 The Results of the Linear and Multiple Regression Against SI 169
6.5 The Results of the Linear and Multiple Regression Against SI - No Basal Nodes 169
6.6 Correlating NSI with Mean Node Degree and Trophic Incoherence 171
6.7 Correlating NSI with Mean Node Degree and Trophic Incoherence - No Basal Node Networks 172
6.8 The Results of the Linear and Multiple Regression Against NSI 173
6.9 The Results of the Linear and Multiple Regression Against NSI - No Basal Nodes 173
6.10 Correlating R with Mean Node Degree and Trophic Incoherence 174
6.11 Correlating R with Mean Node Degree and Trophic Incoherence - No Basal Node Networks 175
6.12 The Results of the Linear and Multiple Regression Against R 176
6.13 The Results of the Linear and Multiple Regression Against R - No Basal Nodes 176
6.14 Pearson's Correlations Between SI with Small World Index and Trophic Incoherence: Mean Node Degree Three 179
6.15 Pearson's Correlations Between NSI with Small World Index and Trophic Incoherence: Mean Node Degree Three 182
6.16 Pearson's Correlations Between R with Small World Index and Trophic Incoherence: Mean Node Degree Three 185
6.17 Pearson's Correlations Between SI with Small World Index and Trophic Incoherence: Mean Node Degree Four 189
6.18 Pearson's Correlations Between NSI with Small World Index and Trophic Incoherence: Mean Node Degree Four 192

6.19 Pearson's Correlations Between R with Small World Index and Trophic Incoherence: Mean Node Degree Four 195

7.1 Timings of the Minimum and Maximum PVT Performance with Respect to DLMO 210
7.2 Table Showing the Pearson's Correlation and p-value for PVT impairment and Mean Node Strength 217
7.3 Table Showing the Pearson's Correlation and p-value for PVT impairment and Trophic Incoherence 219
7.4 The Results of the Linear and Multiple Regression for the First Acquisition After Awakening 224
7.5 The Results of the Linear and Multiple Regression for the Acquisition 11 Hours Before DLMO 224
7.6 Stability Prior to and During the WMZ 227
7.7 Table Showing the p-values for Permutation Tests Comparing Stability with Participants Grouped by Standard Deviation of RT 229
7.8 Stability Prior to and During the WMZ for Groups of High and Low Impairment 229
7.9 Spearman's Rank Correlation Between std RT and Stability for Individuals 231
7.10 Table Showing the Pearson's Correlation and p-value for PVT impairment and Stability 233

B.1 NBS Predict: Logistic Regression 275
B.2 NBS Predict: Support Vector Machine 275
B.3 NBS Predict: Linear Discriminant Analysis 275

C.1 Correlating SI with Mean Node Degree and Trophic Incoherence Using $N_c = 1,000$ 281
C.2 Correlating SI with Mean Node Degree and Trophic Incoherence Using $N_c = 1,000$ - No Basal Node Networks 282

C.3 Correlating NSI with Mean Node Degree and Trophic Incoherence Using $N_c = 1,000$ . . . 282
C.4 Correlating NSI with Mean Node Degree and Trophic Incoherence Using $N_c = 1,000$ - No Basal Node Networks . . . 283
C.5 Correlating R with Mean Node Degree and Trophic Incoherence Using $N_c = 1,000$ . . . 283
C.6 Correlating R with Mean Node Degree and Trophic Incoherence Using $N_c = 1,000$ - No Basal Node Networks . . . 284
C.7 Correlating NSI with Mean Node Degree and Trophic Incoherence Using 30 s285
C.8 Correlating NSI with Mean Node Degree and Trophic Incoherence Using 30 s - No Basal Node Networks . . . 286

D.1 Table Showing the p-values for Permutation Tests Comparing the PVT Performance with Subjects Grouped by PVT Performance . . . 297
D.2 Table Showing the Pearson's Correlation and p-value for PVT impairment and Mean Node Strength with Outliers Removed . . . 300
D.3 Table Showing the Pearson's Correlation and p-value for PVT impairment and Trophic Incoherence with Outliers Removed . . . 300
D.4 Table Showing the Pearson's Correlation and p-value for PVT impairment and Stability with Outliers Removed . . . 301
D.5 Table Showing the Pearson's Correlation and p-value for % Increase in Mean RT and SI with Outliers Removed . . . 301
D.6 Table Showing the Pearson's Correlation and p-value for % Increase in Median RT and SI with Outliers Removed . . . 302
D.7 Table Showing the Pearson's Correlation and p-value for % Increase in std of RT and SI with Outliers Removed . . . 303
D.8 Table Showing the Pearson's Correlation and p-value for the Percentage of Lapses and SI with Outliers Removed . . . 304

D.9 Table Showing the Pearson's Correlation and p-value for Mean RT and SI with Outliers Removed: Acquisition 11 hours before DLMO 305
D.10 Table Showing the Pearson's Correlation and p-value for % Increase in Median RT and SI with Outliers Removed: Acquisition 11 hours before DLMO 306
D.11 Table Showing the Pearson's Correlation and p-value for % Increase in std of RT and SI with Outliers Removed: Acquisition 11 hours before DLMO . 307
D.12 Table Showing the Pearson's Correlation and p-value for the Percentage of Lapses and SI with Outliers Removed: Acquisition 11 hours before DLMO 308
D.13 Uncorrected p-values when Correlating PVT Impairment to SI for the First Acquisition After Awakening 309
D.14 Uncorrected p-values when Correlating PVT Impairment to SI for the Acquisition 11 Hours Before DLMO 310

ACRONYMS

AAL Automated Anatomical Labeling. 30

ADHD Attention Deficit Hyperactivity Disorder. 8

AEDs Anti-Epileptic Drugs. 58

$\mathbf{B}_{-11}$ Acquisition 11 hours Before DLMO. 205

$\mathbf{B}_{FA}$ First EEG Acquisition After Awakening. 205

BCT Brain Connectivity Toolbox. 35

BMI Body Mass Index. 1

BOLD Blood Oxygen Level Dependent. 5

CAR Cortisol Awakening Response. 16

CR Constant Routine. 20

CRP Constant Routine Protocol. 17

DLMO Dim Light Melatonin Onset. 16

DMN Default Mode Network. 8

E-R Erdős-Rényi. 40

ECoG Electrocorticography. 58

ECPs Early Circadian Phenotypes. 13

EEG Electroencephalography. 2

FC Functional Connectivity. 2

FDR False Discovery Rate. 85

fMRI functional Magnetic Resonance Imaging. 2

FNs Functional Networks. 3

FPR False Positive Rate. 44

FWE Family Wise Error. 47

HRF Hemodynamic Response Function. 5

IAAFT Iterative Amplitude Adjusted Fourier Transformed. 33

ICA Independent Component Analysis. 9

ICNs Intrinsic Connectivity Networks. 8

ICPs Intermediate Circadian Phenotypes. 13

iEEG intracranial EEG. 11

KSS Karolinska Sleepiness Scale. 14

LCC Largest Connected Component. 46

LCPs Late Circadian Phenotypes. 13

LECN Left Executive Control Network. 8

LOOCV Leave One Out Cross-Validation. 71, 84

MCCs Minimum Connected Components. 33

MCTQ Munich Chronotype Questionnaire. 13

MDD Major Depressive Disorder. 8

MEG Magnetoencephalography. 4

MN Motor Network. 14

MNI Montreal Neurological Institute. 30

mPFC medial Prefrontal Cortex. 9

MRI Magnetic Resonance Imaging. 4

MSF Mid-point of Sleep on Free-days. 13

MSF_{sc} MSF corrected for sleep on work days. 13

NBS Network-Based Statistic. 45, 112

NSI Node Strength Index. 160

OOP Optimal Operating Point. 44

PC Pearson's Correlation. 33

PCC Posterior Cingulate Cortex. 9

PET Positron Emission Tomography. 4

PLF Phase Locking Factor. 163

PVT Psychomotor Vigilance Test. 14

R Order Parameter Approach. 160

RECN Right Executive Control Network. 8

ROC Receiver Operating Characteristic. 44

ROIs Regions of Interest. 5

rs-FC resting state Functional Connectivity. 14

rs-fMRI resting state fMRI. 3

rs-FNs resting state Functional Networks. 8

RSESA Resting State Epoch Selector Algorithm. 212

RT Reaction Time. 17

SI Synchronisation Index. 160

SSE Sum of Square Errors. 167

$\mathbf{std}_{\mathrm{RT}}$ standard deviation of RT. 207

SVM Support Vector Machines. 44

TE Echo Time. 73

TMS Transcranial Magnetic Stimulation. 26

TNR True Negative Rate. 44

TPCM Tikhonov Partial Correlation Matrix. 74

TPR True Positive Rate. 44

TR Repetition Time. 73

UF^{2}C User-Friendly Functional Connectivity. 73

WMZ Wake Maintenance Zone. 12

CHAPTER 1

INTRODUCTION

Our lives are dominated by circadian rhythms. Driven by the light-dark cycle, circadian rhythms provide an evolutionary advantage, anticipating events such as changes in light or temperature [144]. However, the phase of our internal circadian rhythm is imperfectly aligned with the light-dark cycle, resulting in significant inter-individual variability. This variability is characterised by chronotype: defined on a spectrum from early ('Morning Larks') to late ('Night Owls').

Modern society and chronotype are incompatible bedfellows. The 9-5 working day is at odds with the internal circadian rhythm of late chronotypes, whilst early chronotypes suffer during the evening as many events last into the night. This constant misalignment has led to noticeable negative impacts on health. For example, late chronotype is associated with an increased risk of cancer, type 2 diabetes, increased Body Mass Index (BMI) and obesity [95]. However, there has been an increased drive to understand the effect of chronotype on the brain as late chronotype is also a known risk factor for the development of depression [122] as well as being predictive of variability in cognitive outcomes across the day [56].

Misalignment between internal circadian rhythms and societal constraints can result in sleep deprivation. The effects of sleep deprivation, and associated fatigue, in humans are well documented. Indeed fatigue is considered a contributing factor to the Chernobyl nuclear reactor meltdown, the ill-judged launch of the fatal Challenger space shuttle and

the 2013 Metro-North train crash [48, 51]. A report sponsored by the U.S. Department of Transportation [97] found that high levels of fatigue in train crews not only increased the average cost of human factor rail accidents by 300% but also increased the risk of an accident by 65% compared to a reduction of 30% when train crews are deemed not to be suffering from fatigue. Within the UK alone, sleep deprivation was estimated to cost the economy $50 billion in 2015 due to higher levels of absenteeism or presenteeism [81] and on average presenteeism is estimated to reduce productivity by 1.6% [88].

Therefore, investigating the effect of sleep deprivation on various bodily mechanisms has understandably been a focus of many studies. This has involved blood work [77] as well as investigations into the effects on organs such as exploring associations with cardiovascular health [140] and chronic kidney disease [18]. However, the brain is affected by sleep deprivation more than any other organ [63], with sleep deprivation linked to mental health through mental distress [15] and depression [93] as well as reduced performance on tasks [52, 133].

The effect of chronotype and sleep deprivation is known to impact the brain through cognition and mental health; therefore, understanding the effect of these processes on the brain is of vital importance to overcome these issues.

However, the brain is a complex, multi-scale system with spatial scales from molecules to whole-brain regions. As a consequence, rigorous mathematical tools to understand brain activity are still in development. However, functional Magnetic Resonance Imaging (fMRI) and Electroencephalography (EEG) as non-invasive recording techniques, combined with Functional Connectivity (FC) are useful tools for analysing the brain at the macroscale.

Indeed, the role of functional brain networks in supporting healthy brain function and the disruptions that lead to impaired performance and disease are increasingly understood in many fields, such as depression [124] and cognition both in terms of cognitive architecture [148] and cognitive ageing [84, 186].

Therefore, this thesis will use and analyse functional brain networks to increase our

understanding of the differences between extreme chronotypes and how functional brain networks are associated with sleep deprivation. An increased understanding could help to mitigate the wide-ranging social, economic and medical impacts people currently face.

1.1 Outline of Chapters

Initially, Chapter 2 will present a literature review of imaging modalities and how fMRI and EEG have previously been used to produce functional brain networks. Then relevant studies in the fields of chronobiology, sleep deprivation, as well as an introduction to excitability will be discussed. Afterwards, mathematical methods common within the field of Functional Networks (FNs), sleep and excitability will be detailed in Chapter 3.

Then four results chapters will be presented. First, a dataset of early and late chronotypes will be analysed using machine learning trained on FN features to see if differential information about chronotypes is embedded in resting state fMRI (rs-fMRI) data. This will be presented across Chapters 4 and 5, first using a more traditional graph metric approach and then using a more novel classifier utilising network-based statistics. Then in Chapter 6 the effect of sleep deprivation is simulated using Kuramoto oscillators to understand the interplay between network structure and excitability. Chapter 7 will then focus on a sleep deprivation dataset that will be analysed to understand how the effect of sleep deprivation can be predicted using only information from a baseline acquisition.

Finally, an overall discussion of the results is presented, and future work that could be completed in the field is discussed in Chapter 8.

CHAPTER 2

LITERATURE REVIEW

2.1 Imaging Modalities

As outlined in the Introduction, circadian rhythms and sleep deprivation can affect cognitive and mental health outcomes. These will be discussed in more detail in Sections 2.2 and 2.3. Investigating the impact that such processes have on the brain is vital for understanding how to prevent such problems. A common way to measure brain activity is to use non-invasive neuroimaging devices such as Magnetic Resonance Imaging (MRI), fMRI, EEG, Magnetoencephalography (MEG) and Positron Emission Tomography (PET). In particular, fMRI and EEG datasets are analysed in this thesis, and further details about these methods are provided in Sections 2.1.2 and 2.1.3.

Macroscale brain networks are commonly used when interpreting the data recorded from these imaging modalities. For example, we could model the physical connections in the brain (structural connectivity), create a graphical representation of statistical relationships in recorded brain activity (functional connectivity) or model the dynamics occurring in the brain in order to explain the observed activity (effective connectivity).

2.1.1 Structural, Functional and Effective Connectivity

These three different types of connectivity result in networks with differing interpretations. For completeness, an overview of all three connectivities is provided below, however for an in-depth review, the reader is referred to Fornitio et al. [69].

Structural connectivity considers the physical links between white matter. At a macroscale level, these networks are inferred using diffusion tractography, which uses the preferential diffusion of water along the axonal tract of neurons to establish edges in the network between different brain regions [70]. This is based purely upon anatomical links in the brain and means that the analysis is quite intuitive, with nodes presenting brain regions and edges showing the axonal tracts along which information can pass.

FC is defined as the dependence (most commonly some form of statistical correlation) between remote neurophysiological events [72]. A common technique for analysing FC is through graph theory using FNs, which is explained in Section 3.1.1 with graph metrics introduced in Section 3.1.1.6. In fMRI, the nodes in the FN represent brain regions, known as Regions of Interest (ROIs), and edges represent the statistical relationship between these regions. For EEG networks in sensor space, each node represents the contribution of that electrode from the brain, and edges are the statistical relations between these contributions.

It is important to note that FC has no inherent restrictions in either the direction or strength of edges in the network. However, the indirect nature of calculating neural activity using fMRI from the Blood Oxygen Level Dependent (BOLD) signal (with a time scale of ~16 s controlled by the Hemodynamic Response Function (HRF) [76]) can restrict the accuracy of non-linear and directed approaches. For instance, Smith et al. [177] created a 'ground truth' FN and simulated fMRI data before FC was used to estimate the ground truth network. The percentage of edge directions in the ground truth that were correctly replicated within the simulation remained close to 50% for most of the 26 FC approaches used, with a peak at 65% accuracy; hence edge directionality was not much higher than random chance. However, the increased temporal resolution of EEG

allows a greater breadth of FC measures to be employed, such as phase-based approaches: Phase Locking Factor (see Section 6.2.6), Phase Locking Index [181] and Synchronisation Likelihood [180].

FC can be split into static and dynamic functional connectivity. Static connectivity is where a single brain network per participant is created by averaging across the entire time-series. In contrast, dynamic connectivity splits a time-series into N smaller epochs and so creates N networks, where epochs can either overlap or be distinct. This dynamic approach enables the values of graph metrics for each network within an epoch to be compared and analysed for changes with respect to time.

Finally, it was proposed by Aertsen and Preißl in 1991 [3] that 'effective connectivity should be understood as the experiment and time-dependent, simplest possible circuit diagram that would replicate the observed timing relationships between the recorded neurons'. This idea was adapted by Karl Friston in 2011 to refer to the influence that 'one neural system exerts over another, either at a synaptic or population level' [72]. Combining these two ideas gives effective connectivity: a network model of the brain with nodes representing neural systems (e.g. neurons at a microscale scale and brain regions at a macroscale) and weighted directed edges representing the causal influence between them, such that the interactions can reproduce observed brain activity. This requires not only a neuroanatomical model to provide the areas involved but also a mathematical model to dictate how the regions are connected [25]. Notably, Friston's definition does not rely upon the subjective notation of 'simplest'. This better reflects the complex nature of neural activity since the brain's adaptable behaviour suggests there are multiple ways a process could occur at any one time.

It is important to note that the purposes of functional and effective connectivity are fundamentally different and this thesis will focus on FC. Ultimately, the focus on FC was chosen to allow contributions from more regions in the brain, to remove the reliance on models with additional assumptions and to enable the creation of a framework to test the predictive capacity of the data, such as the assignment of a class label i.e. early or late

chronotype.

2.1.2 fMRI

The ability to produce 3-D anatomical images without the need for any invasive or ionising procedures is the benefit of MRI, which produces images of the body with high spatial accuracy. This technology is relatively new, with the first MRI on a live human occurring in 1977 - the development of the technology is outlined by Edelman [55].

MRI creates images in the following way. First, hydrogen protons in the brain will precess, like a spinning top, in randomly oriented directions. When the MRI produces a strong magnetic field, the previously randomly oriented hydrogen protons will align and precess about the direction of the field. Under the influence of the resonant radio frequency for hydrogen protons, the proton's precession angle will shift away from the magnetic field, and the protons enter a high-energy state. Once the radio frequency is stopped, the protons will realign with the magnetic field. This movement will release the radio frequency energy in the protons, which is interpreted by the scanner to produce the MRI image. The local magnetic properties of protons in the grey and white matter will differ, resulting in different shades in the MRI images [13].

FMRI is an extension of MRI that monitors brain activity and can be used to calculate FC. It is mostly measured through the BOLD signal but can be measured from blood flow using Artial Spin Labelling within voxels - the 3-D analogue of a pixel. Both approaches are dependent on the HRF; therefore the temporal resolution of fMRI is a weakness in the data collected [76]. Also, fMRI is typically used as part of a task-based paradigm in order to identify the regions which respond to the given experimental task compared to a control task, but care must be taken that it is indeed the experimental task eliciting the response [76].

Finally, rs-fMRI is where the brain activity in voxels is recorded without any external stimulus and hence is when the participant is merely resting; this could include both eyes-open and eyes-closed scans.

Rs-fMRI time-series are commonly analysed through graphical approaches and seed-based functional connectivity methods. In graphical approaches, the FC between all ROIs is calculated to create a FN, where ROIs are the nodes and edges represent the statistical relationship between the ROIs. Graph theoretical approaches where network properties are analysed for differences are outlined in Section 3.1. Seed-based analysis calculates the statistical relationship between the BOLD activity in a single seed voxel with all other voxels. In essence, creating a FN with only the connections to the seed present. Clusters of voxels with a high correlation to the seed are typically analysed and contrasted across cohorts.

Resting-state scans are especially useful when trying to understand how brain activity differs in patient cohorts compared to healthy controls, where the effect is constant and not just seen in the presence of a task. For example, Lee et al. [120] outline examples of how resting state Functional Networks (rs-FNs) from patients with Epilepsy, Alzheimer's disease, schizophrenia, autism, Major Depressive Disorder (MDD) and Attention Deficit Hyperactivity Disorder (ADHD) have been analysed. Furthermore, within Epilepsy research, background activity is typically used to infer information about seizure likelihood, as seizures can be rare and unpredictable. Being able to infer information about epileptic seizures using FNs from rs-fMRI, without requiring the recording of a seizure, presents a huge advantage for helping diagnosis and treatment.

2.1.2.1 Intrinsic Connectivity Networks

ROIs in the brain are spatially independent groupings of voxels. However, different ROIs can be involved in the same process. Therefore, ROIs can be grouped together to form Intrinsic Connectivity Networks (ICNs) - subnetworks of spatially distinct ROIs with similar temporal patterns. ICNs can correspond to functions in the brain and include anti salience, post salience, auditory, basal ganglia, dorsal Default Mode Network (DMN), ventral DMN, Language, Left Executive Control Network (LECN), Right Executive Control Network (RECN), sensorimotor, visual and visuospatial [43]. In particular, the DMN

is active in the absence of cognitive demand and is known to show diurnal variation in FC [17] and exhibit lower FC following sleep deprivation [44]. For instance, the Posterior Cingulate Cortex (PCC) and medial Prefrontal Cortex (mPFC) are two ROIs within the DMN that are predictive of the differing cognitive performance of extreme chronotypes [57].

ICNs can be detected using both task-based and resting-state paradigms and are fairly consistent across the two approaches [176]. For instance, Independent Component Analysis (ICA) is a data-driven approach for creating ICNs specifically for the recorded activity of the participants in that study. ICNs are then thresholded to separate them into distinct ROIs. ROI masks created using ICA can also be applied to future fMRI studies. For example, Brunno et al. [43] used the ROI ICA mask created by Shirer et al. [169].

2.1.3 EEG

While fMRI allows a high spatial resolution, temporal resolution is low and it is an expensive modality. Therefore, EEG is a common alternative chosen for its high temporal resolution, provided by monitoring voltages in the brain via the scalp, as well as relative low cost and ease of access.

This technique of measuring electrical activity in the brain was pioneered by Richard Caton [23] when he made neurophysiological recordings of animals in 1875. It was not until 1924 that Hans Berger, a German psychiatrist, decided to employ this on humans, fathering a method that would be recognisable as EEG [23].

EEG is typically non-invasive, with scalp electrodes placed on the head using the standard 10-20 system, as seen in Figure 2.1. This ensures the electrodes are consistently placed above certain brain regions despite inter-individual differences in head size. The adopted labelling of electrodes uses letters to abbreviate the positions where the electrodes are placed on the scalp, combined with numbers to denote the distance from the centre line of the head drawn from the nasion to the inion. Odd and even numbers denote the

left and right-hand side of the scalp respectively, and 'z' is reserved for the centre.

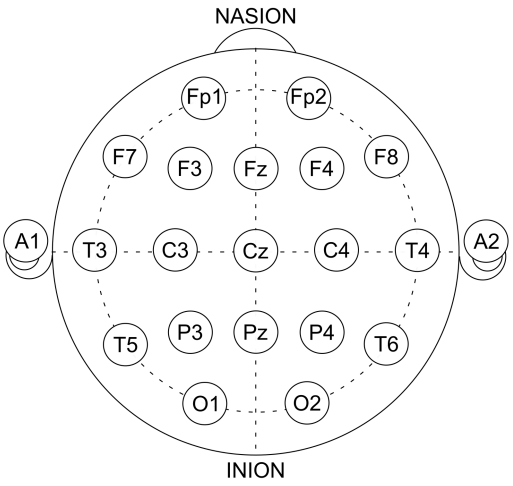


Figure 2.1: **10-20 Electrode Placement.** The common placement of electrodes on the scalp. Here we have pre-frontal (Fp), frontal (F), central (C), temporal (T), parietal (P), occipital (O) and mastoid (A).

EEG recording devices can be portable thanks to electrode caps, making EEG suitable for monitoring participants over extended periods. This is especially important for understanding how dynamics in the brain change during extended protocols such as sleep deprivation.

However, spatial resolution - especially for scalp electrodes - is less precise than that of fMRI. This is due to the distinction between source space and sensor space. Source space is the place in the brain where the electrical signal is produced. The sensor space EEG recording on the scalp is then the aggregated electrochemical signal passing between billions of neurons; this is explained in detail in Cohen et al. [38]. Multiple biological layers between the signal and the sensor cause different filtering effects - the most obvious of which are the skull, scalp muscles and finally the scalp itself. Therefore, it is typically unclear which region a signal originates from unless source localisation is used and even then deep brain regions cannot generally be included. In addition, the brain is not the only organ to create electrical signals; therefore noise can be introduced via the eyes, tongue and heart [23]. Consequently, it is important to ensure EEG recordings are not distorted by such artifacts.

Once an artifact-clean portion of EEG recording is found, a common approach for analysis is to bandpass filter the signal. Initially, this may involve filtering into a broad frequency range, such as 0.5-30 Hz. This allows retention of the main frequency components whilst removing frequencies where the signal-to-noise ratio may be too low as well as removing the issue of power line noise, which can alter the signal near 50Hz. Broadband filtered signals can then be analysed for their spectral features. This may involve filtering the signal further to specific frequencies such as delta band (0.5-4 Hz), theta band (4-8 Hz), alpha band (8-14 Hz), beta band (14-30 Hz) and gamma band (>30 Hz). However, these band definitions are inconsistent across studies and it is common for these band ranges to vary by about 1-2 Hz within EEG literature [141].

A variant of EEG is intracranial EEG (iEEG), where a grid of electrodes is placed directly onto the brain, overcoming the poor spatial resolution typical of EEG. Furthermore, depth electrodes can be used and placed at any depth in the brain resulting in increased spatial resolution. However, the deeply invasive nature of this procedure means this is not commonly used outside the treatment of specific neurological conditions.

2.2 Chronobiology

FNs will be used to study circadian rhythms and chronotype within this thesis, these are introduced and discussed below.

2.2.1 Circadian Rhythms

Almost all bodily functions depend fundamentally on temporal oscillations. A diversity of biological clocks tightly interconnect to control processes over time scales of hours such as sleep stages or body temperature through to days and months, for example, hormone release or the female menstrual cycle [111].

Processes that oscillate with a period of around a day are called *circadian*. These include neurobehavioral (i.e. attention or mood), hormonal (i.e. melatonin or cortisol se-

cretion), and physiological (i.e. heart rate or body temperature) [205]. Circadian rhythms in the context of sleep refer to the naturally occurring oscillatory nature of a human's high and low sleep propensity [20].

Natural selection has led to nearly all living creatures having an endogenous circadian rhythm that is entrained by zeitgebers, 'time givers', with the strongest being the 24-hour cycle of the sun [40]. However, the processes that interact and contribute to the activity patterns of an individual are extremely complex, with both extrinsic factors such as zeitgebers as well as intrinsic factors such as the body's release of hormones contributing to the emergence of circadian rhythms.

In order to understand these processes, the field of sleep-wake dynamics and human circadian rhythms has been growing over the years. The field started in 1938 when Nathaniel Kleitman undertook an experiment with a forced desynchrony protocol over a period of a month within an underground cave [108]. The time isolation environment removed environmental clues that could have entrained the circadian rhythm, whilst the forced desynchrony protocol shortened (e.g. 20 h) or extended (e.g. 28 h) the natural sleep-wake schedule of the participants compared to the entrained circadian period of 24 h [205]. The constant dim-light conditions enabled him to find that the natural period of our unentrained circadian rhythm is actually ~ 25 h. In addition, the 28 h days with 9 h of sleep allowed him to understand and study our endogenous circadian rhythm under free-running conditions. This protocol is now used to disentangle the circadian and homeostatic processes of sleep, which are introduced in Section 3.3.

In addition to sleep times, circadian rhythms can also influence individual performance. For instance, during the Wake Maintenance Zone (WMZ) - a circadian push to wakefulness during the evening before bed - performance on tests can be boosted, despite extremely negative external conditions such as prolonged sleep deprivation, see Section 2.2.3. Furthermore, participants can see a reduced performance despite being well-rested, such as initially after awakening due to sleep inertia [27].

The phase and amplitude of an individual's circadian rhythm are also of concern. The

amplitude is typically measured as the peak-to-trough of harmonic functions fitted to either melatonin concentrations or core body temperature. Circadian amplitude can then be used as a proxy for circadian strength and can provide important information. For instance, it is theoretically possible that people with high amplitude circadian rhythms experience less of a phase shift in their circadian rhythm due to zeitgebers than people with a low circadian amplitude [205]. However, the intensity of any zeitgeber effect will depend on the time of the stimulation in relation to the circadian rhythm [87].

Furthermore, the phase relationship between a person's circadian rhythm and the external environment differs markedly between individuals, contributing to the classification of people according to their chronotypes [17].

2.2.2 Chronotypes

Chronotype defines the relationship between the internal circadian physiology of an individual and the external 24 h light-dark cycle. The Munich Chronotype Questionnaire (MCTQ), see Section 2.2.2.1, is a standard questionnaire for chronotype classification, which relies on Mid-point of Sleep on Free-days (MSF), as defined in eq 2.1. Classification can also be determined using actigraphy data and the timing of peaks in cortisol and melatonin concentrations from blood or saliva samples [59].

Chronotype classification falls across a spectrum, with Early Circadian Phenotypes (ECPs) and Late Circadian Phenotypes (LCPs) sitting at the two extremes and Intermediate Circadian Phenotypes (ICPs) in the middle. These two extreme phenotypes are often colloquially referred to as 'Morning Larks' and 'Night Owls'. Upon removing external social obligations, the sleep of ECPs and LCPs will show little difference - except for the phase between circadian rhythm and clock time. Indeed, extreme ECPs will wake up at the same time that extreme LCPs are falling asleep. For a typical population, the distribution is almost Gaussian with a slightly longer tail for LCPs [66].

Chronotype distributions differ depending on the population, but the MSF corrected for sleep on work days (MSF_{sc}), eq 2.2, can vary widely within a population, spanning

three-quarters of the day [158]. Two examples of chronotype distributions are presented later in Figure 4.2. More specifically, chronotype has been found to vary depending on age, with chronotype drifting later during adolescence before shifting earlier with older age, as well as sex with females showing a tendency for earlier chronotype than males [66].

Chronotype is a known risk factor for a variety of common health conditions. In particular, LCPs report lower sleep quality and more daytime sleepiness and, as explained in the Introduction, are associated with an increased risk of physical health complications [95], poor mental health [122] and the effect of chronotype on FC is predictive of cognitive outcomes across the day [56].

However, despite LCPs being at a higher risk many studies either only consider ICPs or chronotype is not accounted for at all, despite the fact it could explain a lot of the inter-individual variation seen in existing group studies. Some studies have considered the link between chronotype and FC, but so far no significant differences have been found between the graph metrics of extreme chronotypes [62, 64].

However, limited success has been achieved when considering the link between chronotypes and FC using seed-based analysis. For example, Facer-Childs et al. [57] seeded in the mPFC and PCC within the DMN. For both seeds, using the contrast ECP>LCP, the respective clusters were predictive of attentional performance as measured through a Psychomotor Vigilance Test (PVT). In addition, resting state Functional Connectivity (rs-FC) recorded from mPFC was predictive of Stroop performance[1], and PCC was predictive of subjective sleepiness measured using the Karolinska Sleepiness Scale (KSS). Facer-Childs also completed a similar analysis within the Motor Network (MN) system [58], where the MN rs-FC of extreme chronotypes was shown to contribute to individual variability in motor performance. On the other hand, Fafrowicz et al. [60] seeded in thirty-six different regions throughout the brain. The correlation of the resulting clusters'

[1]Stroop Test: While variations of the test exist the main principle is that two colour stimuli are presented simultaneously through the word of a colour being printed and the font colour used. Sometimes the stimuli will be congruent (i.e. the word red in a red font) and sometimes they will be incongruent (i.e. the word red in a blue font). The participant can then either be asked for to say the word or the colour of the font and the reaction time is recorded.

FC to time of day, chronotype, and time of day × chronotype were considered. The effect of chronotype manifested itself differently in these studies: chronotype alongside rs-fMRI was successfully used as a predictor of cognition by Facer-Childs et al. [57], whereas Fafrowicz et al. [60] failed to find a significant difference between extreme chronotypes with rs-fMRI and instead only found significant time of day effects.

2.2.2.1 Munich Chronotype Questionnaire

A typical first classification of chronotype can be found through the MCTQ, which was first introduced by Roenneberg et al. [158]. This questionnaire considers the sleep patterns of an individual on both 'working' and 'free' days and was developed as a quantifiable basis for classification - here working and free imply the presence and lack of restrictions on sleep and wake times respectively. This differs from previous questionnaires such as the one used by Torsvall and Åkerstedt in 1980, which relied upon subjective questions such as "If you always had to rise at $6:00$, what do you think it would be like?" [192]. The important distinction between free and working days in the MCTQ allows the MSF (eq 2.1) to be 'sleep corrected' for any sleep debt that has occurred on working days MSF_{sc} (eq 2.2) - sleep debt is discussed in more detail in Section 2.3.1. This correction is applied under the assumption that sleep debt impacts chronotype in a linear relationship. These terms can be understood through their equations [157]:

$$\text{MSF} = \text{sleep onset} + \frac{\text{sleep duration}}{2}, \tag{2.1}$$

$$\text{MSF}_{\text{sc}} = \text{MSF} - \frac{\text{sleep duration on free days} - \text{average weekly sleep duration}}{2}. \tag{2.2}$$

Facer-Childs et al. [56] then classified participants as follows (for the UK):

$$\mathrm{MSF_{sc}} \begin{cases} \leq 04:00 & \Rightarrow \mathrm{ECP} \\ \geq 05:30 & \Rightarrow \mathrm{LCP} \\ \text{Otherwise} & \Rightarrow \mathrm{ICP}. \end{cases} \tag{2.3}$$

While the use of the MCTQ allows for a quantitative boundary between ECPs and LCPs, in reality MSF and $\mathrm{MSF_{sc}}$ are continuous rather than categorical. The boundaries for $\mathrm{MSF_{sc}}$ used in eq 2.3 should be seen as a guide to the likely chronotype and are not absolute. Therefore, the classification of participants, especially near the boundaries, should be cross-referenced across multiple measures such as Dim Light Melatonin Onset (DLMO) and Cortisol Awakening Response (CAR); see Section 2.2.2.2 for more information. In addition, the times selected should be adjusted for different populations to take into account factors such as the time zone, social expectations, light exposure, and age of those taking the MCTQ as the reference population can affect the chronotype classification [156].

2.2.2.2 Dim Light Melatonin Onset and Cortisol Awakening Response

The gold standard for determining circadian phase (and therefore chronotype) is the measuring of intrinsic factors such as the level of melatonin and cortisol to determine DLMO and CAR times respectively [59]. The concentration of melatonin and cortisol in the body is measured through saliva or blood samples and the time of DLMO and CAR is usually the point where the concentration of the hormone increases past a certain threshold - specific to that hormone. The concentration of cortisol will increase towards the end of the biological night and will continue rising after awakening for a short period before decreasing during the day [182]. However, melatonin will increase in concentration before sleep, peaking during the biological night before decreasing [12]. Both hormones provide a reliable objective measure for the circadian phase, which is not influenced by societal constraints - unlike sleep timing.

2.2.3 Wake Maintenance Zone

Within the natural oscillation of the circadian rhythm, there is a period of time known as the Wake Maintenance Zone. The WMZ has been identified as a period where the circadian system maximally promotes wakefulness and performance shortly before sleep is promoted [47, 133]. For example, McMahon et al. [133] define the WMZ as 3 hours prior until 5 minutes after DLMO.

As the timing of DLMO is controlled by the internal circadian rhythm of the individual, the WMZ will show similar inter-individual variation to that of chronotype in terms of phase and strength can also vary. For LCPs the later phase of their circadian rhythm in combination with the WMZ can cause additional problems because any attempts to shift their sleep onset time earlier, to compensate for unnaturally early awakening times, could lead them to attempt falling asleep during their WMZ. Sleeping during the WMZ could then result in lower quality sleep due to a greater risk of sleep disruption [168].

Papers focusing on the WMZ are becoming increasingly common, see Figure 2.2, therefore, highlighting the importance of the WMZ. The effect of the WMZ during sleep deprivation studies is of particular interest. Indeed, during sleep deprivation performance on vigilance and complex attention as well as recognition and working memory tasks has been found to generally decrease with time awake [133]. However, the WMZ has been found to improve performance in complex attention and working memory tasks on the second day of a Constant Routine Protocol (CRP) - where external conditions such as light, temperature, food, movement and wakefulness are kept constant - even after 37 h awake. Indeed McMahon et al. found a significant impairment when comparing tests at 27 h awake to 24 h previously, whilst the comparison at 37 h awake (during the WMZ) produced results similar to the baseline 24 h prior [133]. This highlights the ability within complex attention and working memory tests for heightened performance during the WMZ, showing it can partially counteract the effect of prolonged sleep deprivation.

The effect of the WMZ as measured using PVT is less clear. Shekleton et al. [168] found PVT Reaction Time (RT) and lapses decreased during the WMZ compared to the

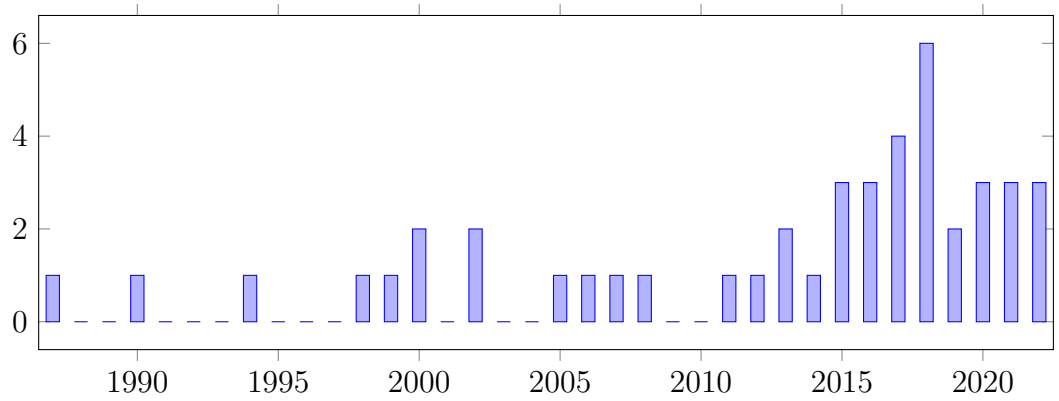


Figure 2.2: **Yearly Pubmed Publications after searching "Wake Maintenance Zone".** The number of publications each year when searching for the term "Wake Maintenance Zone" on PubMed. No papers existed before 1987.

tests taken in the 3 hours preceding the WMZ. However, when comparing across days of the sleep deprivation protocol a decrease in performance was seen both prior to the WMZ and during the WMZ. This is consistent with the PVT performance reported by McMahon et al. [133] where significant decreases in performance occurred across days of the sleep deprivation protocol despite testing during the WMZ. While the drop during the WMZ reported by Shekleton et al. was less severe than before the WMZ this result differs from the non-significant differences in performance on the complex attention and working memory tests by McMahon et al. [133]. Consequently, the effect of the WMZ may therefore be task dependent and needs to be better understood.

The effect of the WMZ on task performance suggests the WMZ may also affect the underlying brain regions responsible for completing the task. Circadian induced changes to FNs could offer insight into the processes of fatigue and more importantly how resilience to fatigue occurs. However, only limited research exists linking the WMZ to brain activity. For instance, Zeeuw et al. [46] found that absolute EEG power was higher when comparing the WMZ on the second day of a sleep deprivation protocol to the first day's WMZ, no research currently exists on how brain networks change.

The research into the different effects of sleep deprivation during different tasks, both inside and outside the WMZ, offers insight into how workplaces can organize the timings of responsibilities to maximize performance or decrease the risk of accidents. This could

be particularly useful in jobs that involve shift work or have a tendency for long hours. This could involve ending shifts such that driving home occurs during the WMZ [168] or tasks that require greater focus and precision are completed during the WMZ [133], benefiting the individual and businesses respectively.

2.3 Sleep Deprivation

Although it is not entirely clear if sleep duration has worsened over the past few decades [211] the Centres for Disease Control currently estimates that in America more than one-third of adults are regularly not sleeping sufficient amounts [33]. Sleep deprivation can take two forms: acute and chronic. Acute refers to short periods of sleep deprivation, for example a night of reduced sleep or no sleep over a small number of consecutive sleep periods. In contrast, chronic refers to the continued loss of sleep over a prolonged period of time, the American Academy of Sleep Medicine defines this as three months or over [184]. Typically this will involve sleep being restricted by a small amount each day i.e. a loss of 2 h of sleep per night. Sleep debt and 'social jetlag' can lead to chronic sleep deprivation that typically has differing effects on different chronotypes, this is explored more in Section 2.3.1.

Acute and chronic sleep deprivation are on opposite sides of the sleep loss spectrum, however for monophasic sleepers there is a common link: individuals, by the nature of sleeping less, are forced to be awake for longer continuous periods of time [52]. However, for polyphasic sleepers, it is possible that total sleep could decrease while each period of awakening is only a few hours. Therefore, typically the effect of sleep deprivation is not just the result of less sleep but also an excess of time awake. This concept is explored by Doren et al. [53] where participants were either undergoing total sleep deprivation or a 'nap' protocol with two 2 h naps equally spaced each day over 88 h. Both groups were therefore suffering from sleep deprivation but the nap group maintained near baseline PVT RT while 18 h into the experiment PVT performance significantly deteriorated for the total sleep

deprivation group. Highlighting that the deterioration was due to continuous time awake rather than total time awake. Although eventually, the cumulative sleep deprivation over a time period of weeks will result in similar levels of performance deterioration in the nap group as seen from total sleep deprivation over days [52]. Consequently, understanding the extreme case of acute sleep deprivation not only provides insights for people in professions where sleep deprivation is frequent, such as healthcare [170] or the military [134], but could also provide insight into the daily effects of sleep deprivation, which is prevalent in the world population.

The state instability hypothesis [53] - the ability to sporadically achieve baseline performance after total sleep deprivation due to the interaction of homeostatic and circadian processes as well as the participant's own compensatory effort, rather than the complete inability to complete tasks - has been theorised from the results of sleep deprivation studies. Indeed, Doran et al. [53] found that the standard deviation in RTs on a PVT test for each participant increased with time awake under a linear regression analysis and the average trend across all participants followed a combination of homeostatic and circadian processes. Thereby providing support for the state instability hypothesis. Doren et al. even suggested that sleep deprivation creates an 'unstable state that fluctuates within seconds', which is neither classified as awake nor asleep.

A key area of research is focused on predicting an individual's vulnerability to sleep deprivation without the need to sleep deprive them first, which may be possible due to trait-like differences to the effects of sleep deprivation. For instance, in Van Dongen et al. [49] participants were repeatedly subjected to three bouts of 36 h of Constant Routine (CR) sleep deprivation with 2 weeks of recovery between sessions. The effect of sleep deprivation was then measured subjectively using KSS and objectively through PVT lapses and performance on a word detection task. Throughout the three measurements, large inter-individual differences existed, while intra-individual results were relatively stable. Therefore, they concluded that trait-like vulnerability (or alternatively robustness) to sleep deprivation existed. When investigating potential causes for the trait-like vul-

nerability, both prior sleep history and baseline performance were unable to explain the differences. Interestingly, across the three measures, the rankings of the participant's average performance across the sleep deprivation protocols differed. For instance, one participant had the lowest impairment in the word detection task but the 3rd highest impairment in KSS, highlighting the difference between perceived and objective effects. Similar inter-individual differences in vulnerability were seen within the performance of 10 active-duty fighter pilots on a flight simulator during 38 h of sleep deprivation [50], highlighting systematic differences even between highly trained professionals when replicating a real-world task.

Inspired by Van Dongen et al. [49] Floros et al. [67] investigated potential reasons for differences in the vulnerability to sleep deprivation within an ADHD cohort, where half maintained normal-sleep (8-9 h in bed) and half were sleep deprived in laboratory conditions. The inattention trait, assessed using the Brown Attention Deficit Disorder Scale, was found to predict the variability in RT on a Stroop test, only in the sleep-deprived group. Therefore, the inattention of participants at baseline was predictive of impairment as measured using RT variability. The authors suggest that vulnerability to sleep deprivation 'is linked to a small cognitive buffer capacity'. Although the conclusions of this study were based on an ADHD cohort, a similar mechanism may underpin vulnerability to sleep deprivation in the general population. However, as neither group was tested under both conditions in combination with the known trait-like vulnerability to sleep deprivation the findings from this study should be replicated using a repeated measures design to ensure robustness.

Furthermore, many different imagining modalities have been used to assess the functional changes in the brain resulting from sleep deprivation, for instance, MEG [147], EEG [101, 110, 137, 195] (see Section 2.1.3) and fMRI [63, 172] (see Section 2.1.2).

For example, a similar study to Van Dongen et al. [49], which also investigated trait-like vulnerability to sleep deprivation, was completed by Chua et al. [37]. Participants completed 26 h of constant wakefulness twice. Inter and intra individual vulnerability to

sleep deprivation, measured using PVT aligned with the findings of Van Dongen et al. [49]. However, the study also looked for other explanations of the variation between participants. Indeed they found that individual differences in baseline measures (recordings during the first 16 h) in PVT response, blink rate, heart rate, heart rate variability and EEG spectral power in theta, alpha, and beta frequency bands were each able to explain at least 50% of the variability between participants. Extending the findings by Van Dongen et al. [49] past trait-like differences in only cognitive responses to also trait-like differences in ECG and EEG measures. Similarly, imaging measures were linked to sleep deprivation as Mu et al. [139] found that people with low baseline (measure at $09:00$ local time) global brain levels, measured using fMRI, were more vulnerable to sleep deprivation on a working memory task.

Furthermore, EEG was used to study sleep deprivation by Kar et al. [101], who found that sleep deprivation and, in particular the increased fatigue associated with increased time awake, is linked to increased node degree, clustering coefficient, small world index and a decrease in characteristic path length. In addition, the small world index was found to decrease in the delta and theta frequency bands and increase in the sigma ($12 - 14$ Hz) band [137]. However, contradictory findings do occur as Miraglia et al. [137] stated that sleep deprivation causes a shift to a more regular organization while Koenis et al. [110] found a shift towards a more random network structure through decreases in clustering coefficient and characteristic path length albeit only in the alpha band. Also, EEG [195] studies have found evidence that prefrontal and frontal regions are affected through clustering coefficient decreasing in the alpha band and path length increasing in the theta band and the minimum spanning tree increasing in diameter. Also, it was found that in sleep deprivation protocols, where EEG was measured with eyes-open recordings, higher delta/theta activity (4-5 Hz) as measured using power density was found to correlate with higher subjective sleepiness and reduced performance on some cognitive tests [46]. However, an increase in EEG activity in the alpha band only correlated with decreased performance on PVT, 2-Back and Negative Affect tests [46]. A

similar analysis was completed by Cajochen et al. [30] in which the change in the power density of a specific EEG band in frontal EEG channels was correlated to subjective sleepiness, RT and performance lapses (RTs > 500 ms) in PVT. It was found that low frequencies ($\sim 1.5-8.5$ Hz) had significant positive correlations across all three measures and some specific 0.5 Hz bins between $13-18$ Hz. It is also worth noting that within high alpha (~10.5 Hz) the correlation was actually negative, showing the decrease in alpha power with increasing sleep deprivation. The different approaches studies have taken and the sometimes contradictory findings highlight the lack of consensus in the literature and field as a whole, motivating more studies to contextualise these results further.

Also, Pesoli et al. [147] found that the diameter of the minimum spanning tree of the network significantly increased in size in the alpha band following a night of sleep deprivation using MEG. In addition, fMRI has been used to assess the FC, between brain regions in both resting-state acute deprivation [123] and task-based chronic deprivation [63] recordings. FMRI allows individual brain regions to be assessed and the DMN, visual network, limbic system [63] and thalamus [167, 172] were all shown to be affected. For instance, the thalamus lost its hub status following sleep deprivation [172]. Interestingly, not only is the DMN affected but it has been shown that sleep deprivation can affect the connectivity between midline posterior and anterior regions in the DMN with Wang et al. [202] finding the DMN shows increased modularity after sleep deprivation at both an individual and group level. Furthermore, under the effect of 34 h of sleep deprivation Liu et al. [123] reported that rs-fMRI networks showed the shortest absolute path length was significantly shorter and the small world index was significantly higher after prolonged sleep deprivation.

Therefore, the effects of sleep deprivation on the brain and its FNs have been studied in great detail. This is in part due to the health benefits that could arise from better managing the effects of prolonged wakefulness and the huge financial implications for work environments.

2.3.1 Sleep Debt and Social Jetlag

Sleep debt occurs when an individual is not sleeping the amount required by their body. This deficit in sleep can accumulate over time, leading to cognitive impairment. For example, Van Dongen et al. [52] ensured participants had their sleep time restricted to either 4 or 6 h per night for a period of 14 days. This chronic sleep restriction severely impacted the participant's performance as measured using PVT lapses. Indeed, 14 days of 4 h of sleep resulted in PVT lapses similar to 2 nights of total sleep deprivation. Furthermore, nightly sleep periods of 6 h over ~ 12 days still resulted in performance levels similar to 1 night of total sleep deprivation. However, it is worth noting that despite a continued decrease in performance on the PVT test and increasing sleep debt the participant's subjective sleepiness quickly plateaued. Suggesting a mismatch between cognitive performance and an individual's ability to interpret the effect of sleep debt.

Sleep debt may also arise due to circadian misalignments such as societal constraints or shift work. For instance, a common type of sleep debt has been coined 'social jetlag' [206] to indicate the similarity between the shift in sleep timing that occurs at the end of the working week with someone flying across multiple timezones on Friday before flying back at the end of the weekend [155]. It should be noted that social jetlag by itself does not guarantee sleep debt, but with additional societal pressure can commonly occur together. While for most people jetlag is an issue faced on an irregular basis, for many LCPs social jetlag is a chronic issue they face until retirement [155]. In particular, most working schedules favour ECPs, with 09 : 00 being a typical start time for many businesses, however since only ~29% of the population are considered ECPs [157] this leads to many LCPs suffering from a misalignment of their internal and external daily rhythms. One study that replicates the effect of chronic sleep deprivation, which LCPs can suffer due to social jetlag, is by Farahani et al. [63]. They restricted participants' sleep by 35% over a period of a week and then took task-based fMRI. The reported results were significantly increased characteristic path length and decreased small world index under sleep restriction compared to well-rested conditions. The contradictory results of Farahani

et al. and Liu et al. [123] could have been due to differences in experimental conditions (sleep restriction vs sleep deprivation), differences in scanning acquisition (task-based vs resting state) or differences in the methodological pipelines.

At the alternative end of the spectrum, sleep debt can arise for ECPs on free days as they are prone to societal pressure, especially from LCPs, to interact into the late evening [158]. Therefore, gaining a greater understanding of chronotypes could help to better understand and then overcome such issues.

In addition, sleep debt can be exacerbated due to shift work. Shift work, particularly that occurring at night, is often misaligned with an individual's internal circadian rhythm such that they are working during their biological night and trying to sleep when the circadian drive for wakefulness is maximal. This results in less sleep leading to sleep debt accumulating [80, 91].

However, it is currently debated if circadian misalignment or sleep loss and associated sleep debt is the cause of the negative impacts facing shift workers, and extreme chronotypes, as the two concepts are typically entwined [7].

2.4 Introduction to Excitability

At the microscale of a neuron, the concept of excitability is well defined - one such definition is: 'a perturbation to a state variable beyond a certain threshold elicits a response in that state variable much larger than the perturbation while a subthreshold perturbation elicits only a small amplitude response' [89]. This easily leads to excitability being viewed as part of a dynamical system.

One of the most famous examples of excitability is the Hodgkin-Huxley model for the Giant Squid Axon [90], which models how an action potential occurs in a neuron. Here a strong enough signal will change the permeability of the axon membrane creating a change in the electrochemical gradient between the inside of the neuron and the outside to alter, causing an upward spike in voltage. If the upward spike is high enough the spike in voltage

will propagate down the axon in a process known as an action potential and the neuron will fire. The threshold value allows greater control over neuronal firing, preventing the brain from being overloaded with noisy signals from unwanted action potentials from low signal inputs. Therefore, within the Hodgkin-Huxley model more excitability could be biologically translated into being closer to the threshold for which an action potential occurs.

In addition, in some cases excitability is defined as the overall ratio of excitation to inhibition [103]. For example, if there are more excitatory neurotransmitters, such as Glutamate, near a neuron then the neuron will be more excitable. In a similar manner, the inhibitory neurotransmitter GABA would lead to a less excitable neuron.

However, the macroscale concept of excitability is harder to define. Traditionally, excitability has been measured through the size of evoked cortical activity to a perturbation caused by an external magnetic (Transcranial Magnetic Stimulation (TMS)) or electrical stimulation [125, 135]. The use of stimulation-evoked responses has been considered the gold standard [135] for measuring excitability. The strength of the stimulus can easily be altered and responses have been well studied i.e. a limb twitch or the amplitude of the voltage response in the brain, making it a popular approach within the field. Indeed, Ly et al. [125] considered the excitability of participants over a 29 h sleep deprivation protocol using TMS. As consistent with Meisel et al. [135] a significant increase in the amplitude of the TMS response occurred between the first and last scan.

However, TMS has practical limitations as excitability is considered at a macroscale but only to the level of the brain area being stimulated. Therefore, alternative computational methods based on FNs are increasingly used to understand the excitability of brain networks. Indeed, within Schmidt et al. [164] the synchronisation of Kuramoto Oscillators, which is explained in detail in Section 3.2, is used as a proxy for excitability. Within the study, a significantly lower critical coupling is needed to synchronise the oscillators in the epilepsy cohort than in controls in theta (3–6 Hz) and low-alpha (6–9 Hz). Therefore, within the context of the study global synchronisation and the critical coupling strength

can be viewed as measures of excitability.

CHAPTER 3

INTRODUCTION TO METHODS

This thesis relies on several techniques, many of which are already commonly used within both the fields of neuroscience and mathematics. Key methods are outlined below to provide a basis for the results presented in later chapters.

3.1 Analysis of Large-Scale Brain Networks

The brain is a complex interconnected structure with approximately 86 billion neurons [86]. Focusing on the microscopic activity and connections between every neuron would not be feasible. Indeed, technology does not exist to access whole brain data at such a detailed level. Consequently, an increasingly common technique within neuroscience is to consider the brain from a macroscopic perspective [26] using fMRI and EEG data. Such data can be analysed and interpreted within the framework of network analysis and FNs are considered throughout this thesis.

3.1.1 Functional Network Pipeline

The pipeline needed to analyse fMRI and scalp EEG data using FC follows a fairly standardised form, therefore only an overview of this process is given below. However, the way in which they are implemented varies with imaging modality. Consequently, more detail will be provided in Chapter 4 for an fMRI dataset and Chapter 7 for an EEG

dataset.

This is not intended to be an exhaustive list of how FNs can be analysed but represents common methodological approaches, with a focus on those used in later chapters and an outline is provided in Figure 3.1.

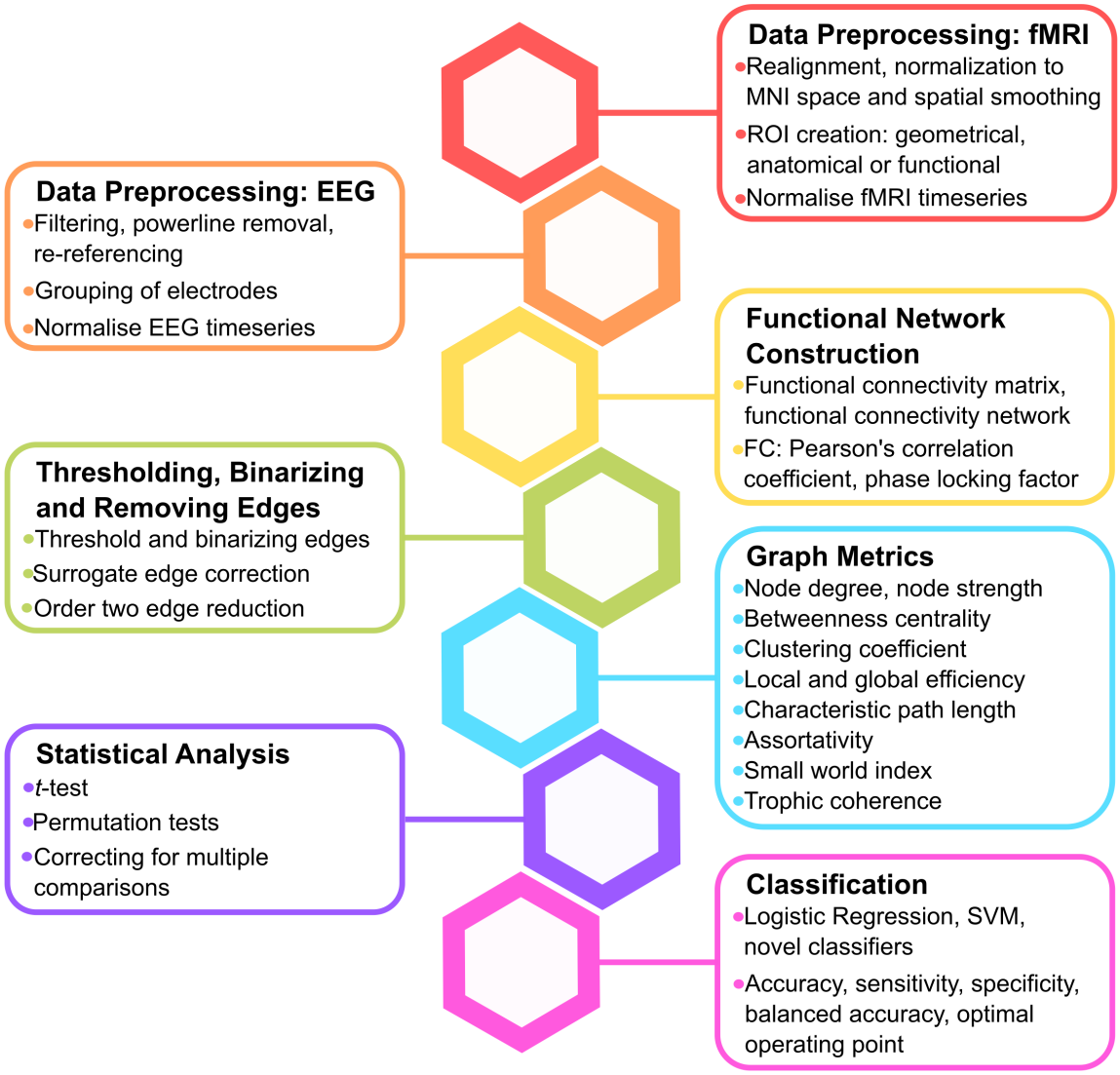


Figure 3.1: **Functional Network Flowchart.** After data acquisition this highlights the common steps used to produce graph metrics from FNs for the purpose of statistical testing and classification. The list is not exhaustive but covers the areas either typically used or methodologies used in later chapters.

3.1.1.1 Data Acquisition

First, data is acquired using fMRI or EEG to collect a BOLD signal or electrical signal, respectively. This will create multiple time-series for the brain activity corresponding to a voxel in fMRI or an electrode in EEG. The specifics of the collection protocol will change depending on the nature of the study.

3.1.1.2 Data Preprocessing: fMRI

Post-collection, data is preprocessed, ensuring each scan is clean and easily comparable. Within fMRI, common preprocessing procedures include realignment, normalization to Montreal Neurological Institute (MNI) space and spatial smoothing [5]. This enables voxels to be grouped together creating ROIs. Parcellating the brain through grouping time-series is especially important in fMRI, as there could easily be in excess of 100,000 voxels[1] and the individual activation of a single voxel is unlikely to be of interest at the scale of the whole brain [188]. Also, producing FNs with 100,000 nodes would reduce tractability, and increase computational time, whilst the high levels of noise in individual voxels could skew analysis through a low signal-to-noise ratio [45].

The choice of parcellation could be based on spatial position, anatomical connectivity, functional connectivity, or task-related activation of the voxels [188]. A purely spatial choice of parcellation will involve an arbitrary geometric clustering of near voxels using their spatial coordinates, as explained by Thirion et al. in [188]. An anatomical parcellation will consider anatomical landmarks within the brain such as those provided by sulco-gyral anatomy [188]. For instance, Automated Anatomical Labeling (AAL) is an anatomical parcellation, which is reliant on spatial position but is also governed by brain topology. FC and task-related activation parcellations consider the time-series of voxels and group voxels with similar time-series, typically using a clustering approach or ICA.

However, while parcellation is commonly done, the specific choice of parcellation can

[1] A conservative estimate for the volume of a human brain would be $1,060$ cm^3 [191] if a voxel size of 8 mm^3 is used then the number of voxels would be approximately $132,500$, which would create a network of $132,500^2$ edges if voxels rather than ROIs were used.

be problematic, since there is currently no consensus on which is optimal [63]. In many cases it has been shown that functional parcellations are better than structural for a range of success measures including the ability to classify cognitive states using rs-fMRI data [169] and goodness of fit to a probabilistic model for a dataset [188]. In addition, Smith et al. [177] considered how the mixing of BOLD signal time-series from nodes within simulated networks would affect their ability to recreate a FN i.e. the 'ground truth'. This mixing of node output is reminiscent of what would happen if structural ROIs, with different spatial boundaries to functional ROIs, were used to assess FC. The resulting ability to detect an edge in a FC ground truth across the 38 FC measures considered is then reduced from 90%, which was achieved by the most successful methods when no mixing of BOLD signals occurred, to less than 20%. Indeed structural parcellations have been shown to be so ineffective that geometric parcellations perform better [188].

For fMRI each time-series may then be normalised such that it has a mean 0 and standard deviation 1 - allowed under the null hypothesis of Gaussian noise [10]. This is a standard assumption used frequently within the field of fMRI, for example within the Human Connectome Project and UK Biobank datasets.

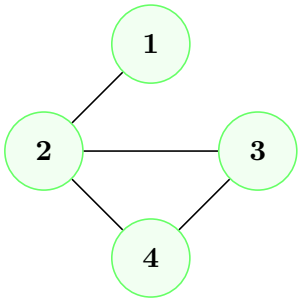
3.1.1.3 Data Preprocessing: EEG

Within EEG pipelines filtering, power-line removal and referencing are common steps [153]. The lower spatial resolution of EEG results in significantly fewer channels than voxels, with many clinical settings using a variant of the 10-20 electrode placement, as seen in Figure 2.1, and recording ~20 channels. However, the number of electrodes can vary from 6 up to high-density 256-channel EEG [36]. Therefore, it is rarer for the time-series from EEG electrodes to be grouped, instead each channel is typically treated as a node in the network where each time-series represents the contribution to that electrode from the brain. However, sometimes nodes may be created by grouping channels in close physical proximity; for example frontal, parietal or occipital channels from each brain hemisphere may each form a node [150].

The time-series from each EEG channel may then be normalised such that it has a mean 0 and standard deviation 1, which has been shown to increase the predictive capacity when trying to localise the region of seizure onset in simulated iEEG networks compared to no normalisation [194].

3.1.1.4 Functional Network Construction

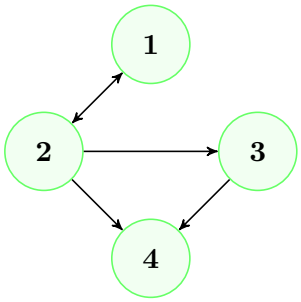
Once each time-series has been extracted, artifact-free epochs with a good signal-to-noise ratio are selected for further analysis. The statistical dependency between pairs of time-series then determines the FC. This information can then be represented on a FN, with each ROI or electrode representing a node on the network and the FC measure providing the edge weight between nodes. Analogously, this can be represented in a functional connectivity matrix, where the i, j^{th} entry represents an edge from node j to node i. The network can be undirected (Figures 3.2a and 3.2b) or directed (Figures 3.2c and 3.2d).



(a) Undirected Binary FN

$$\begin{bmatrix} 0 & 1 & 0 & 0 \\ 1 & 0 & 1 & 1 \\ 0 & 1 & 0 & 1 \\ 0 & 1 & 1 & 0 \end{bmatrix}$$

(b) Undirected Adjacency Matrix



(c) Directed Binary FN

$$\begin{bmatrix} 0 & 1 & 0 & 0 \\ 1 & 0 & 0 & 0 \\ 0 & 1 & 0 & 0 \\ 0 & 1 & 1 & 0 \end{bmatrix}$$

(d) Directed Adjacency Matrix

Figure 3.2: **Undirected and Directed Functional Networks and Corresponding Adjacency Matrices.**

For binary networks the presence or lack of an edge is denoted by the edge having a value 1 or 0 respectively. However, weights can also be assigned to the edges in which

case $w_{i,j}$ is the strength of the FC from node j to node i (Figures 3.3a and 3.3b).

FN strength can vary within different ranges depending on the type of FC used. For example, Pearson's Correlation (PC) is a linear correlation between two signals and ranges between $[-1, 1]$. If the two signals are x and y then the Pearson's Correlation Coefficient is given by,

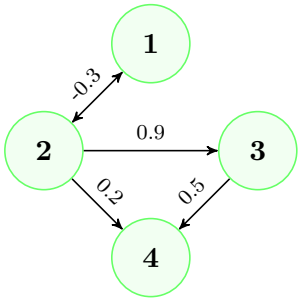
$$r_{PC} = \frac{\sum_{t=1}^{L}(x(t) - \bar{x})(y(t) - \bar{y})}{\sqrt{\left(\sum_{t=1}^{L}(x(t) - \bar{x}) \sum_{t=1}^{L}(y(t) - \bar{y})\right)}}, \tag{3.1}$$

where $\bar{x}$ and $\bar{y}$ denote the sample means and L is the number of timepoints in both signals. Furthermore, PLF, introduced by Lachaux et al. [118], is based on the phase between two signals and ranges between $[0, 1]$, see Section 6.2.6 for more details.

3.1.1.5 Thresholding, Binarizing and Removing Edges

Once FC is calculated between each pair of nodes a common next step is to decide which information - if any - to remove, through the deletion of edges and binarization. Thresholding is used to remove connections when edge weights are less than a given thresholding value, $\bar{t}$, i.e. $w_{i,j} = 0$ if $w_{i,j} < \bar{t}$. The threshold can be either absolute, such that the same value is used for thresholding every network (Figure 3.3c), or proportional such that the top $x\%$ of strongest edges remain in each network. Thresholding focuses the analysis on edges with the highest strength to try and avoid spurious edges in the network (false positives) [213]. An alternative is to use a network feature to define the threshold such as selecting the Minimum Connected Components (MCCs), the highest threshold that retains connectedness, or the minimum spanning tree, a network with no cycles connecting all nodes with the minimum total weight such as 'time'.

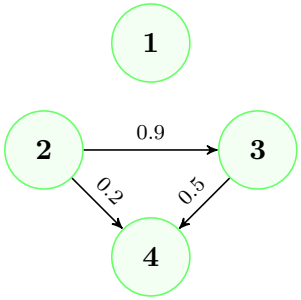
In addition, edges could be removed using surrogate correction. This identifies edges where the connections are sufficiently strong compared to the edge created by noisy uncorrelated versions of the time-series. Indeed, a large number of surrogate networks can be created by using Iterative Amplitude Adjusted Fourier Transformed (IAAFT) time-series - a Fourier-based method which ensures the autocorrelation and power spectrum of



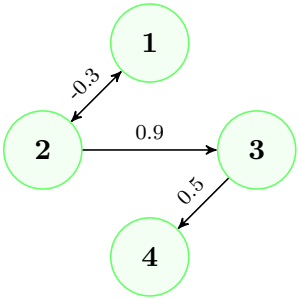
(a) Weighted Directed FN

$$\begin{bmatrix} 0 & -0.3 & 0 & 0 \\ -0.3 & 0 & 0 & 0 \\ 0 & 0.9 & 0 & 0 \\ 0 & 0.2 & 0.5 & 0 \end{bmatrix}$$

(b) Weighted Adjacency Matrix



(c) $\bar{t} = 0.1$



(d) Order Two Reduction

Figure 3.3: **The Functional Network and Corresponding Adjacency Matrix for Weighted Network and Edge Reduction Techniques. (a)** A toy weighted FN and **(b)** its weighted adjacency matrix. **(c)** The disconnected subnetwork after a threshold of $\bar{t} = 0.1$ is applied. **(d)** The edges remaining after an order two edge reduction is applied. Here $w_{4,2}$ is removed as that path has a 'time' of 5 units while the stronger alternative path from node 2 to 3 to 4 has a 'time' of $3.\dot{1}$ units.

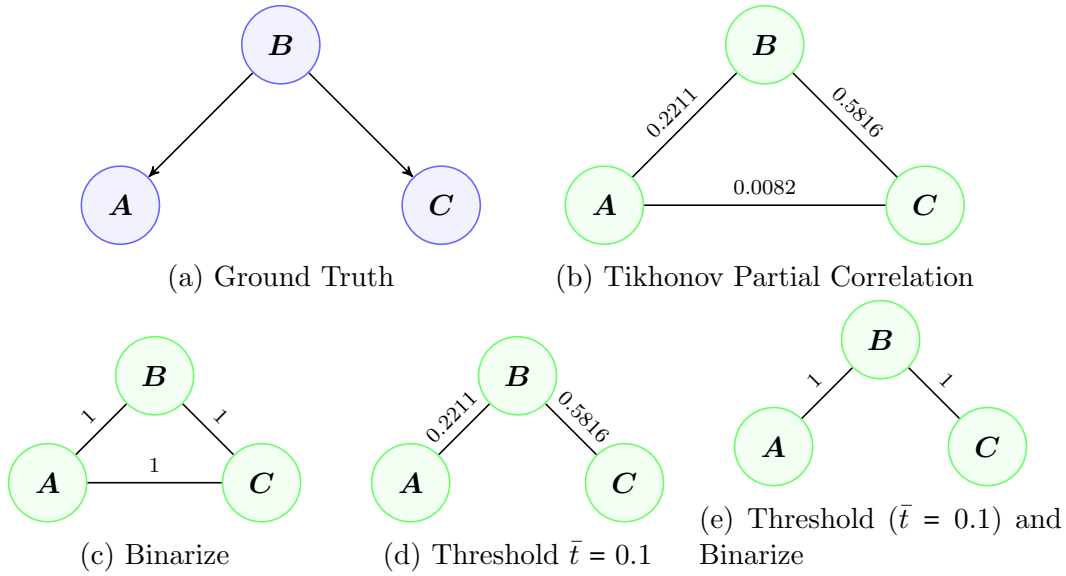
the time-series are preserved [161]. Then edges with a weight considered non-significant, $p > 0.05$, compared to a null distribution of surrogates will be replaced by 0 [207].

Also, an edge reduction technique can be used, which removes an edge if there is a stronger alternative path between those ROIs, see Figure 3.3d. In this case, FC is viewed as a 'speed', 'distance' along an edge has the value 1 and therefore a stronger alternative path can be viewed as a route which requires less 'time'.

A combination of these edge removal techniques can be used depending upon which best aid the research question. In some cases, the full weighted network is used. However, depending on the FC it is typical that only edge weights of the same sign ($+ve / -ve$) are analysed together for easier interpretation of the results.

While the 'ground truth network' of real data cannot be known, edge reduction techniques are used as removing edges with low FC, non-significance edges and non-dominant

edges helps to increase sparsity and tractability and are thought to remove false positive edges, as highlighted by Figure 3.4.



(a) Ground Truth (b) Tikhonov Partial Correlation

(c) Binarize (d) Threshold $\bar{t} = 0.1$ (e) Threshold ($\bar{t} = 0.1$) and Binarize

Figure 3.4: **Relationship Between Ground Truth and Simulated Functional Networks. (a)** The ground truth. **(b)** The simulated undirected weighted FN created using Tikhonov Partial Correlation. The time-series of the three ROIs are each governed by, $A = 0.3B + \epsilon_1$, $B \sim_{iid} N(0, 1)$ and $C = 0.8B + \epsilon_2$, where ϵ_1 and ϵ_2 are random noise from the distribution $N(0, 1)$. **(c)** The FN after binarizing (b). **(d)** The FN after thresholding (b) at $\bar{t} = 0.1$. **(e)** The FN after thresholding at $\bar{t} = 0.1$ and binarizing (b).

3.1.1.6 Graph Metrics

Upon creating FNs, a common step is to use graph theory to consider the structure of the network by calculating both local and global graph metrics [26, 160]. More information about node degree, node strength, betweenness centrality, clustering coefficient, global and local efficiency, characteristic path length, assortativity, small world index and trophic incoherence is provided later in this Section.

The literature surrounding the use of graph metrics to analyse brain activity is an area that is reasonably new, gaining popularity in the past decade or so, after the release of the Brain Connectivity Toolbox (BCT), a MATLAB (MathWorks, USA) toolbox, first presented by Rubinov et al. [160]. This is a toolbox designed to infer network structures from data and to allow their properties to be easily calculated. Therefore, graph

metrics have been used to analyse fMRI data across many contexts from epilepsy [43] to differentiating between cognitive states [169].

Graph metrics are calculated throughout the later chapters. How to calculate the graph metric and an explanation of its interpretation is provided below for a binary matrix $\mathbf{A}$ with elements $a_{i,j}$ and a weighted matrix $\mathbf{W}$ with elements $w_{i,j}$ both with N nodes.

Node Degree and Node Strength For a binary undirected network, the number of edges connected to node i is the node degree, k_i,

$$k_i = \sum_{j=1}^{N} a_{i,j}.$$

This represents the number of nodes attached to node i [71]. The average node-degree for a network is given by,

$$\langle k \rangle = \frac{1}{N} \sum_{i=1}^{N} k_i.$$

Node strength is a weighted variant of node degree with s_i representing the strength of the connection of node i to its neighbours, therefore,

$$s_i = \sum_{j=1}^{N} w_{i,j},$$

and mean node strength is given by,

$$\langle s \rangle = \frac{1}{N} \sum_{i=1}^{N} s_i.$$

In addition, node degree can be extended to directed networks through the in-degree and out-degree of a node,

$$k_i^{\text{in}} = \sum_{j=1}^{N} a_{i,j} \qquad\qquad k_i^{\text{out}} = \sum_{j=1}^{N} a_{j,i}, \tag{3.2}$$

and similarly the in-weight and out-weight of a node is given by,

$$s_i^{\text{in}} = \sum_{j=1}^{N} w_{i,j} \qquad\qquad s_i^{\text{out}} = \sum_{j=1}^{N} w_{j,i}. \tag{3.3}$$

Betweenness Centrality Betweenness centrality considers the importance of node i in the context of the shortest paths in the network by calculating the fraction of shortest paths that pass through node i. It is calculated using the formula,

$$B_i = \sum_{i \neq j \neq k} \frac{n_{jk}^{i}}{n_{jk}},$$

where n_{jk} is the number of shortest paths between nodes k and j and n_{jk}^{i} is the number of shortest paths between nodes k and j which pass through node i. The notion of the shortest path can easily be extended to include edge weights and directionality. The mean betweenness centrality is then given by,

$$\langle B \rangle = \frac{1}{N} \sum_{i=1}^{N} B_i.$$

Clustering Coefficient Local and Global The clustering coefficient, C_i, shows how nodes local to node i are connected. A higher clustering coefficient suggests that if node i is removed from the network many paths will still exist between its neighbours, hence indicating a resilient network section.

A common way to calculate the clustering coefficient and the formula used in BCT for binary undirected networks is,

$$C_i = \frac{\text{number of edges between neighbours of } i}{\text{number of possible edges between neighbours of } i}, \tag{3.4}$$

where $0 \leq C_i \leq 1$ and can be considered at a global scale using [203],

$$\langle C \rangle = \frac{1}{N} \sum_{i=1}^{N} C_i. \tag{3.5}$$

For directed binary networks the definition for C_i extends to the ratio between all directed triangles which include node i and all possible triangles that node i could form. Also, for weighted networks the approach is similar to the binary case but the cube root of the edge weights is calculated before the length of 3 node cycles is used for determining the clustering coefficient [61].

Global and Local Efficiency Global efficiency measures the ability of a network to send information in parallel. This considers the inverse of the shortest path between all nodes in the network and hence shorter paths lead to increased global efficiency [119], the formula is given by,

$$E^{\text{glob}} = \frac{1}{N(N-1)} \sum_{i \neq j \in \mathbf{D}} \frac{1}{d_{i,j}}, \tag{3.6}$$

where $\mathbf{D}$ is the distance matrix with elements $d_{i,j}$ giving the shortest distance from node j to i and it has been normalised by the number of possible edges in the network. In the weighted case the element $d_{i,j}$ represents the fastest 'time' from j to i where $w_{i,j}$ represents the 'speed' of the connection from j to i. For the directed case $d_{i,j}$ is the shortest directed path from node j to i.

Local efficiency is linked to global efficiency however this shows how efficiently the neighbours of a node could communicate if the node was removed [119]. Therefore, eq 3.6 is still used however the network being considered is $\mathbf{A}_i$ (or $\mathbf{W}_i$) - the subgraph of the neighbours of i - with distance matrix $\mathbf{D}_i$. The formula is given by,

$$E_i^{\text{loc}} = \frac{1}{N(N-1)} \sum_{i \neq j \in \mathbf{D}_i} \frac{1}{d_{i,j}}.$$

Taking the average of the local efficiency gives mean local efficiency,

$$\langle E^{loc} \rangle = \frac{1}{N} \sum_{i=1}^{N} E_i^{\text{loc}}.$$

Characteristic Path Length The path length between two nodes is the smallest distance between those two nodes. The characteristic path length, λ_L, is then the mean path length for all possible pairs of nodes. The formula is given by,

$$\lambda_L = \frac{1}{N(N-1)} \sum_{i \neq j} d_{i,j}.$$

For weighted and directed networks, similarly to Efficiency, the definition for $d_{i,j}$ is slightly amended to take these factors into account. For a disconnected graph, this would result in at least one path length of infinity and hence a characteristic path length of infinity. This highlights how decisions about thresholding and connectedness may affect graph metrics.

Assortativity The assortativity of a graph indicates a node's preference to attach to nodes with a similar degree [187]. Having an assortative network will increase the network's overall resilience since if one node experiences failure its neighbours can more easily assume the role as hubs will be more interconnected.

The formula for assortativity on a binary undirected network is given by [121],

$$r_{ass} = \frac{\frac{1}{N_E} \sum_{(i,j) \in E} k_i k_j - \left(\frac{1}{N_E} \sum_{(i,j) \in E} \frac{1}{2}(k_i + k_j) \right)^2}{\frac{1}{2N_E} \sum_{(i,j) \in E} (k_i^2 + k_j^2) - \left(\frac{1}{N_E} \sum_{(i,j) \in E} \frac{1}{2}(k_i + k_j) \right)^2},$$

where N_E is the total number of edges in the network and E is the set of edges in the network. The formula for weighted networks is fairly analogous, with W_E representing

the total weight of the network,

$$r_w = \frac{\frac{1}{W_E}\sum_{(i,j)\in E} w_{i,j}s_i s_j - \left(\frac{1}{W_E}\sum_{(i,j)\in E}\frac{w_{i,j}}{2}(s_i + s_j)\right)^2}{\frac{1}{2W_E}\sum_{(i,j)\in E} w_{i,j}(s_i^2 + s_j^2) - \left(\frac{1}{W_E}\sum_{(i,j)\in E}\frac{w_{i,j}}{2}(s_i + s_j)\right)^2}.$$

Finally, the formula for the directed network is given by,

$$r_d = \frac{\frac{1}{N_E}\sum_{(i,j)\in E} k_i^{\text{out}} k_j^{\text{in}} - \left(\frac{1}{N_E}\sum_{(i,j)\in E}\frac{1}{2}(k_i^{\text{out}} + k_j^{\text{in}})\right)^2}{\frac{1}{2N_E}\sum_{(i,j)\in E}({k_i^{\text{out}}}^2 + {k_j^{\text{in}}}^2) - \left(\frac{1}{N_E}\sum_{(i,j)\in E}\frac{1}{2}(k_i^{\text{out}} + k_j^{\text{in}})\right)^2}.$$

Small World Index The graph metric that reconciles the two different objectives of functional integration and segregation is the small world index [203]. The small world index, S, is seen as a measure of efficiency, as measured through comparisons with suitable random graphs. A common example is corresponding Erdős-Rényi (E-R) random graphs, which have the same fundamental properties of the original network, with the same number of nodes and on average the same number of edges - as assigned through edges having a probability p_{ER} of existing. The small world index then compares the characteristic path length, λ_L, and clustering coefficient, C, for the original graph and the corresponding values from E-R random graphs. The small world index was studied in detail by M. D. Humphries and K. Gurney [96] and is given the following quantitative definition.

Definition 3.1.1. A network is said to be a small world network if $S > 1$. Where,

$$S = \frac{C^s}{\lambda_L^s} \text{ such that } C^s = \frac{C}{C^{\text{rand}}} \text{and } \lambda_L^s = \frac{\lambda_L}{\lambda_L^{\text{rand}}}.$$

Here the superscript 'rand' denotes the mean of the metric across the ensemble of random networks. A high small world index indicates a high clustering and low characteristic path length, which can be interpreted as enabling efficient transfer of information across a network. In an anatomical network this would represent efficient placement and

use of neuronal tracts. However, the interpretability of this metric is less clear from a FC perspective, which considers statistical relationships between brain regions rather than physical connections. It is important to note that the small world index for a disconnected graph is 0.

Alternatively, analytic approximations for the clustering coefficient and characteristic path length for E-R random graphs are given by [96],

$$C^{an} \approx \frac{\langle k \rangle}{N} \text{ and } \lambda_L^{an} \approx \frac{\ln\left((N-1)\left(\langle k \rangle^2 - \langle k \rangle\right) + \langle k \rangle^2\right) - \ln\left(\langle k \rangle^2\right)}{\ln\left(\frac{\langle k \rangle^2}{\langle k \rangle}\right)} \approx \frac{\ln(N)}{\ln\left(\langle k \rangle\right)}. \quad (3.7)$$

For directed and weighted networks, the process is similar and again definition 3.1.1 is used. However, the creation of C^{rand} and λ_L^{rand} slightly differs. In this case (for networks with no self-links and at most one directed edge between two nodes) the edges in the network are randomised such that a new network is created with the same weight distribution as the original network, but the position of the edges is randomised [75]. Multiple different randomisations are done to create a null distribution, which can be used to calculate C^{rand} and λ_L^{rand}.

Trophic Levels and Trophic Incoherence Trophic levels and incoherence are local and global graph metrics respectively. They can only be calculated on directed networks, which must be at least weakly connected. The concept of trophic incoherence has evolved over time from the context of an animal's level in a food web [104] to the stability of food webs [100], economy and trade [6], and even the spread of epidemics and neuronal avalanches [107] throughout networks. The definition of trophic incoherence has also been generalised to include strongly connected networks and therefore removes the reliance on *basal* nodes - nodes with an in-degree of 0. Consequently, enabling coherence to be extended into a diverse range of contexts including regulatory networks in biology and even the coherence of book translations between languages [126].

The most intuitive context for understanding trophic incoherence is within a food

chain. Here basal nodes defined as nodes with a trophic level of 0 will represent plants at the bottom of the food chain, pure herbivores would have a trophic level of 1 and various predators would have higher trophic levels until the apex predator at the top has the highest trophic level.

However, models for food webs very rarely contain cycles [107], which is an important feature of FNs. In the context of the brain, the trophic level of a node could be considered in terms of information flow or regional influence within the network. For example, basal nodes will only influence other regions, however nodes with the highest trophic level will receive large amounts of information from the network.

The trophic level, h_i, of node i is then defined by the solution to the linear system of equations [126],

$$\Lambda h = v;$$

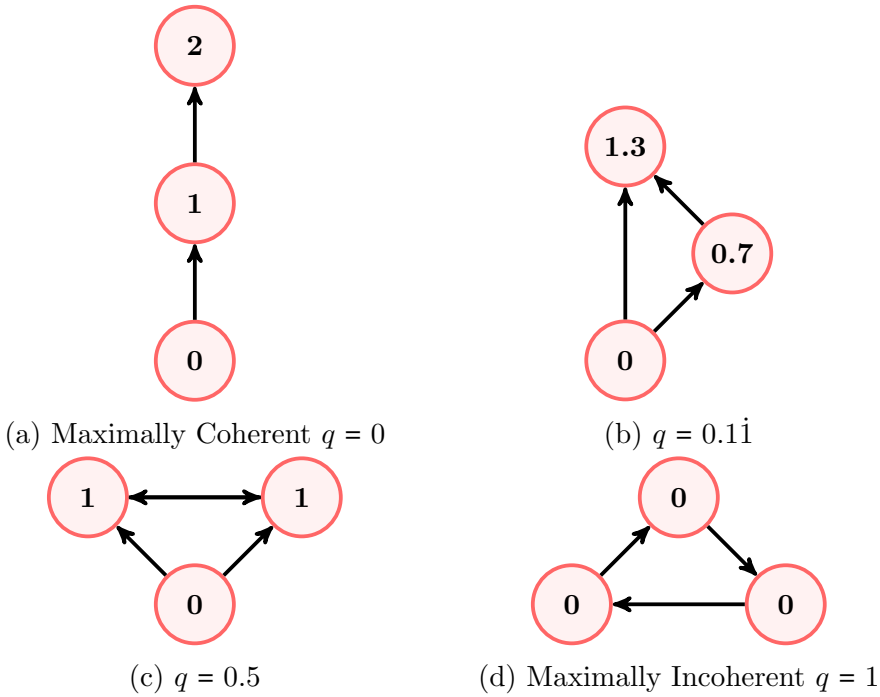
where

$$\mathbf{\Lambda} = \text{diag}(u) - \mathbf{W} - \mathbf{W}^{'} \text{ and } u_i = s_i^{\text{in}} + s_i^{\text{out}} \text{ and } v_i = s_i^{\text{in}} - s_i^{\text{out}},$$

where $'$ denotes matrix transpose. Both binary and weighted networks can be considered, here the weighted version is given but the binary version is analogously defined using $\mathbf{A}$ and eq 3.2 rather than eq 3.3. While trophic levels can provide a lot of information about the node's position in a network, tropic incoherence summarises the ability for the network to be split into clearly defined trophic levels and therefore how directed the network is. Trophic incoherence, $0 \leq q \leq 1$, is calculated by,

$$q = \frac{\sum_{i,j} w_{i,j}(h_i - h_j - 1)^2}{\sum_{i,j} w_{i,j}}.$$

If directedness is clear (Figures 3.5a and 3.5b) the network is coherent and q is near 0. If directedness is unclear 3.5d the network is incoherent and q is near 1. Intermediate values (Figure 3.5c) occur due to the combination of indirect and direct paths, basal nodes and cycles.



(a) Maximally Coherent q = 0 (b) q = 0.1i̇

(c) q = 0.5 (d) Maximally Incoherent q = 1

Figure 3.5: **Trophic Incoherence Examples.** Here the spectrum of trophic incoherence is presented **(a)** maximum coherence **(b)** and **(c)** showing low to intermediate levels of trophic incoherence respectively and **(d)** maximum incoherence. In each case the number inside the node is the trophic level of the node, with 0 indicating a basal node.

3.1.1.7 Statistical Analysis

Once the properties of each participant's FN have been calculated statistical analysis can be completed, common statistical tests include t-test for data with a normal distribution and permutation tests for non-parametric data. For example, if a patient cohort is compared to a control cohort then significant differences between the graph metrics of the two groups could provide insight into the patient cohort and potentially provide a biomarker for the purposes of diagnosis, through machine learning. For instance, the mean node degree of FNs from people with epilepsy is statistically higher than controls [35]. In addition, healthy participants can be compared to themselves under an experimental protocol in a similar manner. For example, the small-worldness of participants, when sleep deprived, is found to be significantly higher than their small-worldness at baseline [123]. It is important when completing statistical tests to correct for multiple comparisons, to avoid false positives. For example, the Benjamini-Hochberg method can be used to correct p-values

by taking into account the number of comparisons [11].

3.1.1.8 Classification

Graph metrics can also be used within machine learning to train a classifier. Examples of classifiers used in this thesis include logistic regression and Support Vector Machines (SVM). Classifiers have wide potential utility, including diagnosis or testing the robustness of the differences between the two cohorts.

A classifier's performance can be measured in multiple ways, these can include measures such as sensitivity (True Positive Rate (TPR) eq 3.8), specificity (True Negative Rate (TNR) eq 3.9), False Positive Rate (FPR) (eq 3.10) and accuracy (eq 3.11),

$$\text{TPR} = \frac{\text{TP}}{\text{TP} + \text{FN}} \quad (3.8) \qquad \text{TNR} = \frac{\text{TN}}{\text{TN} + \text{FP}} \quad (3.9) \qquad \text{FPR} = \frac{\text{FP}}{\text{TN} + \text{FP}} \quad (3.10)$$

$$\text{Accuracy} = \frac{\text{TP} + \text{TN}}{\text{TP} + \text{TN} + \text{FP} + \text{FN}}, \tag{3.11}$$

with T, F, P and N standing for true, false, positive and negative respectively. Sensitivity and specificity can also be summarised together by considering the Optimal Operating Point (OOP). The OOP is used in Receiver Operating Characteristic (ROC) analysis to select the most optimal result which combines high TPR and low FPR, such that OOP represents how close a classifier would be to the coordinate $(0, 1)$ in an FPR-TPR graph. We will use the equation,

$$\text{OOP} = 1 - \frac{\sqrt{(1 - \text{TPR})^2 + (\text{FPR})^2}}{\sqrt{2}}. \tag{3.12}$$

Here OOP has been normalised to ensure values between $[0, 1]$ and subtracted from 1 so that a high fraction equates to high accuracy.

It is important to note that these performance measures may not provide results if

the classifier allows for test data to be unclassified. For instance, if all of group 1 are unclassified such that TP and FN both equal 0 then TPR is meaningless.

Statistical significance between the graph metrics of two groups can indicate success in classification. However, statistical significance does not guarantee success as a clinical biomarker. For example, Schmidt et al. [165] found that the classification of patients and controls using mean node degree produces only 3.3% sensitivity and 15.8% specificity, despite Chowdhury et al. [35] finding significant differences between the mean node degree of the two cohorts. It is worth noting the classifier used was extremely conservative and required 100% in the alternate measure i.e. 3.3% sensitivity given 100% specificity.

3.1.2 Network-Based Statistic

An alternative to graph metric pipelines is an approach called Network-Based Statistic (NBS). Used in Chapter 5, this approach was first introduced by Zalesky et al. [212], when published alongside a freely available NBS toolbox for MATLAB. The original purpose of NBS was to establish a connected component known as a *dysconnected* subnetwork where the patient group showed weaker connections than the control group or vice versa[1]. This was not always possible before this method, due to the need to correct for the multiple comparisons testing each edge creates.

NBS is neither a seed-based method nor a connectivity-based method, but an intermediate. For example, NBS does not require a seed like seed-based approaches, neither is it used to calculate graph metrics per subject like many connectivity-based approaches. However, there are similarities between NBS and these methods. For instance, NBS utilises connectivity-based approaches both through the method requiring a FN for each participant and the method producing a single group-level FN - the dysconnected network. Also, like seed-based approaches, NBS utilises contrasts and statistical tests to understand directed group-level differences - in this case the differences in the edge weights between

[1]Not to be confused with a disconnected (sub)network, which occurs when at least one node has no path to at least one other node in the (sub)network.

two ROIs rather than two clusters. Therefore, NBS encompasses a mixture of the two methods whilst also being distinctly different.

The steps for implementing NBS are summarised in Figure 3.6 and explained below for a network with N nodes.

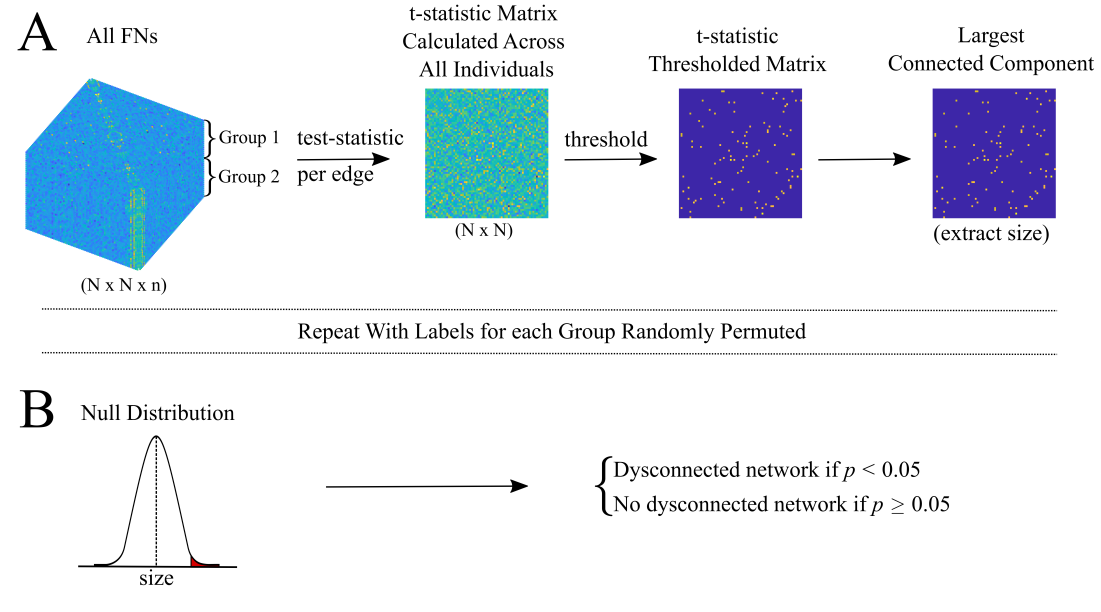


Figure 3.6: **Summary Pipeline for Network Based-Statistic. (A)** The stacked FNs ($N \times N$) of all n participants with labels assigning them to Group 1 or Group 2, from which a t-statistic matrix can be calculated across all participants per edge. The t-statistic matrix is then thresholded and the largest connected component as well as its size is extracted. This process is then repeated with the Group 1 and Group 2 labels randomly permuted to create a null distribution of the largest connected component sizes. **(B)** The size of the actual largest connected component is compared to the null distribution to obtain a p-value. When the largest connected component is significant ($p < 0.05$) a significant dysconnected network exists, otherwise no significant dysconnected network is found.

The test-statistic considered can vary depending on the experimental data but a t-test is presented by Zalesky et al. [212]. Therefore, for each edge in turn across the participant's FNs a one-sided t-test is carried out with either contrast $[1, -1]$ or $[-1, 1]$, hence producing an $N \times N$ matrix of t-statistics. The t-statistic matrix is then thresholded using an absolute t-statistic threshold, $\bar{t}_s$. Finally, only the suprathreshold edges in the Largest Connected Component (LCC) remain. The novel feature of NBS is the significance test that is now completed to overcome the issue of multiple comparisons that arises from

$\frac{(N\times N)-N}{2}$ (for an undirected network) t-tests. The significance test compares the 'size' of the connected component to a null distribution of $\hat{N}$ connected component 'sizes' created from randomising the groups to which participants are assigned. A Family Wise Error (FWE) corrected p-value is then calculated as the number of random permutations with a 'size' larger than the actual 'size', normalised by the number of random permutations. The term 'size' can refer to either the number of edges or the total weight of the t-statistics in the LCC. It is noted in the NBS Toolbox Reference Manual [214] using 'size' to refer to weight is better for strong, focal or distributed effects within relatively few edges, whereas the number of edges is better for relatively weak effects across a large proportion of connections. A common disadvantage to NBS is the requirement to select $\bar{t_s}$, with no rigorous selection process. Indeed, the only recommendation in the NBS Toolbox Reference Manual [214] is to try a range of threshold values.

A recent expansion to NBS is NBS Predict [166], which aims to classify individuals using parameters from the dysconnected networks. Within the NBS Predict pipeline once again a t-test is calculated for each edge. However, unlike NBS where the t-test is used to create a t-statistic matrix within NBS Predict the test-statistic matrix contains the associated p-values for each t-test. This p-value matrix is then thresholded at a chosen level of significance, such as 0.05. Here only edges with a p-value less than or equal to the threshold remain and the LCC, with N_E edges, is extracted. For each remaining edge the corresponding functional connectivity values for all participants are used to train a classifier with N_E features. The inbuilt classifier models are logistic regression, SVM classification or Linear Discriminant Analysis.

3.2 Kuramoto Model

The Kuramoto model of coupled phase oscillators is one model commonly used to investigate synchronisation and will be used in Chapters 6 and 7.

Synchronisation is a concept with a diverse range of applications from the synchronisa-

tion of fireflies' flashing to the beating of heart cells [2]. Within the brain, synchronisation can refer either to neurons firing simultaneously or brain regions synchronising. Indeed hypersynchronised firing of neurons is linked to epilepsy and seizures [164] and has led to synchronisation being used as a proxy for excitability within brain networks [135]. Therefore, phenomenological models of coupled oscillators have been used to understand synchronisation and by extension excitability.

The Kuramoto model was introduced by Yoshiki Kuramoto [116] and reviewed by Strogatz [183]. The model uses a population of N phase oscillators travelling around the unit circle in the complex plane ($|z| = 1$ st $z \in \mathbb{C}$). The dynamics of the j^{th} oscillator within a single population of N phase oscillators is given by the coupled ODEs:

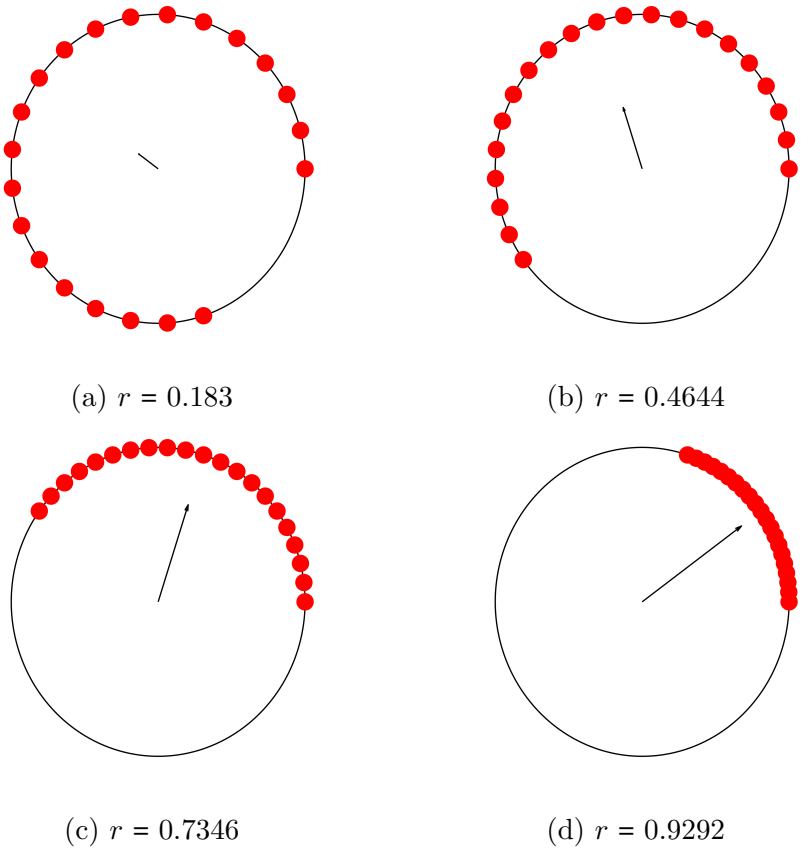
$$\frac{d\theta_j}{dt} = \omega_j + \frac{K}{N}\sum_{k=1}^{N}\sin\left(\theta_k - \theta_j\right) \text{ for } j = 1, \ldots, N. \tag{3.13}$$

For oscillator j: θ_j is the phase, ω_j is its natural frequency drawn from the frequency distribution $g(\omega)$, and K is the coupling strength between the oscillators. Here, all the oscillators are coupled together, and each will try to attract other oscillators to their natural frequency with strength K.

The average behaviour of the oscillators can then be quantified by:

$$z(t) = r(t)e^{i\phi(t)} = \frac{1}{N}\sum_{k=1}^{N} e^{i\theta_k}, \tag{3.14}$$

where $0 \leq r(t) \leq 1$, typically referred to as the Kuramoto Order Parameter, indicates the coherence of the oscillators and $0 \leq \phi(t) < 2\pi$ gives the average angle of the oscillators. The value of the order parameter represents, for a specific timepoint, the magnitude of the complex number created by adding the position of all the oscillators together - divided by N to ensure a value between 0 and 1. If $r(t) = 1$ then every oscillator is at exactly the same point on the unit circle at time t. However, if $r(t) = 0$ then oscillators or groups of oscillators are equally distributed around the unit circle such that their positions are equally balanced. Examples of various values of r are displayed in Figure 3.7.



(a) r = 0.183 (b) r = 0.4644

(c) r = 0.7346 (d) r = 0.9292

Figure 3.7: **Example r Values for Kuramoto Oscillators with Different Phase Ranges.** For each range of phase values **(a)** $[0, 0.8{\times}2\pi]$, **(b)** $[0, 0.6{\times}2\pi]$, **(c)** $[0, 0.4{\times}2\pi]$ and **(d)** $[0, 0.2 \times 2\pi]$ the order parameter, r, for each range has been calculated and is also represented by the length of the arrow.

Synchronisation is included in the model through the coupling parameter K. The coupling strength is an important parameter and there will exist a critical value, K_c, such that $K < K_c$ will result in $r \approx 0$, where any values of $r \neq 0$ are purely the result of transient behaviour, while $K > K_c$ will see r increasingly tend towards 1, the speed of which will be dictated by the value of K, this is represented in Figure 3.8.

When Kuramoto first introduced the model in 1984 [116] the system included a finite number of oscillators. However, a common approach is to consider the mean-field approximation when $N \to \infty$ [14, 22, 164, 173] and a rotating frame of reference is used. This allows analytical investigations into the stability of the steady-state solutions and provides conditions for the coupling parameter under which synchronisation is possible.

The Kuramoto model's ability to capture complex bio-physical events despite its rela-

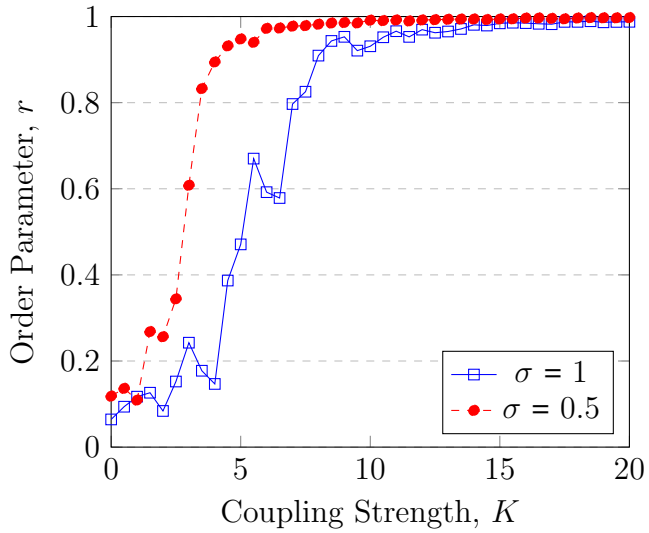


Figure 3.8: **Relationship Between the Order Parameter and the Coupling Strength for a Single Population.** The Order Parameter for various values of the coupling strength. Both simulations were computed using a forward Euler scheme with $T = 100$ and $dt = 0.05$ with 100 oscillators whose natural frequencies are drawn from two Gaussian distributions with mean 1 and standard deviations of 1 and 0.5 respectively. Here the average $r(t)$ over the last 10 seconds of the simulation is plotted. The value of K_c is higher for larger values of σ.

tively simple nature has seen the model used and extended in various ways to allow context specialisation. For example, time-delayed coupling between oscillators (Kuramoto-Sakaguchi) [2, 14], the introduction of stochasticity through noise (Langevin equation) [2, 22] and allowing coupling to only affect an oscillator's nearest neighbours [2].

In addition, a useful extension is to increase the number of populations from 1 to P [14, 164, 173] allowing multi-scale modelling of the brain from mesoscale to macroscale. For context, each population could be a different tree of fireflies or a different organ in the body [8]. In neuroscience, each population would represent a different region in the brain whilst the movement of oscillators within a region will represent mesoscale populations of neurons such as cortical columns. Each individual population of oscillators is considered fully connected, while the connections between populations are determined by an adjacency matrix, as seen in Figure 3.9. This extension allows multi-scale modelling of the brain in a relatively simple and elegant phenomenological model.

There are multiple ways additional populations could be added to the model. For ex-

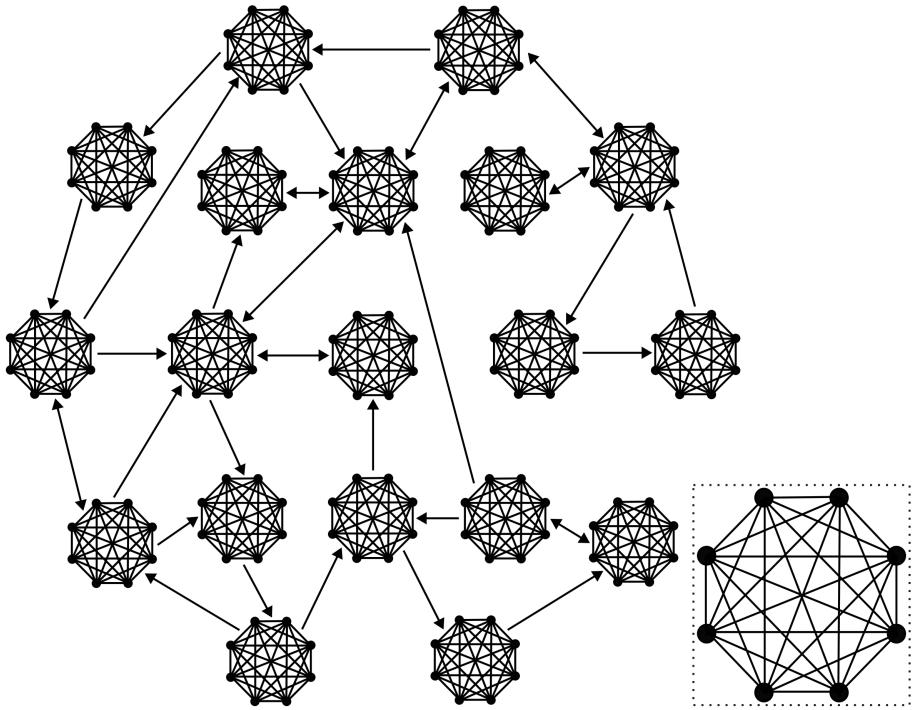


Figure 3.9: **Multiscale Kuramoto Diagram.** A schematic showing the oscillators in a multiscale Kuramoto network. Within each population, the oscillators are connected to all other oscillators in the population, as seen in detail in the dashed box. Also, each population is connected to other populations via a directed adjacency matrix.

ample, Martens et al. [129] showed that the mean-field approximation for two populations of fully connected coupled oscillators with uniform coupling strength and equal distributions, differing only by their mean frequencies of ω_1 and ω_2 is equal to 1 population of oscillators with the bimodal frequency $g(\omega_1) + g(\omega_2)$. However, in most cases, additional populations are assumed to have oscillators drawn from the same distribution and it is the effect of the network topology that is of interest. This is because when considering multiple populations global synchronisation can arise when each individual population has a local coupling, K_{cc}, less than the critical coupling required for local synchronisation ($K_{cc} < K_c$) but the structure of the network allows global synchronisation to manifest. In certain contexts, such as epilepsy where the seizure state is believed to emerge as a result of synchrony, this makes the Kuramoto model a popular choice. Hypothesising that synchronized and non-synchronised states represent epileptic and non-epileptic brain activity respectively. Indeed, Schmidt et al. [164] considered how generalized seizures

can arise from focal seizures by the addition or removal of a single directed edge in the network. Highlighting the useful nature of multi-scale modelling.

In the case of multiple populations, eq 3.13 is naturally extended such that within population $c \in \{1, \ldots, P\}$ the dynamics of oscillator $j \in \{1, \ldots, N_c\}$ is given by:

$$\frac{d\theta_j^c}{dt} = \omega_j^c + \sum_{\gamma=1}^{P} \eta_\gamma \frac{K_{c\gamma}}{N_\gamma} \sum_{k=1}^{N_\gamma} \sin\big(\theta_k^\gamma - \theta_j^c\big). \tag{3.15}$$

Here ω_j^c denotes the natural frequency of oscillator j in population c drawn from the distribution $g_c(\omega)$, $\eta_c = \frac{N_c}{N}$ where η_c and N_c are the proportion and number of oscillators in population c respectively and N is the total number of oscillators across the populations. Also, $K_{c\gamma}$ is an element in the matrix $\mathbf{K}$, which gives the coupling strength from population γ to population c. Hence, the position of all oscillators in population c is directly affected by the position of all oscillators in population γ, if there exists an edge from γ to c. The coupling strength $\mathbf{K}$ is a combination of global and local coupling strength defined by:

$$\mathbf{K} = K_g \mathbf{A} + \mathbf{K_{cc}} \odot \mathbf{I_P}. \tag{3.16}$$

K_g is the global coupling strength, $\mathbf{K_{cc}}$ is the column vector giving the local coupling strength for population c and $\mathbf{I_P}$ is the $P \times P$ identity matrix. Also, $\mathbf{A}$ gives the network topology between all P populations, this can be binary or weighted. Here $\odot$ is defined to be elementwise multiplication, which is required if the local coupling strength differs per population. If the local coupling is the same for all populations then the coupling matrix is given by:

$$\mathbf{K} = K_g \mathbf{A} + K_{cc} \mathbf{I_P}, \tag{3.17}$$

where K_{cc} is the scalar for local coupling strength. Therefore, the coupling strength is determined by both the oscillators in a population and the influence of oscillators in connected populations and is modulated by both a local and global coupling strength. In addition, eq 3.14 can be easily extended to the case of multiple populations by letting the

local order parameter of a node be defined by,

$$z_c(t) = r_c(t)e^{i\phi_c(t)} = \frac{1}{N_c}\sum_{k=1}^{N_c} e^{i\theta_k^c(t)}, \tag{3.18}$$

while the global order parameter for the network is defined by,

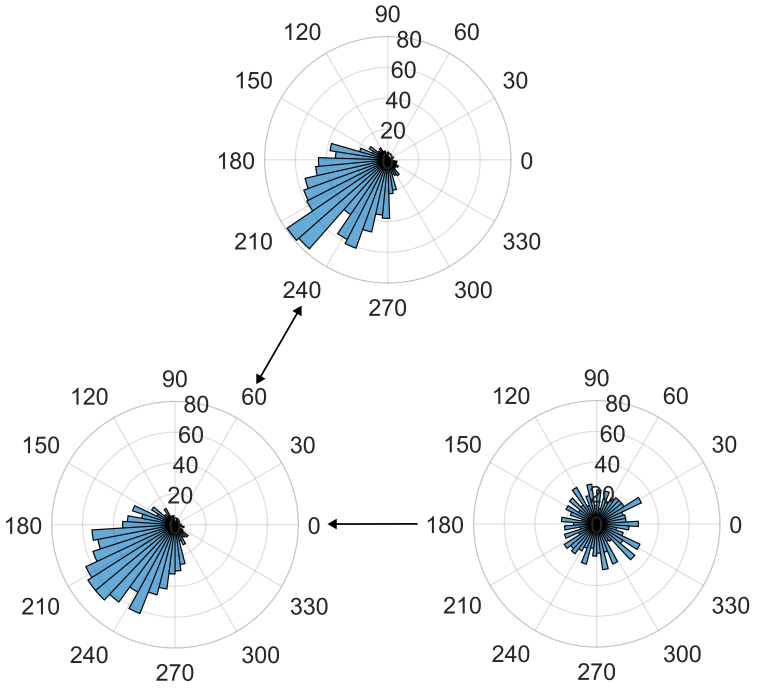
$$Z(t) = \sum_{c=1}^{P} \eta_c z_c(t).$$

An example, of a Kuramoto simulation for three populations of oscillators, is given in Figure 3.10. The network structure has a basal node (in-degree of zero), which never achieves local synchronisation as seen through the consistently low values of $r(t)$. As it is a basal node the network is unable to induce local synchronisation and the low local coupling strength, as seen in Figure 3.8, is unable to induce local synchronisation either. Therefore, this population adds noise into the system hindering the local synchronisation of the connected population and therefore global synchronisation. While the bidirectional edge connecting the other two populations helps those populations reach synchronisation through the cyclic feedback loop.

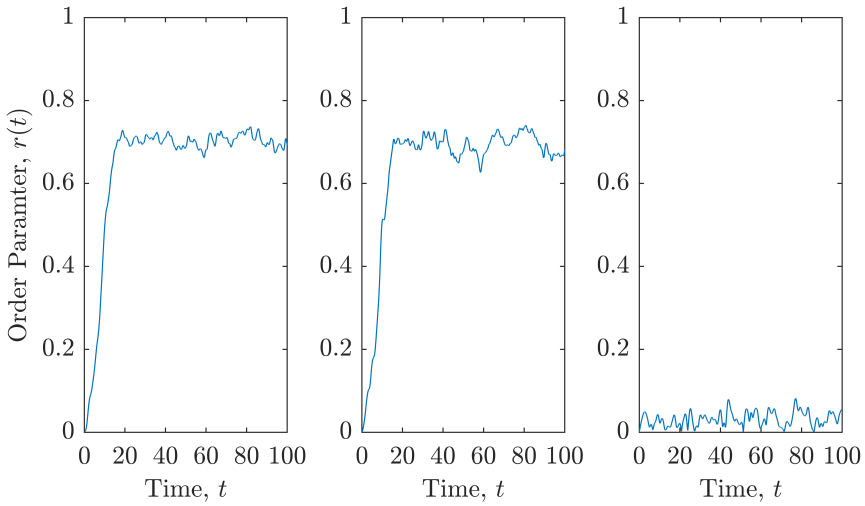
Again it is common for mean-field approximations to be used to understand the steady-state solution. As outlined in Appendix A in the case of $N_c \to \infty$ and $N \to \infty$ such that η_c remains constant, a system of coupled ODEs can describe the dynamics of r_c and ϕ_c over time,

$$\frac{dr_c}{dt} = -r_c + \frac{1-r_c^2}{2}\sum_{\gamma=1}^{P} \eta_\gamma K_{c\gamma} r_\gamma \cos\big(\phi_\gamma - \phi_c\big) \tag{3.19}$$

$$\frac{d\phi_c}{dt} = \frac{1+r_c^2}{2r_c^2}\sum_{\gamma=1}^{P} \eta_\gamma K_{c\gamma} r_\gamma \cos\big(\phi_\gamma - \phi_c\big) \tag{3.20}$$



(a) Functional Network and Histogram for $\theta(T)$



(b) Order Parameter $r(t)$ for each Kuramoto Population

Figure 3.10: **Three Node Kuramoto Simulation.** Simulated results for a toy network connecting three populations of Kuramoto oscillators. Each population has $N_c = 1,000$ oscillators, which are equally spaced around their respective unit circles at time $t = 0$, and the model is simulated using a forward Euler method over $T = 100$ s with time-step $dt = 0.005$. In all cases, $g_p(\omega)$ is a Gaussian function with mean 9 and standard deviation 1, the K_{cc} is constant at 1.15 and $K_g = 5$. **(a)** The connections between each population and the final angular position of the oscillators at $T = 100$ s, **(b)** the time-series of $r(t)$ for each population starting at the top and going anti-clockwise.

Now global synchronisation is defined by,

$$r_g(t) = \frac{1}{P}\left|\sum_{c=1}^{P} r_c e^{i\phi_c(t)}\right|. \tag{3.21}$$

These mean-field approximations are useful for determining the conditions required for synchronisation. For instance, if we assume a rotating frame of reference then $\phi_\gamma - \phi_c \to 0$ as $t \to \infty$. If in addition we linearise eq 3.19 then we have,

$$0 = -r_c + \frac{1}{2}\sum_{\gamma=1}^{P} \eta_\gamma K_{c\gamma} r_\gamma, \tag{3.22}$$

while eq 3.20 is $\frac{d\theta}{dt} = 0$. Now using eq 3.17 we have

$$r_c \frac{2 - \eta_c K_{cc}}{K_g} = \sum_{\gamma=1}^{P} \eta_\gamma A_{c\gamma} r_\gamma. \tag{3.23}$$

In the case that every population has the same number of oscillators then $\eta_c = \frac{1}{P}$; therefore eq 3.23 becomes,

$$r_c \frac{2P - K_{cc}}{K_g} = \sum_{\gamma=1}^{P} A_{c\gamma} r_\gamma. \tag{3.24}$$

We note that eq 3.24 is an eigenvalue problem and by looking for non-trivial solutions we have,

$$\frac{2P - K_{cc}}{K_g} = \lambda,$$

where λ is the eigenvalue of $\mathbf{A}$. Since the largest eigenvalue explains the most variance it is sufficient for a linear approximation to only consider the largest eigenvalue $\lambda_{\max}$, therefore for a given K_{cc} we have that the critical value for global coupling i.e. the minimum value needed for synchronisation, is given by,

$$K_g = \frac{2P - K_{cc}}{|\lambda_{\max}|}.$$

Note that this derivation for K_g only works for certain network topologies, for nodes not

within the strongly connected component may not synchronise for this value of K_g and basal nodes may prevent this value of K_g resulting in synchronisation.

3.2.1 Order Parameter: R

The order parameter approach was first suggested by Meisel et al. [135]. It uses the order parameter $r(t)$ to create a single macroscale representative value of synchronisation over the simulation. Providing a quantitative value for how synchronised brain regions are to each other.

Each of the P EEG channels (real or simulated) will be summarised by a single oscillator; therefore, there will be one population and P oscillators. The position of oscillator $c \in \{1, \ldots, P\}$ at time t is then given by the complex number $z_c(t) = e^{i\theta_c(t)}$. The argument $\theta_c(t)$ for channel c is time-dependent as each oscillator traverses the periodic trajectory created by the unit circle $|z| = 1$ in the complex plane. A notion of synchronicity can then be introduced by considering the absolute sum of all the oscillators,

$$r(t) = \frac{1}{P}\left|\sum_{c=1}^{P} e^{i\theta_c(t)}\right|, \tag{3.25}$$

as in eq 3.14. The order parameter, $r(t)$, gives a value for the synchronous behaviour between all channels at a specific timepoint, t. The value of the order parameter represents, for a specific timepoint, the magnitude of the complex number created by adding the position of all the oscillators together - divided by P to normalise the value.

Meisel et al. [135] then introduced the order parameter, R, which is the mean of $r(t)$ over the number of timepoints, L,

$$R = \langle r(t) \rangle = \frac{1}{L}\sum_{t=1}^{L} r(t), \tag{3.26}$$

providing a single value for the synchronisation of the brain network.

For the simulated EEG time-series the average phase of a population is given by eq

3.15, therefore $r(t)$ and R can be calculated directly. Here a high R represents that each population has a similar average phase for the majority of the timepoints.

For the recorded EEG signal each time-series is preprocessed first before the synchronisation between channels can be calculated. For example, using the band-passed filtered EEG time-series, $x_c(t)$ for channel c the phase trace, $\theta_c(t)$, can be obtained through it's Hilbert transform $H[x_c(t)]$:

$$H[x_c(t)] = \frac{1}{\pi}\text{P.V.}\int_{-\infty}^{\infty}\frac{x(\tau)}{t-\tau}d\tau, \text{ for } x \in \mathbf{R},$$

where P.V. represents the Cauchy Principal Value [105, 106]. The Hilbert transform is a common approach within signal processing analysis and is key to being able to calculate the phase of a time-series,

$$\theta_c(t) = \arctan\left(\frac{H[x_c(t)]}{x_c(t)}\right). \tag{3.27}$$

In order to make sure that the phase trace covers the entire phase range of the unit circle, $[-\pi, \pi]$, rather than the range of arctan which is $(-\frac{\pi}{2}, \frac{\pi}{2})$, the signs of the Hilbert transform and the phase trace must be taken into account:

$$\theta_c(t) = \begin{cases} \theta_c(t) & \text{if } x_c(t) > 0, H[x_c(t)] > 0 \text{ or } H[x_c(t)] < 0, x_c(t) > 0, \\ \theta_c(t) + \pi & \text{if } x_c(t) < 0, H[x_c(t)] > 0, \\ \theta_c(t) - \pi & \text{if } x_c(t) < 0, H[x_c(t)] < 0. \end{cases} \tag{3.28}$$

Mathematically, the Hilbert transform performs a $-\frac{\pi}{2}$ phase shift on the frequency components of the real time-series $x_c(t)$ to produce the complementary imaginary part $iy_c(t)$. Therefore, if $x_c(t) = A\cos(\omega t)$ then the Hilbert transform is given by $y_c(t) = A\sin(\omega t)$ [215]. The phase trace, as calculated by eq 3.27 and eq 3.28, is then the same as the argument of the complex number,

$$z_c(t) = x_c(t) + iH[x_c(t)] = e^{i\theta_c(t)}.$$

Then $r(t)$ and R can be calculated using eq 3.25 and eq 3.26. Here a high R represents that each channel has a similar phase for the majority of the timepoints.

Also, it is shown that phase synchronisation correlates very well with stimulation-evoked responses as a marker for excitability at an individual subject level. Since the amplitude of evoked cortical potentials has been used in literature as a measure of excitability this correlation provides an alternative method for quantifying excitability. For proof of concept over a period of 24 h, electrical stimulation was applied to $n = 2$ patients every 10 minutes, then the amplitude of the evoked response was compared to the level of synchronisation as measured from the resting-state Electrocorticography (ECoG) data - a type of iEEG - from just prior to each stimulation. It was found that the amplitude of the electrical stimulation, measured as the highest peak to lowest trough, and the synchronisation parameter correlated at a level of 0.52-0.57. In addition, cortical excitability was monitored in epilepsy patients who were altering their intake of Anti-Epileptic Drugs (AEDs) in preparation for surgical treatment. By monitoring excitability through synchronisation using EEG, the level of synchronisation followed an inverse relationship with AED intake with the synchronisation difference between days of low and high AED load being very significant, $p \leq 0.001$, in 7 out of 10 patients and significant, $p \leq 0.05$, in a further 2 patients [135]. Since AEDs are designed to reduce excitability in the brain with an aim of reducing seizures this once again provides evidence for the link between excitability and synchronisation where synchronisation of the Kuramoto oscillators is viewed as an excitable state. However, the metric R presented by Meisel et al. provides a measure of how synchronised all of the channels are rather than the synchronisation between specific regions.

In addition, order parameter approaches can easily be collected from resting-state data for a wide variety of participants without the risk of adverse reactions, such as the risk of epileptic seizures, which may be induced by stimulation-evoked responses.

For simulated EEG time-series the position of all oscillators in a population on the unit circle at a given time is dictated by either eq 3.13 or eq 3.15. However, you could

create a simulated EEG time-series and calculate the order parameter for population c in the same way as above using the simulated signal given by,

$$s_c(t) = \frac{1}{N_c} \sum_{k=1}^{N_c} \cos\big(\theta_k^c(t)\big).$$

3.3 Two Process Model

Within the field of sleep and circadian research, the two process model is a defining descriptive model. Its name encompasses the two main processes that are thought to control sleep: a circadian process and a homeostatic drive for sleep, also known as sleep pressure. The processes are useful for the interpretation of results and are included in the pipeline for Chapter 6. Within the model, sleep and wakefulness are seen as self-regulating processes that vary between upper and lower circadian-modulated thresholds. Indeed, homeostatic pressure sees the drive to sleep increase during wakefulness until sleep is induced at the upper threshold, thereafter sleep pressure decreases until reaching the lower limit and wakening occurs, as seen in Figure 3.11.

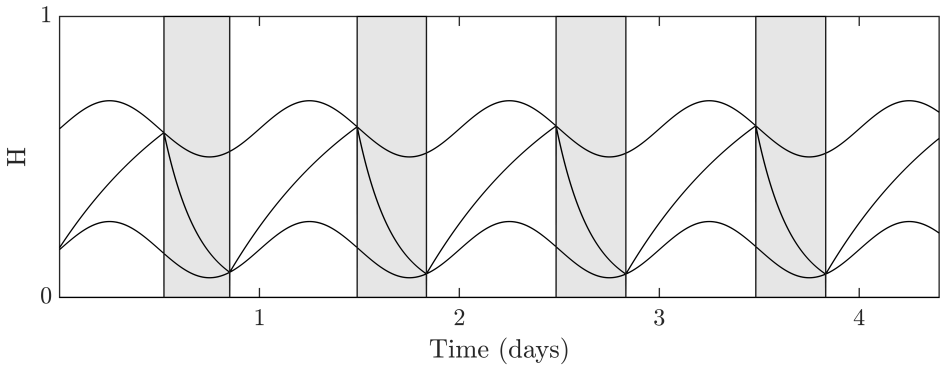


Figure 3.11: **Application of the Two Process Model.** The two process model as simulated over 4 days replicated from Skeldon et al. [174] with: $H_0 = 0.177$, $\chi_w = 18.2$, $X_s = 4.2$, $U = 1$, $a = 0.1$, $T_{l_0} = 0.17$, $T_{h_0} = 0.6$ here periods of sleep are denoted by the grey patches.

Various versions of the model's equations have been proposed since the basic conceptualisation was presented by Borbély et al. [19]. The current exponential variation of

the model as presented by Skeldon et al. [174] can be easily interpreted as a homeostatic pressure, $H(t)$, that increases exponentially during wake,

$$H(t) = U + (H_0 - U)e^{\frac{(t_0-t)}{\chi_w}}, \tag{3.29}$$

from the position $0 \leq H_0 \leq U$ at time t_0 towards the upper asymptote U and exponentially decreases during sleep,

$$H(t) = H_0 e^{\frac{(t_0-t)}{\chi_s}}, \tag{3.30}$$

towards the lower asymptote 0. Here χ_w and χ_s represent homeostatic time constants for the two conditions of wake and sleep respectively. Skeldon et al. [174] give approximations for these values as 18.2 h and 4.2 h respectively. The homeostatic process is then bound by a lower, $T_l(t)$, and upper threshold, $T_h(t)$,

$$\begin{aligned} T_l(t) &= T_{l_0} + aC(t), \\ T_h(t) &= T_{h_0} + aC(t), \end{aligned}$$

where $T_{l_0} \leq T_{h_0}$ give the mean value of their respective thresholds and $a \geq 0$, is chosen to reproduce desired dynamics [41, 174]. A common first approximation of $C(t)$ is a sine wave,

$$C(t) = \sin(\omega(t - \alpha)), \tag{3.31}$$

where α is a phase shift and ω is the frequency, typically chosen such that the period is 24 h. However, Skeldon et al. [174], referencing Daan et al. [41], gave an alternative function for the circadian process by plotting values of $H(t)$ after participants were forced to awaken at different times of the day. This can be approximated by the series expansion,

$$\begin{aligned} C_1(t) = 0.97\sin(\omega(t-\alpha)) + 0.22\sin(2\omega(t-\alpha)) + 0.07\sin(3\omega(t-\alpha)) \\ + 0.03\sin(4\omega(t-\alpha)) + 0.01\sin(5\omega(t-\alpha)). \end{aligned} \tag{3.32}$$

Figure 3.11 shows a simple application of the model given above using eq 3.31 as an oscillator entrained to the light-dark cycle of the sun. As noted by Hagenauer et al. [82] the beginning of sleep is driven by the homeostatic pressure, $H(t)$, while the end of sleep is extended due to the circadian influence.

The equation for the homeostatic process has evolved since the model's introduction in the 1980s. For example, while both the wake and sleep equation for $H(t)$ are exponential in nature now, originally only the need for a non-linear function during sleep was noted as during wakefulness this process was originally modelled as a linear increase [19, 41]. This reflected the non-proportional increase in sleep time that occurs after sleep deprivation. An extreme example of this sleep characteristic was seen when only 14 h of recovery sleep occurred after the longest recorded sleep-deprivation study, which covered 11 days and 25 minutes [28]. It was only through the analysis of the power density of human sleep EEG under normal and sleep-deprived conditions [41] that exponential equations as well as approximations for these rates of increase and decrease were introduced.

In addition, the equation for the circadian process has also changed. Currently, both a lower and upper threshold are utilised however, originally a single square wave was used to represent times of activity and rest dictated by clock time, although it was noted a sine wave was an alternative choice [19]. When two circadian thresholds were considered initial implementations first considered constant linear thresholds [41] before eq 3.31 and eq 3.32 were introduced.

This model is purely phenomenological and aims to encapsulate qualitatively the basic aspects of sleep while disregarding intricacies such as processes that cause circadian modulation as well as the effects of sleep staging and its potential impact on the build-up and dissipation of sleep pressure [19, 41]. Indeed, while it is postulated that the suprachiasmatic nucleus is responsible for circadian gating no explicit system is required by the model. However, physiological data is needed for parameter estimation. Data such as EEG-recorded slow wave activity during non-REM sleep, as well as theta activity during wakefulness, are currently used to predict parameters in $H(t)$, while melatonin secretion

and core body temperature can help determine parameters in $C(t)$ [21].

However, despite the lack of basis in the biological system, the model is incredibly adaptable for a range of experimental protocols. For instance, Daan et al. [41] considered in detail how the model can be altered to understand sleep deprivation (halting the influence of the upper threshold $T_h(t)$), see Figure 3.12, the duration of recovery sleep, forced bed rest (reducing the difference between T_{l_0} and T_{h_0}), free running conditions (changing the period of the $C(t)$ to 25 h) and shift work (where $T_h(t)$ and $T_l(t)$ are forced to equal U during the work period and during a 90 minute buffer zone before and after the shift). In all cases, the adapted model showed similarity to experimental data. In addition, Daan et al. [41] added noise to thresholds. This was used to represent that the behavioural response to fatigue is not deterministic and that a natural level of variance occurs due to people's response to external constraints. In these examples, external factors are included in the model through changes to $C(t)$. The alternative choice of influencing $H(t)$ was dismissed because for instance, sitting in the dark, warm environment of a lecture theatre would not unduly increase sleep pressure but may increase fatigue as represented by a decrease in $T_h(t)$ [138].

Not only has the two process model been used to understand sleep timing, but the two functions in the two process model have been adapted and extended in multiple ways to understand fatigue, performance, diseases and chronotypes.

3.3.1 Extensions to the Two Process Model

A common use of the functions in the two process model is to investigate and predict the extent to which participants are impacted by sleep deprivation, shift work and in general the extended period of wakefulness that is associated with these events.

For example, one extension to the model was through the calculation of 'fatigue', defined as $H - T_h$ and proposed by Daan et al. [41]. Fatigue calculated under both normal and sleep deprived conditions is shown in Figures 3.13 and 3.14 respectively. Under sleep deprivation the modelled value was shown to follow the participants' subjective self-rating

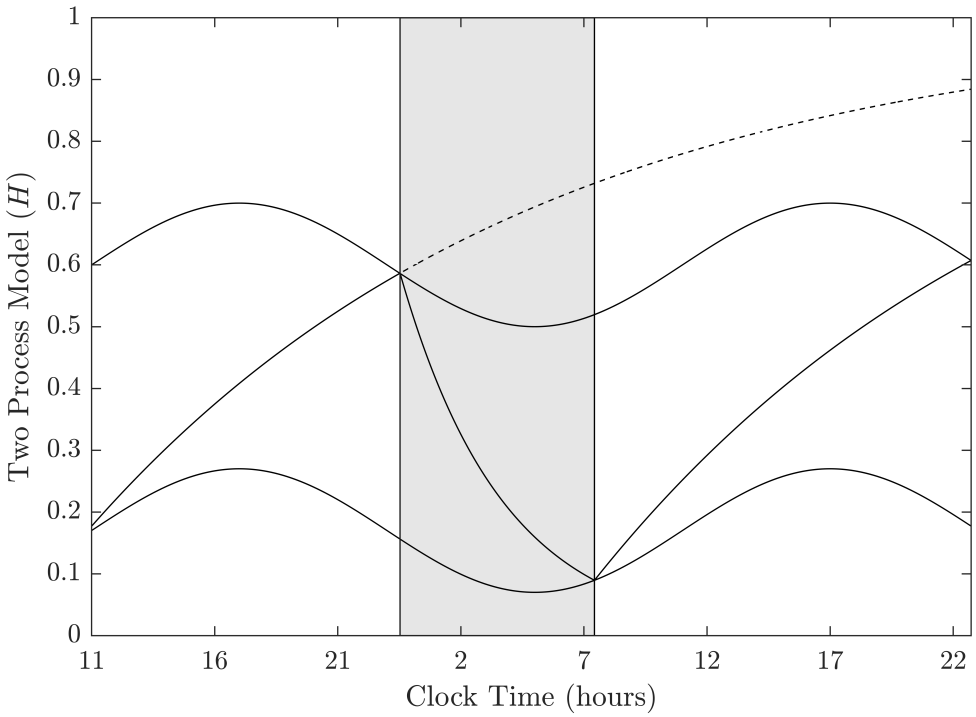


Figure 3.12: **Sleep Deprivation Within the Two Process Model.** The two process model under normal (solid line) and sleep deprived (dashed line) conditions, which is implemented through halting the influence of the upper threshold. This was simulated using $H_0 = 0.177$, $\chi_w = 18.2$, $X_s = 4.2$, $U = 1$, $a = 0.1$, $T_{l_0} = 0.17$, $T_{h_0} = 0.6$ here sleep under normal conditions is denoted by the grey patch.

of fatigue [41].

In addition, van Dongen [48] used the equations from the two process model (eq 3.29, eq 3.30 and eq 3.32) to predict an individual's 'performance impairment' given an individual's sleep schedule. Since a sleep schedule is imposed the periods of sleep and wakefulness are not dictated by $H(t)$ reaching the thresholds $T_l(t)$ or $T_h(t)$ but instead swap between wake and sleep at the given times. A function C is fixed and then performance impairment is given by $H - C$. In particular, given a potential sleep schedule for the driver of the Metro-North train, performance impairment can be used to help explain how the 2013 crash could have happened as seen in Figure 3.15.

Furthermore, the two process model was used to predict levels of 'alertness' in individuals. However, it should be noted that the two process model's ability to calculate alertness is less accurate during the morning after awakening. This is due to sleep inertia

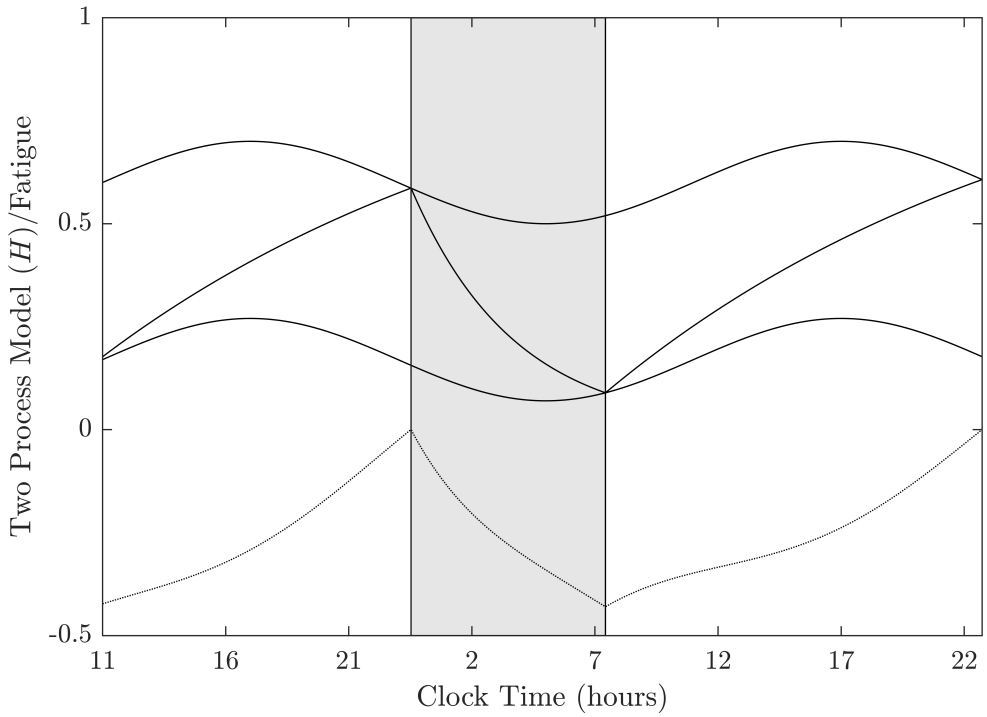


Figure 3.13: **Predicting Fatigue Using the Two Process Model.** The two process model (solid line) and fatigue $H - T_h$ (dotted line) as simulated using H_0 = 0.177, χ_w = 18.2, X_s = 4.2, U = 1, a = 0.1, T_{l_0} = 0.17, T_{h_0} = 0.6 [174], here sleep is denoted by the grey patch.

which prevents 'maximal alertness' after awakening. Consequently, the two process model was extended to a three processes model, incorporating sleep inertia term to increase the accuracy of alertness prediction for ~ 3h after awakening [68].

Also, the two process model has been used to understand disease phenotypes. For example, a comprehensive review of how sleep modelling has been used to study and understand disease was conducted by Abel et al. [1]. In particular, Proserpio et al. [151] suggested that fragmented sleep as well as longer and more frequent awakenings during the night could be explained by a reduction in the distance between T_{l_0} and T_{h_0}. Furthermore, Tonetti et al. [189] studied ADHD and interpreted higher motor activity during the second part of the night and a lack of a post-lunch dip in patients with ADHD as potential evidence for a lower homeostatic sleep pressure in the patients compared to healthy controls. In addition, Tononi et al. [190] suggested that the two process model could actually explain the synaptic homeostasis of sleep-wake regulation. This hypothesis

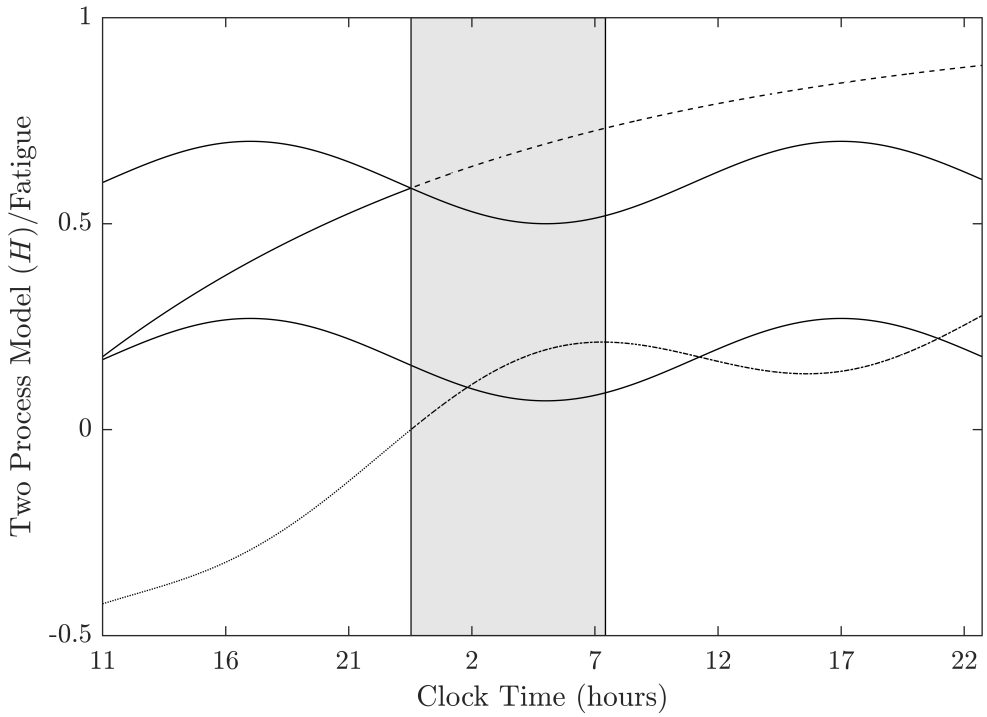


Figure 3.14: **Predicting Fatigue Under Sleep Deprivation Using the Two Process Model.** The two process under sleep deprivation (dashed line) and fatigue $H - T_h$ (dash dotted line) as simulated when a participant is sleep deprived by halting the influence of the upper threshold $T_h(t)$. The solid line for H and the dotted line for fatigue are where values are the same as the no sleep deprivation case, seen in Figure 3.13. This simulation uses $H_0 = 0.177$, $\chi_w = 18.2$, $X_s = 4.2$, $U = 1$, $a = 0.1$, $T_{l_0} = 0.17$, $T_{h_0} = 0.6$ [174], here the normal period sleep would have occurred is denoted by the grey patch.

was then used by Wolf et al. [208] to help explain a possible mechanism for why sleep deprivation actually benefits individuals with MDD. Indeed, Wolf et al. presented a figure in which MDD patients have an identical time-series for Process H as controls however it is shifted down - potentially due to lower thresholds T_{l_0} and T_{h_0}. However, the threshold H must reach for long-term potentiation (persistent strengthening of synapses) is the same for both groups. Therefore, it is only through sleep deprivation that the homeostatic sleep pressure of MDD patients reaches a high enough level to induce long-term potentiation, whilst it is within the normal range for controls. In addition, Matsuura et al. [131] used the two process model to predict the sleep-wake cycle of infants with autism by adding a nap term to the upper threshold, $T_h(t)$.

Furthermore, analysis by Hagenauer et al. [82] explained the move to a later chrono-

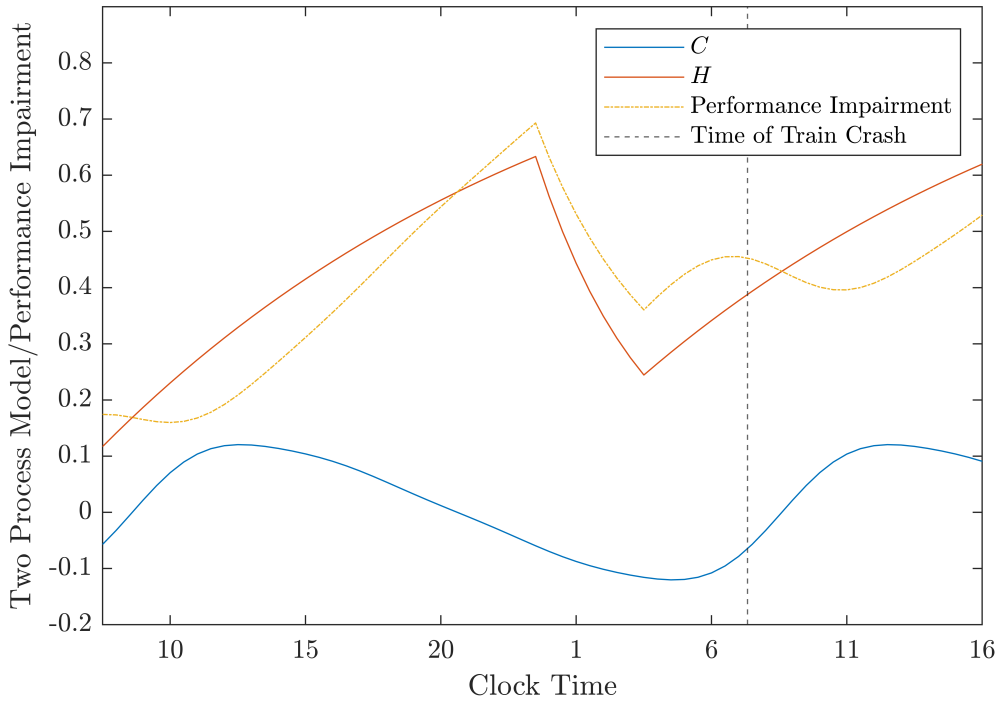


Figure 3.15: **Predicting Performance Impairment for the Metro-North Train Crash.** The prediction of performance impairment $H - C$ calculated using the circadian and homeostatic process. Here the simulated driver went to sleep at $24:00$ and awoke at $03:30$ [48]. The dashed vertical line shows the time of the crash, which is near the local maximum for performance impairment. Here $C = 0.12C_1(t)$ (eq 3.32) $H_0 = 0.177$, $\chi_w = 18.2$, $X_s = 4.2$ and $U = 1$.

type seen when children transition to adolescents by altering the homeostatic time constants in $H(t)$. They showed that by increasing χ_w and χ_s together from 56% to 133% of an adults value (i.e. making these processes occur over a longer time) that sleep onset is phase-delayed however the duration of sleep is only marginally decreased. It is interesting to note that only increasing χ_w sees a similar phase-delayed response however sleep duration also decreases by hours, making it no longer biologically accurate. These results are true over a range of circadian amplitudes and initial conditions. This offers an insight into how the model can be used to understand chronotypes and is certainly a non-trivial finding compared to changing the phase of the circadian oscillator to reflect the pattern of ECPs or LCPs.

Overall, the two process model has allowed greater insight into various sleep-related

processes and can be used to represent sleep-wake timings and performance outcomes in a range of contexts.

CHAPTER 4

CLASSIFICATION OF HUMAN CHRONOTYPE BASED ON FMRI GRAPH THEORETICAL METHODS

4.1 Introduction

Chronotype describes the individual relationship between a person's internal circadian rhythm and the light-dark cycle of the sun. However, these two cycles are not perfectly aligned for all individuals. Indeed, the spectrum of chronotypes in society leads to vastly different relationships between people's circadian rhythm, the sun and the societal day. In particular, this is felt most keenly by extreme chronotypes, especially LCPs when constrained to a 9-5 working day, as discussed in Sections 2.2.2 and 2.3.1.

For LCPs, the near-constant misalignment many face during their daily life is associated with an increased risk of cancer, type 2 diabetes, increased BMI and obesity [95]. Furthermore, chronotype has been associated with poor mental health outcomes, as late chronotype is a known risk factor for the development of depression [122] and chronotype was found to be predictive of variability in cognitive outcomes across the day [56], using a seed-based analysis. Therefore, extending previous chronotype research from seed-based FC to the analysis of FNs is a natural progression to allow a greater understanding of the macroscale effects on the brain. Indeed, one way to analyse FNs is through the calculation of graph metrics, as discussed in Section 3.1.1.

However, current literature related to FC in chronotype studies is limited, as discussed in Section 2.2.2. Indeed, at the time of analysis, there were no papers with a direct focus on applying graph theoretical approaches to whole brain rs-fMRI networks when analysing chronotype; limiting the ability to base methodological decisions on the results of previous studies. Therefore, we took inspiration from the related field of sleep deprivation, due to the sleep debt that LCPs can suffer from in a 9-5 society [155], as explained in Section 2.3.1. Post-analysis two papers by Farahani et al. [62, 64] were published and a comparison with these results is provided below in the discussion.

Overall, this Chapter will quantify differences in the graph metrics calculated from the FNs of extreme chronotypes using classifiers. This will be assessed through the creation of a classifier using machine learning techniques, which will label a test subject as an ECP or an LCP. Discovering how graph metrics differ between ECPs and LCPs could indicate the presence of different mechanisms within the FNs of the two extreme phenotypes. In addition, an increased understanding of the relationship between chronotype and FNs could provide insight into the increased risk of mental health, differences in cognitive outcomes, the reason for the disparity of such impacts along the chronotype spectrum, and areas upon which to focus future research. Moreover, a greater understanding of how chronotype impacts the brain's FN could provide support for practical changes in society, such as the school day starting later for adolescent children [142] or greater flexibility in workplace hours [196].

4.2 Methodology

The chronotype dataset used in this research was provided by the Centre for Human Brain Health, at the University of Birmingham with the aid of Professor A. Bagshaw. The original data was collected by Dr E. R. Facer-Childs, while a PhD student at the Birmingham University Imaging Centre. Information directly relevant to this study is provided, for a full description of the methodology the reader is directed to Facer-Childs

et al. [56]. The graph theoretical part of the pipeline from Section 4.2.6 to Section 4.2.11 is represented in Figure 4.1.

4.2.1 Ethical Approval

Ethical approval was provided by the Research Ethics Committee at the University of Birmingham, before any data acquisition started. Participants had at least 48 h before the start of the study to read over information sheets and consent forms, and were free to end their participation at any time. In addition, the University of Birmingham's Advisory Group on the Control of Biological Hazards approved the COSHH risk assessments and biological assessment forms that were completed. All the data and samples were given by participants voluntarily and were fully anonymised [56].

4.2.2 Participants

Thirty eight participants were enrolled into the study, with an average age of 22.7 $\pm$ 4.2 years (mean $\pm$ standard deviation), of whom 24 were female. Exclusion criteria included (1) prior diagnosis of any sleep, neurological or psychiatric disorders (2) use of medication that would knowingly affect sleep (3) an intermediate chronotype classification. For two weeks prior to the scanning sessions, participants were instructed to follow their preferred sleep pattern, with no restrictions imposed by the study except for 2 h before the scanning sessions when alcohol and caffeine consumption as well as exercise were prohibited.

Participants attended three scanning sessions at the local times of $14:00$, $20:00$ and $08:00$ the following day. Where possible individual participant scanning sessions were organised to occur on separate days to ensure testing took place at the specified time. However, on the rare occasion this was unavoidable, and two participants were scheduled for the same day, scanning took place on either side of the targeted time.

One ECP (Subject 11) had their $14:00$ rs-fMRI scan excluded due to excessive movement.

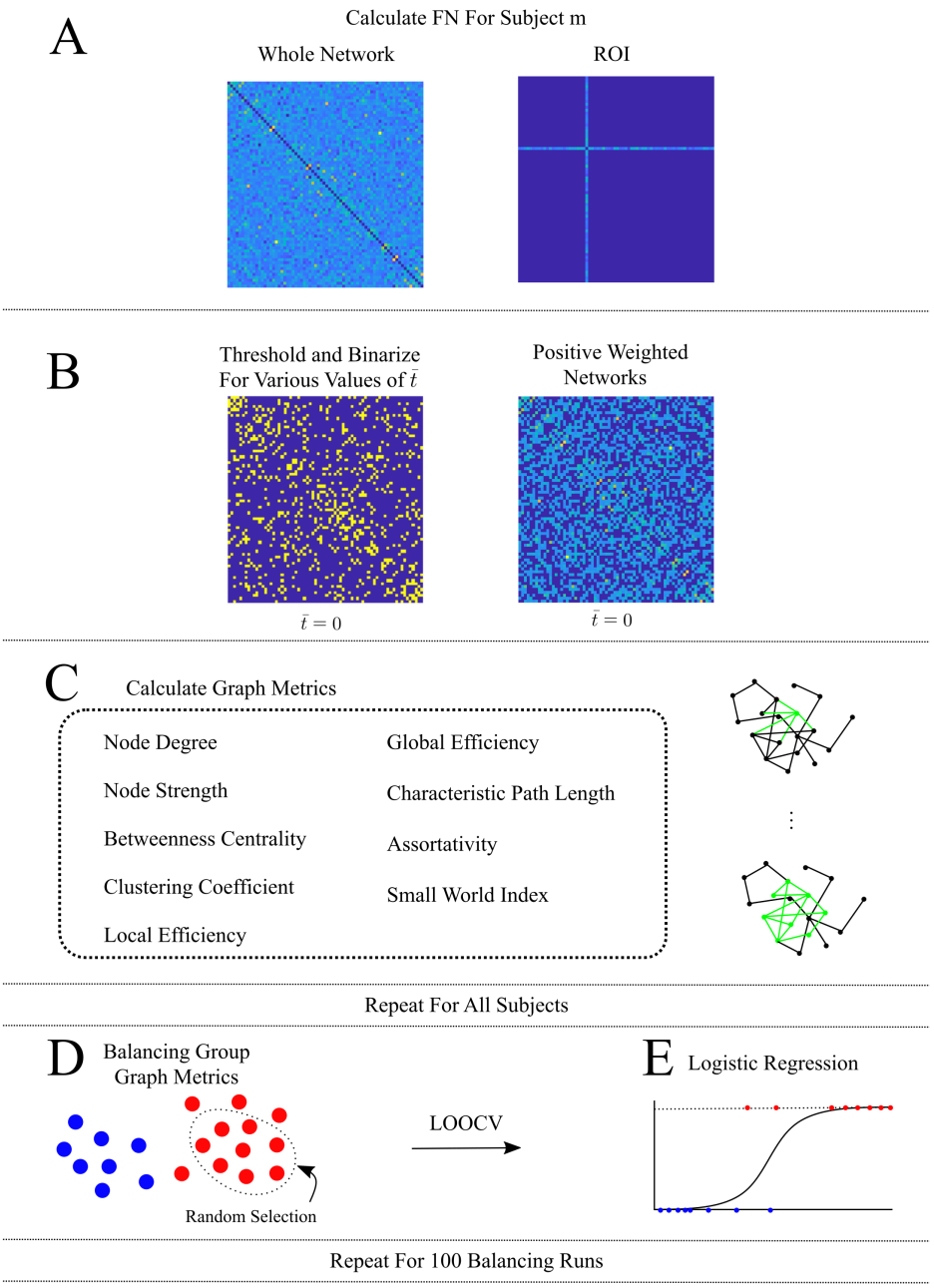


Figure 4.1: **Summary Pipeline for Graph Metric Classifier.** **(A)** A participant's whole brain FN created using Tikhonov partial correlation, and a nodal subnetwork for mPFC or PCC **(B)** The FN is then either thresholded and binarized for various values of $\bar{t}$ from 0 up to the minimum percolation threshold across all participants or thresholded at $\bar{t}$ = 0 to create a positive weighted network. **(C)** The graph metrics are then calculated for that participant. Steps (A), (B) and (C) are repeated for all participants. **(D)** The size of the two groups is equalised through a balancing run - reducing the number of LCPs to match ECPs. **(E)** Using a Leave One Out Cross-Validation (LOOCV) approach a logistic regression classifier is trained and performance is summarised by accuracy and OOP.

4.2.3 Chronotype Labeling

16 participants were classified as ECPs (age 24.7 ± 4.6 years, 9 females) and 22 as LCPs (age 21.3 ± 3.3 years, 15 females). Chronotypes were initially indicated by the outcome of the MCTQ using eq 2.3. To ensure correct labellings, especially for those near the boundary in eq 2.3, chronotype was further validated by the analysis of DLMO and CAR times, using the process outlined in Facer-Childs et al. [57]. This involved collecting saliva samples at specified intervals on two separate days during the week of testing, on one occasion in the morning upon waking and on another at night preceding sleep. These days were different to the ones scanning occurred on, as sleep patterns were disrupted on scanning days. This resulted in n = 38 CAR times and n = 32 DLMO times. DLMO was not calculated for 2 ECPs and 4 LCPs due to either insufficient saliva samples or technical difficulties in the process.

Furthermore, sleep onset and wake-up times measured from actigraphy data validated the choice of labelling [59]. Across all 5 categories (MSF_{sc}, DLMO, CAR, time of sleep onset and time of awakening) the differences between the groups were significant ($p < 0.0001$) [57].

A comparison of the participants' chronotype distribution, using MSF_{sc}, compared to a general population is made in Figure 4.2 where ECPs and LCPs have MSF_{sc} $02:24 \pm 00:10$ and $06:52 \pm 00:17$ respectively [1].

4.2.4 fMRI Scanning Specifications

A Philips Achieva 3 Tesla MRI scanner with a 32-channel head coil was used to collect the imaging data for all participants. This involved a 5-minute T1-weighted scan to create a standard high-resolution anatomical image of the brain (1 mm isotropic voxels) before a 15-minute eyes-open resting-state scan was obtained. The scans captured the entire brain using gradient echo echo-planer imaging oriented parallel to the AC-PC line with

[1] The four participants classified as LCP despite having a $05:00 \leq MSF_{sc} < 05:30$ had their CAR and DLMO times compared to the other 18 LCP participants to validate their inclusion as LCPs.

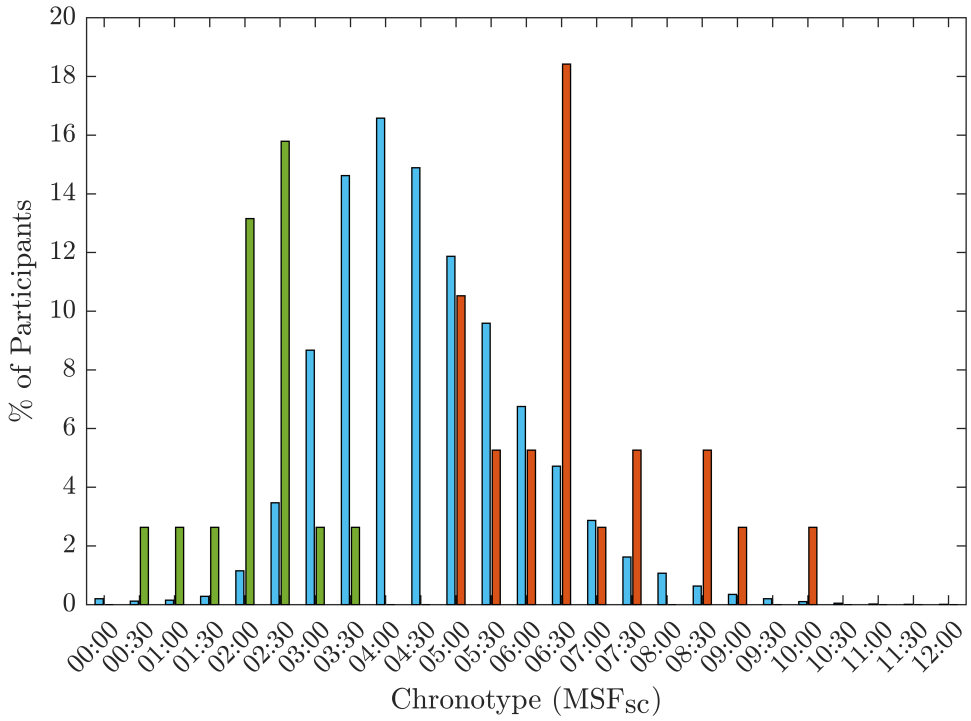


Figure 4.2: **Distribution of Extreme Chronotypes Within the Dataset.** Bar chart showing the distribution of MSF_{sc} comparing the general population (group 1: blue), mainly of Germany, Switzerland and the Netherlands, with the participants in the study (group 2: green, red). The data for the general population was adapted from Roenneberg et al. [157] showing an almost normal distribution. The data for the participants group was created from the MCTQ information provided and is separated into ECP (green) and LCP (red). Inclusion properties for each half hour are the same with the first given by $00:00 \leq MSF_{sc} < 00:30$.

the following parameters: 450 volumes, TR = 2,000 ms, TE = 35 ms, flip angle = 80°, $3 \times 3 \times 4$ mm^3 voxels. Respiratory and cardiac fluctuations were monitored using equipment also provided by Philips [56].

4.2.5 fMRI Preprocessing

The data in this study were already preprocessed by Facer-Childs. This was completed using User-Friendly Functional Connectivity (UF^{2}C) introduced by de Campos et al. [43] a toolbox extension run through MATLAB, which relies upon SPM12 [145] as well as PhysIO [102], which was needed for physiological noise correction. Preprocessing involved standardised methodologies including re-orientation of scans, motion correction,

co-registration, spatially normalising scans to MNI space, spatially smoothing the data with a 6mm Gaussian kernel, high pass temporal filtering ($>$ 0.01 Hz) and correction for physiological noise [56, 130].

4.2.6 Functional Network Construction

The brain was parcellated into 70 functional ROIs previously used by de Campos et al. [43] and based upon the 90 functional ROIs used by the Stanford Find Lab presented in Shirer et al. [169]. This excluded ROIs in the cerebellum due to incomplete coverage of the cerebellum during functional scanning. Information about the ROIs used in the study, including MNI coordinates, is provided in Table 4.1. The average time-series for all voxels within each ROI was then extracted before each time-series was standardised to mean 0 and standard deviation 1.

FNs were then calculated for each participant using Tikhonov partial correlation. A symmetric weighted adjacency matrix with a size 70×70 was created for each participant, for each individual scanning session, called a Tikhonov Partial Correlation Matrix (TPCM). The off-diagonal edge weights are in the range $[-1, 1]$, whilst all values in the leading diagonal are set to NaN as self-links are not interpretable under partial correlation techniques.

Partial correlation was chosen to reduce the contribution from indirect connections [127, 128] as well as its superior performance at replicating ground truth networks considered in simulated data studies [177, 200, 201]. Furthermore, Pervazi et al. [146] did an extensive review of partial correlation as well as various regularisation techniques and recommended Tikhonov partial correlation.

An overview of Tikhonov partial correlation is provided here, based upon the approach used by Pervaiz et al. [146], and is explained in detail in Section 4.2.6.1. The regularisation technique requires adding a scaled identity matrix to the covariance matrix of each participant before partial correlation is calculated using the inverse of the (regularised) covariance matrix, known as the (Tikhonov) precision matrix. The scalar α, known as

Node	ICN Index	ICN	MNI Coordinates	Node	ICN Index	ICN	MNI Coordinates
1	1	Anti Salience	[-33 45 28]	36	6	Ventral DMN	[0 -59 59]
2	1	Anti Salience	[-45 11 2]	37	6	Ventral DMN	[23 19 53]
3	1	Anti Salience	[-1 13 51]	38	6	Ventral DMN	[28 -37 -13]
4	1	Anti Salience	[27 43 33]	39	6	Ventral DMN	[44 -77 37]
5	1	Anti Salience	[41 13 5]	40	7	Language	[-53 21 4]
6	2	Post Salience	[-39 33 34]	41	7	Language	[-52 -5 -16]
7	2	Post Salience	[-58 -41 45]	42	7	Language	[-52 -35 1]
8	2	Post Salience	[-9 -55 67]	43	7	Language	[-54 -59 27]
9	2	Post Salience	[11 -31 49]	44	7	Language	[49 25 -5]
10	2	Post Salience	[19 -51 75]	45	7	Language	[56 -49 13]
11	2	Post Salience	[60 -36 45]	46	8	LECN	[-27 17 52]
12	2	Post Salience	[-12 -27 9]	47	8	LECN	[-29 43 2]
13	2	Post Salience	[-36 -15 -1]	48	8	LECN	[-42 -67 49]
14	2	Post Salience	[12 -17 13]	49	8	LECN	[-58 -45 -7]
15	2	Post Salience	[40 -9 -3]	50	8	LECN	[-14 -31 7]
16	3	Auditory	[-54 -15 10]	51	9	RECN	[39 25 47]
17	3	Auditory	[56 -11 13]	52	9	RECN	[37 49 5]
18	4	Basal Ganglia	[15 -5 13]	53	9	RECN	[48 -56 53]
19	4	Basal Ganglia	[-14 -7 11]	54	9	RECN	[5 35 50]
20	4	Basal Ganglia	[-45 19 28]	55	9	RECN	[11 -1 19]
21	4	Basal Ganglia	[47 27 21]	56	10	Sensorimotor	[-31 -21 63]
22	5	Dorsal DMN	[-3 47 22]	57	10	Sensorimotor	[39 -20 61]
23	5	Dorsal DMN	[-48 -71 41]	58	10	Sensorimotor	[1 -15 67]
24	5	Dorsal DMN	[19 35 53]	59	10	Sensorimotor	[-2 -29 -15]
25	5	Dorsal DMN	[0 -55 31]	60	11	Visual	[-28 -91 7]
26	5	Dorsal DMN	[1 -17 41]	61	11	Visual	[30 -91 13]
27	5	Dorsal DMN	[50 -67 39]	62	11	Visual	[0 -79 17]
28	5	Dorsal DMN	[-2 -11 7]	63	12	Visuospatial	[-27 -3 61]
29	5	Dorsal DMN	[-24 -35 -5]	64	12	Visuospatial	[-32 -55 51]
30	5	Dorsal DMN	[26 -23 -13]	65	12	Visuospatial	[-49 7 32]
31	6	Ventral DMN	[-12 -61 21]	66	12	Visuospatial	[-48 -67 -1]
32	6	Ventral DMN	[-25 9 60]	67	12	Visuospatial	[27 -1 61]
33	6	Ventral DMN	[-28 -39 -11]	68	12	Visuospatial	[38 -49 53]
34	6	Ventral DMN	[-36 -85 39]	69	12	Visuospatial	[49 9 33]
35	6	Ventral DMN	[12 -57 19]	70	12	Visuospatial	[50 -61 -5]

Table 4.1: **The Nodes, ICNs and MNI Coordinates used for 70 Functional Connectivity ROIs.** Here Node 22 is the PCC and Node 25 is the mPFC.

the regularisation parameter, was optimised by minimising the difference between the average precision matrix across all participants and the Tikhonov precision matrix of each individual participant. This optimisation was completed by summing over all participants the element-wise difference between the average and individual precision matrix before squaring each element. Since the resulting matrix is symmetric, the square root of the

sum of only the upper triangular elements was calculated. By considering a range of values of the parameter α, the choice which minimises this square root sum is considered optimal, α_{opt} [146].

For this study, using data from all three scanning sessions α_{opt} = 0.0259. The breakdown of α_{opt} for each scanning session and chronotype is provided in Table 4.2 with a general trend that as the size of the subgroup increases the higher α_{opt} becomes.

Subgroups	Morning	Afternoon	Evening	All Scanning Sessions
ECPs	0.0230	0.0233	0.0235	0.0255
LCPs	0.0212	0.0229	0.0238	0.0241
All Chronotypes	0.0239	0.0251	0.0258	0.0259

Table 4.2: **The Optimum α Values for Various Subgroups of the Dataset.**

Optimising α across all available data rather than for each subset corresponds with the choice of Pervaiz et al. [146]. This choice was made to ensure the results of any further analysis for different scanning sessions can be directly compared under the assumption of a single α_{opt}; similar logic is used when using group ICA to allow the comparison of participants with the same ROIs [32, 204]. This choice is a conservative way of removing any underlying assumptions about differences in the data, as in essence this step is completely blind to the characteristics of the data allowing greater generalisability of the pipeline to different datasets. However, this will result in greater levels of regularisation than if the scanning sessions were separated.

4.2.6.1 The Mathematics of Tikhonov Partial Correlation

Calculation of Tikhonov partial correlation is given below, extended from an outline provided by Pervaiz et al. [146].

Let $x_{i,j}^{m} \in \mathbb{R}^{L \times N}$ be the i, j^{th} component of the data matrix $\mathbf{X^{(m)}}$ for Subject m for a rs-fMRI scan with L timepoints and N ROIs. Then for the m^{th} participant an empirical

covariance matrix, $\mathbf{\Sigma^{(m)}} \in \mathbb{R}^{N\times N}$, can be calculated using,

$$\mathbf{\Sigma^{(m)}} = \frac{1}{L}\left(\mathbf{X^{(m)}} - \bar{\mathbf{X}}^{\mathbf{(m)}}\right)'\left(\mathbf{X^{(m)}} - \bar{\mathbf{X}}^{\mathbf{(m)}}\right),$$

where $'$ denotes matrix transpose and $\bar{\mathbf{X}}^{\mathbf{(m)}} \in \mathbb{R}^{L\times N}$ is the matrix created from vertically stacking the temporal average for each ROI L times,

$$\bar{\mathbf{X}}^{\mathbf{(m)}} = \begin{pmatrix} \bar{x}_1^{(m)} & \bar{x}_2^{(m)} & \cdots & \bar{x}_N^{(m)} \\ \bar{x}_1^{(m)} & \bar{x}_2^{(m)} & \cdots & \bar{x}_N^{(m)} \\ \vdots & \vdots & \ddots & \vdots \\ \bar{x}_1^{(m)} & \bar{x}_2^{(m)} & \cdots & \bar{x}_N^{(m)} \end{pmatrix}; \qquad \bar{x}_j^{(m)} = \frac{1}{L}\sum_{i=1}^{L} x_{i,j}.$$

Now the Tikhonov covariance matrix is given by,

$$\mathbf{\Sigma}_\alpha^{\mathbf{(m)}} = \mathbf{\Sigma^{(m)}} + \alpha\mathbf{I_N}, \tag{4.1}$$

where $\mathbf{I_N} \in \mathbb{R}^{N\times N}$ is an identity matrix. The positive constant α controls the strength of the regularisation while the matrix $\mathbf{I_N}$ acts as the target matrix during the inversion process [115]. Therefore, $\alpha = 0$ will result in partial correlation whilst higher values of α will increasingly force off-diagonal elements closer to 0 and diagonal elements closer to 1, see Section 4.2.6.2 for a toy example demonstrating this. The Tikhonov precision matrix, $\mathbf{\Omega}_\alpha^{\mathbf{(m)}} \in \mathbb{R}^{N\times N}$, with elements $\Omega_{\alpha_{i,j}}^{(m)}$ or to simplify notation $\omega_{i,j}^{(m)}$, can then be calculated as,

$$\mathbf{\Omega}_\alpha^{\mathbf{(m)}} = \left(\mathbf{\Sigma}_\alpha^{\mathbf{(m)}}\right)^{-1} = \omega^{\mathbf{(m)}},$$

using Cholesky decomposition, as explained by Cholesky and Krishnamoorthy [114], to computationally calculate the inverse of the Tikhonov covariance matrix. Finally, the TPCM can be calculated element-wise for $i \neq j$ such that each element is given by,

$$w_{i,j}^{(m)} = \frac{-\omega_{i,j}^{(m)}}{\sqrt{\omega_{i,i}^{(m)}\omega_{j,j}^{(m)}}}.$$

By definition, partial correlation requires two variables to compare whilst controlling for at least one other; therefore $i = j$ and the resulting $\omega_{i,i} = -1$ is meaningless. Hence, values on the main diagonal of the TPCM have been set to NaN and no self-links can be identified by this method.

The selection of the optimal regularisation parameter α in eq 4.1 is based upon minimising an objective function.

First, let $\bar{\mathbf{\Sigma}} \in \mathbb{R}^{N\times N}$ be the average empirical covariance for all n participants calculated by taking the element-wise mean across $\mathbf{\Sigma^{(m)}}$ for the n participants. Also, let $\bar{\mathbf{\Omega}} = \left(\bar{\mathbf{\Sigma}}\right)^{-1} \in \mathbb{R}^{N\times N}$ be the precision matrix associated with the average empirical covariance matrix, with elements $\bar{\Omega}_{i,j}$. A matrix $\mathbf{\Gamma_{\alpha}^{(m)}} \in \mathbb{R}^{N\times N}$ with elements, $\Gamma_{\alpha_{i,j}}^{(m)}$, can then be defined using,

$$\Gamma_{\alpha_{i,j}}^{(m)} = \left(\sum_{m=1}^{n}\left(\Omega_{\alpha_{i,j}}^{(m)} - \bar{\Omega}_{i,j}\right)\right)^2 = \left(\sum_{m=1}^{n}\left(\omega_{i,j}^{(m)} - \bar{\Omega}_{i,j}\right)\right)^2.$$

Each element is calculated by summing the difference between the i,j^{th} element of the average precision matrix and each participant's corresponding α specified Tikhonov precision matrix element before squaring the result.

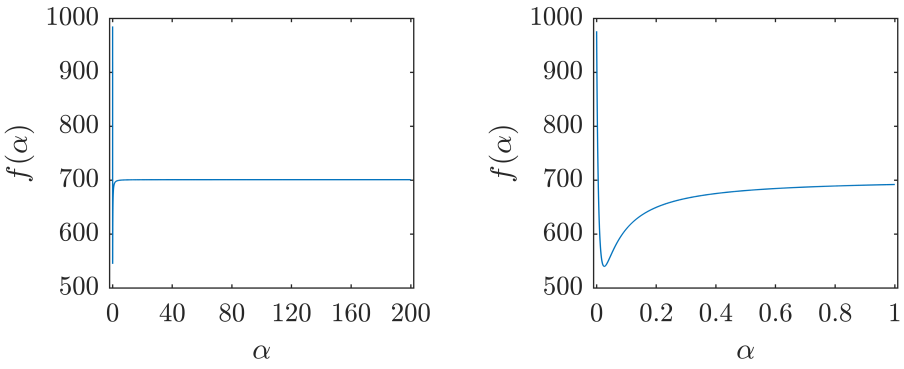
Therefore, α_{opt} is the value of α which minimises the square root of the sum of the upper triangular elements in $\mathbf{\Gamma}_{\alpha}$ and hence is selected for Tikhonov partial correlation,

$$\alpha_{\text{opt}} = \underset{\alpha}{\text{argmin}}\left(\sqrt{\sum_{i<j}\Gamma_{\alpha_{i,j}}}\right) = \underset{\alpha}{\text{argmin}}\left(f(\alpha)\right). \tag{4.2}$$

Potential α values should be considered over a range $[\alpha^{\text{lower}}, \alpha^{\text{upper}}]$, here $[0.0001, 1]$ in steps of 0.0001 was considered (Figure 4.3b) after initially scanning over a wider range $[0, 200]$ (Figure 4.3a). However, for new datasets it would still be important to check the data is standardised, α_{opt} is unique and that $\alpha_{\text{opt}} \neq \alpha^{\text{upper}}$. The value of $\alpha^{\text{upper}} = 1$ has been artificially set based on the profile of $f(\alpha)$ for this dataset ensuring the range captures the minimum. If $\alpha_{\text{opt}} = \alpha^{\text{upper}}$ it would be important to understand the behaviour

of $f(\alpha)$, to ensure that the argmin has indeed been found. A simple example of $f(\alpha)$ monotonically decreasing highlights potential issues as a search range of $[0, \alpha^{\text{upper}}]$ would always result in $\alpha_{\text{opt}} = \alpha^{\text{upper}}$ for all choices of α^{upper} despite no optimum actually existing.

Note that this provides one value of α for which to regularise the n participants being considered. In this case $\alpha_{\text{opt}} = 0.0259$ was optimised across all 113 scans, as seen in Figure 4.3b. This small value for the regularisation parameter is sensible given $L > N$ and therefore a stable matrix inversion should be theoretically possible without regularising i.e. with $\alpha = 0$.



(a) [0, 200] (b) [0.0001, 1]

Figure 4.3: **Finding argmin($f(\alpha)$) for Varying Ranges.** **(a)** The function $f(\alpha)$ for $\alpha \in [0, 200]$ where $\alpha_{\text{opt}} = 0.02$ **(b)** The function $f(\alpha)$ for $\alpha \in [0.0001, 1]$ where $\alpha_{\text{opt}} = 0.0259$.

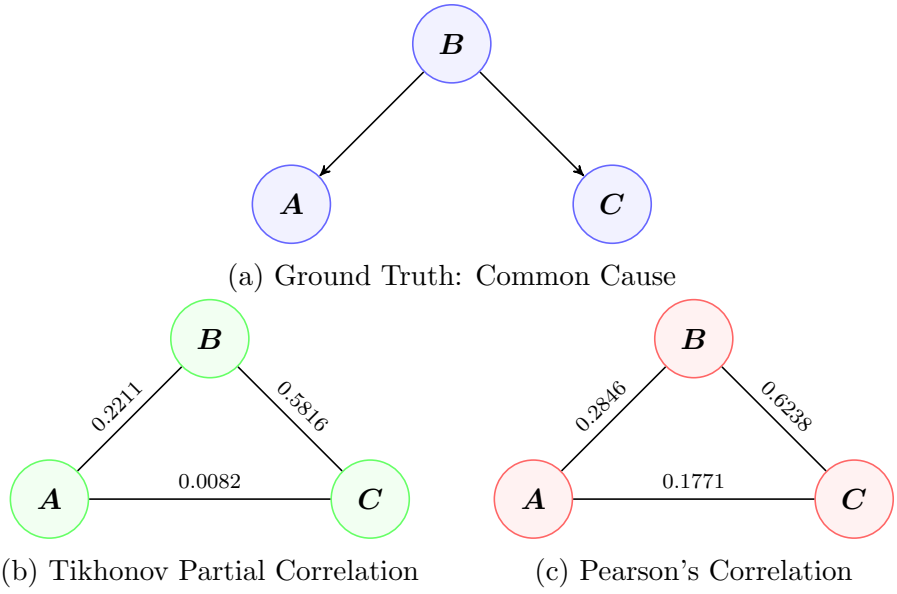
The values in the TPCM then represent the strength of statistical connection between different ROIs. If $\omega_{i,j} = 0$ then under the assumption of fMRI data having Gaussian noise there will be no edge between ROIs i and j [10].

4.2.6.2 Simulated Toy Example For Tikhonov Partial Correlation

To compare Tikhonov and Pearson's correlation, the most common type of FC [65], and highlight the impact of α a toy example is considered, governed by the same equations as in Figure 3.4 inspired by Wang et al. [201]. The network used for the simulation is called a common cause network named because two nodes both have one common source node, as seen in Figure 4.4a. The Tikhonov partial correlation procedure requires a group in

order to determine α_{opt}, therefore the simulated group was based upon 15 participants, whose time-series were all governed by the same equations with different random noise time-series used for node B.

To ensure the effect of random noise did not affect the results, 1,000 cohorts of 15 participants were simulated and results were averaged across the 1,000 repeats. The differences between the ground truth, Pearson's correlation and Tikhonov partial correlation are displayed in Figure 4.4. Note the Tikhonov partial correlation matrix is the same network previously considered in Figure 3.4 and as seen under thresholding and binarizing Tikhonov partial correlation will produce a network close to the ground truth if $\bar{t} > 0.0082$, which would not be true for Pearson's correlation if $\bar{t} < 0.1771$.



(a) Ground Truth: Common Cause

(b) Tikhonov Partial Correlation

(c) Pearson's Correlation

Figure 4.4: **Comparison of Tikhonov and Pearson's Correlation in a Common Cause Network. (a)** The ground truth for a common cause network. **(b)** The FN for one simulated subject created from averaging the results across 1,000 simulated cohorts each with 15 participants. Showing the ability for Tikhonov partial correlation to almost replicate the lack of connection between ROIs A and C. **(c)** The FN for one simulated participant created from averaging the results across 1,000 simulations using Pearson's correlation. Note the higher edge weight between nodes A and C.

In addition, the functional connectivity matrices for one of the simulated subjects when the level of regularisation was artificially set is shown in Figure 4.5. A range of α values as well as α_{opt} are considered and the colour scale has been kept constant showing

that as α increases the mean squared error when comparing off-diagonal edges to zero decreases.

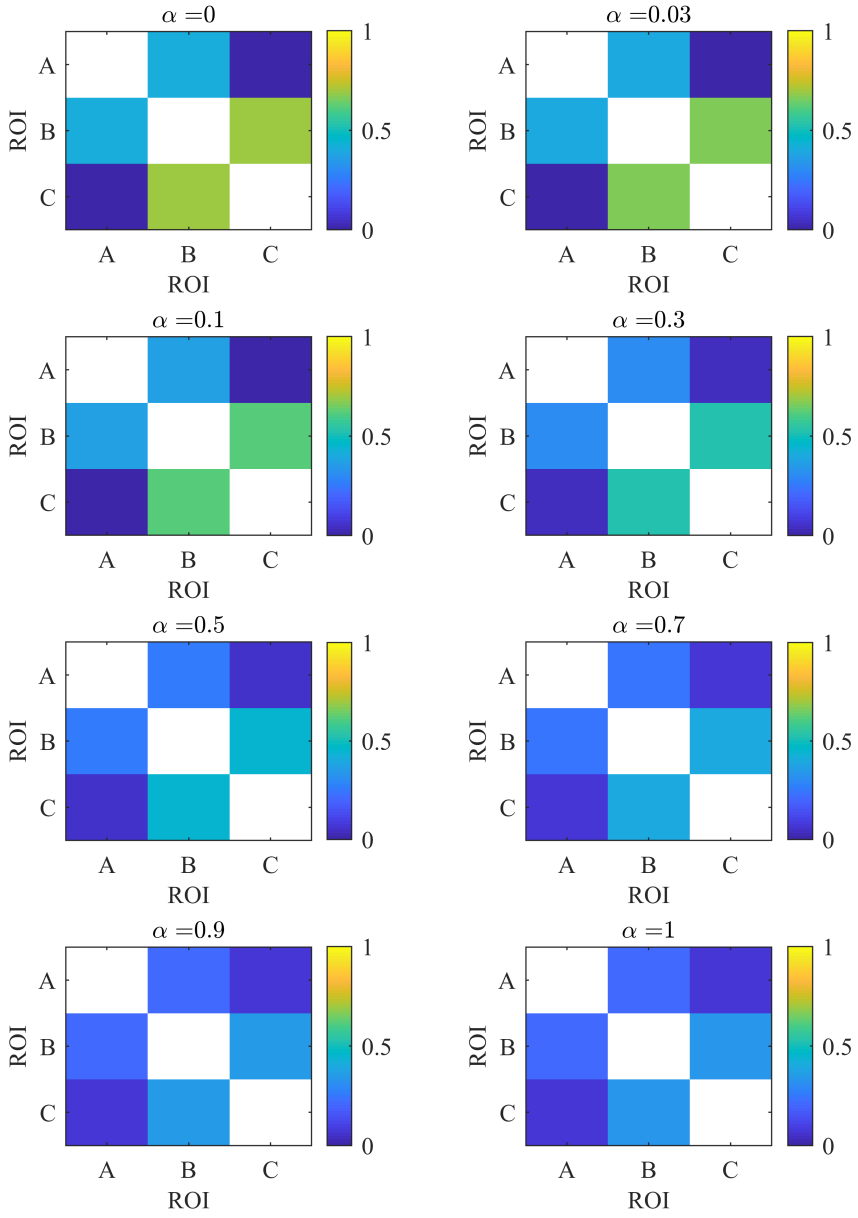


Figure 4.5: **Simulated Toy Examples Varying α for Tikhonov Partial Correlation.** Functional connectivity matrices for 1 simulated participant - out of 15 - after varying the value of the regularisation parameter α. The value α = 0.03 is the optimum α for the group as calculated using the procedure outlined in Section 4.2.6.1. Note, the main diagonal in all matrices has been set to NaN.

4.2.7 Thresholding and Binarization

Using Tikhonov partial correlation produced undirected, weighted edges. For the training of some classifiers, these were then thresholded and binarized. The threshold, $\bar{t}$, for binarizing the edges ranged incrementally between lower and upper limits allowing graph metrics to be given as a function of the threshold. The lower threshold in all cases was 0, which ensured only positive Tikhonov partial correlations remained. The upper threshold, $\bar{t}_{\max}$, was selected as a multiple of 0.01 such that the remaining network was connected for all participants in the scanning session, as done by Liu et al. [123]. This is the equivalent of selecting the minimum *percolation* threshold across the participants within each scanning session. This creates more physiologically accurate networks, as different brain regions are known to be connected both structurally and functionally.

In addition, to ensure the choice of binarizing the network did not vastly alter the success of any classification the FNs were also thresholded at $\bar{t} = 0$ ensuring positive weighted networks were considered.

4.2.8 Graph Metrics

With no previous FN chronotype studies a pragmatic approach for selecting graph metrics was to consider a limited number ranging across local and global measures. These are node degree (node strength was also considered in the weighted case), betweenness centrality, clustering coefficient, local efficiency, global efficiency, characteristic path length, assortativity and small world index, as introduced in Section 3.1.1.6. In the case of local measures (the first 4 out of 8 (5 out of 9) graph metrics) the mean across all nodes was calculated in the context of the whole brain. For the classifiers based on the ROIs PCC or mPFC only the local measures were calculated.

The graph metrics were calculated using BCT, except for the small world index, which was calculated using the analytical approach (given in eq 3.7) for the binary case. In the weighted case, unpublished code was used as outlined in 3.1.1.6.

4.2.9 Spatial Scales

The full 70 node FNs were analysed using global graph metrics as well as the mean across all local metrics. In addition, the local graph metrics for two ROIs from the DMN were also considered, the mPFC and PCC. This was due to seed-based clusters for each of the two regions, under the contrast ECP>LCP being predictive of attentional performance as measured through PVT [57].

4.2.10 Balancing Groups

The relative size of the ECP and LCP subgroups within the training data might have introduced bias as the total sample size was small, and the subgroups were unbalanced. Therefore, balancing runs were used to reduce the effect of the uneven sample sizes. In each balancing run a random subset of LCPs was chosen to match the number of ECPs in the training data. To remove bias that may have occurred from the randomly selected subset, 100 balancing runs were completed for the training and testing of each classifier. Therefore, the performance of the classifier based on a specific graph metric and threshold is given as the mean over the 100 balancing runs. Due to the balancing runs random chance is 50% for each run. While other approaches such as different weighting for the two groups [85] is a potential approach to overcome imbalanced datasets, balancing runs allow a more direct comparison between the two classification techniques (logistic regression and SVM) used in this Chapter.

4.2.11 The Classifier

A logistic curve was fitted to the available data such that each logistic regression curve was trained using one graph metric and the participant's chronotype class (ECP represented by 0 or LCP represented by 1). The value of the test subject's graph metric can then be used to find the intersection with the logistic curve, a value less than or equal to 0.5 resulted in the test subject being labelled an ECP whilst a higher value meant the subject

was labelled an LCP.

The choice to use a classifier trained on one graph metric at a time was to increase the ability to interpret the results rather than having to understand the complexity of the brain in an 8 or 9 dimensional space. However, to ensure the classifiers were not hindered by this decision, a comparison to an SVM classifier trained using all available graph metrics was made for each threshold in the binary case. Both classifiers were implemented using standard MATLAB functions.

As the chronotype dataset is relatively small with at most 32 participants (due to balancing runs) for a scanning session the training and test datasets were selected using a Leave One Out Cross-Validation (LOOCV) approach. This is $k-$fold validation where k is equal to the number of participants and is useful for small datasets, allowing the classifier to be trained on the largest amount of data while still enabling the classifier's performance to be representative of the dataset as a whole. Each classifier's performance was then summarised using accuracy (eq 3.11) as well as OOP (eq 3.12).

4.2.12 Statistical Analysis

A statistical comparison between the graph metrics of the two extreme chronotypes was also completed for the whole network in the binary case for each threshold and the weighted case. This was completed to aid the interpretation of the classifiers performance. In each case, the graph metrics were compared using non-parametric permutation testing and the p-values were corrected for multiple comparisons using the Benjamini-Hochberg method [11, 78].

4.3 Results

The results for the three scanning sessions are given below in the chronological ordering of the study with Afternoon results in Section 4.3.1, Evening results in Section 4.3.2 and Morning results in Section 4.3.3.

4.3.1 Afternoon Scanning Session

The results for the Afternoon when averaged over 100 balancing runs of a logistic regression classifier are given in this section. The results for the thresholded binary FNs at the whole brain level and the corresponding distributions are given in Figures 4.6 and 4.7 respectively.

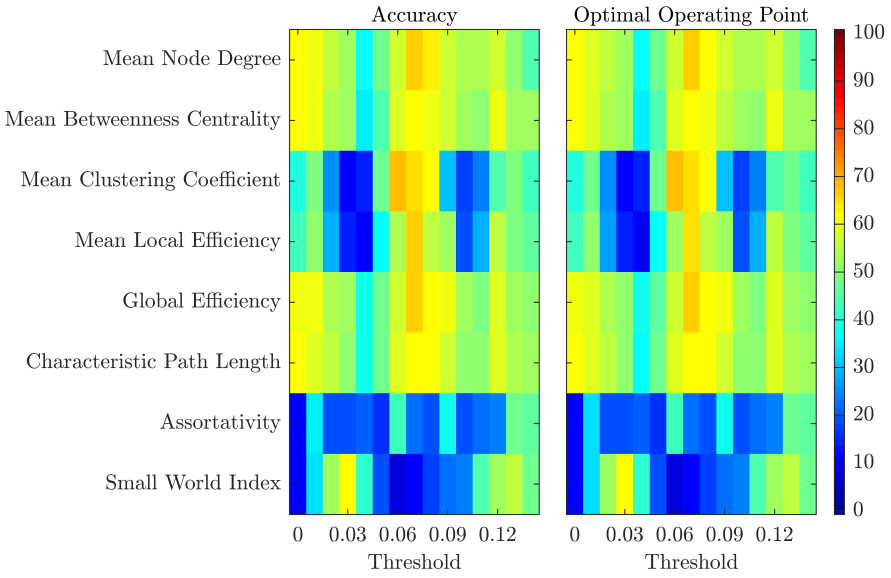


Figure 4.6: **Result of Logistic Regression Classifiers for the Afternoon Scan: Whole Network - Binarized.** The accuracy and OOP resulting from training a logistic regression classifier using graph metrics calculated for the whole network when binarized for non-negative thresholds increasing in steps of 0.01 from 0 to the percolation threshold for the Afternoon scan. The results plotted are the mean of 100 balancing runs.

Within Figure 4.6 the highest average accuracy over 100 balancing runs was 67.6% achieved by the mean clustering coefficient for $\bar{t}$ = 0.06 and the results for mean node degree, local efficiency and global efficiency produced similar levels of accuracy at $\bar{t}$ = 0.07. It is worth noting that the peaks in accuracy generally occurred near the middle of the thresholds considered, indicating the lowest edge weights were not considered important in the differentiation process. This differs in the other scanning sessions, as seen in Figures 4.14 and 4.22. The distributions given in Figure 4.7 provide evidence for why the classifier was not more successful. When a Benjamini-Hochberg [78] False Discovery Rate (FDR) correction method was used to compensate for testing at multiple thresholds as well as

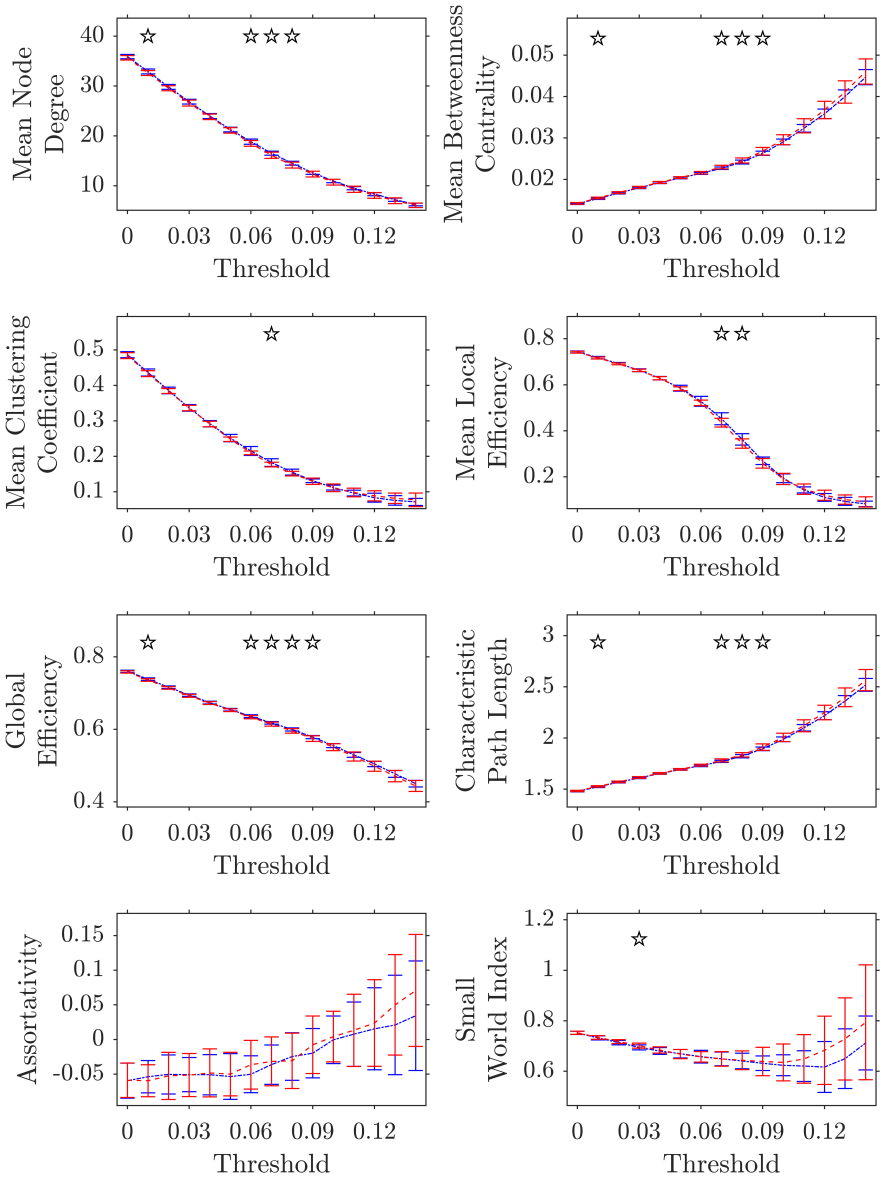


Figure 4.7: **Distribution of Graph Metrics for the Afternoon Scan: Whole Network - Binarized.** The values for various graph metrics for both ECPs (-·-·-) and LCPs (- - - - -) calculated for the whole network when binarized for non-negative thresholds increasing in steps of 0.01 from 0 to the percolation threshold for the Afternoon scan. The standard deviation between participants in that group is shown by the error bars. The ☆ indicates where the difference between ECPs and LCPs is significant $p < 0.05$ (uncorrected).

using different graph metrics no significant differences between the graph metrics of the two groups remained (Figure 4.7). The lack of significantly different graph metrics may have hindered the ability for the training data to be efficiently separated and hence the low accuracy within the logistic regression classifier.

In addition, the thresholded and binarized results at the nodal level for the mPFC and PCC are given in Figures 4.8 and 4.9.

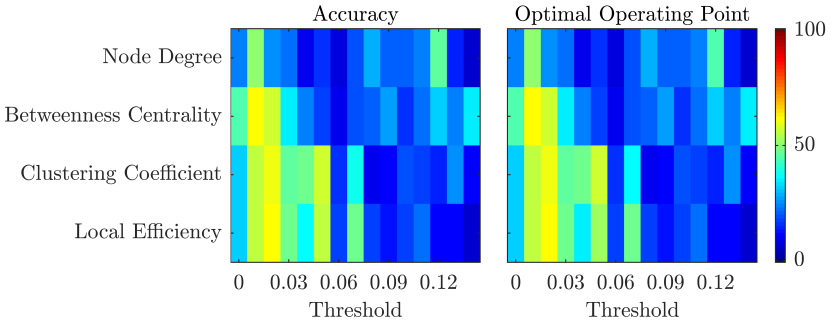


Figure 4.8: **Result of Logistic Regression Classifiers for the Afternoon Scan: mPFC - Binarized.** The accuracy and OOP resulting from training a logistic regression classifier using graph metrics calculated for the mPFC when binarized for non-negative thresholds increasing in steps of 0.01 from 0 to the percolation threshold for the Afternoon scan. The results plotted are the mean of 100 balancing runs.

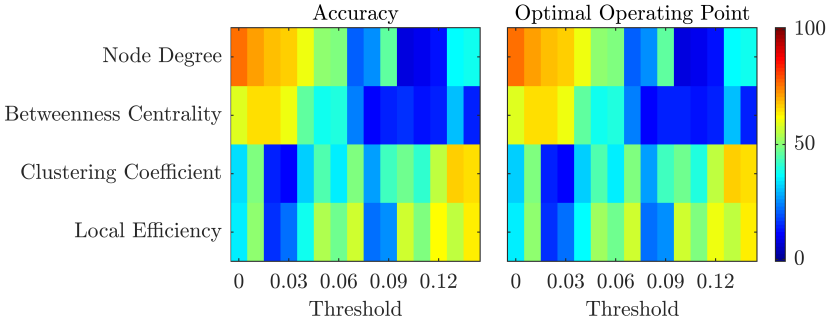


Figure 4.9: **Result of Logistic Regression Classifiers for the Afternoon Scan: PCC - Binarized.** The accuracy and OOP resulting from training a logistic regression classifier using graph metrics calculated for the PCC when binarized for non-negative thresholds increasing in steps of 0.01 from 0 to the percolation threshold for the Afternoon scan. The results plotted are the mean of 100 balancing runs.

Here we see that the classifier trained using mPFC performed similarly across the betweenness centrality, clustering coefficient and local efficiency near $\bar{t} = 0.02$ reaching an accuracy of $\sim 61\%$. However, for the PCC the accuracy peaked at 76% for the node degree with $\bar{t} = 0$ and the accuracy was fairly robust as the threshold increased over the next couple of steps. Therefore, it appears the presence of a positive edge was more important than the weight itself. This is surprising as a threshold of $\bar{t} = 0$ may be thought to add

noise into the system by increasing the contribution from low positively weighted edges rather than actually adding differential information.

Furthermore, the results for the positive weighted networks for all 70 ROIs and the corresponding scatterplots are given in Figure 4.10 and Figure 4.11 respectively.

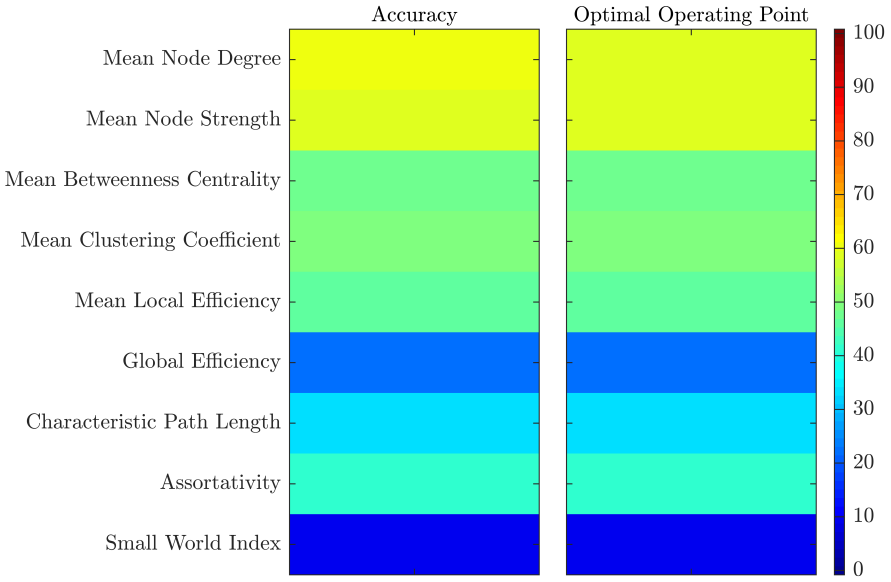


Figure 4.10: **Result of Logistic Regression Classifiers for the Afternoon Scan: Whole Network - Positive Weighted.** The accuracy and OOP resulting from training a logistic regression classifier using graph metrics calculated for the whole network using positive edge weights for the Afternoon scan. The results plotted are the mean of 100 balancing runs.

The accuracy was lower than that achieved for the corresponding thresholded networks as accuracy peaked at 61.2% for the mean node degree, which performed slightly better than the weighted alternative mean node strength. Again the distribution provides an explanation for the poor accuracy, as the two groups greatly overlapped, which would have prevented efficient training of the classifier. Indeed, the ECPs and LCPS did not significantly differ for any of the graph metrics, even before correcting for multiple comparisons, as measured using a permutation test.

Also, the nodal results for the positive weighted networks are presented in Figures 4.12 and 4.13 for the mPFC and PCC respectively. These results reflected those already seen in Figures 4.8 and 4.9. Indeed the classifier trained using the mPFC was barely above

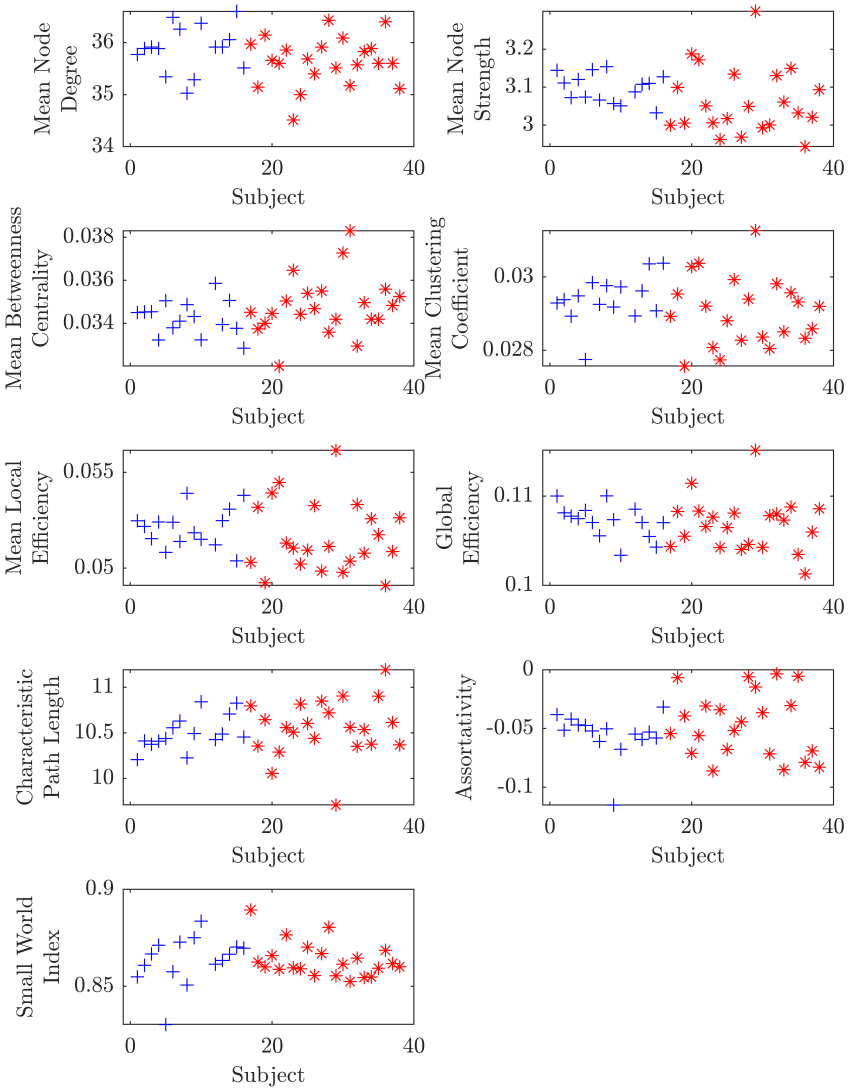


Figure 4.11: **Scatterplots of Graph Metrics for the Afternoon Scan: Whole Network - Weighted.** The values for various graph metrics for ECPs (+) and LCPs (✳) were calculated for the whole network using positive edge weights for the Afternoon scan.

random chance and accuracy peaked at 53.9% for betweenness centrality. However, the classifier trained using the PCC performed better. For instance, using the mean node degree of the PCC resulted in 75.5% accuracy.

In addition, as a final comprehensive step to understand the overall power of all the graph metric information, an SVM classifier was trained using the binarized networks for all thresholds up to the percolation threshold. The results are given in Table 4.3 with accuracy peaking at 70.1% - an improvement in peak accuracy compared to the logistic regression classifier but by a minimal amount. Therefore, suggesting that while

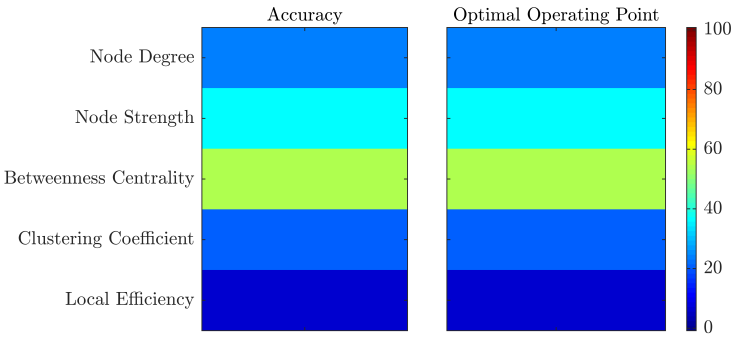


Figure 4.12: **Result of Logistic Regression Classifiers for the Afternoon Scan: mPFC - Positive Weighted.** The accuracy and OOP resulting from training a logistic regression classifier using graph metrics calculated for the mPFC using positive edge weights for the Afternoon scan. The results plotted are the mean of 100 balancing runs.

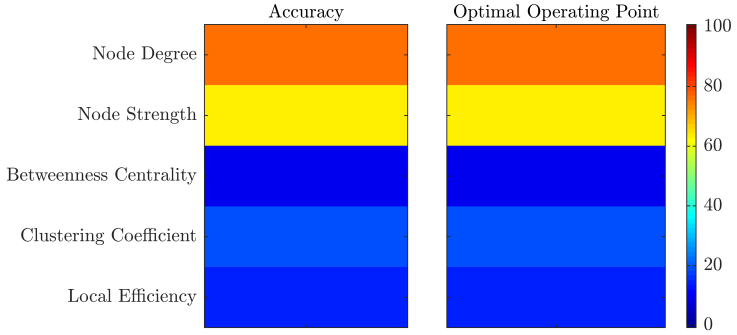


Figure 4.13: **Result of Logistic Regression Classifiers for the Afternoon Scan: PCC - Positive Weighted.** The accuracy and OOP resulting from training a logistic regression classifier using graph metrics calculated for the PCC using positive edge weights for the Afternoon scan. The results plotted are the mean of 100 balancing runs.

the combination of graph metrics provided more differentiable information compared to the use of individual metrics, the effect was limited.

Threshold	Accuracy	Optimal Operating Point
0	55.07 ± 9.18	52.17 ± 10.34
0.01	54.43 ± 4.19	50.11 ± 5.73
0.02	51.70 ± 9.77	51.29 ± 9.79
0.03	50.77 ± 6.42	49.11 ± 5.80
0.04	28.93 ± 18.51	28.62 ± 18.31
0.05	34.93 ± 22.77	34.19 ± 22.27
0.06	59.07 ± 4.40	58.95 ± 4.32
0.07	70.10 ± 3.59	68.43 ± 4.58
0.08	65.13 ± 4.86	63.08 ± 5.19
0.09	67.20 ± 7.97	62.19 ± 9.24
0.1	51.60 ± 18.80	50.58 ± 18.13
0.11	51.57 ± 21.98	49.30 ± 21.12
0.12	57.60 ± 13.96	55.90 ± 13.77
0.13	55.20 ± 15.57	53.35 ± 15.74
0.14	44.43 ± 20.12	41.70 ± 19.16

Table 4.3: **Results of SVM Classifier for the Afternoon Scan: Whole Network - Binarized.** The results for training an SVM classifier using all available graph metrics calculated for the whole network when binarized for non-negative thresholds increasing in steps of 0.01 from 0 to the percolation threshold for the Afternoon scan. The results presented are the mean±std for the 100 balancing runs.

4.3.2 Evening Scanning Session

The results for the classifier using the Evening dataset are displayed in Figure 4.14, and the accompanying distributions are given in Figure 4.15.

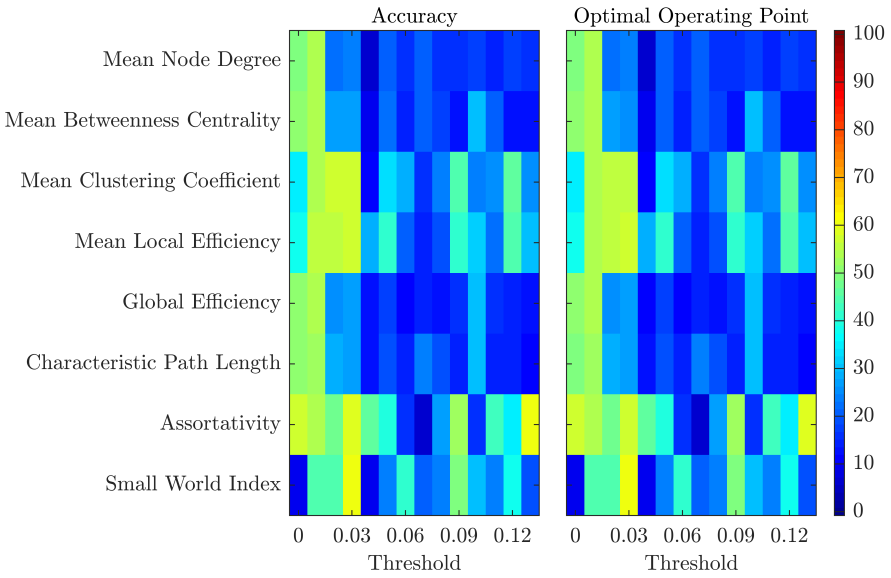


Figure 4.14: **Result of Logistic Regression Classifiers for the Evening Scan: Whole Network - Binarized.** The accuracy and OOP resulting from training a logistic regression classifier using graph metrics calculated for the whole network when binarized for non-negative thresholds increasing in steps of 0.01 from 0 to the percolation threshold for the Evening scan. The results plotted are the mean of 100 balancing runs.

Within Figure 4.14 the highest average accuracy over 100 balancing runs was 60.1% achieved by assortativity at $\bar{t}$ = 0.13. In addition, assortativity and small-worldness both achieved an accuracy of ~ 57% for $\bar{t}$ = 0.03. Furthermore, the majority of the graph metrics have a peak in accuracy near $\bar{t}$ = 0.02, with accuracy generally declining as the threshold increases. The performance of the classifier can be explained by the distributions given in Figure 4.15. Indeed, only assortativity for $\bar{t}$ = 0.03 was significantly different, however significance did not survive the Benjamini-Hochberg correction for multiple comparisons [78] - hindering the training of any classifier.

In addition, colorplots of the results at the nodal level for mPFC and PCC, when the network was thresholded and binarized, are given in Figures 4.16 and 4.17 respectively. The peak accuracy for the mPFC was for betweenness centrality with 61.5% at $\bar{t}$ = 0.08.

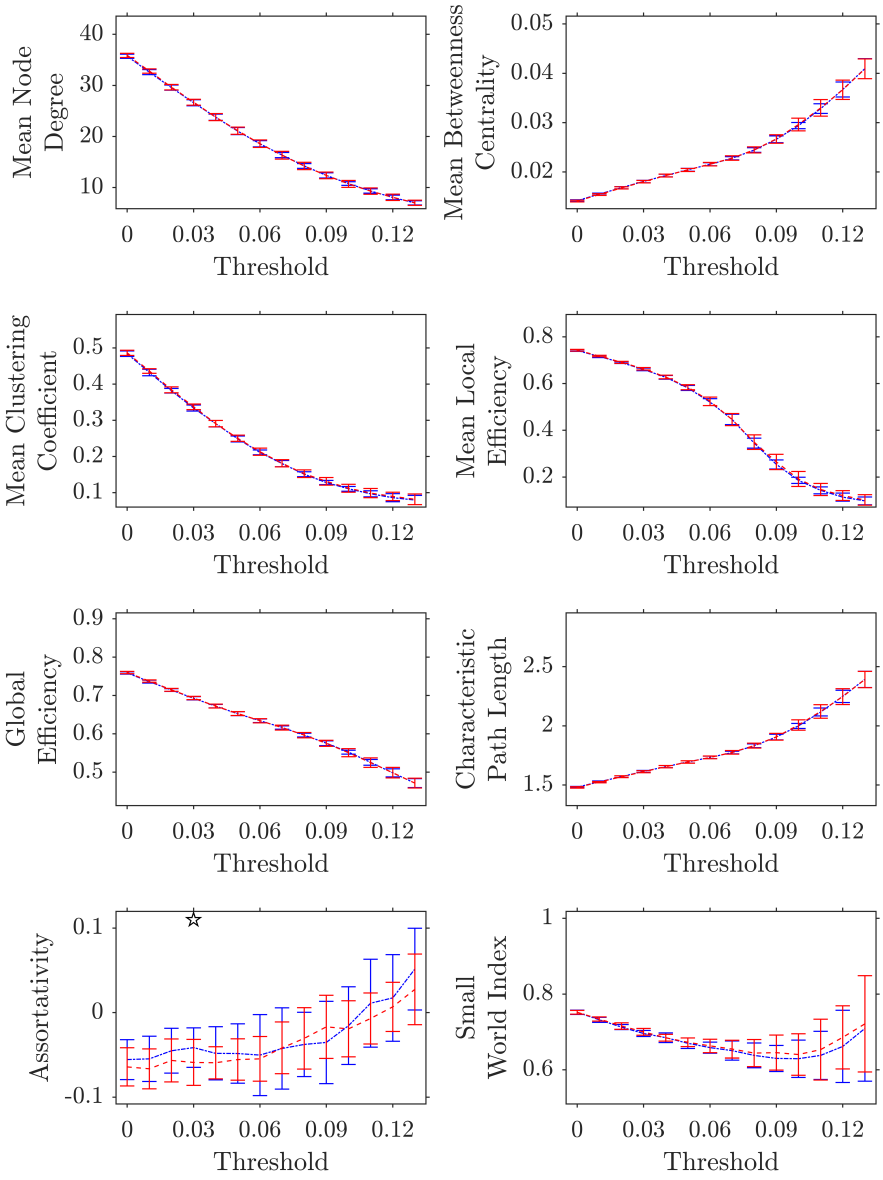


Figure 4.15: **Distribution of Graph Metrics for the Evening Scan: Whole Network - Binarized.** The values for various graph metrics for both ECPs (-·-·-) and LCPs (- - - - -) calculated for the whole network when binarized for non-negative thresholds increasing in steps of 0.01 from 0 to the percolation threshold for the Evening scan. The standard deviation between participants in that group is shown by the error bars. The ☆ indicates where the difference between ECPs and LCPs is significant $p < 0.05$ (uncorrected).

The results for the PCC were higher as accuracy peaked at 67.1% for local efficiency at $\bar{t} = 0.09$.

The results of the classifier trained using graph metrics from weighted networks and scatterplots of the corresponding graph metrics for the Evening scan are given in Figure

4.18 and Figure 4.19 respectively.

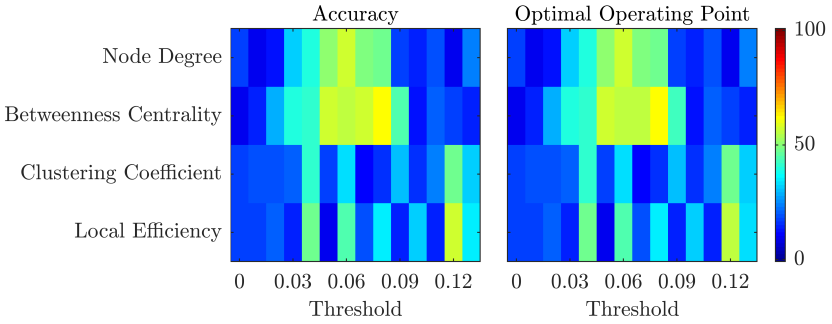


Figure 4.16: **Result of Logistic Regression Classifiers for the Evening Scan: mPFC - Binarized.** The accuracy and OOP resulting from training a logistic regression classifier using graph metrics calculated for the mPFC when binarized for non-negative thresholds increasing in steps of 0.01 from 0 to the percolation threshold for the Evening scan. The results plotted are the mean of 100 balancing runs.

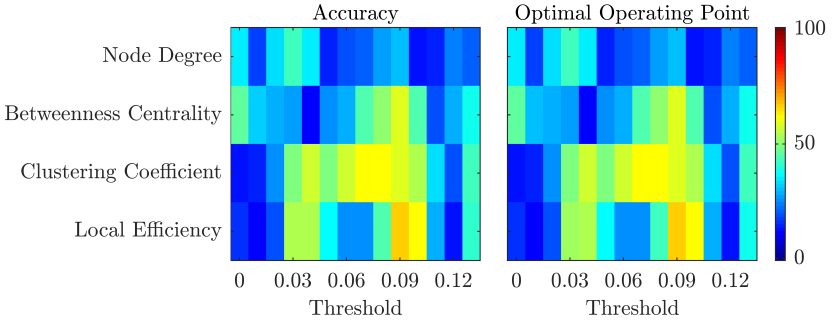


Figure 4.17: **Result of Logistic Regression Classifiers for the Evening Scan: PCC - Binarized.** The accuracy and OOP resulting from training a logistic regression classifier using graph metrics calculated for the PCC when binarized for non-negative thresholds increasing in steps of 0.01 from 0 to the percolation threshold for the Evening scan. The results plotted are the mean of 100 balancing runs.

Accuracy was barely above random chance; indeed mean node degree, mean betweenness centrality and assortativity reached ~ 52%. Before correcting for multiple comparisons, the assortativity of the two groups was significantly different however, after using the Benjamini-Hochberg method of correcting for multiple comparisons [78] no significance remained.

Also, the results for the classifier trained on the ROIs mPFC and PCC are given in Figures 4.20 and 4.21 respectively. For the mPFC accuracy reached ~ 56% for both the

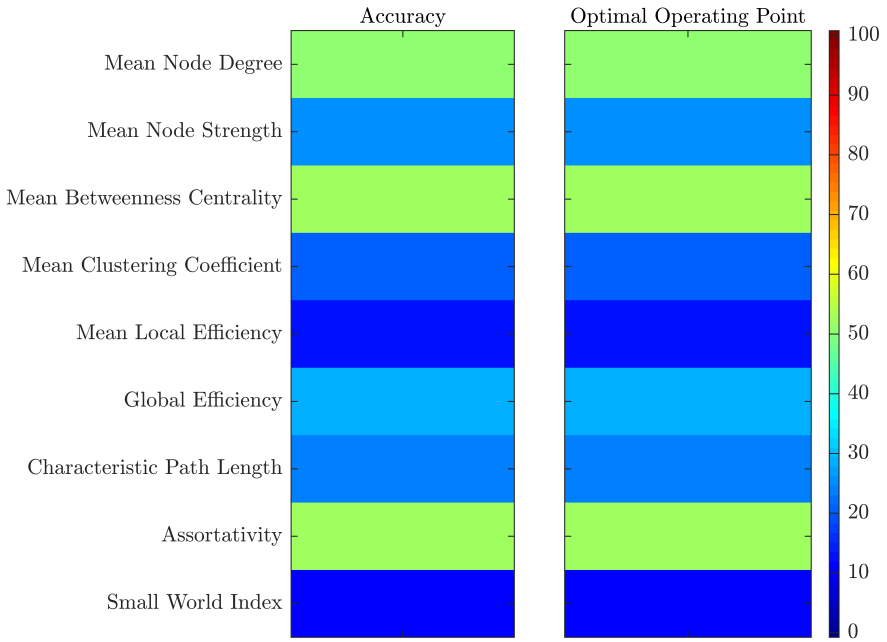


Figure 4.18: **Result of Logistic Regression Classifiers for the Evening Scan: Whole Network - Positive Weighted.** The accuracy and OOP resulting from training a logistic regression classifier using graph metrics calculated for the whole network using positive edge weights for the Evening scan. The results plotted are the mean of 100 balancing runs.

clustering and local efficiency whilst for the PCC the accuracy was never above random chance.

Finally, the results for SVM classifiers when trained using thresholded and binarized networks are given in Table 4.4 for each threshold value. In all cases, the accuracy was less than random chance, and the SVM classifier performed worse than the logistic regression classifier.

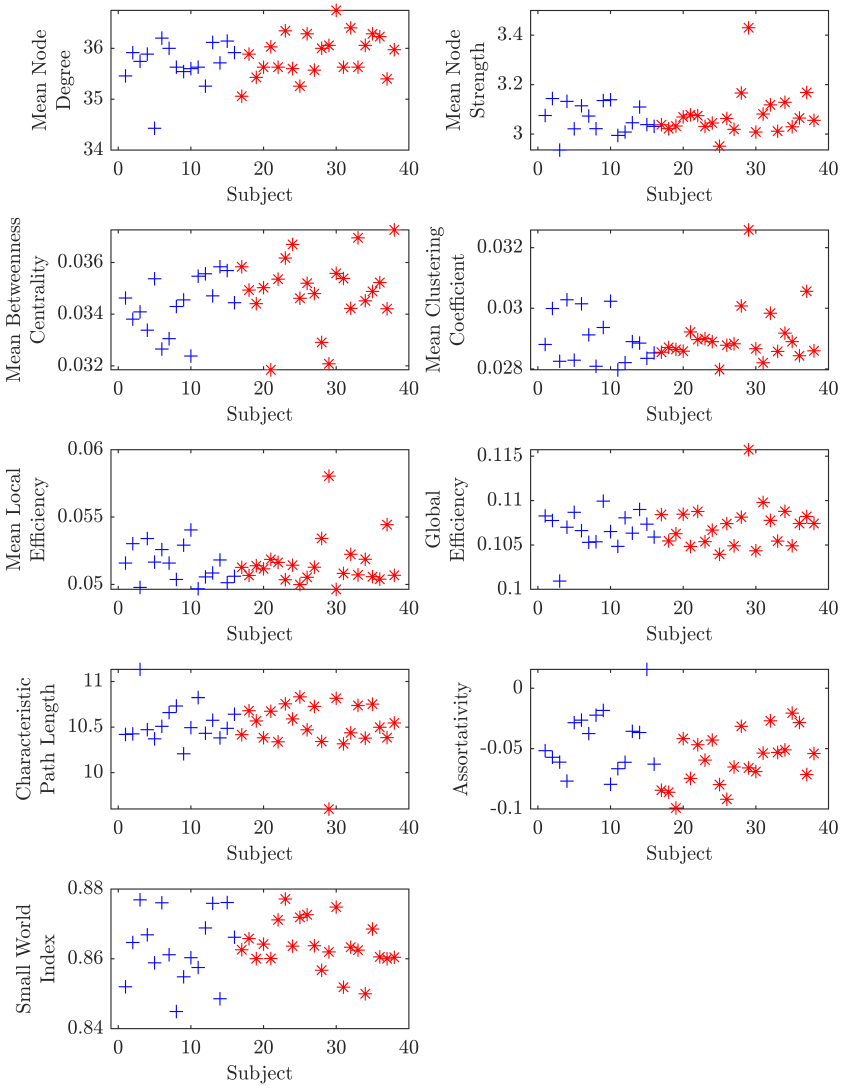


Figure 4.19: **Scatterplots of Graph Metrics for the Evening Scan: Whole Network - Weighted.** The values for various graph metrics for ECPs (+) and LCPs (*) were calculated for the whole network using positive edge weights for the Evening scan.

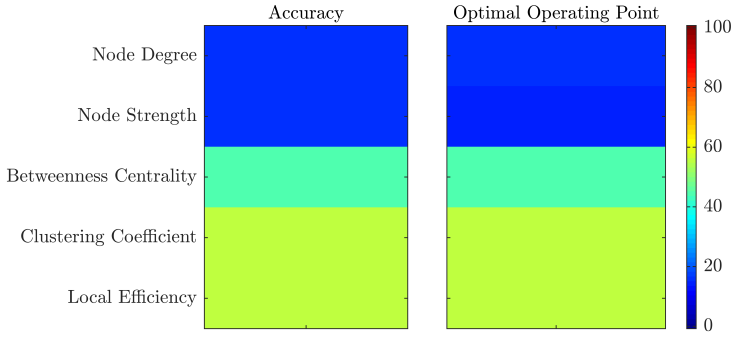


Figure 4.20: **Result of Logistic Regression Classifiers for the Evening Scan: mPFC - Positive Weighted.** The accuracy and OOP resulting from training a logistic regression classifier using graph metrics calculated for the mPFC using positive edge weights for the Evening scan. The results plotted are the mean of 100 balancing runs.

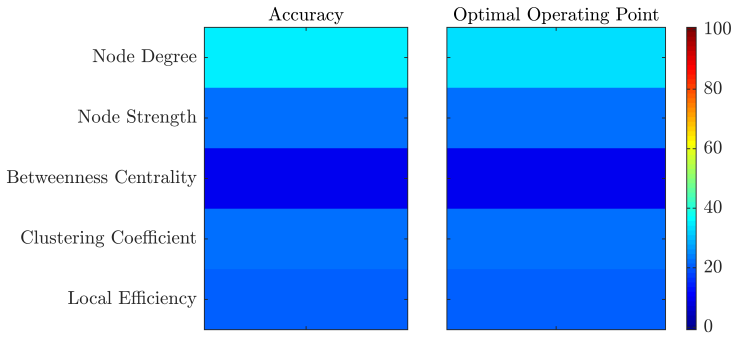


Figure 4.21: **Result of Logistic Regression Classifiers for the Evening Scan: PCC - Positive Weighted.** The accuracy and OOP resulting from training a logistic regression classifier using graph metrics calculated for the PCC using positive edge weights for the Evening scan. The results plotted are the mean of 100 balancing runs.

Threshold	Accuracy	Optimal Operating Point
0	28.75 ± 14.66	25.27 ± 12.28
0.01	50.19 ± 11.11	47.57 ± 11.39
0.02	17.72 ± 20.54	17.67 ± 20.50
0.03	18.19 ± 22.19	18.00 ± 22.00
0.04	9.09 ± 15.94	8.93 ± 15.70
0.05	9.63 ± 17.07	8.84 ± 15.40
0.06	4.78 ± 12.97	4.00 ± 10.43
0.07	8.69 ± 18.01	8.08 ± 16.66
0.08	9.81 ± 19.79	9.49 ± 19.13
0.09	6.13 ± 14.92	5.90 ± 14.03
0.1	15.63 ± 24.57	15.41 ± 24.24
0.11	11.59 ± 18.16	11.40 ± 17.89
0.12	4.16 ± 9.31	3.80 ± 8.28
0.13	2.78 ± 9.54	2.57 ± 8.81

Table 4.4: **Results of SVM Classifier for the Evening Scan: Whole Network - Binarized.** The results for training an SVM classifier using all available graph metrics calculated for the whole network when binarized for non-negative thresholds increasing in steps of 0.01 from 0 to the percolation threshold for the Evening scan.The results presented are the mean±std for the 100 balancing runs.

4.3.3 Morning Scanning Session

The results for the whole brain when thresholding and binarizing the FNs from the Morning scan are presented in Figure 4.22 alongside the distributions for the two groups in Figure 4.23.

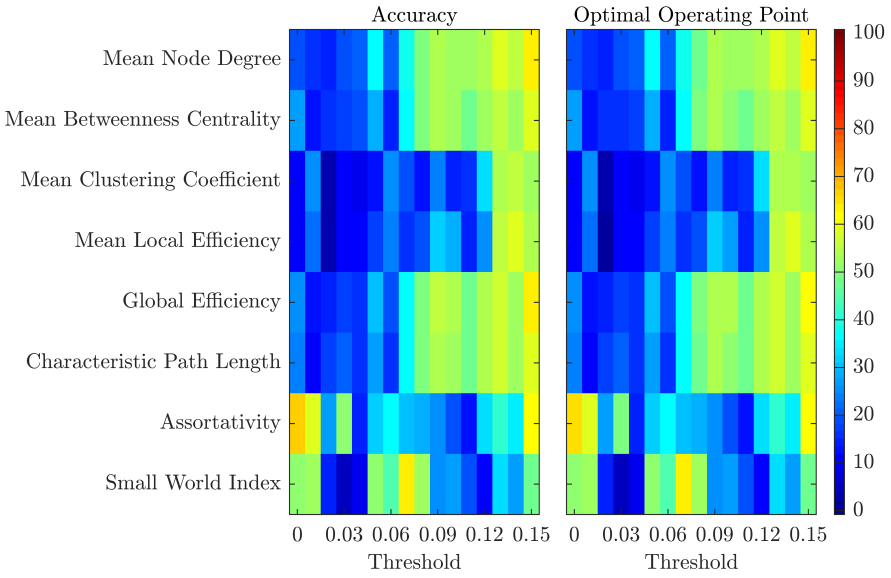


Figure 4.22: **Result of Logistic Regression Classifiers for the Morning Scan: Whole Network - Binarized.** The accuracy and OOP resulting from training a logistic regression classifier using graph metrics calculated for the whole network when binarized for non-negative thresholds increasing in steps of 0.01 from 0 to the percolation threshold for the Evening scan. The results plotted are the mean of 100 balancing runs.

The accuracy peaked for assortativity at $\bar{t}$ = 0 at 66%. However, the general trend for the graph metrics other than assortativity and small world index, was an increase in accuracy as the threshold increased towards the percolation threshold. In Figure 4.23 the two groups were not significantly different for any measure after using the Benjamini-Hochberg method of correcting for multiple comparisons [78]. However, the graph metrics which significantly differed across chronotype groups when uncorrected align closely with the highest accuracies in Figure 4.22.

The colorplot for the results when using the ROIs mPFC and PCC to train the classifier under thresholded and binarized conditions are then given in the Figures 4.24 and 4.25 respectively. The mPFC peaked in accuracy at 65.9% when using node degree at $\bar{t}$ = 0.09

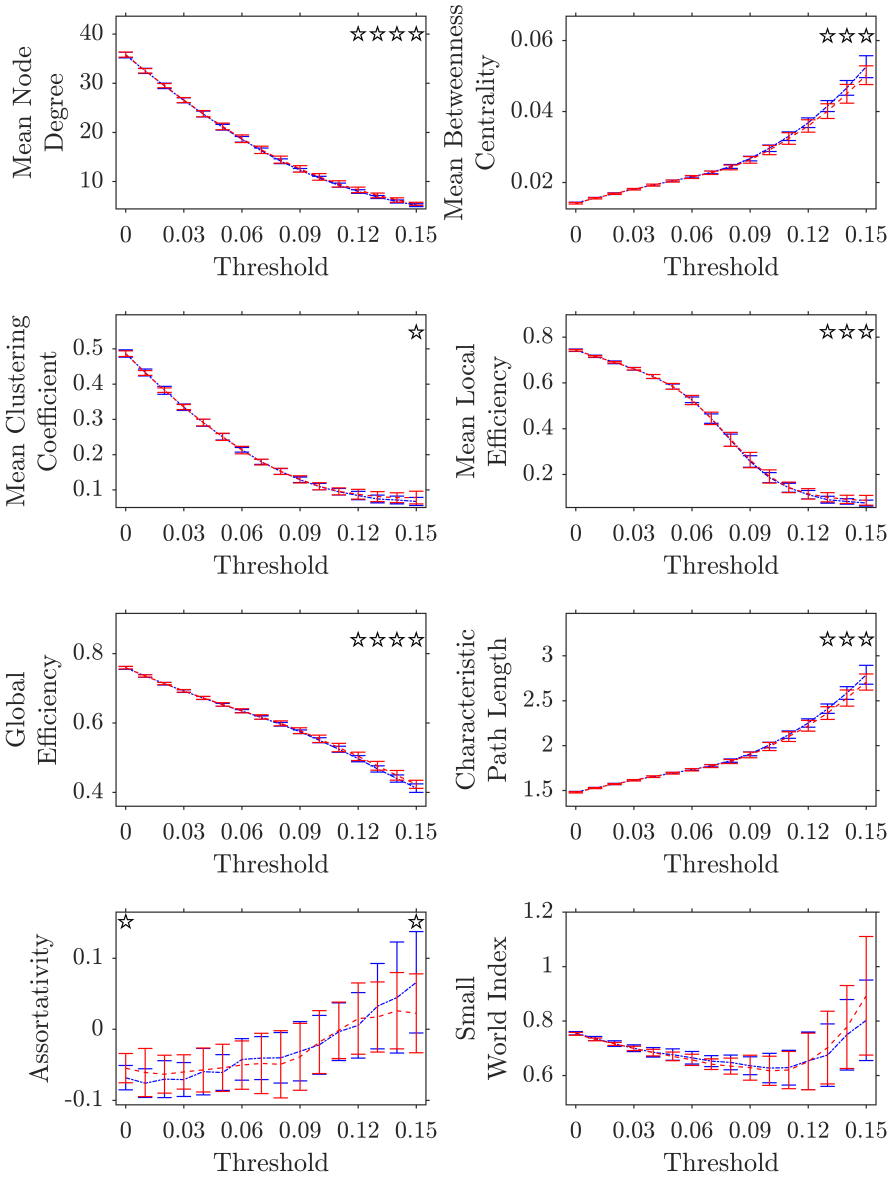


Figure 4.23: **Distribution of Graph Metrics for the Morning Scan: Whole Network - Binarized.** The values for various graph metrics for both ECPs (-·-·-) and LCPs (- - - - -) calculated for the whole network when binarized for non-negative thresholds increasing in steps of 0.01 from 0 to the percolation threshold for the Morning scan. The standard deviation between participants in that group is shown by the error bars. The ☆ indicates where the difference between ECPs and LCPs is significant $p < 0.05$ (uncorrected).

and PCC peaked in accuracy at 64.2% for betweenness centrality at $\bar{t} = 0.15$. There is no discernable trend in the mPFC results with accuracy rarely higher than 55%. However, the PCC did have fairly stable accuracy (~ 61%) when trained on the clustering coefficient

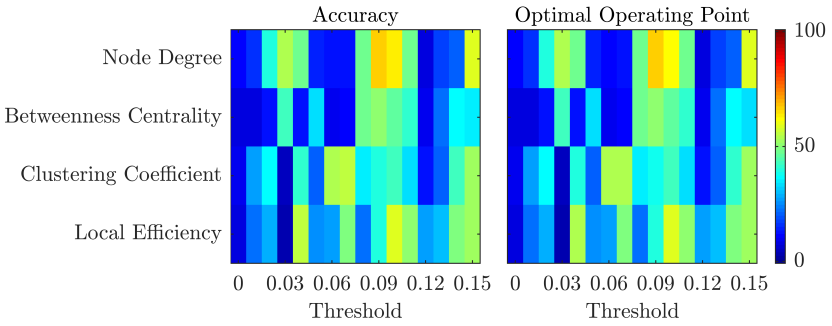


Figure 4.24: **Result of Logistic Regression Classifiers for the Morning Scan: mPFC - Binarized.** The accuracy and OOP resulting from training a logistic regression classifier using graph metrics calculated for the mPFC when binarized for non-negative thresholds increasing in steps of 0.01 from 0 to the percolation threshold for the Morning scan. The results plotted are the mean of 100 balancing runs.

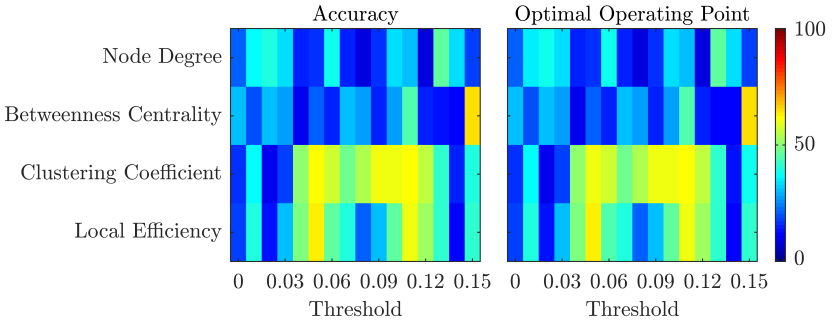


Figure 4.25: **Result of Logistic Regression Classifiers for the Morning Scan: PCC - Binarized.** The accuracy and OOP resulting from training a logistic regression classifier using graph metrics calculated for the PCC when binarized for non-negative thresholds increasing in steps of 0.01 from 0 to the percolation threshold for the Morning scan. The results plotted are the mean of 100 balancing runs.

for thresholds $0.05 - 0.11$.

The results and the scatterplots for the weighted FNs from the Morning scanning session are given in Figure 4.26 and Figure 4.27 respectively.

The highest accuracy achieved was for the global efficiency (61.2%) and the characteristic path length produced a similar level. The distributions of the participant's graph metrics, as displayed in Figure 4.27, show significant differences for mean node strength, global efficiency, characteristic path length and assortativity when uncorrected but no p-values were significant after using the Benjamini-Hochberg method of correcting for multiple comparisons [78].

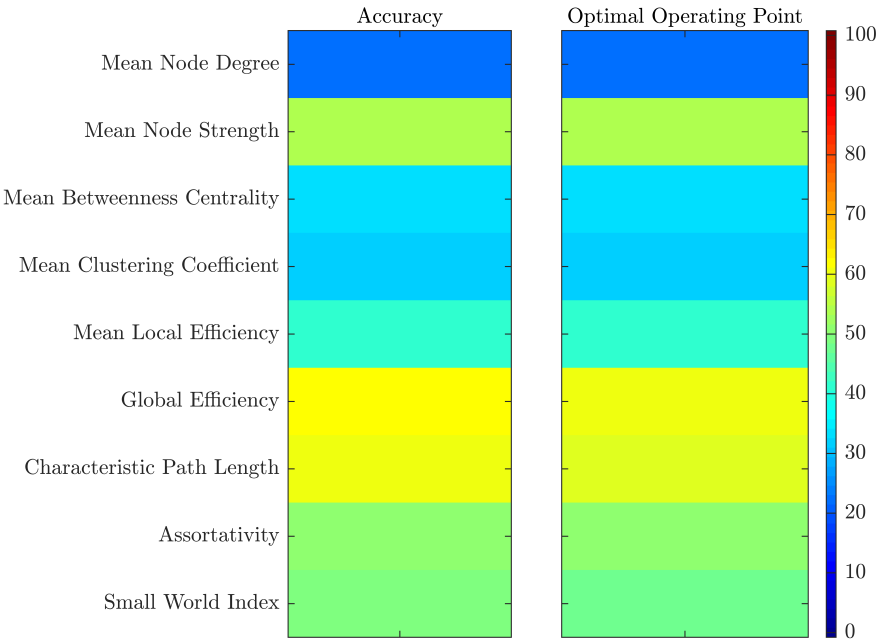


Figure 4.26: **Result of Logistic Regression Classifiers for the Morning Scan: Whole Network - Positive Weighted.** The accuracy and OOP resulting from training a logistic regression classifier using graph metrics calculated for the whole network using positive edge weights for the Morning scan. The results plotted are the mean of 100 balancing runs.

The results when training the classifier using only nodal graph metrics for the PCC or mPFC in the weighted case are given in Figures 4.28 and 4.29 respectively. In all cases the accuracy was poor and never reached over 50%.

Finally, the results of an SVM classifier trained using the thresholded and binarized whole brain FNs for each threshold are given in Table 4.5. The SVM classifier saw a general improvement in accuracy as the threshold increased. Indeed accuracy reached comparable levels of performance with the logistic regression classifier; however, no threshold produced higher accuracy than the 66% achieved for assortativity at $\bar{t} = 0$ (Figure 4.22).

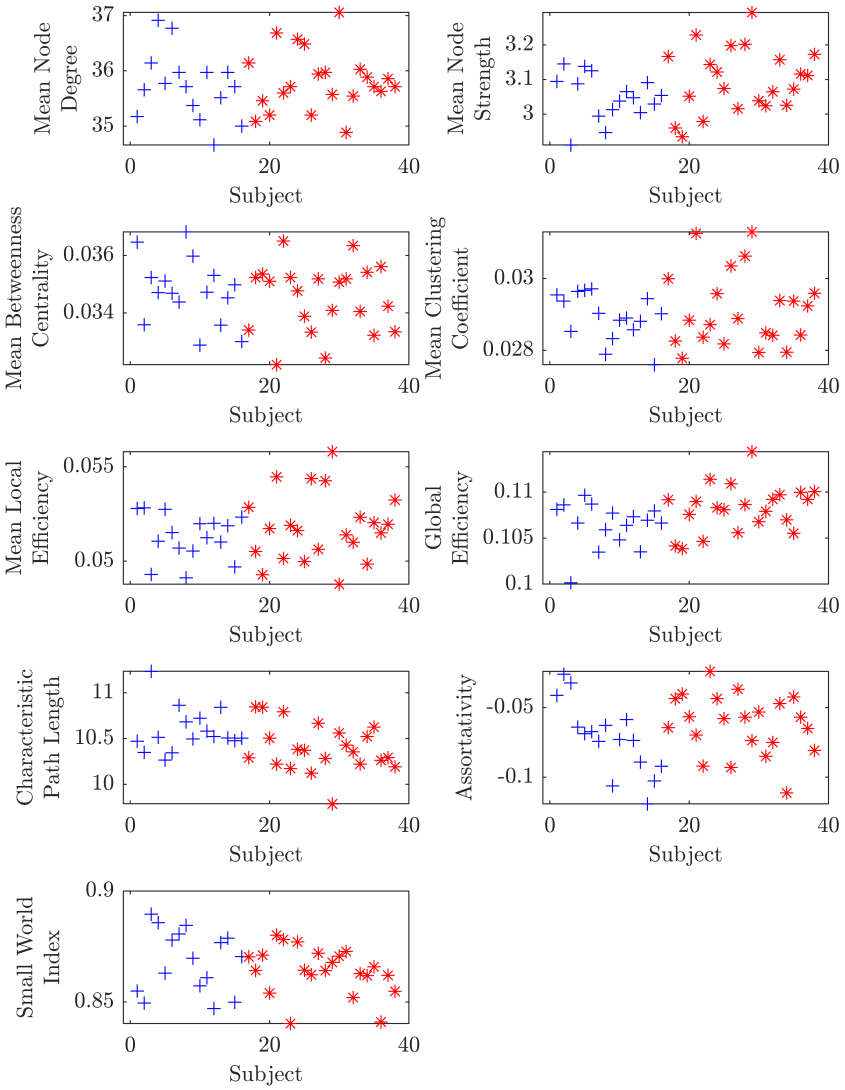


Figure 4.27: **Scatterplots of Graph Metrics for the Morning Scan: Whole Network - Weighted.** The values for various graph metrics for ECPs (+) and LCPs (✳) were calculated for the whole network using positive edge weights for the Morning scan.

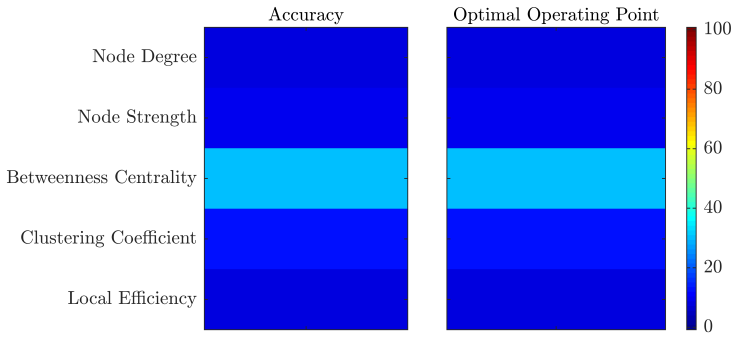


Figure 4.28: **Result of Logistic Regression Classifiers for the Morning Scan: mPFC - Positive Weighted.** The accuracy and OOP resulting from training a logistic regression classifier using graph metrics calculated for the mPFC using positive edge weights for the Morning scan. The results plotted are the mean of 100 balancing runs.

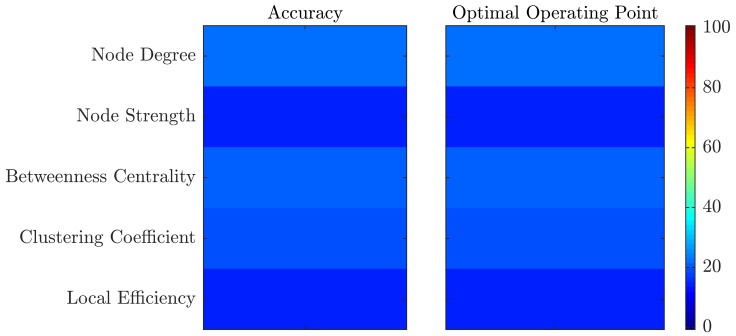


Figure 4.29: **Result of Logistic Regression Classifiers for the Morning Scan: PCC - Positive Weighted.** The accuracy and OOP resulting from training a logistic regression classifier using graph metrics calculated for the PCC using positive edge weights for the Morning scan. The results plotted are the mean of 100 balancing runs.

Threshold	Accuracy	Optimal Operating Point
0	12.22 ± 15.32	12.16 ± 15.24
0.01	4.25 ± 11.30	4.20 ± 11.12
0.02	3.13 ± 8.82	3.05 ± 8.54
0.03	10.50 ± 16.39	10.10 ± 15.65
0.04	15.25 ± 21.10	15.15 ± 20.98
0.05	23.66 ± 19.20	23.60 ± 19.17
0.06	21.31 ± 20.36	21.06 ± 20.18
0.07	31.25 ± 18.54	31.20 ± 18.52
0.08	54.94 ± 9.67	52.26 ± 9.44
0.09	56.44 ± 7.51	49.96 ± 8.35
0.1	49.84 ± 11.90	45.61 ± 11.03
0.11	54.09 ± 10.42	52.40 ± 10.43
0.12	61.38 ± 7.83	59.39 ± 7.16
0.13	62.22 ± 5.20	58.60 ± 5.96
0.14	58.13 ± 5.24	53.01 ± 6.54
0.15	61.78 ± 6.42	58.64 ± 6.83

Table 4.5: **Results of SVM Classifier for the Morning Scan: Whole Network - Binarized.** The results for training an SVM classifier using all available graph metrics calculated for the whole network when binarized for non-negative thresholds increasing in steps of 0.01 from 0 to the percolation threshold for the Morning scan. The results presented are the mean±std of 100 balancing runs.

4.4 Discussion

Throughout this Chapter, an investigation into whether or not chronotype is embedded within rs-FN was undertaken. This was completed to gain an understanding of whether or not the FNs of extreme chronotypes contain differential information. A graph metric approach was used due to the lack of success in differentiating extreme chronotypes using seed-based approaches [60] and due to the graph metric pipelines being a standard type of analysis for establishing differences between fMRI derived FNs in many fields, in particular, the related field of sleep deprivation [63, 123, 172]. Logistic regression classifiers were trained using the graph metrics of ECPs and LCPs, at a range of spatial scales for binary and weighted networks. Then the accuracy of the classifiers was used as a proxy for how differentiable the two extreme chronotypes are from a FN perspective. SVM classifiers were also trained and a comparison with the performance of the logistic regression classifiers was made.

For the Afternoon scanning session, the highest accuracy the classifier achieved was seen for the node degree of the PCC in the context of the whole network. A result of 76% accuracy indicates that the PCC ROI provides some differentiable information, especially as the respective OOP was similarly high, indicating a balance between the correct classification of ECPs and LCPs. The poorer performance when mPFC was considered in Figure 4.8 highlights that this differentiability is not true for DMN ROIs in general, but instead the effect is highly localised. This contrasts the results by Facer-Childs et al. as the rs-FC of both the mPFC and PCC were found to be predictive of performance. Indeed, the mPFC could predict performance on both the PVT and Stroop test, while the PCC was only predictive of PVT performance [57]. However, this does provide more evidence for the association between chronotype and the DMN.

The lower accuracy when averaging across the whole brain could indicate that chronotype does not impact all ROIs in the same manner. Indeed if differing regions see a similar but opposing effect, then averaging over all regions could remove the impact of chronotype. This could highlight that averaging across all ROIs removes too much information

and nodal classifiers may be required to understand chronotype in the context of FNs. Naturally, this raises the question of whether differentiability could occur in other ROIs. However, there is limited literature to suggest other ROIs to consider and repeating the analysis for the 68 remaining ROIs would produce additional multiple comparison issues. Although ROIs in the motor network may be a potential future focus as indicated by Facer-Childs et al. [58].

The classifiers trained on the Evening scanning session performed worse than the Afternoon. In general, accuracy across these classifiers rarely exceeded 60%. This is reflected in the lack of separation seen in the distributions of the graph metrics (Figures 4.15 and 4.19), with a low number of significant differences between the graph metrics even without correcting for multiple comparisons. Similar to the Afternoon session, the highest accuracy was seen for the PCC node, this time using local efficiency. Therefore, whilst differentiable information is still present in the Evening scan, as the classifier produces accuracy higher than random chance (50%), the ability of a graph metric classifier to classify subjects correctly is diminished compared to the Afternoon. Also, the SVM classifier performed worse or equal to random chance for all thresholds and performed worse than the logistic regression classifier. This is likely to be because very few graph metrics produced even moderate levels of differentiation, so despite training on 8 graph metrics there was little usable information and indeed the lower-performing graph metrics seem to have added noise into the classifier.

In the Morning scanning session, the peak accuracy (66%) was seen for the whole brain network when thresholded and binarized, however, the accuracy level was lower than the highest accuracy for the Afternoon scan (76%). Unlike the Afternoon and Evening scans the classifiers trained using the PCC ROI did not perform better than the classifiers trained using the whole brain FN. This suggests that in the Morning, the PCC does not contain more information than the average node in the network. Also, the results of the SVM classifier are slightly lower but not too dissimilar to the results of the logistic regression classifier.

It is worth noting that the weighted versions of the classifier perform similarly to the corresponding maximum accuracy in the thresholded and binarized network, as seen in the Afternoon scan, or the performance was actually worse, as seen in the Evening scan. This indicates it is better to consider the results for different thresholds despite the issues that arise from multiple comparisons, which aligns with the suggestion of Rubinov and Sporns [160]. For instance, for the PCC information seems to be embedded in the presence of an edge rather than the weight of the edge as seen through the higher accuracy for node degree over node strength (Figure 4.13). The effect of thresholding on networks is an increasingly studied step of the methodological pipeline. In the creation of networks with proportional thresholding, a higher threshold is seen to remove excess spurious connections [193] and has been shown to increase the association with the predictive outcome, in that case age [24]. For higher absolute thresholds, the reduction in spurious connections will also occur. Therefore, the reduced performance for positive weighted networks could be due to the presence of spurious connections. However, as the threshold $\bar{t} = 0$ performed so highly in the Afternoon (Figure 4.9), which would have included the same spurious connections as the weighted version, it is unclear why the weighted version performed worse in general.

The graph metrics and results align very closely to those used in two concurrent chronotype studies completed by Farahani et al. [62, 64], which aimed to find significant differences between the extreme chronotypes. These papers were published after the analysis for this section was completed. Across these works a total of 15 graph metrics were calculated ranging from local scale to mesoscale and global scale. There is a high crossover of graph metrics and the results of this chapter and the two papers are consistent, with Farahani et al. finding no significant differences between the graph metrics of the two groups. However, we had an extended protocol through the inclusion of an Afternoon scan and an extended methodology through the training of classifiers. This could indicate why Farahani et al. [62, 64] did not see any significant differentiation between ECPs and LCPs as they had no Afternoon scanning session, instead scanning in the morning and

evening only.

Interestingly, this study asked participants to live their normal life for two weeks prior to the scan. University students during a period of time with no lectures were used in this study and hence participants had no requirements to artificially end their sleep; therefore, LCPs were acutely sleep deprived for the Morning Scanning Session. Based on the sleep deprivation literature, it was initially hypothesised that the Morning Scanning Session would show greater differentiation between ECPs and LCPs due to the potential confounding factor of acute sleep deprivation. In addition, the Evening scanning session could show the effect of tiredness due to ECPs experiencing heightened levels of sleep pressure as they will have been awake for more hours than the LCPs. However, this was not the case, and indeed the Afternoon scanning session, when neither group should be disadvantaged, actually showed the greatest differentiation. It is unclear why there was a slight increase in accuracy for the Afternoon scanning session compared to the Morning and Evening. But since this effect was restricted to the PCC it may be that the effect of chronotype is highly localised or the involvement of the PCC in the compensatory mechanisms for ECPs and LCPs differs. In addition, the singular morning of sleep restriction LCPs faced on the day of the scan may not be enough to mimic the chronic sleep restriction in participants in Farahani et al. [63] or the single prolonged sleep deprivation in Liu et al. [123].

The lack of differentiation in the graph metrics and the limited success of the classifiers could be due to the relatively small group size or even methodological choices. For instance, the maximum threshold was chosen to ensure that every participant still had a connected network. However, there is a general trend in the Morning scanning session, as seen in Figure 4.22, that as $\bar{t}$ approaches the percolation threshold the accuracy increases. It may be that accuracy continues to increase past the percolation threshold. Although, investigating higher thresholds would require ignoring the assumption that all networks are connected. In addition, while between this study and Farahani et al. [62, 64] a large number of graph metrics have been considered, it is still viable that a different graph

metric could see higher levels of differentiation at a network or ROI level. Additional graph metrics were not considered here to avoid further comparisons. The metrics chosen here were due to their common use when analysing FNs [83, 98] however, different graph metrics could be a future avenue of research.

In addition, it is worth noting that the success of Facer-Childs et al. [57, 58] was based on a seed-based analysis pipeline. However, there are two key distinctions between this graph metric pipeline and the seed-based approach used by Facer-Childs et al. First, the seed-based approach considers the contrast between the FC of clusters belonging to the two cohorts being studied. Therefore, in seed-based approaches, importance is not purely based on that cluster's FC but how the FC of the two subgroups compare. Hence seed-based pipelines are established in a way to emphasis differences. Secondly, it is important to note that seed-based approaches work on accepting a voxel into a cluster on a voxel-by-voxel basis. Therefore, while ROIs and clusters are comparable in terms of their anatomical purpose, their sizes may differ. For instance, the mPFC and PCC clusters in Facer-Childs et al. [56] only had 384 and 431 voxels, respectively, under the contrast ECP>LCP. However, the mPFC and PCC ROIs in this report had 1,555 and 5,257 voxels, respectively. The disparity between the ROI and cluster size could be a reason why the mPFC did not train a successful classifier. Indeed, the PCC ROI includes only 8% of the voxels in the cluster and the mPFC includes 25%. Indeed, these extra voxels could have obscured ECPs having a higher FC in the mPFC ROI. It follows that exploring graph metric pipelines where ROI are defined by a seed-based approach completed prior to this analysis may be of interest. Alternatively, a different parcellation could have been applied. For example, using $\sim 1,000$ ROIs rather than 70, may have enabled more specialisation of voxels to assigned ROIs.

Since the clusters found by Facer-Childs et al. [57] suggest that the regions of difference between extreme chronotypes are spatially specific, smaller ROIs combined with a nodal comparison of graph metrics, rather than averaging over all ROIs, could improve classification accuracy in the future. Furthermore, it could indicate that a greater focus

on contrasts between groups is required rather than just focusing on the edges with high values. This second idea is explored in Chapter 5. Although it is worth noting that seed-based methods are not always successful as Fafrowicz et al. [60] did not find significant differences between extreme chronotypes when seeding in thirty-six regions throughout the brain.

It is possible that choosing to optimise α across all available scans rather then per scanning session contributed to the reduced relative success in the Morning and Evening compared to the Afternoon. However, as seen in Table 4.2, the scan with the most similar α_{opt} was the Evening scanning session differing only by 0.0001. As the Evening scanning session did not produce any classifiers which overly performed compared to the other sessions, this choice of α_{opt} does not seem to have benefitted the Evening scan. In addition, the Afternoon scan, which had the highest performing classifier, had an α_{opt} in the middle of the range, so it is unlikely that the increased regularisation led to this increase in accuracy or the Morning scanning session, which has the lowest α_{opt}, would have seen a similar if not increased effect.

Throughout this study FNs created from the rs-fMRI data collected from extreme chronotypes have been used to calculate graph metrics for the purpose of creating classifiers and exploring the differences between the two groups. The relative success of the classifiers would then provide an insight into how the effect of extreme chronotype is embedded in rs-fMRI data.

This study has shown that classifiers which perform above random chance exist for each of the three scanning sessions. However, the Afternoon scanning session contained the classifier with the highest accuracy at 76%. This is the first indication of being able to differentiate chronotypes using rs-FC after the lack of success in seed-based approaches [60] and FNs [62, 64]. Indeed, the analysis indicates that the node degree of the PCC ROI is the most informative combination when scanned in the Afternoon. This is a highly specific criterion for how to select the data to train a classifier, which focuses on the DMN, supporting the importance of the PCC as found by Facer-Childs et al. [56].

Indeed, the specific nature could provide some evidence that circadian differences in the absence of prolonged sleep deprivation do not produce widespread changes to the brain's FN and instead are highly localised. Although these conclusions are based on a moderate classification accuracy of 76% and more research is needed to understand how information about chronotype is present in rs-FNs. Also, the analysis by Facer-Childs et al. [57] was completed using the same dataset, therefore further validation on an external dataset would be required.

From this Chapter, we have seen evidence that the graph metrics of extreme chronotypes only differ a limited amount and that the highest differentiability is limited to the nodal properties of a single ROI. Therefore, focusing on specific connections between ROIs could be needed to train a more successful classifier. Hence, the next Chapter will consider a new classification framework based on Network-Based Statistic. This approach will utilise contrasts and t-tests to assess the difference between the two chronotype groups at the level of an individual edge, which could help to isolate the differentiable information in the FNs.

CHAPTER 5

CLASSIFICATION OF HUMAN CHRONOTYPE BASED ON FMRI NETWORK-BASED STATISTICS[1]

5.1 Introduction

As discussed in Chapter 4 there is an increasing desire to understand how chronotype affects functional brain activity. However, while there has been some success using seed-based approaches, which motivates the hypothesis that chronotype affects brain activity, success is not consistent across chronotype literature. For instance, as discussed in Section 2.2.2, there has been no success in expanding the positive findings from Facer-Childs et al. [57] to either other seed-based approaches [60] or functional brain networks through a graph metric methodological pipeline, as reported by Farahani et al. [62, 64] and Chapter 4.

Key differences between seed-based approaches and graph metric approaches include the ability to focus on the activity related to a single voxel as well as the analysis being based on contrasts. Whereas in a graph metric pipelines differences are only considered once the network has been produced and the graph metric has been calculated. How-

[1]The work presented in this Chapter is based on: S. L. Mason, L. Junges, W. Woldman, E. R. Facer-Childs, B. M. de Campos, A. P. Bagshaw, and J. R. Terry. Classification of human chronotype based on fMRI network-based statistics. *Frontiers in Neuroscience* 17:1-22, 2023. SM, LJ, JT, AB, and EF-C: conception and design. EF-C and AB: data collection. SM, BC, LJ, WW, JT, and AB: data analysis and interpretation. All authors: drafting and revising the manuscript. [130]

ever, the graph metrics of these two non-patient extreme chronotype cohorts did not significantly differ and did not train a classifier with high accuracy, as seen in Chapter 4.

Therefore, we consider whether Network-Based Statistic (NBS), as introduced in Section 3.1.2, may be better suited, than seed-based or graph metric connectivity-based pipelines, for differentiation between ECPs and LCPs. Hence, we introduce a classifier to assess the ability of NBS-derived dysconnected networks to classifying individuals as an ECP, an LCP or unclear. Within NBS, a t-statistic thresholding step is required. Therefore, we originally create a classifier, with an objective method for selecting this threshold. The t-statistic threshold selection criteria is based on the assumption of connectedness for the undirected dysconnected networks. In particular, t-statistic thresholds which create MCCs are utilised, therefore ensuring all ROIs are present with an undetermined number of edges. With no prior knowledge of the participants this accounts for the potential uniqueness in an individual's subnetwork of importance by assuming all ROIs provide information and must therefore form part of the subnetwork.

Broadly, the classifier uses NBS to create and compare the dysconnected networks resulting from labelling a test subject as first an ECP and then an LCP. We compare the significance of these dysconnected networks at specific t-statistic thresholds, alongside their size (number of edges), to classify the test subject - significance and larger networks are taken as an indication of correct labelling.

Additional analyses were performed using the classifier within a classification framework to examine time of day effects. In addition, the stability of the classifier on subsets of the dataset created from leaving out one participant at a time, was considered leading to an investigation into the reasons why the removal of certain subjects resulted in large changes in accuracy and possible ways to mitigate this effect.

Overall, chronotype can greatly affect both the day-to-day life as well as the long-term physical and mental health of individuals, as discussed in Section 2.2.2. However, little information is known about the effect of chronotype on rs-FNs. In this Chapter, we use a novel approach of a classification framework based on NBS to understand if differential

information between extreme chronotypes is present in rs-fMRI data. Data from three scanning sessions across the day are considered; therefore the ability of the NBS classifier to differentiate ECPs and LCPs at different times of the day will also be assessed, as it is unlikely the rs-FNs of the two groups will differ in the same manner across the entire day. Given the lack of significant differences in the graph metrics [62, 64] and seed-based functional connectivity [60] of ECPs and LCPs in current literature, finding scenarios of clear differentiation between the two groups would provide evidence that chronotype can affect rs-FNs and motivate future studies.

5.2 Methodology

The chronotype dataset studied in this Chapter already was introduced in Chapter 4 and the methodology is consistent up to and including Functional Network Construction (Sections 4.2.1 to 4.2.6).

5.2.1 Network-Based Statistic

After calculating FNs for all participants, we used NBS to determine dysconnected networks[1]. The group level difference in edge weights for every edge in the Tikhonov partial correlation functional networks across participants was determined using a t-test under a specific contrast - either ECP>LCP or ECP<LCP. In this case each element - in the 70×70 t-statistic matrix - represents the difference in the mean edge weights between the two groups resulting in a symmetric matrix whose elements are the output of a two-sample one-sided t-test. The t-statistic matrix was then thresholded and the LCC of suprathreshold edges, called a dysconnected network, was selected as the subnetwork of interest. Here the dysconnected network is a subnetwork of edges that show the highest difference in FC between the two phenotypes. The significance of a dysconnected network

[1]Not to be confused with a disconnected (sub)network, which occurs when at least one node has no path to at least one other node in the (sub)network.

was determined using non-parametric permutation testing (n=5,000) to create a FWE corrected p-value. This test compares the intensity (the total weight of the edges) of the connected component to a null distribution of connected component intensities created by randomising the group to which each participant is assigned. The p-value was then calculated as the fraction of random permutations whose intensity is larger than that of the measured dysconnected network, a diagram of this process is given in Figure 3.6.

5.2.2 NBS Threshold Selection

Thresholding is a key step within the traditional NBS methodology, due to the same reasons highlighted in Section 3.1.1.5. When seeking to label each test subject as an ECP and subsequently an LCP, a t-statistic threshold is required for each labelling. The choice of the t-statistic threshold in the original NBS literature is somewhat arbitrary, with no rigorous method suggested [214]. Here we suggest a process for determining these t-statistic thresholds, which is as follows:

For each individual test subject $m \in \{1, 2, \ldots, 38\}$, label the test subject an ECP while letting the training set retain their chronotype label (determined by MCTQ, saliva samples and actigraphy data). Using the NBS pipeline calculate the 70×70 t-statistic matrix across all subjects using the selected contrast; ECP>LCP or ECP<LCP. Each element represents the difference in the mean edge weights between the two groups of extreme chronotypes when the test subject has been artificially placed in the ECP group. Then set t_E^m as the highest t-statistic threshold such that the network of suprathreshold edges is connected. This value t_E^m is known as the percolation threshold. Similarly, repeat the steps above with the test subject m labelled an LCP to find the percolation threshold for the LCP labelling, setting t_L^m to this value.

The importance of setting t-statistic thresholds t_E^m and t_L^m as percolation thresholds is directly linked to the creation of MCCs, which were first presented and fully explained by Vijayalakshmi et al. [197]. Effectively, the MCC is a pragmatic balance between the sparsity and density of a network. Interestingly, Vijayalakshmi et al. found the MCC to

be sensitive to subtle changes in FNs resulting from changes to cognitive load in EEG recordings, which were difficult to detect using other methods.

5.2.3 The Classifier

To determine whether an individual is an ECP or an LCP, we developed a classifier that considers whether the individual fits best within a family of known ECPs or LCPs. The main steps are summarised in Figure 5.1.

Let CL_t^m denote the dysconnected network created by assigning subject m the chronotype label (CL) at t-statistic threshold t, calculated using the NBS toolbox [212]. For the two possible chronotype labellings of the test subject and the two t-statistic thresholding values t_E^m and t_L^m four subnetworks are created: $E_{t_E}^m$, $L_{t_L}^m$, $E_{t_L}^m$ and $L_{t_E}^m$. Each subnetwork will have its own FWE-controlled p-value where $n = 5,000$ random permutations of class labels were used to create a null distribution. Here $p < 0.05$ was considered to be significant, and intensity was used when calculating the p-value. The NBS reference manual [214] suggests that calculating the FWE p-value using intensity rather than the number of edges is beneficial for detecting subtle (distributed but sparse) effects throughout the network, rather than focal effects within a specific component of the network. From here, the classifier was constructed as follows:

Step one is to consider the significance of $E_{t_E}^m$ and $L_{t_L}^m$. If only one of these is significant, the classification of subject m is the significant chronotype label CL. If neither are significant the classification of subject m is unclear. If both are deemed to have a significant size compared to a null distribution then further steps are needed.

Step two is to consider the significance of the two remaining percolation thresholds for each CL: $E_{t_L}^m$ and $L_{t_E}^m$. In this case, if only one of these is significant, the classification of subject m is the significant chronotype label CL. If neither are significant then the classification of subject m is unclear. If both are deemed to have a significant intensity compared to a null distribution, one further step is required.

Step three is to consider the number of edges $|CL_t|$ of the dysconnected networks in

t-statistic threshold pairs. For the four significant subnetworks $E^m_{t_E}$, $L^m_{t_L}$, $E^m_{t_L}$ and $L^m_{t_E}$, the chronotype label with the higher number of edges indicates the label that the classifier will assign to subject m - all comparisons are shown in Figure 5.1. This is based upon the assumption that for any edge, correctly labelling a subject will result in greater separation between the two groups edge weights, which should be reflected in higher t-statistic values. Therefore, at a specific t-statistic threshold, more edges should survive the thresholding step when correctly labelled in contrast to being incorrectly labelled.

Due to the inclusion of the test subject in the classifier, labelled as an ECP or an LCP more advanced techniques such as nested cross-validation cannot be used. Also, note that due to the potential for test subjects to be labelled 'unclear', we define accuracy to be the number of subjects classified correctly divided by the total number of subjects. Similarly, misclassification is the number of subjects given a label of ECP or LCP incorrectly divided by the total number of subjects. Finally, unclear is the number of test subjects given the label unclear divided by the total number of subjects. Hence, accuracy, misclassification and non-classified will add up to 1. In addition, sensitivity can be considered as the number of test subjects classified as ECP divided by the number of ECP subjects and specificity is analogously defined for LCP subjects. Therefore, it should be noted that an unclear classification will not increase accuracy, sensitivity or specificity. Also, through the t-tests the classifier is based on the comparison of two distribution means therefore the imbalance in numbers between ECPs (n = 16) and LCPs (n = 22) will not provide a bias towards the classification of the larger group. To clarify that the imbalance in group sizes does not bias classification in this framework, balanced accuracy - the mean of sensitivity and specificity - is also presented within the tables of results.

A summary of the main steps of the classification process are given in Appendix B.1.

5.2.4 Varying the t-statistic Threshold

A method for selecting the threshold values at which to threshold the t-statistic matrix has already been outlined in Section 5.2.2. However, the threshold selection process was reliant

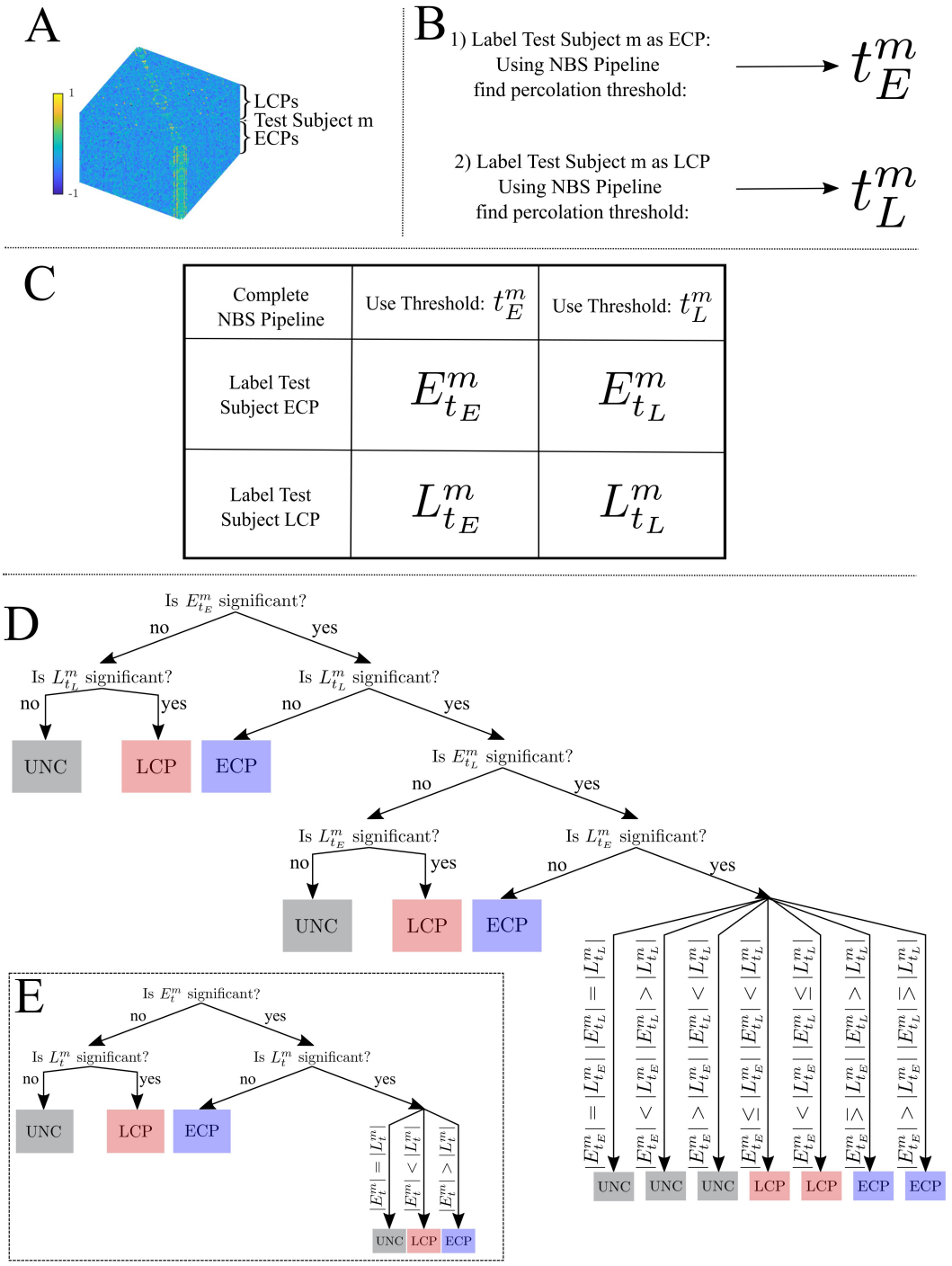


Figure 5.1: **Summary Diagram Showing the NBS Classification Pipeline. (A)** All subjects Tikhonov Partial Correlation matrices ($70 \times 70 \times$ number of subjects) where test Subject m has a label unknown to the classifier. **(B)** Using the NBS pipeline to find the percolation threshold when the test subject has been labelled an ECP and then an LCP. **(C)** The four dysconnected networks which are created from the two thresholds and two labellings. **(D)** The three steps of the classifier to classify Subject m as an ECP, an LCP or unclear. **(E)** The reduced classifier needed in the special case, $t_E^m = t_L^m = t^m$.

on the assumption that all ROIs provide differential information. To understand the impact of this assumption we also decided to range the t-statistic thresholding parameter from 0 to 4.5 in increments of 0.01. Therefore, only one t-statistic threshold is selected for both chronotype labellings.

As the t-statistic threshold range extended beyond the percolation threshold some dysconnected networks did not include all ROIs. Therefore, for certain t-statistic thresholds multiple distinct dysconnected networks existed. In this case, we selected the dysconnected network with the smallest FWE p-value. When multiple dysconnected networks had the same p-value then the dysconnected network with the highest number of edges was selected. If multiple dysconnected networks had the same number of edges then for the purpose of classification they were indistinguishable to the classifier and one was selected arbitrarily.

After selecting the dysconnected networks it can be noted that when t_E^m and t_L^m are equal (i.e. $\exists\ t^m \in \mathbf{R}^+$ s.t. $t_E^m = t_L^m = t^m$) the classifier can be applied as described in Section 5.2.3, however to reduce redundancy step one can be removed and step three can be streamlined as shown in Figure 5.1. For instance, the case ($|E_{t_E}^m| > |L_{t_E}^m|$ and $|E_{t_L}^m| < |L_{t_L}^m|$) would no longer plausible as in that case $E_{t_E}^m = E_{t_L}^m$ and $L_{t_E}^m = L_{t_L}^m$.

Dysconnected networks for select thresholds were then considered and displayed visually using BrainNet Viewer [210] [1].

5.2.5 Investigating the Stability of the Classifier

When creating a classifier on small datasets, such as the 38 participants available in this study, a sensible step is to validate the classifier on a similar but independent dataset. This allows you to assess whether the classifier is overfitted to the original data and hence its applicability to different datasets. However, with no access to an alternative existing dataset, surrogate datasets were created using the original data. These partial datasets were created by removing one subject in turn from each scanning session; therefore,

[1] `http://www.nitrc.org/projects/bnv`

creating 113 new datasets, across the three scanning sessions (n = 37 Afternoon, n = 38 Evening and n = 38 Morning).

For each of these new datasets the methodology as outlined above was completed. With accuracy now given as the fraction of correctly labelled subjects calculated from a LOOCV analysis on N-1 subjects. Changing the number of subjects will affect the MCC created using NBS both in terms of the size as well as the specific edges included. This will in turn affect the classification of networks in step one and step two through the significance of MCCs changing when a subject is removed, as well as the different number of edges affecting step three of the classifier.

Given the overlap between the partial and full datasets we expect the accuracy levels to be consistent. Indeed, any discrepancies in the accuracy, when a single subject is removed, could indicate potential problems with the classifier or that some characteristics of the participant's data are inherently different and influential.

5.2.6 Varying the Threshold for Significance

The dysconnected networks that are created using NBS are considered significant if their p-value is less than the significance threshold, α = 0.05, such that $p < 0.05$ indicates significance. The threshold of 0.05 is somewhat arbitrary and selected due to the consistent use of this threshold throughout the literature. However, the classification pipeline is not solely concerned with the significance of the dysconnected networks, rather whether or not information about chronotype is embedded within them such that classification can occur. Therefore, the threshold for significance was varied in the range $[0, 1]$ in steps of 0.01 to understand its effect on the success of the classifier. This is similar to NBS Predict [166], however within NBS Predict the p-value of the dysconnected network is not even calculated as feature selection is considered irrespective of family-wise error.

The effect of changing the significance threshold was considered for both the original datasets as well as the partial datasets, as mentioned in Section 5.2.5.

Note that a significance threshold of zero guarantees that every network is non-

significant; therefore every classification is unclear due to step one. A non-zero but low significance threshold would result in the majority of subjects being classified due to step one - the significance of the network. As the significance threshold increases step two will be used for classification and finally once the significance threshold is high enough such that all 4 networks ($E_{t_E}, E_{t_L}, L_{t_E}, L_{t_L}$) are significant then step three - the number of edges - is used. After reaching the significance level such that all four dysconnected networks are significant, the accuracy will remain constant for all significance thresholds higher than this. Therefore, the choice of significance threshold equates to the contribution each step of the classifier makes.

5.3 Results

For completeness a comparison to NBS Predict was performed, with the results given in Appendix B.2.

5.3.1 Classifier Performance

Having selected the t-statistic thresholds t_E^m and t_E^m the classifier can be used as presented in Section 5.2.3. The results for each of the three scans under the two contrasts are presented below. In addition, the classifier labels assigned to each Subject are given in Table 5.2.

5.3.1.1 Afternoon Scanning Session

For the contrast ECP>LCP, Subject 22 was mislabelled as an ECP on step one while all other subjects were labelled as unclear by step one, resulting in an accuracy of 0%. For the contrast ECP<LCP, accuracy was 0% with all subjects being classified by step one.

5.3.1.2 Evening Scanning Session

For the contrast ECP<LCP, every subject was labelled as unclear by step one, due to $E^m_{t_E}$ and $L^m_{t_L}$ being non significant for all subjects, resulting in an accuracy of 0%.

For the contrast ECP>LCP, 97.37% accuracy was achieved due to only Subject 36 being misclassified as an ECP. The resulting subnetwork when all subjects are correctly labelled (i.e. NBS as presented by Zalesky et al. [212] used with t-statistic threshold 1.692) is given in Figure 5.4 and its topology is considered in Table 5.3. The breakdown of how many ECPs and LCPs were classified at each step is presented in Table 5.1.

	ECP	LCP	Total
Step one	10	14	24
Step two	1	1	2
Step three	5	$7^{\dagger}$	12
Accuracy %	100	95.5	97.3

Table 5.1: **Table Showing the Breakdown of Classifications at each Step.** The number of ECPs and LCPs that are classified at each step of the classification pipeline is presented in the table as well as the accuracy of the classification. The † denotes Subject 36 who was incorrectly labelled at step three of the classifier.

5.3.1.3 Morning Scanning Session

For the contrast ECP>LCP every subject was labelled as unclear by step one, due to $E^m_{t_E}$ and $L^m_{t_L}$ being non significant for all subjects, resulting in an accuracy of 0%. For the contrast ECP<LCP accuracy was 0%, with all subjects being classified by step one.

Subject	Afternoon ECP<LCP	Afternoon ECP>LCP	Evening ECP<LCP	Evening ECP>LCP	Morning ECP<LCP	Morning ECP>LCP
1	UNC	UNC	UNC	ECP	UNC	UNC
2	UNC	UNC	UNC	ECP	LCP	UNC
3	UNC	UNC	UNC	ECP	UNC	UNC
4	UNC	UNC	UNC	ECP	UNC	UNC
5	LCP	UNC	UNC	ECP	UNC	UNC
6	LCP	UNC	UNC	ECP	UNC	UNC
7	LCP	UNC	UNC	ECP	UNC	UNC
8	UNC	UNC	UNC	ECP	UNC	UNC
9	UNC	UNC	UNC	ECP	UNC	UNC
10	LCP	UNC	UNC	ECP	LCP	UNC
11	NA	NA	UNC	ECP	UNC	UNC
12	UNC	UNC	UNC	ECP	UNC	UNC
13	UNC	UNC	UNC	ECP	LCP	UNC
14	UNC	UNC	UNC	ECP	UNC	UNC
15	UNC	UNC	UNC	ECP	UNC	UNC
16	LCP	UNC	UNC	ECP	UNC	UNC
17	UNC	UNC	UNC	LCP	UNC	UNC
18	UNC	UNC	UNC	LCP	UNC	UNC
19	UNC	UNC	UNC	LCP	ECP	UNC
20	UNC	UNC	UNC	LCP	ECP	UNC
21	UNC	UNC	UNC	LCP	UNC	UNC
22	UNC	ECP	UNC	LCP	UNC	UNC
23	ECP	UNC	UNC	LCP	UNC	UNC
24	UNC	UNC	UNC	LCP	UNC	UNC
25	UNC	UNC	UNC	LCP	UNC	UNC
26	ECP	UNC	UNC	LCP	ECP	UNC
27	UNC	UNC	UNC	LCP	ECP	UNC
28	UNC	UNC	UNC	LCP	UNC	UNC
29	UNC	UNC	UNC	LCP	UNC	UNC
30	UNC	UNC	UNC	LCP	UNC	UNC
31	ECP	UNC	UNC	LCP	UNC	UNC
32	UNC	UNC	UNC	LCP	UNC	UNC
33	UNC	UNC	UNC	LCP	UNC	UNC
34	UNC	UNC	UNC	LCP	UNC	UNC
35	UNC	UNC	UNC	LCP	UNC	UNC
36	ECP	UNC	UNC	ECP	ECP	UNC
37	ECP	UNC	UNC	LCP	ECP	UNC
38	ECP	UNC	UNC	LCP	UNC	UNC
Accuracy(%)	0	0	0	97.3	0	0
Balanced Accuracy(%)	0	0	0	97.7	0	0
Percentage Classified ECP or LCP (%)	29.7	2.7	0	100	23.7	0

Table 5.2: **The Labels Assigned by the Classifier for the Different Scanning Sessions and Contrasts.** Here Subjects 1-16 are ECPs while 17-38 are LCPs, as labelled using non-imaging data.

5.3.2 How the t-statistic Threshold Impacts Classifier Performance

As can be seen from Table 5.2, the performance of the classifier was strongly dependent on the time of day that the scan was taken, with accuracy differing greatly between the Evening and other scanning sessions. Since the accuracy of the classifier for the Afternoon and Morning scans was restricted by dysconnected networks being non-significant at step one of the classifier, when the percolation threshold was used, we now consider the accuracy of the classifier when selecting a single t-statistic threshold, varying over the range $[0, 4.5]$ in increments of 0.01. This relaxes the requirement of all ROIs contributing to the network when choosing the t-statistic threshold for defining the dysconnected network and allows the classifier to be used within a classification framework of understanding if differential information exists with a larger enough effect for classification to occur and if so how the performance of the classifier varies with the t-statistic threshold. Under these conditions, the classifier is the simplified version presented when $t_E^m = t_L^m = t^m$ where t^m is preselected.

First, we consider the accuracy values when applying the classifier for the three scanning sessions and two contrasts when varying the t-statistic threshold value. These results are presented in Figure 5.2. The highest accuracy values for the Afternoon scanning session occur for t-statistic thresholds near 2.2 when ECP<LCP ($\sim$ 97%). The contrast ECP>LCP does not result in any non-zero accuracy values. For the Evening scanning session, non-zero accuracy exclusively occurred for the ECP>LCP contrast. For this contrast, non-zero accuracy occurs between 0.71 and 2.28 with accuracy peaking at 97%. In the Morning scanning session, non-zero accuracy was only seen for the ECP<LCP contrast, with accuracy $\sim$ 90% for both thresholds.

In Table 5.3 we display the topologies of four distinct dysconnected networks corresponding to the regions of non-zero accuracy in Figure 5.2. In addition, Figures 5.3 - 5.6, visualise the four dysconnected networks using glass brains. For the Evening [ECP>LCP] scan the threshold of 1.692 is chosen as it is the percolation threshold when all subjects

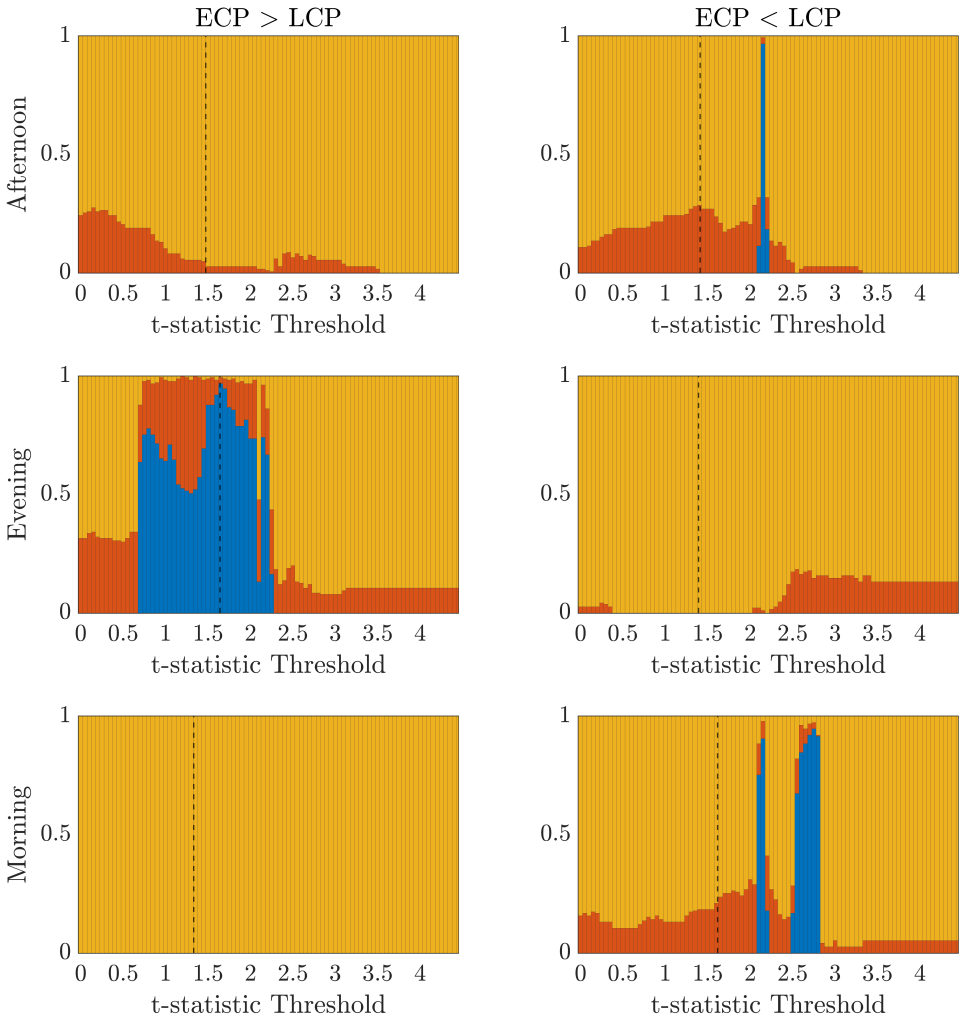


Figure 5.2: **Classifier Performance as a Function of t-statistic Threshold.** Stacked bar charts showing the percentage of subjects classified correctly, incorrectly and unclear respectively (blue, red, yellow) when successively selecting the t-statistic threshold from the range $[0, 4.5]$ in increments of 0.01. The dashed lines indicate the percolation threshold for correct labelling as found using Section 5.2.2.

are correctly labelled as in Section 5.3.1.2. Since non-zero accuracy did not occur for the Afternoon [ECP>LCP], Evening [ECP<LCP] nor the Morning [ECP>LCP] scanning sessions, no topological features from these scans are considered. Due to the overlap in the t-statistic thresholds that produce high accuracy near at 2.2 in the Morning [ECP<LCP] and Afternoon [ECP<LCP] scanning session, these dysconnected networks at threshold 2.19 were compared for similarity. Notably, only one edge is present in both networks linking nodes 48 (LECN) and 64 (Visuospatial).

It is important to note that we do not use this approach to construct a classifier or

Scanning Session		Threshold	Number of Edges	Number of Nodes	Accuracy (%)	Average Node Degree	Highest Node Degree (ROI)
Afternoon	[ECP<LCP]	2.19	55	53	97.3	1.57 ± 1.22	5 (1)
Evening	[ECP>LCP]	1.69	146	70	97.3	4.17 ± 2.03	10 (60)
Morning	[ECP<LCP]	2.19	53	48	92.1	1.51 ± 1.29	4 (34,48,53,59)
Morning	[ECP<LCP]	2.79	6	7	94.7	0.17 ± 0.54	2 (14,26,52,55,64)

Table 5.3: **Table Showing Key Topological Features of Four dysconnected Networks.**

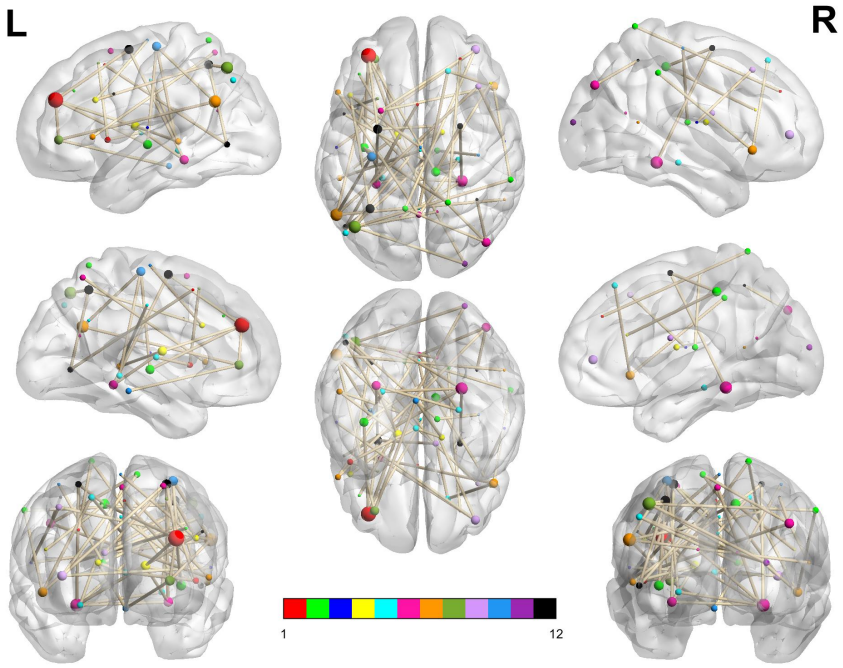


Figure 5.3: **Dysconnected Network Produced using NBS for the Afternoon Scanning Session using ECP<LCP and t-statistic Threshold 2.19.** The size of each node is determined by the node degree. The top row from left to right are the lateral view of the left hemisphere, top view and the lateral view of the right hemisphere. The middle row from left to right are the medial view of the left hemisphere, bottom view and the medial view of the right hemisphere. The bottom row shows the anterior side on the left and the posterior on the right. The interconnected networks (ICNs) 1-12 are given in Table 4.1.

select a parameter for future datasets, due to the issue of multiple comparisons introduced by varying the threshold over a wide range. The purpose of presenting these results is to provide insight into the somewhat unintuitive differences observed, dependent on time of day, and to understand if differential information does exist if scanning sessions other than the Evening when the MCC assumption is removed.

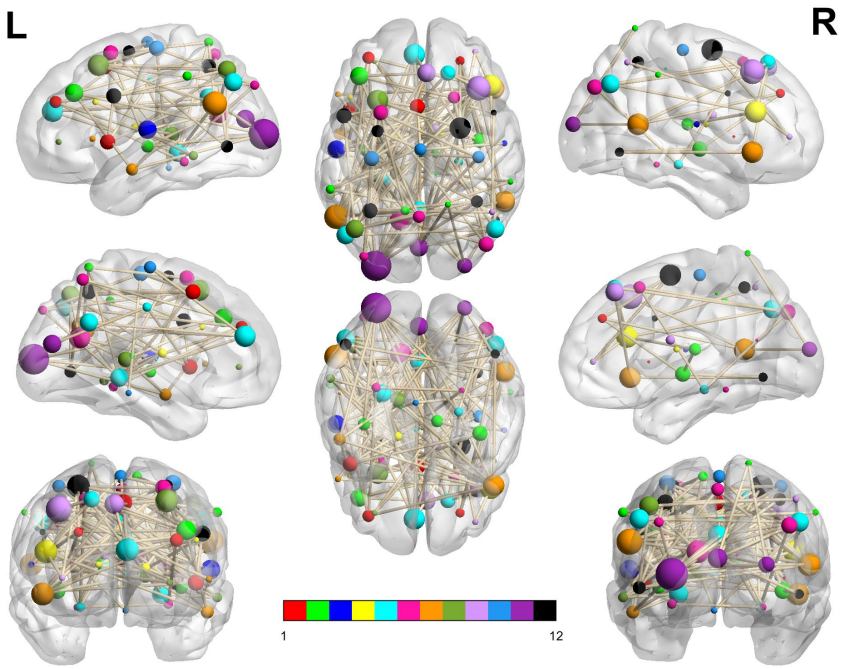


Figure 5.4: **Dysconnected Network Produced using NBS for the Evening Scanning Session using ECP>LCP and t-statistic Threshold 1.692.** The size of each node is determined by the node degree. Subfigure information is the same as Figure 5.3.

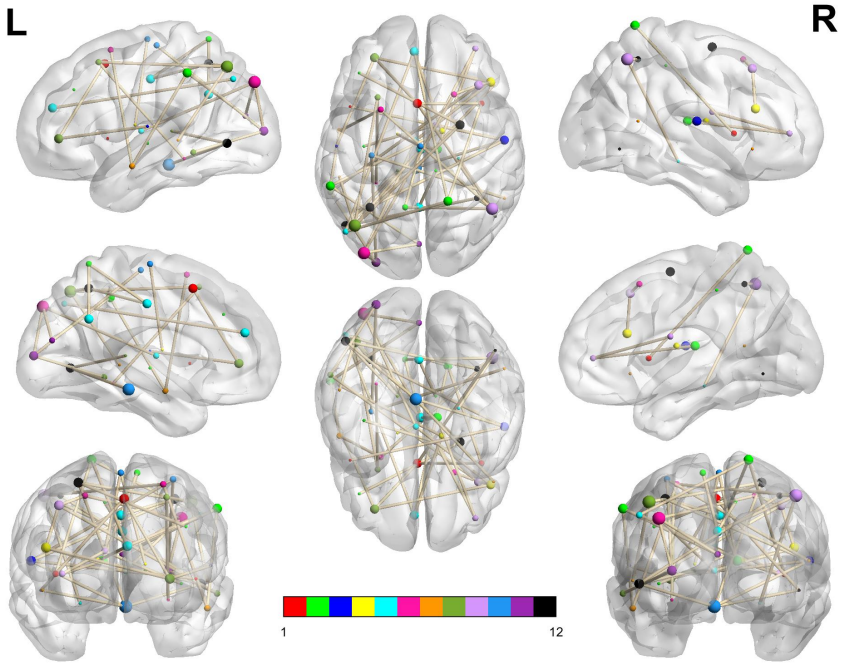


Figure 5.5: **Dysconnected Network Produced using NBS for the Morning Scanning Session using ECP<LCP and t-statistic Threshold 2.19.** The size of each node is determined by the node degree. Subfigure information is the same as Figure 5.3.

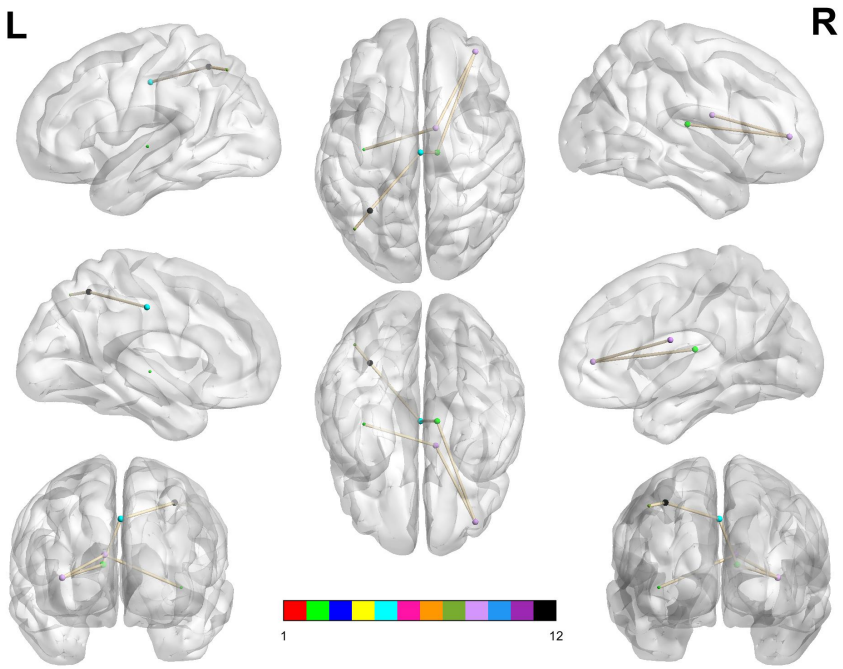


Figure 5.6: **Dysconnected Network Produced using NBS for the Morning Scanning Session using ECP<LCP and t-statistic Threshold 2.79.** The size of each node is determined by the node degree. Subfigure information is the same as Figure 5.3.

5.3.3 Investigating the Stability of the Classifier

So far the results of the classifier for the original datasets have been presented. However, to validate the classifier it is important to understand how the classifier performs on the partial datasets, created by sequentially leaving out participants. Therefore, the results of using the classifier, as presented in Section 5.2.5, on each of the new datasets created by removing one subject in turn, from both the training set and the test set, are presented below.

5.3.3.1 Afternoon Scanning Session

The fraction of subjects who are labelled correct, incorrect and unclear when a particular subject is removed is shown in Tables 5.4 and 5.5 for the contrasts ECP>LCP and ECP<LCP respectively.

For the contrast ECP>LCP accuracy was zero for all subjects due to the majority of subjects classified as unclear. When comparing these results to the corresponding column

in Table 5.2 we see a high consistency, as all but one subject was classified as unclear.

For the contrast ECP<LCP there are certain subjects (5, 6, 7, 10, 16, 23, 26 and 38) whose removal has a positive effect on the accuracy of the classification. Indeed, except for Subject 38, the accuracy is higher than random chance (50%) and in some cases the classifier would be considered high performing. For example, the removal of Subject 16 sees accuracy go from 0% up to 81%.

When comparing the results to the corresponding column in Table 5.2 we see a high correspondence between the incorrectly labelled subjects in Table 5.2 and those subjects whose removal sees a high accuracy, especially for the ECP cohort.

Subject Removed	Accuracy	Unclear	Misclassified
1	0	0.94	0.06
2	0	0.97	0.03
3	0	0.97	0.03
4	0	0.97	0.03
5	0	0.97	0.03
6	0	0.97	0.03
7	0	0.97	0.03
8	0	0.94	0.06
9	0	0.94	0.06
10	0	0.83	0.17
11	NA	NA	NA
12	0	1	0
13	0	1	0
14	0	1	0
15	0	1	0
16	0	0.94	0.06
17	0	0.94	0.06
18	0	1	0
19	0	0.94	0.06
20	0	0.97	0.03
21	0	0.94	0.06
22	0	0.92	0.08
23	0	0.94	0.06
24	0	1	0
25	0	1	0
26	0	0.97	0.03
27	0	0.92	0.08
28	0	0.94	0.06
29	0	1	0
30	0	1	0
31	0	1	0
32	0	0.94	0.06
33	0	0.97	0.03
34	0	1	0
35	0	1	0
36	0	0.97	0.03
37	0	1	0
38	0	0.97	0.03

Table 5.4: **Afternoon [ECP>LCP] Results: Partial Datasets.** The fraction of correct, unclear and incorrect classifications when one subject was removed.

Subject Removed	Accuracy	Unclear	Misclassified
1	0	0.75	0.25
2	0	0.83	0.17
3	0	0.81	0.19
4	0	0.89	0.11
5	0.64	0.03	0.33
6	0.72	0.11	0.17
7	0.69	0.03	0.28
8	0	0.78	0.22
9	0	0.78	0.22
10	0.78	0.003	0.19
11	NA	NA	NA
12	0	0.86	0.14
13	0	0.81	0.19
14	0	0.97	0.03
15	0	0.61	0.39
16	0.81	0.11	0.083
17	0	0.92	0.08
18	0	0.83	0.17
19	0	0.78	0.22
20	0	0.75	0.25
21	0	0.75	0.25
22	0	0.78	0.22
23	0.61	0.06	0.33
24	0	0.72	0.28
25	0	0.86	0.14
26	0.64	0	0.36
27	0	0.89	0.11
28	0	0.75	0.25
29	0	0.78	0.22
30	0	0.86	0.14
31	0	0.69	0.31
32	0	0.94	0.06
33	0	0.81	0.19
34	0	0.94	0.06
35	0	0.72	0.28
36	0	0.67	0.33
37	0	0.67	0.33
38	0.39	0.28	0.33

Table 5.5: **Afternoon [ECP<LCP] Results: Partial Datasets.** The fraction of correct, unclear and incorrect classifications when one subject was removed.

5.3.3.2 Evening Scanning Session

Tables 5.6 and 5.7 show the fraction of subjects who were labelled correct, incorrect and unclear when a particular subject was removed, for the contrasts ECP>LCP and ECP<LCP respectively.

For the contrast ECP<LCP no subject was correctly labelled due to almost all subjects being classified as unclear. When comparing these results to the corresponding column in Table 5.2 we see extremely high consistency.

For the contrast ECP>LCP there are certain subjects (7, 8, 9, 16, 18, 19, 22, 25, 30, 32 and 34) whose removal results in a decrease in accuracy below random chance and far below the 97.3% seen for the full dataset. In addition, the mean accuracy of the other subjects is 79.68% - a reduction from the average of 97.3%. However, it is worth noting that the removal of Subject 36 - the only subject incorrectly classified in the original dataset - sees an increase in accuracy from 0% to 76%.

The low or zero accuracy for those eleven subjects is mainly due to the majority of the subjects being classified as unclear. There was no clear link to differences in the non-imaging data (e.g., actigraphy, DLMO and CAR) that could provide a reason for these subjects having such a clear influence on the classifier's performance.

Subject Removed	Accuracy	Unclear	Misclassified
1	0.65	0.14	0.22
2	0.97	0.03	0
3	0.78	0.08	0.14
4	0.78	0.11	0.11
5	0.95	0.03	0.03
6	0.84	0.03	0.14
7	0	0.76	0.24
8	0	0.81	0.19
9	0	0.73	0.27
10	0.73	0.08	0.19
11	0.65	0.16	0.19
12	0.70	0.14	0.16
13	0.81	0.19	0
14	0.81	0.08	0.11
15	0.95	0.05	0
16	0	0.78	0.22
17	0.70	0.08	0.22
18	0.41	0.32	0.27
19	0	0.78	0.22
20	0.86	0.05	0.08
21	0.95	0	0.05
22	0.43	0.41	0.16
23	0.86	0.05	0.08
24	0.81	0.03	0.16
25	0	0.81	0.19
26	0.84	0.08	0.08
27	0.68	0.05	0.27
28	0.59	0.16	0.24
29	0.92	0.03	0.05
30	0.43	0.38	0.19
31	0.86	0.03	0.11
32	0	0.78	0.22
33	0.76	0.11	0.14
34	0	0.81	0.19
35	0.86	0.05	0.08
36	0.76	0.19	0.05
37	0.62	0.19	0.19
38	0.81	0.05	0.14

Table 5.6: **Evening [ECP>LCP] Results: Partial Datasets.** The fraction of correct, unclear and incorrect classifications when one subject was removed

Subject Removed	Accuracy	Unclear	Misclassified
1	0	1	0
2	0	1	0
3	0	1	0
4	0	1	0
5	0	1	0
6	0	1	0
7	0	1	0
8	0	1	0
9	0	1	0
10	0	1	0
11	0	1	0
12	0	1	0
13	0	1	0
14	0	1	0
15	0	1	0
16	0	1	0
17	0	1	0
18	0	1	0
19	0	1	0
20	0	1	0
21	0	1	0
22	0	1	0
23	0	1	0
24	0	1	0
25	0	1	0
26	0	0.97	0.03
27	0	1	0
28	0	1	0
29	0	1	0
30	0	1	0
31	0	1	0
32	0	1	0
33	0	1	0
34	0	1	0
35	0	1	0
36	0	1	0
37	0	1	0
38	0	1	0

Table 5.7: **Evening [ECP<LCP] Results: Partial Datasets.** The fraction of correct, unclear and incorrect classifications when one subject was removed

5.3.3.3 Morning Scanning Session

The fraction of subjects who were labelled correct, incorrect and unclear when a particular subject was removed is shown in Tables 5.8 and 5.9 for the contrasts ECP>LCP and ECP<LCP respectively.

For the contrast ECP>LCP all subjects were classified as unclear, which is consistent with the corresponding column in Table 5.2 where all subjects were classified as unclear.

For the contrast ECP<LCP there are certain subjects (3, 10, 13, 20, 26, 27, 38) whose removal has a positive effect on the accuracy of the data indeed their removal produces accuracy's higher than random chance (50%). For example, the removal of Subject 13 sees accuracy go from 0% up to 76%.

When comparing the results to the corresponding column in Table 5.2 we see a correspondence between the subjects whose removal sees a high accuracy and incorrectly labelled subjects in Table 5.2. However, Subjects 3 and 38 were not misclassified in Table 5.2 whilst Subjects 2, 19, 36 and 37 were misclassified in Section 5.3.1.3 but their removal had no discernible effect on the classifier.

Subject Removed	Accuracy	Unclear	Misclassified
1	0	1	0
2	0	1	0
3	0	1	0
4	0	1	0
5	0	1	0
6	0	1	0
7	0	1	0
8	0	1	0
9	0	1	0
10	0	1	0
11	0	1	0
12	0	1	0
13	0	1	0
14	0	1	0
15	0	1	0
16	0	1	0
17	0	1	0
18	0	1	0
19	0	1	0
20	0	1	0
21	0	1	0
22	0	1	0
23	0	1	0
24	0	1	0
25	0	1	0
26	0	1	0
27	0	1	0
28	0	1	0
29	0	1	0
30	0	1	0
31	0	1	0
32	0	1	0
33	0	1	0
34	0	1	0
35	0	1	0
36	0	1	0
37	0	1	0
38	0	1	0

Table 5.8: **Morning [ECP>LCP] Results: Partial Datasets.** The fraction of correct, unclear and incorrect classifications when one subject was removed

Subject Removed	Accuracy	Unclear	Misclassified
1	0	0.95	0.05
2	0	0.65	0.35
3	0.73	0.03	0.24
4	0	0.73	0.27
5	0	0.81	0.19
6	0	0.81	0.19
7	0	0.78	0.22
8	0	0.76	0.24
9	0	0.95	0.05
10	0.65	0.05	0.30
11	0	0.95	0.05
12	0	0.89	0.11
13	0.78	0.05	0.16
14	0	0.78	0.22
15	0	0.92	0.08
16	0	0.84	0.16
17	0	0.86	0.14
18	0	0.86	0.14
19	0	0.78	0.22
20	0.62	0.14	0.24
21	0	0.89	0.10
22	0	0.89	0.10
23	0	0.76	0.24
24	0	0.86	0.14
25	0	0.84	0.16
26	0.57	0.16	0.27
27	0.73	0.11	0.16
28	0	0.86	0.14
29	0	0.68	0.32
30	0	0.92	0.08
31	0	0.89	0.11
32	0	0.86	0.14
33	0	0.86	0.14
34	0	0.76	0.24
35	0	0.81	0.19
36	0	0.68	0.32
37	0	0.73	0.27
38	0.65	0.03	0.32

Table 5.9: **Morning [ECP<LCP] Results: Partial Datasets.** The fraction of correct, unclear and incorrect classifications when one subject was removed

5.3.4 How the Significance Threshold Impacts Classifier Performance: Partial Datasets

Due to the sensitivity of the classifier, both in terms of removing subjects resulting in increased accuracy in the Morning and Afternoon scanning session [ECP<LCP] and the reduction in accuracy in the Evening scanning session [ECP>LCP], the influence of the choice of significance threshold was investigated.

It is worth noting that the initial investigation into the classifier's sensitivity to the removal of subjects focused on the subjects themselves. Therefore, an investigation into the metadata of subjects who were misclassified or whose removal led to high differences in accuracy was undertaken. However, as seen in Appendix B.3 the metadata is unable to provide an answer for the classifiers' sensitivity.

Figure 5.7 shows boxplots for all of the n accuracies when one subject in turn was removed from the training and test set for all possible values of the significance threshold α. In addition, the mean and standard deviation for each α value are shown. Figure 5.8 shows the mean value for the fraction of subjects labelled correct, incorrect and unclear for each α value.

As can be seen from Figure 5.7 there is an optimum value of α for each of the scanning sessions, selected as the point where the ratio between accuracy and standard deviation is highest.

However, it is only in the Evening [ECP>LCP] scan that the value of α which results in the maximum accuracy matches the value of α which produces the minimum standard deviation. This occurs at $\alpha = 0.08$ resulting in a mean accuracy of 75.25% showing that there is the possibility to optimise the significance threshold for α and that selecting the traditional significance level of $\alpha = 0.05$ may be too conservative when there are additional steps of the pipeline that help to prevent misclassifications, through the ability to label a test subject unclear.

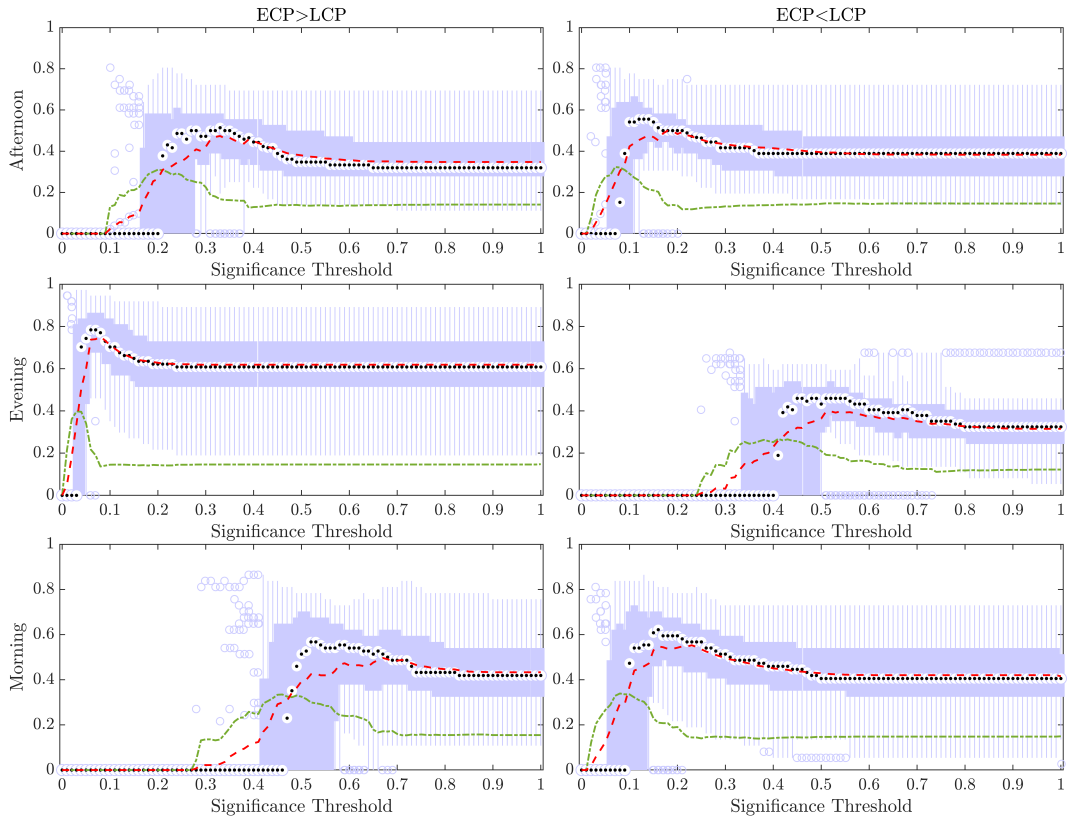


Figure 5.7: **Boxplots Showing the Accuracy When Removing Subjects and Varying Across Thresholds for Significance.** For each value of significance, in the range 0 to 1 in increments of 0.01, a boxplot for the accuracy when removing each subject is shown as as the mean accuracy (red, dashed) and the standard deviation (green, dashed and dotted). The median of the boxplot is given by the black dot while values considered outliers (greater than 2.7 standard deviations away from the mean) are depicted by small blue circles.

5.3.5 How the Significance Threshold Impacts Classifier Performance: Original Datasets

To understand how changing the significance threshold effects the performance of the classifier when considering the original datasets, the results when varying the significance between $[0, 1]$ in increments of 0.01 are shown below.

Figure 5.9 shows a stacked barchart showing the distribution of correct, incorrect and unclear classifications for each possible value of α when ranging from 0 to 1 in increments of 0.01 for the original full datasets. The maximum accuracy of 97% occurs for the Evening [ECP>LCP] scan for α in the range 0.04-0.07. Comparing Figure 5.9 to Figure 5.8 we see

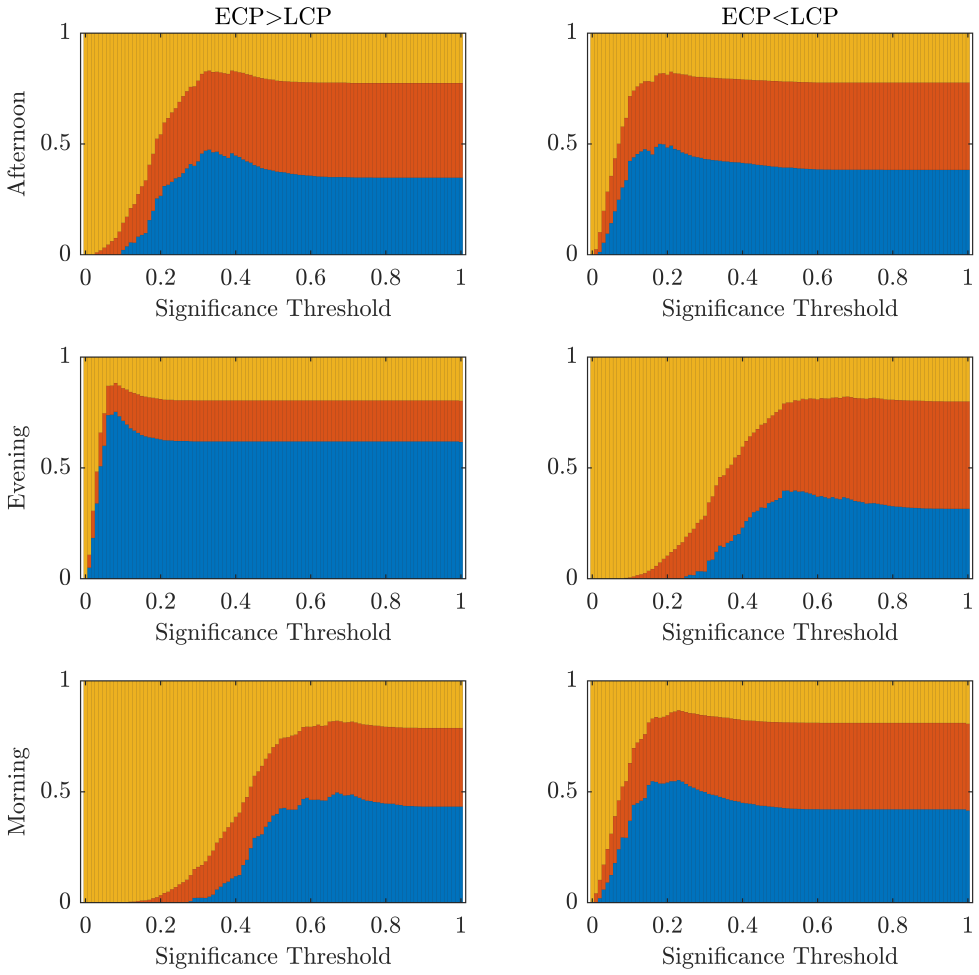


Figure 5.8: **Performance of the Classifier When Removing Subjects and Varying Across Thresholds for Significance.** Stacked bar chart showing the mean fraction of subjects classified correctly, incorrectly, and unclear respectively (blue, red, yellow) when removing one subject in turn and varying across the threshold for significance.

similar trends with accuracy increasing with increasing α up to a point specific to each scan and then steadily declining to a plateau once α is high enough. Table 5.10 shows the values of α for which the maximum accuracy occurs.

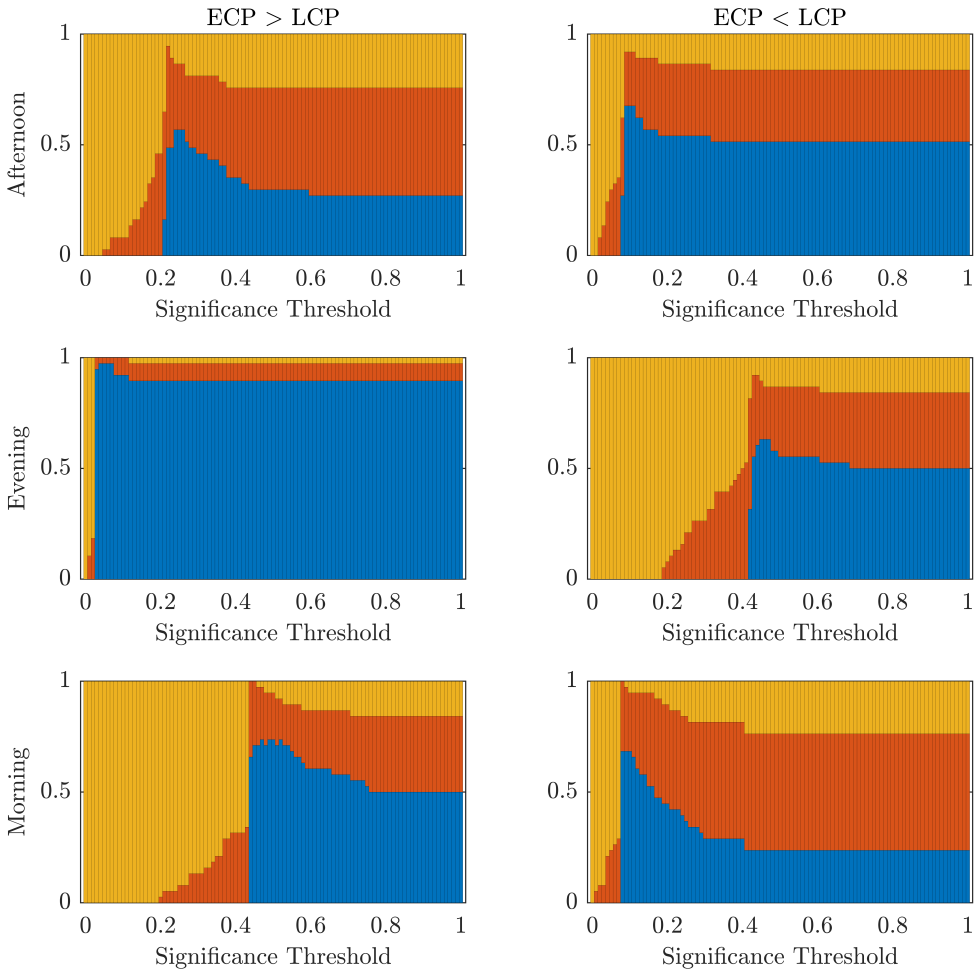


Figure 5.9: **Performance of the Classifier When Varying Across Thresholds for Significance.** The fraction of subjects classified correctly, incorrectly, and unclear respectively (blue, red, yellow) when varying across the threshold for significance.

	ECP>LCP	ECP<LCP
Afternoon	0.24-0.26 (57%)	0.09-0.11 (68%)
Evening	0.04-0.07 (97%)	0.45-0.47 (63%)
Morning	0.47, 0.49, 0.50 (74%)	0.08-0.1 (68%)

Table 5.10: **Values of α which give the Highest Accuracy with the Accuracy Values given in Brackets.**

5.4 Discussion

To the best of our knowledge, this is the first study explicitly aiming to classify an individual's chronotype using rs-fMRI data. While previous studies [57, 58, 92] have identified differences in FC associated with chronotype, the question of whether these differences are sufficient to identify a participant's chronotype solely from fMRI data has not been asked. Following the creation of FNs, NBS was used as the base for a classifier. The classifier is innovative through its evaluation of whether an ECP or LCP classification of the test subject leads to a clearer differentiation between the two classes in a group-level comparison.

In addition, the classifier was presented alongside a principled way to select the t-statistic thresholds, a criticism of NBS. This focused on the two percolation thresholds resulting from the two different chronotype labellings a test subject can be assigned. By concentrating on edges located in dysconnected subnetworks there is evidence that rs-fMRI data does contain enough information to distinguish between ECPs and LCPs. However, this is true only for the Evening [ECP>LCP] scan where we see a high classification accuracy of 97.3% when applying the percolation thresholds.

The high level of accuracy is predominantly due to step one of the classifier, which compares the significance of the MCCs $E^m_{t_E}$ and $L^m_{t_L}$. This step contributed almost one third of the correct classifications, as seen in Table 5.1. Since the MCC, when all subjects are correctly labelled, covers all 70 ROIs with only 146 edges (Table 5.3), it suggests that the key differences between the FNs of extreme chronotype are sparse and distributed

during the Evening scanning session. This indicates that any influences of chronotype and time of day are impacting the brain relatively globally, which is plausible given that they are driven by systemic circadian and sleep drives. This work and others [57, 58] suggest that the impact of chronotype on FNs is relatively subtle, at least within the cortical regions that provide the majority of the data.

This may explain why neither the seed-based approach in Fafrowicz et al. [60], nor the graph metric approach in Chapter 4 nor those completed by Farahani et al. [62, 64] found significant differences between extreme chronotypes. Since the effect of chronotype was subtle and seen only through the group-level comparison of specific edges using a contrast to compare between ECPs and LCPs, this would be lost in many graph metric approaches, which average over many nodes or the entire network reducing the focus on key edges. On the other hand, seed-based approaches that rely on contrasts may identify differences [57, 58], but the focus on specific seeds could limit the ability to identify the distributed effect seen in the Evening [ECP>LCP] scan.

Meanwhile, the five results of 0% accuracy for the chosen thresholds raise questions about why the classifier's performance is so optimised for the Evening scan and why scans at other timepoints seem to have no ability to differentiate between ECPs and LCPs. Some variation in the accuracy of the classifier is to be expected because there are known diurnal variations in the graph metrics calculated from FNs in the morning when compared to the evening. Indeed, Farahanni et al. [62, 64] found that when ECPs and LCPs were pooled into one group significant time of day differences occurred between the Morning and Evening scanning sessions in small-worldness, assortativity and network synchronisation for certain density based thresholds. Therefore, it is likely that the variation in accuracy throughout the day is reflecting dynamic changes in the FNs of extreme chronotypes. Also, Fafrowicz et al. [60] found significant time of day effects when seeding in multiple areas of the brain. In addition, chronotype is known to affect behavioural outcomes in the two groups differently over the course of the day. For instance, Facer-Childs et al. [57] found that patterns of subjective sleepiness as measured using KSS for the

two extreme chronotypes have an inverse relationship therefore the underlying network dynamics associated with such changes are likely to be reflected in times where the FNs of the two groups show stark changes and times of more similarity.

A key assumption in the presented classifier pipeline is that all ROIs provide valuable information and the effect of chronotype is therefore distributed throughout the brain. However, due to the poor performance across the different scanning sessions this assumption seems unsuitable for the Morning and Afternoon scans. Previous studies using the same data [57, 58] have suggested that the differences in FC associated with chronotype and time of day can be restricted to individual nodes, or even sub-portions of individual nodes. The optimal way to define a node (and related issues such as the optimal number of nodes to use etc.) therefore remains an issue and its impact on the classifier requires further research [112, 113, 178].

The choice of the t-statistic threshold was investigated to understand how the restriction of the MCC assumption resulted in 0% accuracy in the other 5 cases. In addition, we wanted to understand if the conclusion from Table 5.2 that the rs-FNs of extreme chronotypes only contain differentiable information in the Evening scan is true or the result of the MCC assumption. Therefore, the classifier was then used within a classification framework to understand if differential information exists. Figure 5.2 shows that when the t-statistic threshold selection process was relaxed it was possible at all three times of the day - under one contrast - to find a t-statistic threshold that resulted in a highly accurate classifier for distinguishing between ECPs and LCPs. This expanded the results presented in Section 5.3.1, which focused on a specific threshold. However, we restricted our recommendations to cases where a principled approach could be taken to defining the threshold, rather than highlighting situations where good classification accuracy could be achieved with an arbitrary threshold. Clearly, the high classification accuracy resulting from the classification framework supports the view that chronotype classification can be undertaken with rs-fMRI data, although further work is needed to develop statistical methods to achieve this without the use of arbitrary thresholds or issues of multiple

comparisons.

Despite the problem of statistical significance arising from multiple comparisons, Figure 5.2 does offer some insights into the effect of chronotype over the day, within this dataset despite the inability to determine parameter choices for future datasets. For instance, the contrast resulting in high accuracy, when varying the t-statistic threshold, changes over the course of the day. Simplistically, this generally follows the pattern of high classification accuracy occurring when the chronotype with increased tiredness (as measured using KSS [57], has a higher FC in the contrast. Hence, the contrast ECP>LCP performs better in the Evening scan when ECPs are likely to be more tired than LCPs. Similar logic follows for the Morning scan, when forcing LCPs to awaken before their natural sleep pattern for an 08 : 00 scanning session will result in increased tiredness for that cohort. Finally, the contrast ECP<LCP produces non-zero accuracy in the Afternoon. However, the range of t-statistic thresholds, which produce non-zero accuracy, is smaller in the Afternoon compared to the Morning. This could be associated to the greater similarity in KSS scores in the two groups at this time. This may suggest that the classification is driven by tiredness (or Process S within the two process model [20] rather than chronotype (related to Process C) per se. Within a real-world setting, and not only in relation to rs-fMRI data, differentiating the impacts of sleep homeostasis and circadian drive is difficult. Future studies using laboratory based CR or forced desynchrony protocols [54, 117] could help to understand how sleep drive and circadian phase are differentially manifested in rs-fMRI data and brain networks more broadly.

Furthermore, the t-statistic thresholds producing high accuracy could provide an insight into how chronotype affects the brain throughout the day. Indeed the size of the dysconnected networks producing high accuracy is markedly different throughout the day. The large range of t-statistic thresholds in the Evening scan resulting in non-zero accuracy start at 0.71, representing a dense distributed effect, while the highest peak in accuracy near 1.7 suggests a sparse but distributed effect. In contrast, in the Afternoon and Morning scans the high t-statistic thresholds near 2.2 suggest a focal effect concentrated on

specific subsets of the brain's FN. Finally, the second peak in the Morning near 2.8 is focused on only 7 nodes and therefore represents a highly spatially specific impact on the brain. More detailed investigation of the spatial distribution of network changes as a function of time of day and chronotype would help to develop these ideas and provide a more specific understanding of how the brain is impacted.

The change in the range of t-statistic thresholds that result in high accuracy explains why the classifier only saw results of 97.3% for the Evening [ECP>LCP] scan, and 0% for the other scans and contrasts. This is because it is the only combination where the percolation threshold when all subjects are correctly labelled, shown by the dashed line in Figure 5.2, falls directly within the range of t-statistic thresholds that consistently sees non-zero accuracy. For the other five combinations this is not the case. This indicates that the assumption of connectedness, the focus on MCCs and the conventional choice of $\alpha = 0.05$, is suitable for the Evening [ECP>LCP] scan, while a different combination of parameters needs to be used to optimize accuracy for the other scans. Given our results and the discussion above, other approaches could be developed to extract the information needed to provide good classification accuracy in the Morning and Afternoon. Therefore, our work would suggest that differential information is present in the data and a time of day effect is seen not only through the change in contrast, which produces high accuracy, but the size of the dysconnected network. As this conclusion is based on an analysis with a large number of comparisons we suggest that the clustering of the thresholds which produce high accuracy results provides support for this claim. Indeed the high accuracy clusters around specific thresholds, which may indicate a real range of maximal difference, beyond random effect. This is because if the high accuracy was merely due to chance from testing enough thresholds then the distribution of highly accurate thresholds would not be clustered together but would be more uniformly distributed across the t-statistic thresholds and contrasts.

In addition, the stability of the classifier was investigated, through the creation of additional surrogate datasets using a leave-one-out approach. This approach was taken

in the absence of an independent dataset for validation, however it should be noted, that while offering some insight into the stability, surrogate datasets cannot truly recreate the level of variability that would be seen in a fully independent dataset. It is clear from the results across all 3 scanning session, as seen in Tables 5.4 - 5.9, that the classifier is highly sensitive to the removal or inclusion of certain subjects. In the case of the Afternoon and Morning scanning sessions the removal of certain subjects led to a considerable increase in accuracy, while in the Evening scanning session subject removal has the opposite effect, reducing accuracy, aside from Subject 36.

We see that when comparing the results from the partial datasets to the original datasets there is a correspondence between improved accuracy when incorrectly labelled subjects in Table 5.2 are removed. This may indicate that these subjects have properties closer to the other chronotype, and hence why their removal improves the classifier. Similarly, we might hypothesise that the near-zero accuracy resulting from the removal of subjects in the Evening scanning session could be because they have properties which clearly identify them as their phenotype and hence their removal reduces the accuracy of the classifier. However, this hypothesis was not supported by differences in the metadata as shown in Appendix B.3. Similarly, the metadata offers no insight into why, for example, Subject 36 was misclassified in the Evening [ECP>LCP] scan. Further work is needed to understand the subtleties of the links between resting brain function measured with fMRI and more established markers of chronotype.

Furthermore, it was observed that a large proportion of the subjects were classified as unclear due to non-significant networks occurring at the traditional 0.05 significance level when the number of subjects was reduced by one. To investigate if differentiable information is present when using higher significance thresholds an investigation into the significance threshold was also completed.

The accuracy of the classifier, as well as the standard deviation of the n different dataset's accuracy for each significance threshold, are presented in Figure 5.7. An optimal choice of significance threshold could be selected for each scanning session and contrast to

maximise the accuracy across the n datasets and minimise the standard deviation. This relationship is the clearest for the Evening scanning session and indeed using $\alpha = 0.08$ shows the improved ability to differentiate chronotypes in the Evening scanning session. For the other scanning sessions and contrasts this relationship is not as distinct, but an optimal ratio between these two factors could be located. Directly relating the parameter choice for significance to the classifier's stability offers a solution for how to improve the classifier's performance in future datasets.

When comparing the optimal significance thresholds seen in Figure 5.7 for the partial datasets, to the optimal values in Table 5.10 for the original datasets, we clearly see that $\alpha = 0.05$ is too conservative for $n - 1$ subjects compared to n subjects. One possible explanation for this is that the number of subjects is quite low and reducing the size further removes important information. Indeed, the optimum value for α decreases for the Evening [ECP>LCP] for 38 subjects (0.04-0.07) compared to when 1 subject has been removed (0.08), indicating that as the number of subjects increases, the stability of the classifier increases. However, it is reasonable to assume this trend will not continue indefinitely and that there will be an optimum number of subjects in the training set such that they provide enough information for classification, while also allowing the test subject to have enough influence that changing their label will have an effect on the t-statistic. This highlights that the classifier is reliant on the fact that changing the label of one subject will lead to a detectable impact on the t-statistics, while also having a large enough training set to ensure there is enough distinction between the two cohorts. This approach is optimised to smaller datasets, where mislabelling one subject will have a greater influence. If the number of subjects increased sufficiently ($n \rightarrow \infty$) it is reasonable to assume the dysconnected networks produced will be the same irrespective of the labelling of the test subject. At that stage this classifier would be redundant and NBS could be used in its traditional form.

For both the partial datasets in Figure 5.8 and the original datasets in Figure 5.9, we see the optimal values of the significance threshold follow a time of day effect similar

to that observed in Figure 5.2. Indeed, we clearly see high differences in the optimal value of α for the different contrasts in the Evening and Morning scan with the optimal significance threshold range being lower when the contrast aligns with the group who are experiencing increased tiredness as measured using KSS [57]. In the Afternoon, while there is a difference in the optimal parameter choice between the two contrasts in agreement with KSS, the difference between the optimum α value in the two contrasts is smaller, which again could be associated to both groups having a more similar state of tiredness.

This pattern matches studies where excitability, as measured through TMS, is higher when participants are more tired [94, 125]. In addition, Petkov et al. [149] showed that the propensity of people with epilepsy to transition into a seizure state is greater for networks with a higher mean degree, which are therefore considered more excitable. If we view higher FC as a proxy for a larger mean degree then the pattern of scanning session, contrast and accuracy would be linked to excitability and consequently tiredness of the two chronotype groups. This suggestion remains to be investigated in more detail, potentially with studies involving explicit sleep deprivation.

Overall, we have provided evidence that when using this classification framework that differentiable information exists in the rs-FNs of extreme chronotypes and this changes over the day. However, to support the use of the classifier as presented in Section 5.3.1 additional research would be required. For instance, this study is limited by the small sample size, therefore future larger independent datasets would be required in order to validate the conclusions about the time of day effects and to ensure the accuracy of the Evening [ECP > LCP] scan is not over-optimistic. However, larger levels of recruitment may be hindered due to the multiple scanning sessions and the extreme chronotypes required by the protocol. In addition, due to the nature of the classifier considering one test subject at a time and determining if an ECP or LCP label is most suited for this subject, the classifier naturally uses a leave-one-out cross-validation approach. However, it should be noted that a leave-one-out approach can result in high variability and over-fitting may occur.

In addition, optimising the parameters of the classifier, which include two thresholding choices, should be the aim of future research. Both the value at which to threshold the t-statistic matrix and the threshold for significance must be selected. In both cases the selection of this value is somewhat arbitrary and typically determined by convention. By varying over these thresholds it becomes clear that there is differentiable and important information present in the Afternoon and Morning scanning sessions and that optimising these parameters will improve the accuracy and importantly the sensitivity of the classifier to new datasets. Further research is needed to understand how a rigorous selection process or different underlying assumptions could result in selecting objective thresholds that optimise accuracy for the Morning or Afternoon scanning session. Such research may also develop new ways in which fMRI can be used in the study of chronotype as well as lead to greater insight into the impact of chronotype on FNs. This study also motivates the future use of other methods for quantifying brain function to investigate human chronotype. For instance, assessing the pipelines' suitability for use with EEG data, which was analysed in Chapter 7, would be a natural extension especially since MCCs were originally shown to be useful at detecting subtle effects on FNs from EEG recordings [197]. This may result in the Morning and Afternoon scans having non-zero accuracy for the percolation thresholds, offer other interesting insights or simply increase the practicality of recording sessions in relation to cost and location. However, compared to fMRI, EEG has limited spatial sampling of the brain, and a lack of sensitivity to deep brain structures, which are known to be important to sleep and circadian regulation.

Furthermore, this study allowed subjects to sleep using their preferred schedule for two weeks prior to the scans. It is currently unknown if the differentiation and accuracy seen at the three scanning times would stay the same if LCPs were constrained to a more traditional work schedule or if high accuracy would occur at a different time of the day. It seems likely that with the additional sleep debt associated with conforming to the societal day, LCPs would be more easily differentiable from ECPs.

In conclusion, we have shown that extreme early and late chronotypes have differen-

tiable information in their rs-fMRI data that can be used to classify them. Indeed, this classifier demonstrates that two groups of participants whose differences are relatively subtle (i.e. not based on a clinical diagnosis) can be differentiated using rs-fMRI, when traditional seed-based and connectivity-based methods have struggled.

Through this study we have proposed a classifier and investigated its sensitivity and robustness to changes in parameters and the training set. In an ideal scenario the removal of individual subjects would have a negligible effect on the classification accuracy. However, we found the accuracy of the classifier to be strongly dependent on individual participants, although these participants did not appear to be unusual based on the physiological and behavioural data we had available. We found conditions under which this could be mitigated by altering a combination of the threshold for the t-statistic, significance threshold for the dysconnected network and contrast being used. For future chronotype datasets it is recommended to use a contrast which reflects the tiredness of the two groups at the time of the scan, while issues around the optimal thresholds for significance and t-statistic thresholds remain to be clarified for scans other than the Evening.

CHAPTER 6

USING THE KURAMOTO MODEL TO INVESTIGATE THE LINK BETWEEN NETWORK STRUCTURE, EXCITABILITY AND SLEEP DEPRIVATION

6.1 Introduction

Prolonging wakefulness and delaying sleep is common within our 24/7 society, typically due to a combination of work and social obligations. This leads to people regularly facing acute or chronic sleep deprivation. The effect of sleep deprivation on the body, has been analysed through changes in metabolite concentration [77], blink rate and ECG [37]. However, the brain is considered to be more impacted by sleep deprivation than any other organ [63], as discussed in Section 2.3.

Therefore, the effect of sleep deprivation on the brain has been studied in multiple ways, from external cognitive task-based protocols [46, 52, 53, 133], to internal effects such as power spectrum changes [37]. Indeed, as discussed in Section 2.3, Van Dongen et al. [49] and Chua et al. [37] repeatedly sleep-deprived the same participants, providing evidence for trait-like vulnerability to sleep deprivation. In particular, Van Dongen et al. [49] saw consistent intra-individual performance when repeating behavioural tasks and high inter-individual differences. Also, Chua et al. [37] found that alpha spectral power over the first 16 h of a 26 h CRP could explain the intra-individual variance seen after

the participants were sleep deprived. Not only indicating the predictive capacity of EEG data but the presence of a frequency specific marker for susceptibility to sleep deprivation. In addition, changes to the graph metrics of FNs as people become progressively more sleep deprived have been studied extensively [101, 172, 195], as discussed in Section 2.3. Furthermore, one common finding in sleep literature is that the excitability of the brain, as measured through TMS, is seen to increase as participants become increasingly sleep deprived [125, 135], as discussed in Section 2.4.

However, despite links between FNs and excitability, especially in the field of epilepsy [164], to the best of our knowledge, no study has considered how baseline FN structure is associated with susceptibility to sleep deprivation. Indeed, trait-like vulnerability to sleep deprivation may be underpinned by trait-like topology of FNs, providing potential biomarkers for susceptibility to sleep deprivation. Therefore, within this Chapter, we explore the possibility that FNs could affect an individual's susceptibility to sleep deprivation. We investigate this using the Kuramoto model, as introduced in Section 3.2. The theoretical framework will allow greater control over network properties and the effect of sleep deprivation will be simulated by altering local excitability. Allowing an investigation into the link between network structure, sleep deprivation and excitability.

The Kuramoto model is a simple phenomenological model of phase oscillators, which has been used in the context of neuroscience to study brain networks. We will use a mutliscale approach such that each population will represent a different region of the brain and each oscillator will represent a mass of neurons - an approach used in the context of epilepsy [164]. All oscillators in a population will be connected by all-to-all coupling; a standard assumption in the Kuramoto model to ensure global synchronisation is driven by macroscale network structure rather than local structure. Furthermore, the populations will be connected via a specified adjacency matrix, $\mathbf{A}$ in eq 3.17 as seen in Figure 3.9. Therefore, the synchronisation of each oscillator is affected not only by the coupled oscillators in their own population but by those oscillators in connected populations. Hence, network synchronisation is the combined effect of local and global coupling strengths and

network topology. The effect of sleep deprivation will be modelled by modulating the local coupling parameter, as explained in Section 6.2.2. Synchronisation measures, introduced in Section 6.2.5, will then be calculated to interpret the interplay of network structure, excitability and sleep deprivation.

Understanding how different networks react to sleep deprivation in a fully controlled environment could indicate which graph metrics are the most informative for predicting how individuals with similar network features will react to sleep deprivation. In the future this could allow predictions on the impact of sleep deprivation from a baseline FN, removing the need to sleep-deprive individuals.

6.2 Methodology

6.2.1 Network Selection

The multi-scale Kuramoto model, as explained in Section 3.2, requires an adjacency matrix denoting the FC between different nodes, within this Chapter binary, directed adjacency matrices are considered. The direction of edges in each adjacency matrix, therefore, provides information about how each node can influence the synchronisation of other nodes in the network.

Networks with 3 and 18 nodes are considered. These networks were chosen due to the tractability of effects on 3 nodes, while 18 node networks are more realistic for potential data.

For all networks self-links were prohibited, as within the model self-links would equate to local coupling, which is accounted for separately, and all nodes were considered identical in their intrinsic excitability properties. Under these conditions any network could be split into one of three distinct groups:

G0 All eigenvalues of the adjacency matrix were equal to zero.

GW Had at least one non-zero eigenvalue and the adjacency matrix was weakly, not

strongly, connected - paths exist between every node if edge directionality is ignored.

GS Had at least one non-zero eigenvalue and the adjacency matrix was strongly connected - paths exist between every node if edge directionality is considered.

No networks from **G0** were simulated; this is because at least one non-zero eigenvalue was required for the calculation of the theoretical relationship between local and global coupling, as outlined in Section 6.2.2. For the three node networks this resulted in 3 networks with two edges being removed and 1 network with 3 edges.

6.2.1.1 Three Node Networks

Three node networks contain interesting topological features such as cycles, loops and basal nodes, despite the limited number of 13 networks. Of the 13 networks four were in **G0**; therefore only 9 were simulated - four in **GW** and 5 in **GS** - as presented in Table 6.1. Each network is denoted by N_j^i where i is the number of nodes, and j is the index.

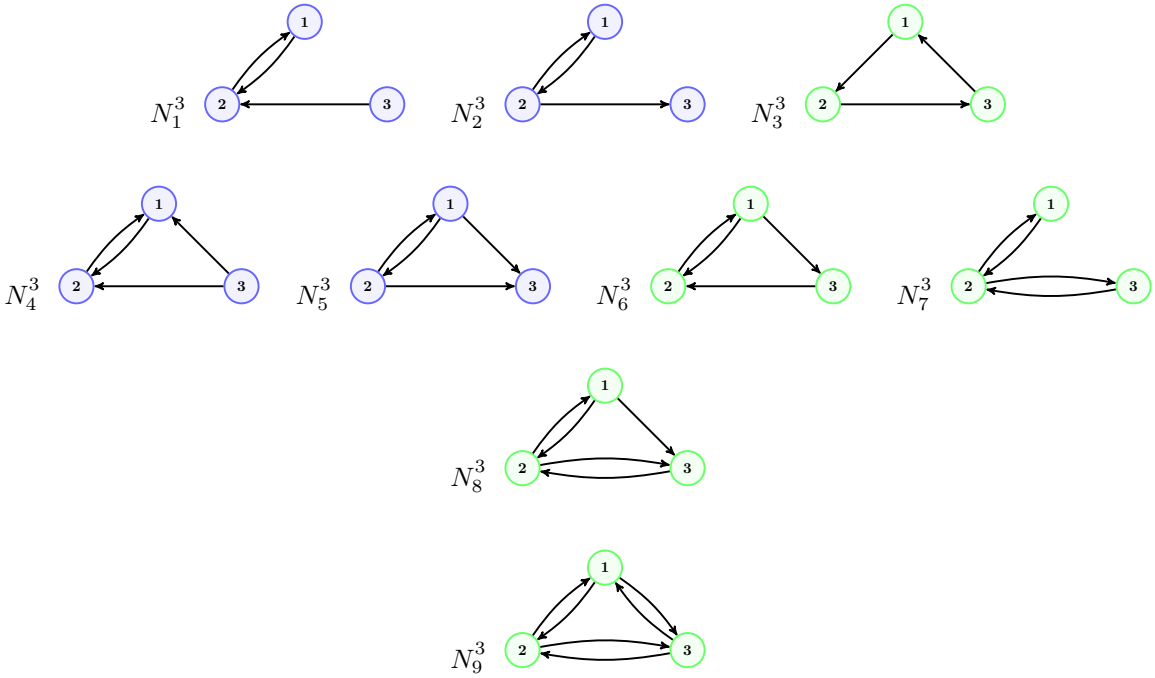


Table 6.1: **Three Node Adjacency Matrices.** Here blue (N_1^3, N_2^3, N_4^3 and N_5^3) indicates the network is in **GW**: it has at least one non-zero eigenvalue and is weakly connected; green ($N_3^3, N_6^3, N_7^3 N_8^3$ and N_9^3) indicates the network is in **GS**: it has at least one non-zero eigenvalue and is strongly connected.

Networks N_2^3 and N_5^3 are in **GW** because node 3 has an out-degree of 0 whilst N_1^3 and N_4^3 are in **GW** because node 3 is a basal node - has an in-degree of 0. Networks $N_3^3, N_6^3, N_7^3, N_8^3$ and N_9^3 are in **GS**. Note that low local synchronisation in a basal node could result in the node acting like a noise input into the system, which would hinder global synchronisation. While at higher levels of local synchronisation, global synchronisation can only occur if the basal node acts as a 'driver', with the network synchronising to it, as the network cannot mediate the synchronisation of the node. Therefore, basal node networks used within the Kuramoto framework will produce simulations with qualitatively different patterns.

6.2.1.2 18 Node Networks

In addition, to the three node networks, theoretical 18 node networks were also considered[1], increasing the complexity of the networks and ensuring the findings were more directly comparable to real EEG networks. The number of possible networks on 18 nodes is too vast to consider in the same systematic way as the three node networks. Consequently, an additional restriction was applied such that each network is in **GS**, removing the potential for basal nodes. This was a pragmatic choice made due to the multitude of potential networks even under the restriction of **GS** networks and the lack of basal nodes in real-world FNs[2].

A subset of 18 node networks from **GS** were created across the small world spectrum (introduced in Section 3.1.1.6) from regular lattices to random networks. Two groups of networks were created using the Watts-Strogatz method with a mean degree of three ($\langle k \rangle = 3$) or four ($\langle k \rangle = 4$). Fixing the mean node degree guaranteed that differences in synchronisation were due to the features of the network and not their respective densities. These mean node degrees were chosen to reflect the values in real networks that could occur in Chapter 7. This is because controls were found to have a mean node degree ~ 6

[1] Equal to the number of EEG channels in the participant data in Chapter 7.
[2] All real networks considered in Chapter 7 are in **GS**.

[35] when using a similar PLF EEG pipeline. However, the pipeline did not include the order two edge reduction technique implemented in Chapter 7, which would reduce the number of edges and hence mean node degree[1]. Also, two mean degrees were chosen to assess the robustness of the results when changing this parameter.

The Watts-Strogatz method first produces a regular lattice structure containing a given number of nodes (P = 18) and a given mean node degree, $\langle k \rangle$, where each node is initially connected to its k nearest neighbours (k = 3 or k = 4). Then with a given probability, p_{ws}, each edge in the network is randomly reconnected, such that no self-loops or edge duplication occurs. A directed version of the Watts-Strogatz method was employed such that node 1 had directed edges towards nodes 2,3 and 4 in the k = 3 case and nodes 2,3,4 and 5 in the k = 4 case. Here p_{ws} values of $0, 0.01, 0.05, 0.1, 0.15, 0.25, 0.35, 0.45$ and 1 were chosen to replicate the small world profile produced by Humphries et al. [96] when increasing the probability from a regular lattice (p_{ws} = 0) to random (p_{ws} = 1) as seen in Figures 6.1 and 6.2. For each p_{ws} five networks were produced, except for p_{ws} = 0 to ensure the lattice only appears once. This created two groups each with 41 networks, numbered sequentially as p_{ws} increases.

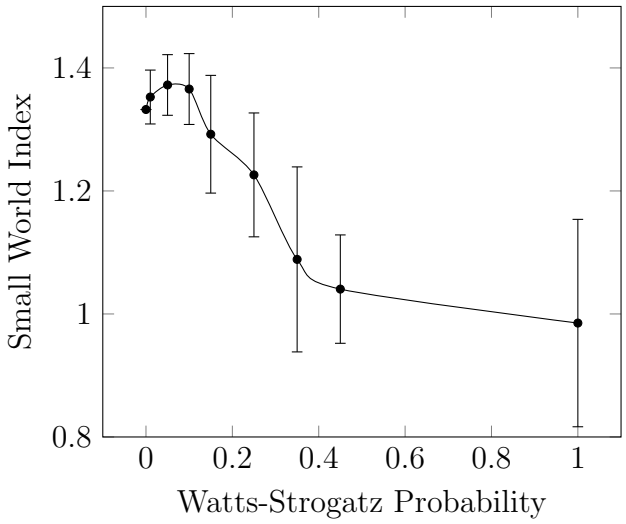


Figure 6.1: **Small World Index of Various Watts-Strogatz Networks for $\langle k \rangle$ = 3**.

[1]Note that the mean node degree of networks created in Chapter 7 are in the range $[1.72, 2.78]$.

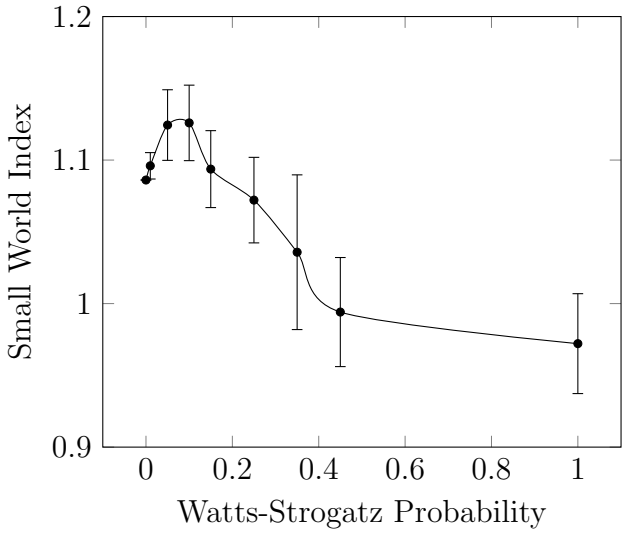


Figure 6.2: **Small World Index of Various Watts-Strogatz Networks for $\langle k \rangle = 4$.**

6.2.2 Selecting Kg and Kcc

For a given network the simulation was repeated for a range of global, K_g, and local, K_{cc}, coupling strengths. The theoretical linear relationship between K_{cc} and K_g was established in Appendix A as:

$$K_{cc}(K_g; P, \lambda_{max}) = 2P - K_g|\lambda_{max}|, \tag{6.1}$$

where P is the number of populations and λ_{max} is the absolute value of the largest eigenvalue of the adjacency matrix given by the FN. Examples of this relationship can be seen in Figure 6.3 for three node networks. If non-zero eigenvalues of the adjacency matrix do not exist, then K_g is considered inconsequential in the synchronisation, hence why no networks from **G0** were considered. Eq 6.1 is derived by considering the linearised steady-state solutions under the assumption of an infinite number of oscillators, drawn from a Cauchy distribution.

Cross et al. found that following sleep deprivation 'the integration within cortical networks increases relative to integration between networks' [39]. To replicate this effect in the theoretical simulations, the local coupling was used as a proxy for the effects of

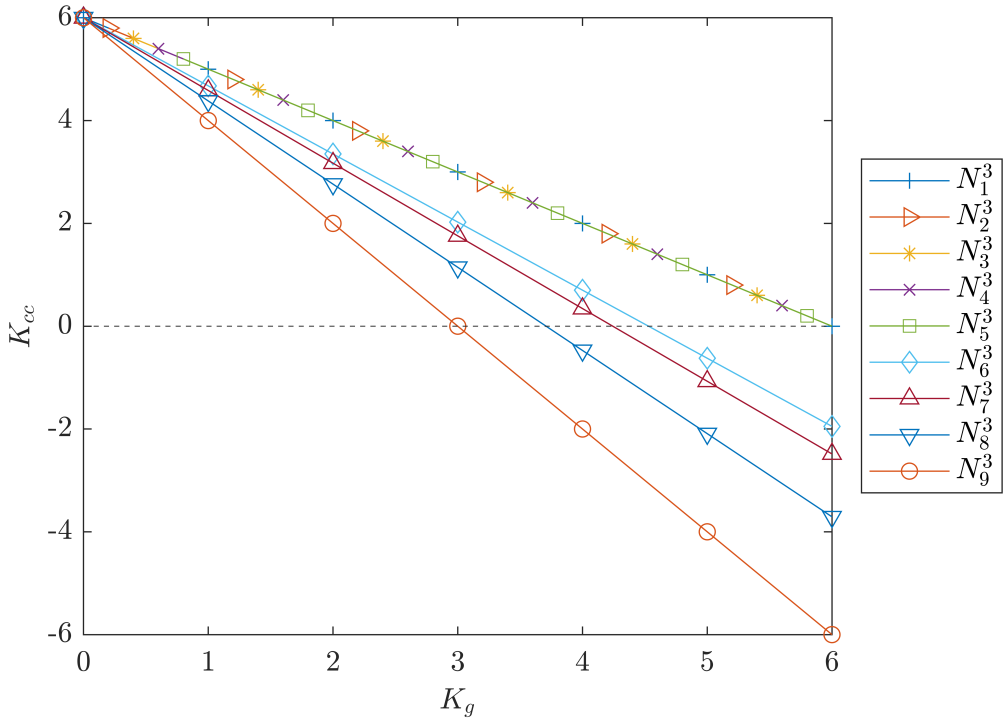


Figure 6.3: **Relationship Between K_{cc} and K_g for Selected Three Node Networks.** The relationship between K_g and K_{cc} is plotted for all three node networks with at least one non-zero eigenvalue associated with its adjacency matrix.

sleep deprivation. Also, the bound,

$$0 < K_g \leq \frac{2P}{|\lambda_{max}|}, \tag{6.2}$$

was used and a range of values were considered to ensure results were independent of the choice of K_g. Eq 6.2 ensured no negative local coupling values were considered. While negative coupling values are mathematically possible they are not used as this would hinder global synchronisation. In addition, $K_g = 0$ was not considered as, via eqs 3.16 and 3.17, this would be the equivalent of removing every edge from the adjacency matrix creating P isolated populations; therefore network effects could not be assessed.

The range for local coupling was chosen as $[0, K_{cc}^{max}]$, where $K_{cc}^{max} = 1.1K_{cc}(K_g) = 1.1\overline{K_{cc}}$, with $\overline{K_{cc}}$ denoting the local coupling value which theoretically produces global synchronisation for the global coupling value K_g in eq 6.1. This range for K_{cc} prevented negative synchronisation, ignored high values and allowed the analysis to be repeated over

a range specific to the synchronisation properties of that network while also taking into account differences between the theoretical and simulation approaches.

For instance, the theory is reliant on an infinite number of oscillators per population from a Cauchy distribution. Here, we used $N_c = 100$ oscillators per node from a Gaussian distribution. This avoided the influence of oscillators from the higher density tails of the Cauchy distributions skewing the natural frequencies and preventing synchronisation. However, despite the differences in the distributions and numbers of oscillators between the model and the theory eq 6.1 still provides an objective way to select the parameter range for K_{cc}, which is related to the properties of each network. This ensures we consider how networks transition into their theoretically synchronised state, ultimately ensuring a consistent comparison between networks.

The manner of how local coupling changes from 0 to K_{cc}^{max} is then defined by the function controlling the effect of sleep deprivation over time as outlined below in Section 6.2.2.1.

6.2.2.1 Functions for the Effect of Sleep Deprivation

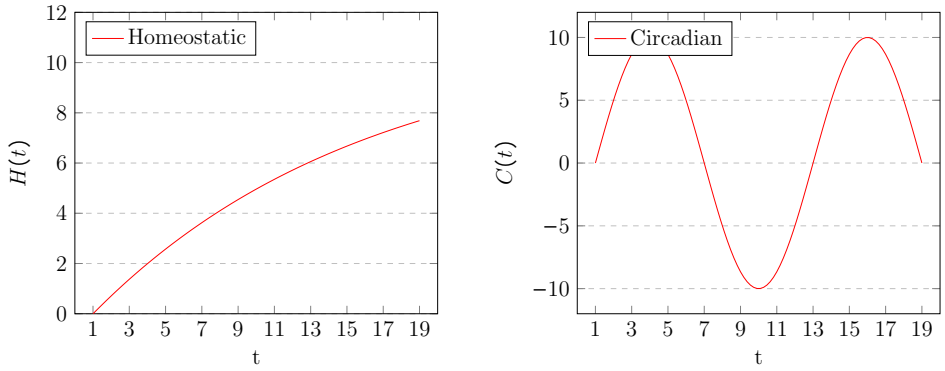
The simulated effect of sleep deprivation was included in the model via changes in the local coupling strength. Indeed, this was included through a combination of processes from the two process model [19] called Total Drive, $D(t)$. This enabled a non-linear increase in sleep pressure through the homeostatic pressure and allowed the function for sleep deprivation to be modulated by an endogenous circadian rhythm [73]. These functions are shown in Figure 6.4.

The homeostatic pressure was modelled by an exponential function which started at 0 at $t = 1$ and increased over 19 timepoints[1], representing 38 h towards the upper asymptote K_{cc}^{max},

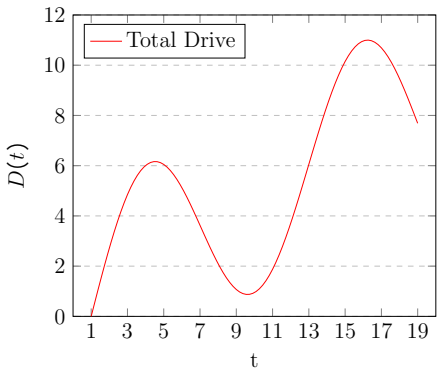
$$H(t) = K_{cc}^{max}\left(1 - e^{-\frac{(t-1)}{\chi}}\right),$$

here $\chi = 15$ is the homeostatic time constant, chosen to avoid negative values of $D(t)$.

[1] Chosen to match the maximum number of datapoints in the real data in Chapter 7.



(a) Homeostatic Pressure (b) Circadian Pressure



(c) Total Drive

Figure 6.4: **Possible Functions for the Drive Towards Sleep.** **(a)** Homeostatic pressure as defined by Borbély [19] here $\chi = 15$ to avoid negative values of $D(t)$ for a range of possible $\overline{K_{cc}}$. **(b)** The circadian rhythm with a period of 12 timepoints (i.e. 24 h). **(c)** Total Drive created through a linear combination of homeostatic and circadian pressure, here $a = 0.4014$ selected such that the peak in $D(t)$ occurs at K_{cc}^{max} when $\overline{K_{cc}} = 10$ calculated using eq 6.3.

The circadian process was modelled by,

$$C(t) = \overline{K_{cc}} \sin\left(\frac{2\pi}{12}(t-1)\right),$$

to ensure a 12 timepoint period. Finally, Total Drive was modelled by a linear combination of the circadian and homeostatic drives to sleep, similar to the drive presented by Phillips et al. [73],

$$D(t) = H(t) + aC(t).$$

Here the parameter $a > 0$ weights the contributions of the circadian process and is selected such that the maximum value for $D(t)$ over the 19 timepoints occurs at the value of K_{cc}^{max}.

Therefore, the following system of equations must be satisfied,

$$\begin{cases} \frac{1}{\chi} K_{cc}^{max} e^{-\frac{(t-1)}{\chi}} + \frac{2\pi a}{12} \overline{K_{cc}} \cos\left(\frac{2\pi}{12}(t-1)\right) = 0 \\ K_{cc}^{max} e^{-\frac{(t-1)}{\chi}} + a\overline{K_{cc}} \sin\left(\frac{2\pi}{12}(t-1)\right) = 0 \end{cases}, \tag{6.3}$$

such that the turning point occurs at the peak value of K_{cc}^{max}.

6.2.3 Kuramoto Model

The Kuramoto model, as explained in detail in Section 3.2, is a phenomenological model of coupled oscillators useful for understanding synchronisation and by extension excitability, as discussed in Section 3.2.1. For a multi-scale model the position of oscillator $j \in \{1, \ldots, N_c\}$ in population $c \in \{1, \ldots, P\}$ is given by,

$$\frac{d\theta_j^c}{dt} = \omega_j^c + \sum_{\gamma=1}^{P} \eta_\gamma \frac{K_{c\gamma}}{N_\gamma} \sum_{k=1}^{N_\gamma} \sin\left(\theta_k^\gamma - \theta_j^c\right).$$

Here ω_j^c denotes the natural frequency of oscillator j drawn from the Gaussian distribution $g_c(\omega)$, $\eta_c = \frac{N_c}{N}$ where η_c and N_c are the proportion and number of oscillators in population c respectively and N is the total number of oscillators across all populations. Also, $K_{c\gamma}$ is an element in the matrix $\mathbf{K}$, which gives the coupling strength between nodes c and γ. The coupling strength $\mathbf{K}$ is a combination of global and local coupling strength defined by:

$$\mathbf{K} = K_g \mathbf{A} + K_{cc} \mathbf{I_P}.$$

Here $\boldsymbol{I_p}$ is the $P \times P$ identity matrix and $\mathbf{A}$ is the adjacency matrix connecting the P populations. Note that $\mathbf{A}$ will be the corresponding adjacency matrix for each network in Section 6.2.1.

6.2.4 Simulating the Time-series

The Kuramoto model was simulated using a forward Euler scheme over time $T = 1,000$ s with timestep $dt = 0.005$. Each Kuramoto population had $N_c = 100$ oscillators each drawn from a Gaussian distribution with mean 9 Hz and standard deviation 0.5 Hz. Note that focusing on 9 Hz was chosen to represent alpha rhythms, however as long as the simulation is sufficiently long compared to the period of the oscillator's frequency multiple frequency distributions could have be chosen. A smaller standard deviation reduces the time required for the Kuramoto model to transition past the state of no synchronisation at the beginning of the simulation and allows the oscillators time to start synchronising, especially in the case $P = 18$ as the network will be complex. The majority of the simulations will be in an area of parameter space where full synchronisation will not occur, therefore after $T = 1,000$ s the network may not be fully synchronised. However, the simulations will still capture the trend towards synchronisation, which can be compared between networks to gain an understanding of the link between coupling strengths and network structure. The time-series for two exemplar networks have been plotted in Appendix C.1, to highlight how differences between networks can occur despite not reaching full synchronisation. Note that for comparison $N_c = 1,000$ was also considered for $P = 3$, with the results given in Appendix C.2.

For each simulation the oscillators were initiated at an equal distance around a unit circle, to ensure the synchronisation of each population was equal and $r(0) = 0$ for all networks. At each timestep the position of oscillator j in population c at time t was updated and the time-series for each Kuramoto population was calculated using [164],

$$s_c(t) = \frac{1}{N_c} \sum_{j=1}^{N_c} \cos\left(\theta_j^c(t)\right). \tag{6.4}$$

The order parameter of population c was defined by,

$$z_c(t) = r_c(t) e^{i\phi_c(t)} = \frac{1}{N_c} \sum_{k=1}^{N_c} e^{i\theta_k^c(t)}. \tag{6.5}$$

6.2.5 Synchrony Measures

After simulating the time-series, global synchronisation was calculated. The level of synchronisation was measured using the time-series directly (Synchronisation Index (SI) and Order Parameter Approach (R)) and via a FN (Node Strength Index (NSI)), which are explained in detail below and outlined in Figure 6.5. SI and R compute synchronisation in different ways. SI considers how local synchronisation in a population changes over the simulations and then averages over populations, while R considers how global synchronisation across populations changes over a simulation and then averages over the simulations. Finally, NSI considers how the mean node strength of FNs, calculated using the simulated time-series (eq 6.4), changes over the simulations and averages over the simulations. Note that node strength was chosen as the basis for a synchronisation measure due to its clear interpretation on three node networks.

6.2.5.1 Synchronisation Index

For each simulated Kuramoto population, the order parameters (eq 6.5) were calculated for each timestep, where $r(t)$ represents how clustered the oscillators in a population are. This was calculated individually for each node $c \in \{1, \ldots, P\}$ and for each simulation $m \in \{1, \ldots, M\}$, where K_{cc} changed for each simulation. By averaging over this time-series, a mean value of synchronisation for population c in simulation m, r_c^m, was produced [135],

$$r_c^m = \frac{1}{L} \sum_{t=1}^{L} r(t), \tag{6.6}$$

where $L = T/dt$ is the number of timepoints in the simulation. The mean of the order parameter, r_c^m, then provides a value in the range $[0, 1]$. A value near 1 means the Kuramoto population quickly synchronised and remained synchronised for most of the simulation while a value near 0 indicates the Kuramoto population remained desynchronised during the time-series and any synchronisation was merely transient disappearing quickly.

Therefore, for each Kuramoto population, a time-series of the synchronisation was

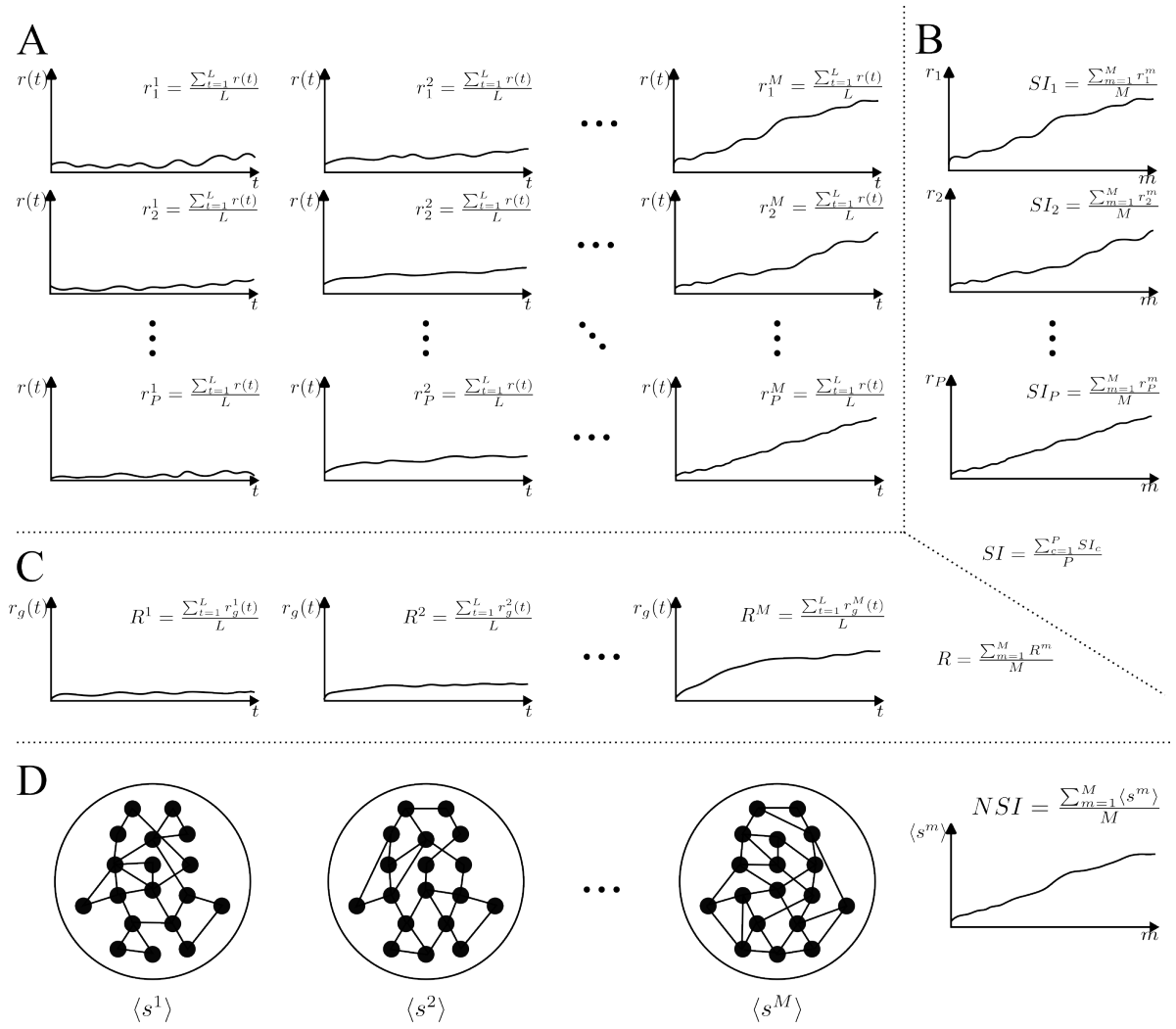


Figure 6.5: **Three Synchrony Measures.** **(A)** For each node $c \in \{1, 2, \ldots, P\}$ and each of the $m \in \{1, 2, \ldots, M\}$ simulations the local order parameter $r(t)$ is plotted, where the r_c^m is the local summary statistic, calculated by averaging $r(t)$ over all L timepoints. **(B)** Plots of how r_c^m changed over m for a given population c, where SI_c is the mean for population c over the simulations and SI is the average over all SI_c. **(C)** Plots of the global order parameter $r_g(t)$ where R^m is the global summary statistic, calculated by averaging $r_g(t)$ over all L timepoints and R is the average of R^m over all simulations **(D)** For simulation m the last 20 s of the simulated time-series for each node is used to calculate the weighted surrogate corrected, directed, order two edge reduced PLF network. For this network, the mean node strength, $\langle s^m \rangle$, is calculated. Then NSI is calculated as the mean of $\langle s^m \rangle$ over all simulations.

created by considering how r_c^m changes over the 19 simulations, see Figure 6.5B. The synchronisation index of population c, SI_c, can then be found by averaging r_c^m over the simulations,

$$SI_c = \frac{\sum_{m=1}^{M} r_c^m}{P}.$$

The synchronisation index, SI, of the network is then found by averaging over the different populations,

$$SI = \frac{\sum_{c=1}^{P} SI_c}{P}$$

Therefore, SI and SI_c give a summary of how the network and a population respectively are affected by changing the local coupling strength at a set global coupling strength.

6.2.5.2 Node Strength Index

Once the time-series for each Kuramoto population has been simulated, each time-series was filtered in a 2 Hz range centred around the simulated mean of 9 Hz. Then the final 20 s of the simulation was used to produce a directed, weighted FN using PLF, which is introduced below in Section 6.2.6. Note that for comparison NSI calculated using the final 30 s was also considered in Appendix C.3 .

The mean node strength, $\langle s^m \rangle$, of each FN from simulation m was then calculated. NSI was then calculated by averaging over the different simulations,

$$NSI = \frac{\sum_{m=1}^{M} \langle s^m \rangle}{M}.$$

Therefore, NSI provides a way to evaluate how the FN, measured from Kuramoto simulations, changes as a function of local coupling strength.

6.2.5.3 Order Parameter Approach

As explained in Section 3.2.1 the local order parameter from each Kuramoto population can be used to calculate a value for the global synchronisation across all P populations as suggested by Meisel et al. [135]. Here the average time-series generated for each Kuramoto population is treated as one of P oscillators on the unit circle and at each timepoint the

global order parameter for simulation m, r_g^m, can be calculated using,

$$r_g^m(t) = \frac{1}{P}\left|\sum_{c=1}^{P} e^{i\theta_c^m(t)}\right|.$$

To produce a summary statistic r_g^m can be averaged over time [135] such that,

$$R^m = \langle r_g^m(t)\rangle = \frac{1}{L}\sum_{t=1}^{L} r_g^m(t).$$

A single statistic of how the increase in local coupling strength affects the synchronisation of the network R can be calculated as the mean of R^m over the 19 simulations,

$$R = \frac{\sum_{m=1}^{M} R^m}{M}.$$

6.2.6 Phase Locking Factor

Phase Locking Factor (PLF) is a technique to estimate FC, where the relation between node j and k is given by [118],

$$\rho_{j,k} = \left|\frac{1}{L}\sum_{t=1}^{L} e^{i(\theta_k(t)-\theta_j(t))}\right|. \tag{6.7}$$

Here $\theta_j(t)$ is the phase angle of signal j at timepoint t. Applying this to each pair of nodes within the network, results in an undirected, weighted adjacency matrix with edge weights in the range $[0, 1]$.

The lag between each pair of signals can be calculated to introduce directedness. The lag between node j and k is calculated using [207]:

$$\eta_{j,k} = \arg\left(\frac{1}{L}\sum_{t=1}^{L} e^{i(\theta_k(t)-\theta_j(t))}\right). \tag{6.8}$$

We set $\rho_{j,k} = 0$ if $\eta_{j,k} \leq 0$ and therefore kept the edges such that there was positive lag. This follows the assumption that if $\eta_{j,k} > 0$ then node j lags behind node k and therefore

the direction of the edge should be from node k to node j. In addition, edges with $\eta_{j,k} = 0$ were removed to avoid zero-lag correlations due to volume conduction [181], whilst not strictly necessary for synthetic networks this ensured the pipeline was consistent with EEG derived FNs.

Therefore, PLF provided a value for the synchronisation between the phases of two oscillators that transverse a complex unit circle. If the phases were perfectly 'locked' on top of each other for all timepoints the argument was 1. However, if the phase of the oscillators become less clustered the argument will decrease such that an argument of 0 occurs for a phase difference of π. This concept is closely linked to synchronisation in Kuramoto model, as introduced in Section 3.2. However, PLF is a pairwise measure for estimating the connectivity between two nodes, and therefore does not provide an estimate of the overall connectivity across all oscillators at once (e.g. multivariate methods).

6.2.7 Graph Metrics

To gain an understanding of which global network properties influence network synchronisation, mean node degree, small world index and trophic incoherence were calculated and correlated to the synchrony measures per K_g value. The small world index can be interpreted as the ease of information flow through a network and is therefore intuitively linked to how global synchronisation will spread in the network [185]. Also, trophic incoherence provides a notion for how directed the edges in a network are, which can indirectly affect how information flows through a network and therefore the global synchronisation of a network, as briefly considered by Rodgers et al. [154]. It is also worth noting that trophic incoherence has been linked to spectral radius [126] which has associations with synchronisation [159].

However, only a limited number of graph metrics are fully defined at the level of three nodes; therefore for $P = 3$, the mean node degree and trophic incoherence were considered. Note that for $P = 18$ the mean node degree was fixed as a result of the Watts-Strogatz method, hence this metric was not calculated.

6.2.8 Statistical Analysis

After the synchronisation measures were calculated, the level of synchronisation was compared to the graph metrics of the FNs. In all cases, Pearson's correlation was used to correlate the synchronisation measure for all participants to the given graph metric. The Benjamini-Hochberg method was used to correct for the problem of multiple comparisons [11].

In addition, for $P = 3$, regression models (linear and multiple) were used to assess the influence of the graph metrics on overall synchronization (as measured by the two different metrics) to better understand the role of trophic incoherence in network synchronisation when mean node degree was allowed to vary.

6.3 Results

6.3.1 Three Node Networks

The Pearson's correlation between the graph metrics and synchronisation measures, as well as the linear and multiple regressions, when $P = 3$, are given below. Note that for comparison $N_c = 1,000$ was also considered for $P = 3$, with the results given in Appendix C.2. The significance for SI did not change, however $K_g = \{1, 1.5\}$ are significant for NSI with $N_c = 1,000$ whilst $K_g = \{0.5, 1, 1.5, 2\}$ for R are no longer significant.

Figure 6.6 is a scatterplot showing the non-significant relationship between trophic incoherence and mean node degree, highlighting they are assessing different properties of the networks. Note that the results for all K_g values are given, however for $K_g \geq 3$ the number of networks considered is reduced due to eq 6.2. Hence, for $K_g = \{5, 5.5\}$ in the multiple regression, there were only three datapoints for two predictors (and an intercept) therefore the degree of freedom is zero and the regression could not be calculated. For $K_g = 6$ there were only two datapoints; so again the regression could not be calculated.

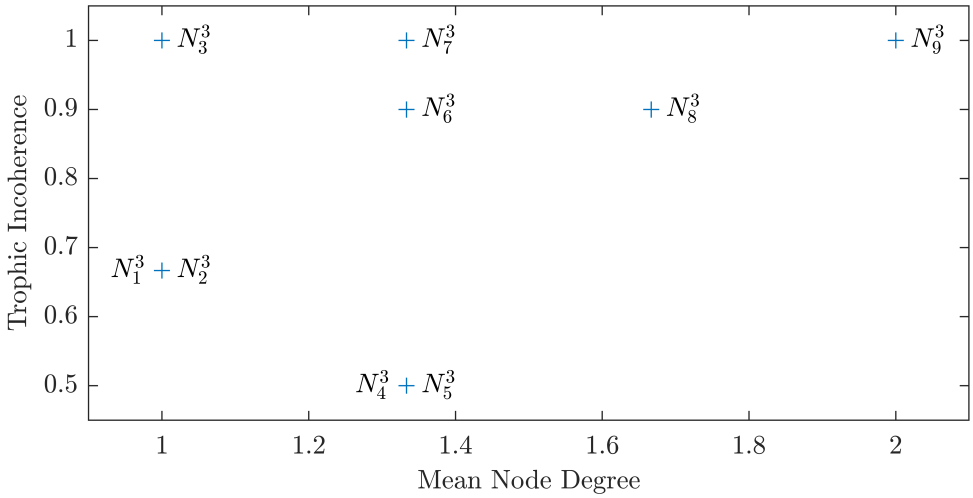


Figure 6.6: **Scatterplot Comparing Mean Node Degree to Trophic Incoherence for Three Node Networks.** The graph metrics for N_1^3 and N_2^3 as well as N_4^3 and N_5^3 are the same. Under Pearson's correlation, the two measures are not significantly correlated, $r_{PC} = 0.3362$ and $p = 0.3763$.

6.3.1.1 Synchronisation Index

The results of correlating SI with mean node degree and trophic incoherence with and without the inclusion of basal node networks are given in Tables 6.2 and 6.3, respectively. In addition, scatterplots of these relations, are given in Figures C.3 and C.4 in the Appendix.

Across the range of the global coupling strengths, we see that trophic incoherence did not significantly correlate with SI, even before correcting for multiple comparisons for the two graph metrics and 12 K_g values. However, we see that for three values of global coupling ($K_g = \{0.5, 1, 1.5\}$) SI correlated with mean node degree. The p-values for mean node degree increase with K_g, this could be because as K_g increases fewer networks were simulated and therefore networks with basal nodes made up a greater proportion of the simulated networks. As basal nodes hinder synchronisation this ultimately reduced the correlation magnitude.

Therefore, the correlations were considered again without the basal node networks N_1^3 and N_4^3. A significant correlation between mean node degree and SI was then also found for $K_g = \{2, 2.5, 3, 3.5, 5, 5.5\}$. Again trophic incoherence did not significantly correlate;

	Trophic Incoherence			Mean Node Degree		
K_g	Correlation	p-value	Adjusted p-value	Correlation	p-value	Adjusted p-value
0.5	0.3537	0.3504	0.3823	0.9667	<0.0001	0.0005*
1	0.5287	0.1434	0.1912	0.9101	0.0007	0.0053*
1.5	0.6335	0.0670	0.1125	0.8426	0.0043	0.0261*
2	0.6337	0.0669	0.1125	0.6998	0.0359	0.0956
2.5	0.6356	0.0658	0.1125	0.5515	0.1237	0.1747
3	0.5959	0.0904	0.1356	0.4455	0.2295	0.2622
3.5	0.5277	0.1789	0.3903	0.2698	0.5181	0.7449
4	0.4926	0.2614	0.4826	0.1112	0.8124	0.9323
4.5	0.4388	0.3840	0.6145	0.0171	0.9743	0.9839
5	0.3542	0.5587	0.7449	-0.1452	0.8158	0.9323
5.5	0.3560	0.5565	0.7449	-0.1474	0.8131	0.9323
6	-0.0161	0.9839	0.9839	0.0161	0.9839	0.9839

Table 6.2: **Correlating SI with Mean Node Degree and Trophic Incoherence.** The Pearson's correlation, p-value and adjusted p-value when comparing SI for each global coupling strength to the mean node degree and trophic incoherence of the network. The p-values were corrected for the range of global coupling strengths as well as the two graph metrics using Benjamini-Hochberg method of correcting for FDR [78]. * denotes significance p-value < 0.05.

indeed the removal of basal nodes actually decreased the magnitude of the correlation for $K_g = \{2, 2.5, 3\}$ by $\sim 20\%$.

To display the difference in the SI values between the networks, normalised synchronisation is displayed in Figure 6.7. For each K_g value SI was divided by the maximum across the networks ensuring a value of synchronisation in the range $[0, 1]$.

In addition, the results of the linear and multiple regressions against SI are given in Tables 6.4 and 6.5, with basal nodes included and excluded respectively. This analysis was completed to assess the contribution of trophic incoherence to network synchronisation. We see that when basal nodes were included, the adjusted R-square was higher for $K_g = \{1, 1.5, 2, 2.5, 3, 3.5, 4\}$ and Sum of Square Errors (SSE) was lower for these global coupling strengths and $K_g = \{4.5, 5, 5.5\}$ when both mean node degree and trophic incoherence were used in the regression compared to just mean node degree. For the three global coupling strengths that had significant multiple regressions ($K_g = \{0.5, 1.1, 5\}$), we see that the adjusted R-square ranges from decreasing by 1.13% to increasing by 12.91% compared to the just mean node degree.

	Trophic Incoherence			Mean Node Degree		
K_g	Correlation	p-value	Adjusted p-value	Correlation	p-value	Adjusted p-value
0.5	0.1878	0.6868	0.7492	0.9825	0.0001	0.0004*
1	0.3103	0.4982	0.6055	0.9870	<0.0001	0.0003*
1.5	0.4195	0.3489	0.5981	0.9830	0.0001	0.0004*
2	0.3731	0.4097	0.6055	0.9752	0.0002	0.0007*
2.5	0.4225	0.3450	0.5981	0.9875	<0.0001	0.0003*
3	0.3059	0.5046	0.6055	0.9959	<0.0001	<0.0001*
3.5	-0.2188	0.6771	0.7492	0.9293	0.0073	0.0195*
4	-0.6953	0.1924	0.4618	0.6139	0.2707	0.5414
4.5	-0.7682	0.2318	0.5057	0.6213	0.3787	0.6055
5	-0.7497	0.4604	0.6055	1.0000	0.0060	0.0181*
5.5	-0.7522	0.4580	0.6055	1.0000	0.0036	0.0123*
6	-1.0000	NaN	NaN	1.0000	NaN	NaN

Table 6.3: **Correlating SI with Mean Node Degree and Trophic Incoherence - No Basal Node Networks.** The Pearson's correlation, p-value and adjusted p-value when comparing SI for each global coupling strength to the mean node degree and trophic incoherence of all networks without a basal node. The p-values were corrected for the range of global coupling strengths as well as the two graph metrics using Benjamini-Hochberg method of correcting for FDR [78]. * denotes significance p-value < 0.05.

When basal nodes were removed, multiple regressions at more global coupling strengths ($K_g = \{0.5, 1, 1.5, 2, 2.5, 3, 3.5\}$) were significant compared to when basal nodes were included. For the seven significant global coupling strengths, the inclusion of trophic incoherence alongside mean node degree had a minimal effect apart from $K_g = 3.5$ where the explained variance increased by 8.78%. However, more global coupling strengths were significant when mean node degree was considered in a linear regression.

		Trophic Incoherence					Mean Node Degree					Trophic Incoherence and Mean Node Degree				
K_g	n	SSE	R-square	Adj R-square	p-value	Adjusted p-value	SSE	R-square	Adj R-square	p-value	Adjusted p-value	SSE	R-square	Adj R-square	p-value	Adjusted p-value
0.5	10,000	0.0020	0.1251	0.0001	0.3659	0.5489	0.0001	0.9345	0.9251	0.0006	0.0046*	0.0001	0.9354	0.9138	0.0007	0.0046*
1	10,000	0.0162	0.2795	0.1766	0.1440	0.3120	0.0039	0.8282	0.8037	0.0007	0.0046*	0.0026	0.8841	0.8455	0.0015	0.0084*
1.5	10,000	0.0331	0.4013	0.3157	0.0707	0.2045	0.0160	0.7100	0.6686	0.0055	0.0238*	0.0084	0.8483	0.7977	0.0052	0.0238*
2	10,000	0.0380	0.4016	0.3161	0.0734	0.2045	0.0324	0.4897	0.4168	0.0393	0.1393	0.0210	0.6687	0.5582	0.0357	0.1392
2.5	10,000	0.0404	0.4040	0.3189	0.0589	0.1914	0.0472	0.3042	0.2048	0.1138	0.2611	0.0317	0.5327	0.3769	0.0938	0.2286
3	10,000	0.0514	0.3551	0.2629	0.0791	0.2057	0.0638	0.1985	0.0840	0.2297	0.4479	0.0460	0.4228	0.2304	0.1793	0.3680
3.5	10,000	0.0644	0.2785	0.1582	0.2684	0.4758	0.0828	0.0728	-0.0817	0.2579	0.4758	0.0601	0.3269	0.0576	0.4461	0.5999
4	5,039	0.0776	0.2426	0.0912	0.3620	0.5489	0.1012	0.01247	-0.1852	0.4287	0.5971	0.0744	0.2737	-0.0894	0.6668	0.7880
4.5	719	0.0835	0.1925	-0.0093	0.5118	0.6564	0.1034	0.00029	-0.2496	0.4006	0.5786	0.0793	0.2330	-0.2783	0.6509	0.7880
5	119	0.0856	0.1254	-0.1661	0.8655	0.9076	0.0958	0.02108	-0.3052	0.9076	0.9076	0.0825	0.1572	-0.6856	0.7395	0.8240
5.5	119	0.0881	0.1267	-0.1643	0.8403	0.9076	0.0987	0.02172	-0.3044	0.9076	0.9076	0.0850	0.1581	-0.6838	0.7359	0.8240
6	23	0.0870	0.0003	-0.4996	0.3478	0.5489	0.0870	0.00026	-0.4996	0.3478	0.5489	0.0944	-0.0848	-2.2544	0.5217	0.6564

Table 6.4: **The Results of the Linear and Multiple Regression Against SI.** The results of the two linear regressions and one multiple regression in terms of the Sum of Square Errors (SSE), R-square and Adjusted R-square (4dp). * denotes significance p-value < 0.05, calculated using non-parametric permutation testing, where $n = \min\{10,000, \bar{n} - 1\}$, where $\bar{n}$ is the number of datapoints, to ensure that the same permutations are not reused when only a few datapoints exist. The p-values were corrected using the Benjamini-Hochberg method of correcting for FDR [78].

		Trophic Incoherence					Mean Node Degree					Trophic Incoherence and Mean Node Degree				
K_g	n	SSE	R-square	Adj R-square	p-value	Adjusted p-value	SSE	R-square	Adj R-square	p-value	Adjusted p-value	SSE	R-square	Adj R-square	p-value	Adjusted p-value
0.5	5,039	0.0017	0.0353	-0.1577	0.6859	0.7262	0.0001	0.9653	0.9584	0.0012	0.0033*	0.0000	0.9789	0.9684	0.0012	0.0033*
1	5,039	0.0128	0.0963	-0.0844	0.5148	0.6177	0.0004	0.9741	0.9690	0.0016	0.0036*	0.0004	0.9742	0.9614	0.0042	0.0079*
1.5	5,039	0.0220	0.1759	0.0111	0.3334	0.4445	0.0009	0.9662	0.9595	< 0.0001	< 0.0001*	0.0005	0.9822	0.9733	0.0008	0.0026*
2	5,039	0.0135	0.1392	-0.0329	0.4120	0.5297	0.0008	0.9511	0.9413	< 0.0001	< 0.0001*	0.0007	0.9575	0.9362	0.0032	0.0064*
2.5	5,039	0.0051	0.1785	0.0142	0.3302	0.4445	0.0002	0.9751	0.9701	0.0016	0.0036*	0.0001	0.9915	0.9872	0.0004	0.0014*
3	5,039	0.0022	0.0936	-0.0877	0.5144	0.6177	0.0000	0.9919	0.9902	0.0016	0.0036*	0.0000	0.9919	0.9878	0.0018	0.0038*
3.5	719	0.0003	0.0479	-0.1902	0.7135	0.7339	0.0000	0.8637	0.8296	< 0.0001	< 0.0001*	0.0000	0.9505	0.9174	0.0111	0.0200*
4	119	0.0001	0.4835	0.3113	0.1176	0.1841	0.0001	0.3769	0.1692	0.1008	0.1650	0.0000	0.7955	0.5909	0.0840	0.1441
4.5	23	0.0000	0.5902	0.3853	0.1304	0.1957	0.0001	0.3860	0.0789	< 0.0001	< 0.0001*	0.0000	0.7365	0.2095	0.2609	0.3757
5	5	0.0000	0.5620	0.1240	0.6000	0.6545	0.0000	0.9999	0.9998	< 0.0001	< 0.0001*	0.0000	1	NaN	0.8000	0.8000
5.5	5	0.0000	0.5658	0.1317	0.6000	0.6545	0.0000	1	0.9999	< 0.0001	< 0.0001*	0.0000	1	NaN	0.6000	0.6545
6	1	NaN	NaN	NaN	NaN	NaN	NaN	NaN	NaN	NaN	NaN	NaN	NaN	NaN	NaN	NaN

Table 6.5: **The Results of the Linear and Multiple Regression Against SI - No Basal Nodes.** The results of the two linear regressions and one multiple regression in terms of the Sum of Square Errors (SSE), R-square and Adjusted R-square (4dp). * denotes significance p-value < 0.05, calculated using non-parametric permutation testing, where $n = \min\{10,000, \bar{n} - 1\}$, where $\bar{n}$ is the number of datapoints, to ensure that the same permutations are not reused when only a few datapoints exist. The p-values were corrected using the Benjamini-Hochberg method of correcting for FDR [78].

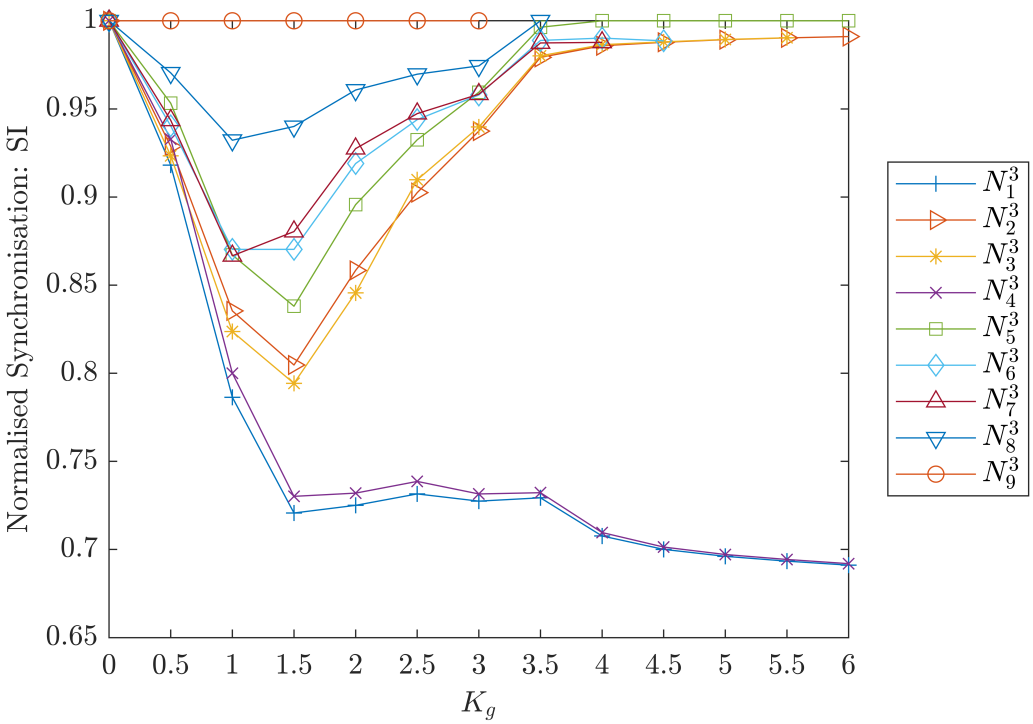


Figure 6.7: **Normalised Synchronisation Index for each Global Coupling Strength.** The SI values have been normalised by the maximum SI per K_g, such that all values are between $[0, 1]$.

6.3.1.2 Node Strength Index

When considering mean node degree we see in Table 6.6 that no significance remains after correcting for multiple comparisons for all the networks. When basal node networks were removed (Table 6.7), the only significant correlation was for $K_g = 3$. Scatterplots of these relations are provided in Figures C.5 and C.6 for mean node degree and trophic incoherence, respectively.

Similarly to SI we see within Tables 6.6 and 6.7 that trophic incoherence did not correlate with the synchronisation measure NSI.

For comparison, NSI was also calculated using the final 30 s of the simulation rather than 20 s in Appendix C.3 - significance was unchanged.

The normalised values of NSI are displayed in Figure 6.8 to show the difference between networks. The quantitatively different nature of the basal node networks was especially clear when using NSI as these two networks saw much lower levels of NSI for most values

	Trophic Incoherence			Mean Node Degree		
K_g	Correlation	p-value	Adjusted p-value	Correlation	p-value	Adjusted p-value
0.5	0.3440	0.3647	0.7294	0.7213	0.0283	0.4525
1	0.5157	0.1553	0.5156	0.6886	0.0403	0.4525
1.5	0.6018	0.0864	0.4525	0.3916	0.2972	0.7134
2	0.5647	0.1131	0.4525	0.3192	0.4025	0.7430
2.5	0.5662	0.1120	0.4525	0.2818	0.4626	0.7622
3	0.5706	0.1086	0.4525	0.2735	0.4764	0.7622
3.5	0.5350	0.1719	0.5156	0.2278	0.5874	0.7832
4	0.5182	0.2334	0.6225	0.0799	0.8647	0.9749
4.5	0.4669	0.3505	0.7294	-0.0167	0.9749	0.9749
5	0.3776	0.5309	0.7787	-0.1779	0.7747	0.9749
5.5	0.3601	0.5516	0.7787	-0.1392	0.8233	0.9749
6	-0.0400	0.9600	0.9749	0.0400	0.9600	0.9749

Table 6.6: **Correlating NSI with Mean Node Degree and Trophic Incoherence.** The Pearson's correlation, p-value and adjusted p-value when comparing NSI for each global coupling strength to the mean node degree and trophic incoherence of the network. The p-values were corrected for the range of global coupling strengths as well as the two graph metrics using Benjamini-Hochberg method of correcting for FDR [78]. * denotes significance p-value < 0.05.

of K_g and even at higher levels of K_g global synchronisation did not occur.

Furthermore, the results of the linear and multiple regressions are given in Table 6.8 when networks with basal nodes are included and Table 6.9 when they are removed. We see that when basal nodes were included none of the regressions were significant. However, when basal nodes were excluded $K_g = \{1, 1.5, 3\}$ were significant for mean node degree but only $K_g = 3$ was significant for the multiple regression. The explained variance was actually lower when trophic incoherence was used in the multiple regression compared to just mean node degree.

	Trophic Incoherence			Mean Node Degree		
K_g	Correlation	p-value	Adjusted p-value	Correlation	p-value	Adjusted p-value
0.5	-0.0012	0.9980	~ 1	0.7721	0.0419	0.1839
1	0.1217	0.7949	0.9343	0.8701	0.0109	0.1268
1.5	0.4920	0.2621	0.4838	0.8483	0.0158	0.1268
2	0.5225	0.2290	0.4579	0.7539	0.0503	0.1839
2.5	0.7470	0.0536	0.1839	0.7278	0.0637	0.1911
3	0.2622	0.5700	0.7201	0.9680	0.0003	0.0083*
3.5	-0.3422	0.5067	0.7164	0.4815	0.3335	0.5717
4	-0.6629	0.2227	0.4579	-0.3722	0.5373	0.7164
4.5	-0.8904	0.1096	0.2631	0.1825	0.8175	0.9343
5	-0.9982	0.0380	0.1839	0.7936	0.4164	0.6662
5.5	-0.9919	0.0811	0.2162	0.6667	0.5354	0.7164
6	-1.0000	NaN	NaN	1.0000	NaN	NaN

Table 6.7: **Correlating NSI with Mean Node Degree and Trophic Incoherence - No Basal Node Networks.** The Pearson's correlation, p-value and adjusted p-value when comparing NSI for each global coupling strength to the mean node degree and trophic incoherence of all networks without a basal node. The p-values were corrected for the range of global coupling strengths as well as the two graph metrics using Benjamini-Hochberg method of correcting for FDR [78]. * denotes significance p-value < 0.05.

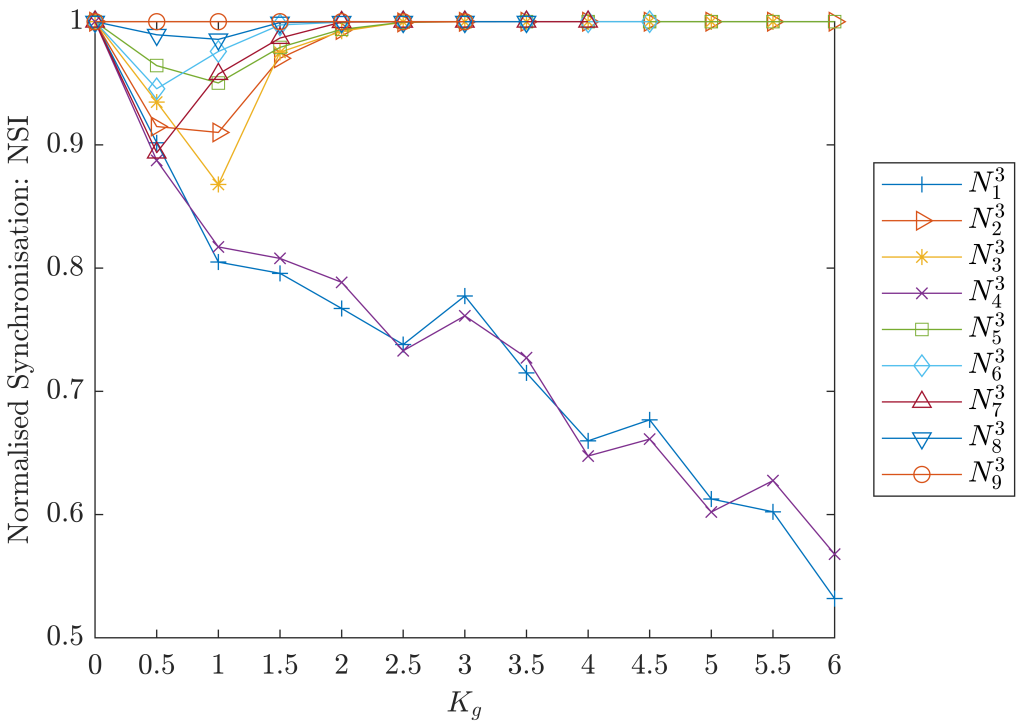


Figure 6.8: **Normalised Node Strength Index for each Global Coupling Strength.** The NSI values have been normalised by the maximum NSI per K_g, such that all values are between $[0, 1]$.

		Trophic Incoherence					Mean Node Degree					Trophic Incoherence and Mean Node Degree				
K_g	n	SSE	R-square	Adj R-square	p-value	Adjusted p-value	SSE	R-square	Adj R-square	p-value	Adjusted p-value	SSE	R-square	Adj R-square	p-value	Adjusted p-value
0.5	10,000	0.0380	0.1183	-0.0076	0.3434	0.5502	0.0207	0.5202	0.4517	0.0211	0.2057	0.0202	0.5318	0.3758	0.1025	0.3634
1	10,000	0.1223	0.2660	0.1611	0.1526	0.4960	0.0876	0.4741	0.3990	0.0388	0.2334	0.0724	0.5652	0.4203	0.0907	0.3634
1.5	10,000	0.1384	0.3622	0.2711	0.0606	0.2954	0.1837	0.1534	0.0324	0.2304	0.5502	0.1296	0.4026	0.2034	0.2172	0.5502
2	10,000	0.2041	0.3189	0.2216	0.0960	0.3634	0.2692	0.1019	-0.0264	0.2602	0.5502	0.1985	0.3378	0.1170	0.3387	0.5502
2.5	10,000	0.2955	0.3206	0.2235	0.0311	0.2334	0.4003	0.0794	-0.0521	0.4934	0.7127	0.2914	0.3300	0.1067	0.3023	0.5502
3	10,000	0.2236	0.3256	0.2292	0.0419	0.2334	0.3067	0.0748	-0.0574	0.4906	0.7127	0.2211	0.3331	0.1108	0.3257	0.5502
3.5	10,000	0.3332	0.2862	0.1673	0.3432	0.5502	0.4426	0.0519	-0.1061	0.3527	0.5502	0.3186	0.3176	0.0446	0.5201	0.7244
4	5,039	0.5016	0.2686	0.1223	0.2715	0.5502	0.6814	0.0064	-0.1923	0.9145	0.9385	0.4866	0.2905	-0.0643	0.6112	0.7449
4.5	719	0.4572	0.2180	0.0225	0.3227	0.5502	0.5846	0.0003	-0.2497	0.7010	0.8284	0.4391	0.2491	-0.2515	0.5953	0.7449
5	119	0.6348	0.1426	-0.1432	0.5714	0.7449	0.7170	0.0316	-0.2911	0.6050	0.7449	0.6169	0.1668	-0.6665	0.9412	0.9412
5.5	119	0.6208	0.1297	-0.1604	0.7731	0.8720	0.6994	0.0194	-0.3075	0.9076	0.9385	0.5940	0.1673	-0.6655	0.8739	0.9385
6	23	0.8118	0.0016	-0.4976	0.3478	0.5502	0.8118	0.0016	-0.4976	0.3478	0.5502	0.9722	-0.1956	-2.5869	0.7826	0.8720

Table 6.8: **The Results of the Linear and Multiple Regression Against NSI.** The results of the two linear regressions and one multiple regression in terms of the Sum of Square Errors (SSE), R-square and Adjusted R-square (4dp). * denotes significance p-value < 0.05, calculated using non-parametric permutation testing, where $n = \min\{10,000, \bar{n} - 1\}$, where $\bar{n}$ is the number of datapoints, to ensure that the same permutations are not reused when only a few datapoints exist. The p-values were corrected using the Benjamini-Hochberg method of correcting for FDR [78].

		Trophic Incoherence					Mean Node Degree					Trophic Incoherence and Mean Node Degree				
K_g	n	SSE	R-square	Adj R-square	p-value	Adjusted p-value	SSE	R-square	Adj R-square	p-value	Adjusted p-value	SSE	R-square	Adj R-square	p-value	Adjusted p-value
0.5	5,039	0.0282	0	-0.2000	0.9931	0.9931	0.0114	0.5961	0.5153	0.0333	0.1091	0.0097	0.6576	0.4863	0.1169	0.2215
1	5,039	0.0492	0.0148	-0.1822	0.8081	0.8312	0.0121	0.7570	0.7084	0.0097	0.0389*	0.0110	0.7795	0.6693	0.0506	0.1215
1.5	5,039	0.0027	0.2421	0.0905	0.2768	0.4746	0.0010	0.7196	0.6635	0.0075	0.0339*	0.0008	0.7799	0.6698	0.0401	0.1121
2	5,039	0.0002	0.2730	0.1276	0.2977	0.4871	0.0001	0.5684	0.4821	0.0405	0.1121	0.0001	0.6630	0.4946	0.1163	0.2215
2.5	5,039	0.0000	0.5581	0.4697	0.0480	0.1215	0.0000	0.5297	0.4357	0.0655	0.1474	0.0000	0.8342	0.7512	0.0274	0.0986
3	5,039	0.0000	0.0687	-0.1175	0.5575	0.6474	0.0000	0.9370	0.9244	0.0008	0.0048*	0.0000	0.9382	0.9073	0.0065	0.0337*
3.5	719	0.0000	0.1171	-0.1036	0.4784	0.5908	0.0000	0.2319	0.0399	0.3505	0.5257	0.0000	0.3780	-0.0367	0.4924	0.5908
4	119	0.0000	0.4394	0.2526	0.2353	0.4235	0.0000	0.1385	-0.1487	0.4034	0.5378	0.0000	0.6228	0.2455	0.4286	0.5510
4.5	23	0.0000	0.7928	0.6892	0.0870	0.1841	0.0000	0.0333	-0.4500	0.6957	0.7366	0.0000	0.8092	0.4277	0.3478	0.5257
5	5	0.0000	0.9964	0.9929	< 0.0001	< 0.0001*	0.0000	0.6299	0.2597	0.4000	0.5378	0.0000	1	NaN	0.6000	0.6545
5.5	5	0.0000	0.9839	0.9677	< 0.0001	< 0.0001*	0.0000	0.4445	-0.1111	0.4000	0.5378	0.0000	1	NaN	0.6000	0.6545
6	1	NaN	NaN	NaN	NaN	NaN	NaN	NaN	NaN	NaN	NaN	NaN	NaN	NaN	NaN	NaN

Table 6.9: **The Results of the Linear and Multiple Regression Against NSI - No Basal Nodes.** The results of the two linear regressions and one multiple regression in terms of the Sum of Square Errors (SSE), R-square and Adjusted R-square (4dp). * denotes significance p-value < 0.05, calculated using non-parametric permutation testing, where $n = \min\{10,000, \bar{n} - 1\}$, where $\bar{n}$ is the number of datapoints, to ensure that the same permutations are not reused when only a few datapoints exist. The p-values were corrected using the Benjamini-Hochberg method of correcting for FDR [78].

6.3.1.3 Order Parameter Approach

The correlations between R, trophic incoherence and mean node degree are given in Table 6.10 and Table 6.11, where basal nodes are included and removed respectively. Scatterplots depicting these relationships are given in Figures C.7 and C.8. We see that mean node degree did significantly correlate with R for $K_g = \{0.5, 1, 1.5, 2\}$ however only when basal nodes were included. Also, we see that trophic incoherence did not significantly correlate for any K_g.

	Trophic Incoherence			Mean Node Degree		
K_g	Correlation	p-value	Adjusted p-value	Correlation	p-value	Adjusted p-value
0.5	0.3485	0.3581	0.6004	0.8569	0.0032	0.0202*
1	0.3754	0.3195	0.5898	0.8542	0.0034	0.0202*
1.5	0.4470	0.2277	0.5418	0.8603	0.0029	0.0202*
2	0.4342	0.2429	0.5418	0.8589	0.0030	0.0202*
2.5	0.6326	0.0675	0.3241	0.5971	0.0895	0.3582
3	0.5470	0.1275	0.4370	0.4213	0.2587	0.5418
3.5	0.4956	0.2117	0.5418	0.3275	0.4284	0.6426
4	0.4842	0.2709	0.5418	0.1834	0.6938	0.8764
4.5	0.4461	0.3752	0.6004	0.0382	0.9428	0.9512
5	0.3503	0.5633	0.7511	-0.1296	0.8355	0.9512
5.5	0.3514	0.5620	0.7511	-0.1300	0.8350	0.9512
6	-0.0488	0.9512	0.9512	0.0488	0.9512	0.9512

Table 6.10: **Correlating R with Mean Node Degree and Trophic Incoherence.** The Pearson's correlation, p-value and adjusted p-value when comparing R for each global coupling strength to the mean node degree and trophic incoherence of the network. The p-values were corrected for the range of global coupling strengths as well as the two graph metrics using Benjamini-Hochberg method of correcting for FDR [78]. * denotes significance p-value < 0.05.

Furthermore, normalised synchronisation, as measured using R is displayed in Figure 6.9. We see that the effect of basal nodes becomes more apparent as K_g increases past $K_g = 2$.

Finally, the results of linear and multiple regressions are given in Table 6.12 and Table 6.13, when basal node networks are included and excluded respectively. We see that after correcting for multiple comparisons only $K_g = 5.5$ (with no basal nodes) was significant. However, only five permutations were used to calculate this p-value therefore the frame-

	Trophic Incoherence			Mean Node Degree		
K_g	Correlation	p-value	Adjusted p-value	Correlation	p-value	Adjusted p-value
0.5	0.3846	0.3943	0.5566	0.8396	0.0181	0.0768
1	0.4015	0.3719	0.5566	0.8357	0.0192	0.0768
1.5	0.3981	0.3764	0.5566	0.8371	0.0188	0.0768
2	0.3985	0.3759	0.5566	0.8421	0.0174	0.0768
2.5	0.4172	0.3517	0.5566	0.8492	0.0156	0.0768
3	0.4149	0.3547	0.5566	0.8542	0.0144	0.0768
3.5	0.2952	0.5701	0.7601	0.8261	0.0427	0.1465
4	0.2291	0.7109	0.8125	0.7496	0.1447	0.4340
4.5	-0.0484	0.9516	1.0381	0.6868	0.3132	0.5566
5	-0.9264	0.2457	0.5566	0.4539	0.7001	0.8125
5.5	-0.9201	0.2563	0.5566	0.4390	0.7107	0.8125
6	1.0000	NaN	NaN	-1.0000	NaN	NaN

Table 6.11: **Correlating R with Mean Node Degree and Trophic Incoherence - No Basal Node Networks.** The Pearson's correlation, p-value and adjusted p-value when comparing R for each global coupling strength to the mean node degree and trophic incoherence of all networks without a basal node. The p-values were corrected for the range of global coupling strengths as well as the two graph metrics using Benjamini-Hochberg method of correcting for FDR [78]. * denotes significance p-value < 0.05.

work to evaluate significance may not be optimised for small numbers of networks. For $K_g = \{0.5, 1, 1.5, 2\}$, the inclusion of trophic incoherence lowered the adjusted R-square for the multiple regression compared to the linear regression with just mean node degree.

		Trophic Incoherence					Mean Node Degree					Trophic Incoherence and Mean Node Degree				
K_g	n	SSE	R-square	Adj R-square	p-value	Adjusted p-value	SSE	R-square	Adj R-square	p-value	Adjusted p-value	SSE	R-square	Adj R-square	p-value	Adjusted p-value
0.5	10,000	0.0079	0.1214	-0.0041	0.3539	0.5751	0.0024	0.7342	0.6962	0.0019	0.0124*	0.0024	0.7383	0.6511	0.0215	0.0839
1	10,000	0.0020	0.1409	0.0182	0.3125	0.5394	0.0006	0.7297	0.6910	0.0025	0.0139*	0.0006	0.7384	0.6512	0.0241	0.0854
1.5	10,000	0.0010	0.1998	0.0855	0.2228	0.5254	0.0003	0.7400	0.7029	0.0009	0.0088*	0.0003	0.7681	0.6908	0.0158	0.0770
2	10,000	0.0006	0.1885	0.0726	0.2393	0.5254	0.0002	0.7377	0.7002	0.0019	0.0124*	0.0002	0.7615	0.6820	0.0182	0.0789
2.5	10,000	0.0015	0.4001	0.3145	0.0676	0.2197	0.0016	0.3566	0.2647	0.0787	0.2265	0.0011	0.5668	0.4224	0.0813	0.2265
3	10,000	0.0140	0.2992	0.1991	0.1197	0.3112	0.0164	0.1775	0.0600	0.2425	0.5254	0.0127	0.3628	0.1504	0.2637	0.5394
3.5	10,000	0.0485	0.2456	0.1199	0.2838	0.5394	0.0574	0.1073	-0.0415	0.3181	0.5394	0.0434	0.3246	0.0544	0.4337	0.6604
4	5,039	0.0640	0.2344	0.0813	0.3175	0.5394	0.0808	0.0336	-0.1596	0.4572	0.6604	0.0589	0.2959	-0.0561	0.5398	0.7259
4.5	719	0.0923	0.1990	-0.0012	0.4562	0.6604	0.1151	0.0015	-0.2482	0.5007	0.6974	0.0864	0.2505	-0.2491	0.5841	0.7594
5	119	0.0963	0.1227	-0.1697	0.7395	0.8482	0.1080	0.0168	-0.3109	0.8067	0.8739	0.0921	0.1616	-0.6768	0.9412	0.9565
5.5	119	0.1162	0.1235	-0.1687	0.7395	0.8482	0.1304	0.0169	-0.3108	0.8067	0.8739	0.1111	0.1626	-0.6746	0.9412	0.9565
6	23	0.1101	0.0024	-0.4964	0.6957	0.8478	0.1101	0.0024	-0.4964	0.6957	0.8478	0.2291	-1.0763	-5.2289	0.9565	0.9565

Table 6.12: **The Results of the Linear and Multiple Regression Against R.** The results of the two linear regressions and one multiple regression in terms of the Sum of Square Errors (SSE), R-square and Adjusted R-square (4dp). * denotes significance p-value < 0.05, calculated using non-parametric permutation testing, where $n = \min\{10,000, \bar{n} - 1\}$, where $\bar{n}$ is the number of datapoints, to ensure that the same permutations are not reused when only a few datapoints exist. The p-values were corrected using the Benjamini-Hochberg method of correcting for FDR [78].

		Trophic Incoherence					Mean Node Degree					Trophic Incoherence and Mean Node Degree				
K_g	n	SSE	R-square	Adj R-square	p-value	Adjusted p-value	SSE	R-square	Adj R-square	p-value	Adjusted p-value	SSE	R-square	Adj R-square	p-value	Adjusted p-value
0.5	5,039	0.0068	0.1479	-0.0225	0.4001	0.4967	0.0023	0.7049	0.6459	0.0171	0.0622	0.0022	0.7233	0.5849	0.0738	0.1563
1	5,039	0.0017	0.1612	-0.0065	0.3790	0.4967	0.0006	0.6984	0.6381	0.0167	0.0622	0.0006	0.7223	0.5834	0.0732	0.1563
1.5	5,039	0.0008	0.1585	-0.0098	0.3786	0.4967	0.0003	0.7008	0.6409	0.0167	0.0622	0.0003	0.7234	0.5851	0.0728	0.1563
2	5,039	0.0005	0.1588	-0.0094	0.3804	0.4967	0.0002	0.7092	0.6510	0.0173	0.0622	0.0002	0.7315	0.5973	0.0687	0.1563
2.5	5,039	0.0003	0.1741	0.0089	0.3667	0.4967	0.0001	0.7211	0.6653	0.0099	0.0595	0.0001	0.7489	0.6233	0.0579	0.1563
3	5,039	0.0002	0.1721	0.0066	0.3659	0.4967	0.0000	0.7296	0.6755	0.0071	0.0514	0.0000	0.7561	0.6341	0.0550	0.1563
3.5	719	0.0001	0.0871	-0.1411	0.5396	0.6476	0.0000	0.6824	0.6030	0.0501	0.1563	0.0000	0.7351	0.5584	0.1349	0.2698
4	119	0.0001	0.0525	-0.2634	0.7059	0.7701	0.0000	0.5618	0.4158	0.2017	0.3457	0.0000	0.6469	0.2939	0.3950	0.4967
4.5	23	0.0000	0.0023	-0.4965	≈1	≈1	0.0000	0.4717	0.2075	0.3478	0.4967	0.0000	0.5106	-0.4683	0.6957	0.7701
5	5	0.0000	0.8583	0.7166	0.2000	0.3457	0.0000	0.2060	-0.5880	0.8000	0.8229	0.0000	1	NaN	0.6000	0.6968
5.5	5	0.0000	0.8465	0.6930	0.2000	0.3457	0.0000	0.1927	-0.6145	0.8000	0.8229	0.0000	1	NaN	< 0.0001	< 0.0001*
6	1	NaN	NaN	NaN	NaN	NaN	NaN	NaN	NaN	NaN	NaN	NaN	NaN	NaN	NaN	NaN

Table 6.13: **The Results of the Linear and Multiple Regression Against R - No Basal Nodes.** The results of the two linear regressions and one multiple regression in terms of the Sum of Square Errors (SSE), R-square and Adjusted R-square (4dp). * denotes significance p-value < 0.05, calculated using non-parametric permutation testing, where $n = \min\{10,000, \bar{n} - 1\}$, where $\bar{n}$ is the number of datapoints, to ensure that the same permutations are not reused when only a few datapoints exist. The p-values were corrected using the Benjamini-Hochberg method of correcting for FDR [78].

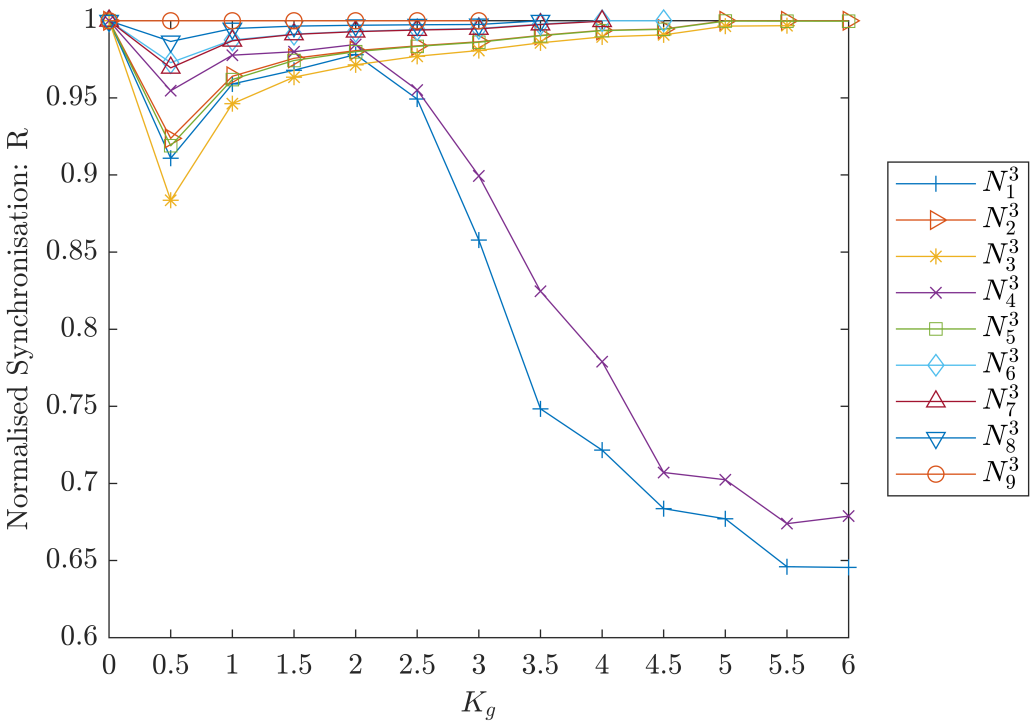


Figure 6.9: **Normalised R for each Global Coupling Strength.** The R values have been normalised by the maximum R per K_g, such that all values per K_g are between $[0, 1]$.

6.3.2 18 Node Networks: Mean Node Degree Three

The results of correlating the three synchronisation measures with trophic incoherence and small world index for $P = 18$ and $\langle k \rangle = 3$ are given below. Figure 6.10 shows a significant relationship between trophic incoherence and small world index. Note that $K_g \leq 12$ due to eq 6.2.

6.3.2.1 Synchronisation Index

Table 6.14 shows the results of correlating both graph metrics individually with SI. In addition, for each global coupling strength, a scatterplot of the relationship between trophic incoherence and small world index with SI is given in Figures 6.11 and 6.12 respectively.

From Table 6.14, we see that trophic incoherence significantly correlated with SI for all K_g values with a very strong positive correlation for all K_g. For the small world index

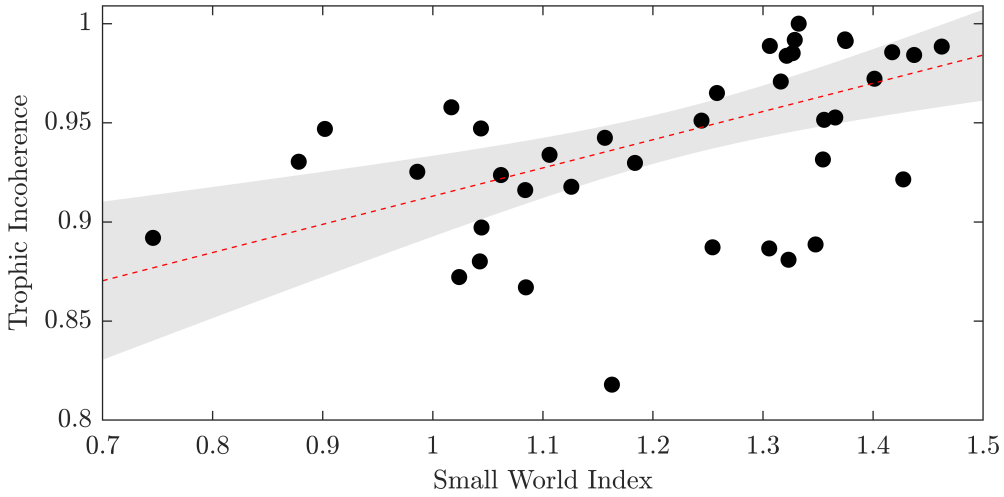


Figure 6.10: **Scatterplot Comparing Small World Index to Trophic Incoherence for 18 Node Networks with Mean Node Degree 3.** Under Pearson's correlation the two measures are significantly correlated, $r_{PC} = 0.5199$ and $p = 0.0003$. For all plots a black dot represents a network, the red dashed line is the linear fit between the two variables and the grey patch represents the 95% confidence interval.

there was a significant correlation for all K_g except $K_g = 1$. However, the effect size of the correlation with the small world index was ~ 40% lower than trophic incoherence for almost all K_g.

When considering the scatterplots in Figure 6.11 we see for $5 \leq K_g \leq 10$ a clear monotonic relationship. However, there were some networks with a trophic incoherence near 0.9 where the SI values span a large range despite only slight differences in trophic incoherence. For instance, two points have a percentage difference of 0.58% in trophic incoherence but for $7 \leq K_g \leq 12$ SI differs by a minimum of 2.55%. This indicates there could be a change in dynamics occurring at $q = 0.9$ or that a different topological feature was affecting synchronisation. However, with a limited number of datapoints near $q = 0.9$, it is difficult to know.

	Trophic Incoherence			Small World Index		
K_g	Correlation	p-value	Adjusted p-value	Correlation	p-value	Adjusted p-value
1	0.5228	0.0005	0.0008*	0.2925	0.0635	0.0635
2	0.8294	<0.0001	<0.0001*	0.4913	0.0011	0.0013*
3	0.8370	<0.0001	<0.0001*	0.4770	0.0016	0.0018*
4	0.9042	<0.0001	<0.0001*	0.4024	0.0091	0.0095*
5	0.9829	<0.0001	<0.0001*	0.5194	0.0005	0.0009*
6	0.9885	<0.0001	<0.0001*	0.4990	0.0009	0.0011*
7	0.9799	<0.0001	<0.0001*	0.5297	0.0004	0.0007*
8	0.9783	<0.0001	<0.0001*	0.4967	0.0010	0.0011*
9	0.9669	<0.0001	<0.0001*	0.5111	0.0006	0.0010*
10	0.9678	<0.0001	<0.0001*	0.5074	0.0007	0.0010*
11	0.9640	<0.0001	<0.0001*	0.5042	0.0008	0.0010*
12	0.9613	<0.0001	<0.0001*	0.5038	0.0008	0.0010*

Table 6.14: **Pearson's Correlations Between SI with Small World Index and Trophic Incoherence: Mean Node Degree Three.** The Pearson's correlation, p-value and adjusted p-value when comparing SI for each global coupling strength to the small world index and trophic incoherence of the network. The p-values were corrected for the range of global coupling strengths as well as the two graph metrics using Benjamini-Hochberg method of correcting for FDR [78]. * denotes significance p-value < 0.05.

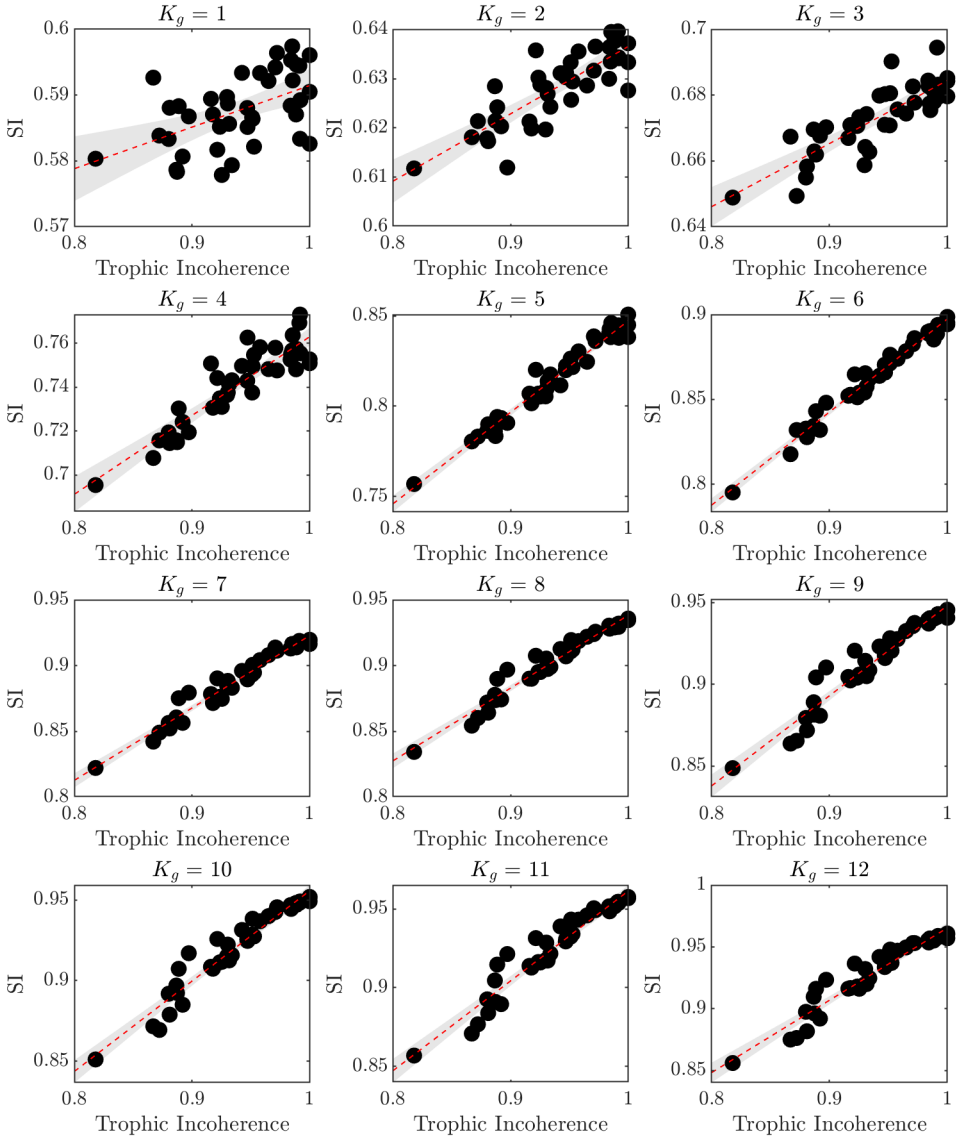


Figure 6.11: **Scatterplots Showing the Relationship Between Trophic Incoherence and SI: Mean Node Degree Three.**

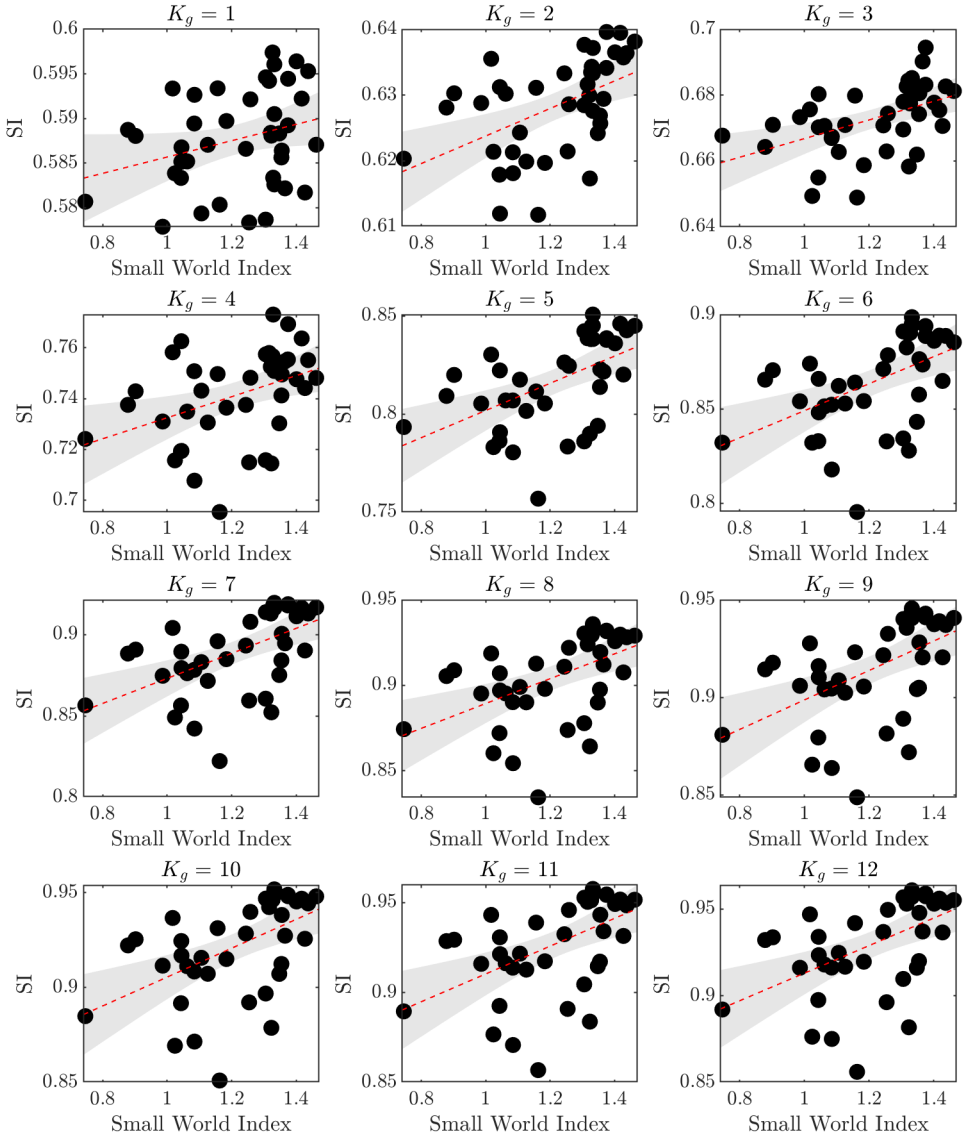


Figure 6.12: **Scatterplots Showing the Relationship Between Small World Index and SI: Mean Node Degree Three.**

6.3.2.2 Node Strength Index

Table 6.15 shows the results of correlating NSI with the two graph metrics for each K_g value, scatterplots corresponding to each correlation are given in Figures 6.13 and 6.14 for trophic incoherence and small world index respectively.

	Trophic Incoherence			Small World Index		
K_g	Correlation	p-value	Adjusted p-value	Correlation	p-value	Adjusted p-value
1	0.4159	0.0068	0.0164*	0.3846	0.0130	0.0277*
2	0.2454	0.1220	0.1464	0.1001	0.5335	0.5335
3	0.3023	0.0547	0.0691	0.1448	0.3663	0.3822
4	0.4914	0.0011	0.0029*	0.1471	0.3587	0.3822
5	0.8220	<0.0001	<0.0001*	0.3058	0.0518	0.0691
6	0.7804	<0.0001	<0.0001*	0.2017	0.2060	0.2354
7	0.8239	<0.0001	<0.0001*	0.3111	0.0477	0.0674
8	0.8356	<0.0001	<0.0001*	0.3434	0.0279	0.0447*
9	0.8571	<0.0001	<0.0001*	0.3717	0.0167	0.0309*
10	0.8492	<0.0001	<0.0001*	0.3598	0.0209	0.0358*
11	0.8766	<0.0001	<0.0001*	0.3816	0.0138	0.0277*
12	0.8337	<0.0001	<0.0001*	0.3374	0.0310	0.0465*

Table 6.15: **Pearson's Correlations Between NSI with Small World Index and Trophic Incoherence: Mean Node Degree Three.** The Pearson's correlation, p-value and adjusted p-value when comparing NSI for each global coupling strength to the small world index and trophic incoherence of the network. The p-values were corrected for the range of global coupling strengths as well as the two graph metrics using Benjamini-Hochberg method of correcting for FDR [78]. * denotes significance p-value < 0.05.

We see that for all values of K_g except $K_g = \{2, 3\}$ there was a significant relationship between trophic incoherence and NSI. However, for small world index, after correcting for multiple comparisons significance only remained for $K_g = \{1, 8, 9, 10, 11, 12\}$, with an effect size $\sim 50\%$ lower than trophic incoherence for $K_g = \{8, 9, 10, 11, 12\}$. In the scatterplots, similar to Figure 6.11, the behaviours seemed to change near $q = 0.9$, with a sharp increase in NSI before levelling off. As this relationship appears more monotonic than linear, Spearman's rank was also calculated; while the magnitude of the correlation increases the significance for trophic incoherence did not change. Within Figure 6.14 there were some networks which seem to be far away from the linear fit. To understand if these networks consistently differ from the linear fit across the synchrony measures an

investigation to how much the simulated value for synchronisation differs from the linear fit was completed in Appendix C.5. There were some networks typically with $p_{ws} \geq 0.15$ that were visually further away from the linear fit. However, only network 25 would be considered an outlier despite neither its level of trophic incoherence nor its small-worldness being extreme across the networks.

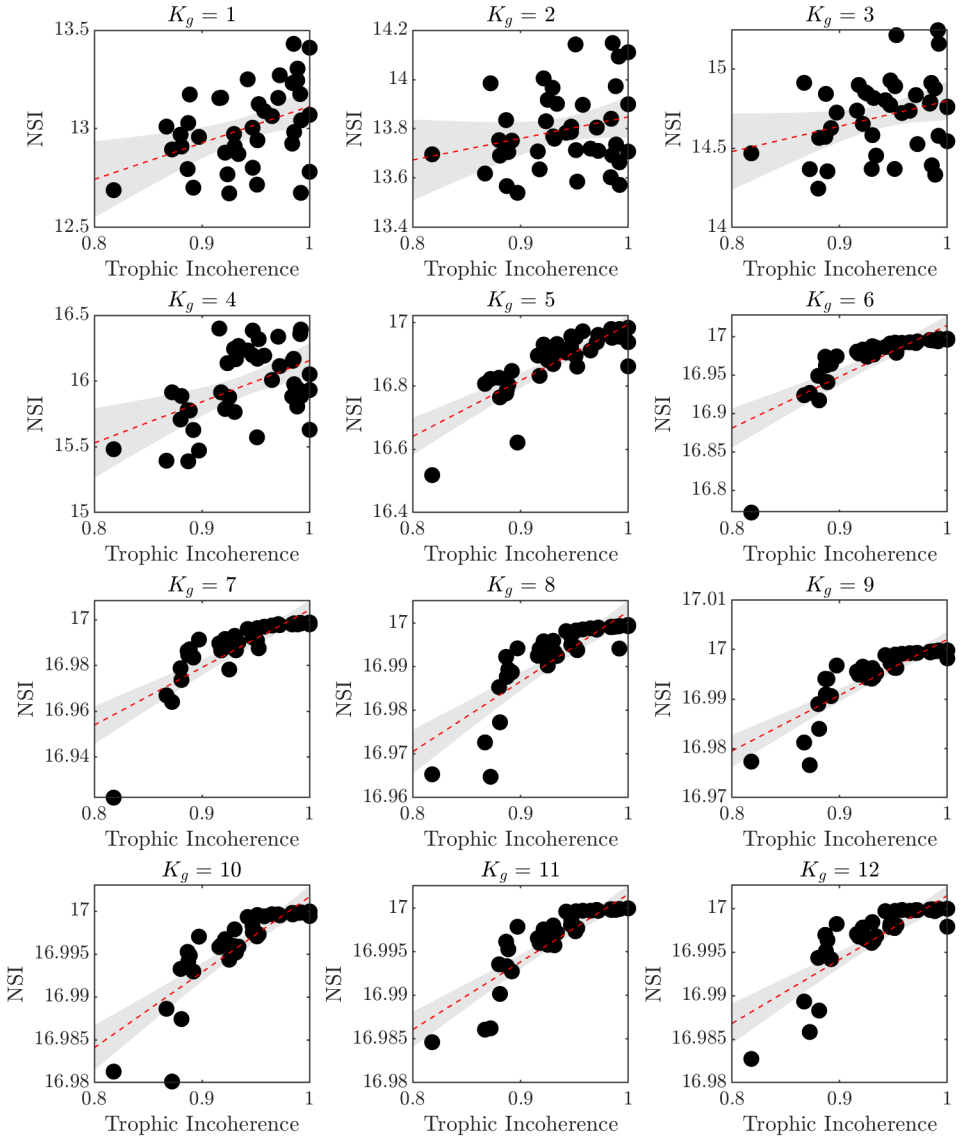


Figure 6.13: **Scatterplots Showing the Relationship Between Trophic Incoherence and NSI: Mean Node Degree Three.**

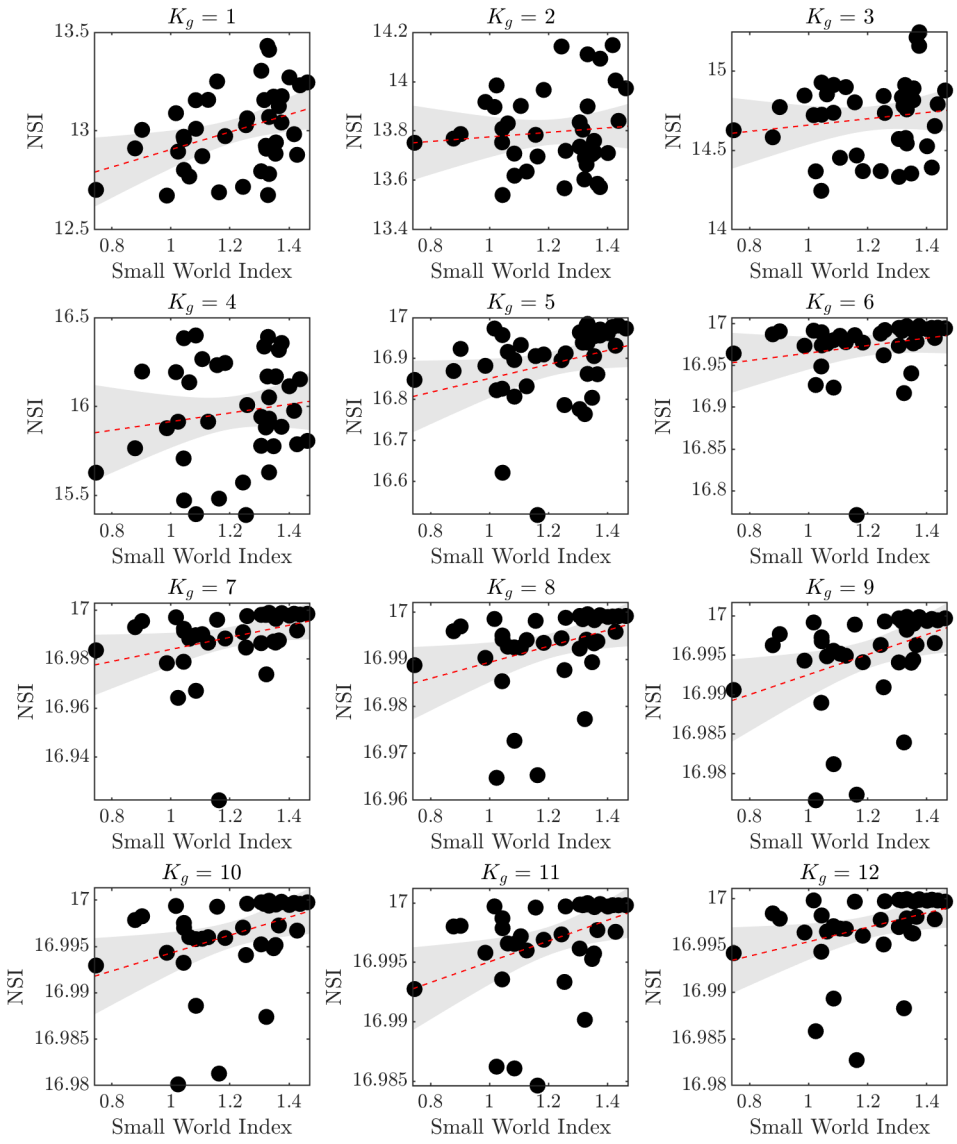


Figure 6.14: **Scatterplots Showing the Relationship Between Small World Index and NSI: Mean Node Degree Three.**

6.3.2.3 Order Parameter Approach

Table 6.16 shows the results for correlating the graph metrics with R. We see that for all K_g values trophic incoherence significantly correlates with R. Also, at $K_g = \{2, 3, 9, 10, 11, 12\}$ small world index significantly correlates with R. In general, the effect size for trophic incoherence was ~ 30% higher than for the small world index. The relations between the graph metrics and R are depicted in Figures 6.15 and 6.16.

	Trophic Incoherence			Small World Index		
K_g	Correlation	p-value	Adjusted p-value	Correlation	p-value	Adjusted p-value
1	0.4226	0.0059	0.0118*	-0.0002	0.9990	0.9990
2	0.5913	<0.0001	0.0002*	0.4442	0.0036	0.0087*
3	0.3602	0.0207	0.0310*	0.3732	0.0162	0.0260*
4	0.4887	0.0012	0.0036*	0.1695	0.2894	0.3020
5	0.3769	0.0151	0.0259*	0.1714	0.2839	0.3020
6	0.5637	0.0001	0.0004*	0.1801	0.2598	0.2970
7	0.6871	<0.0001	<0.0001*	0.3102	0.0484	0.0611
8	0.4532	0.0029	0.0078*	0.2903	0.0656	0.0787
9	0.7005	<0.0001	<0.0001*	0.3841	0.0132	0.0243*
10	0.7950	<0.0001	<0.0001*	0.4238	0.0058	0.0118*
11	0.6328	<0.0001	<0.0001*	0.3204	0.0411	0.0548*
12	0.7728	<0.0001	<0.0001*	0.3423	0.0285	0.0402*

Table 6.16: **Pearson's Correlations Between R with Small World Index and Trophic Incoherence: Mean Node Degree Three.** The Pearson's correlation, p-value and adjusted p-value when comparing R for each global coupling strength to the small world index and trophic incoherence of the network. The p-values were corrected for the range of global coupling strengths as well as the two graph metrics using Benjamini-Hochberg method of correcting for FDR [78]. * denotes significance p-value < 0.05.

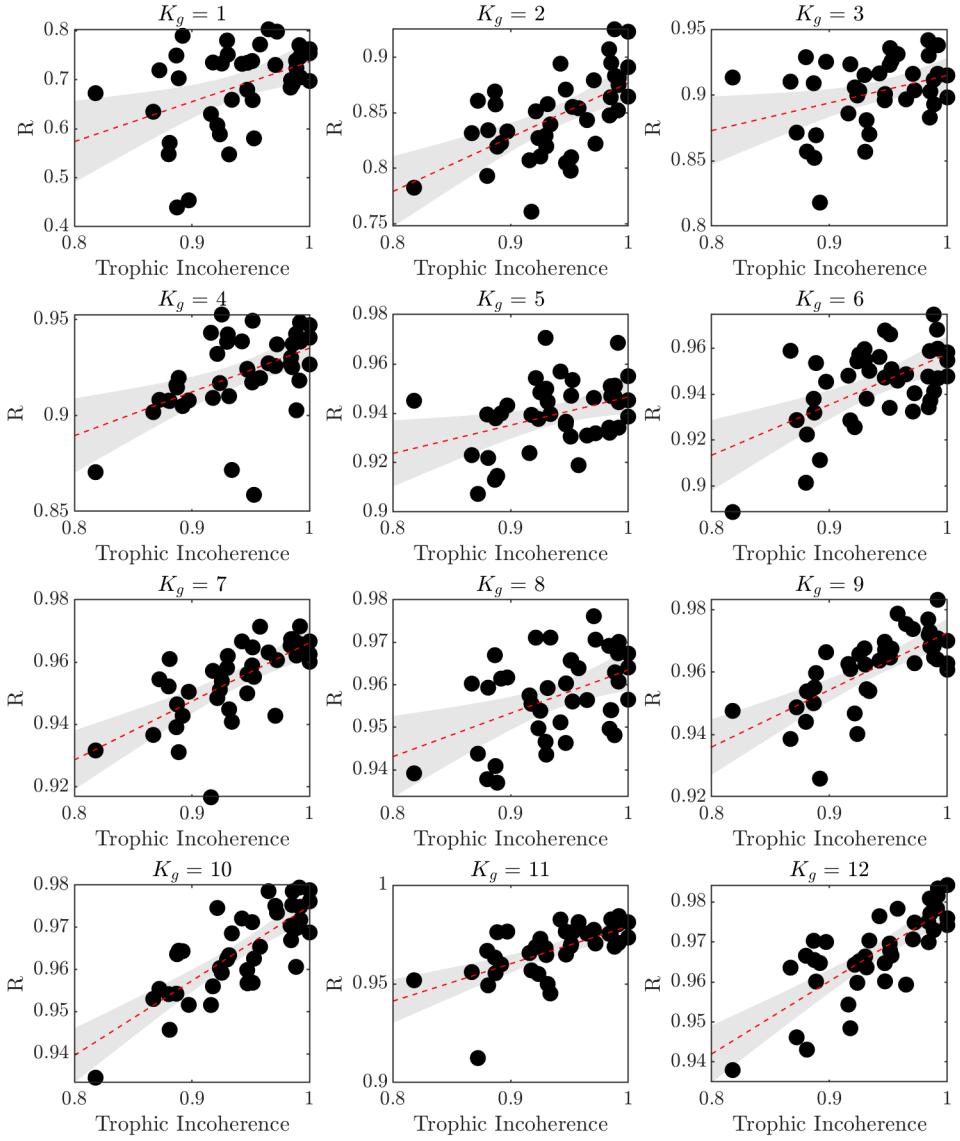


Figure 6.15: **Scatterplots Showing the Relationship Between Trophic Incoherence and R: Mean Node Degree Three.**

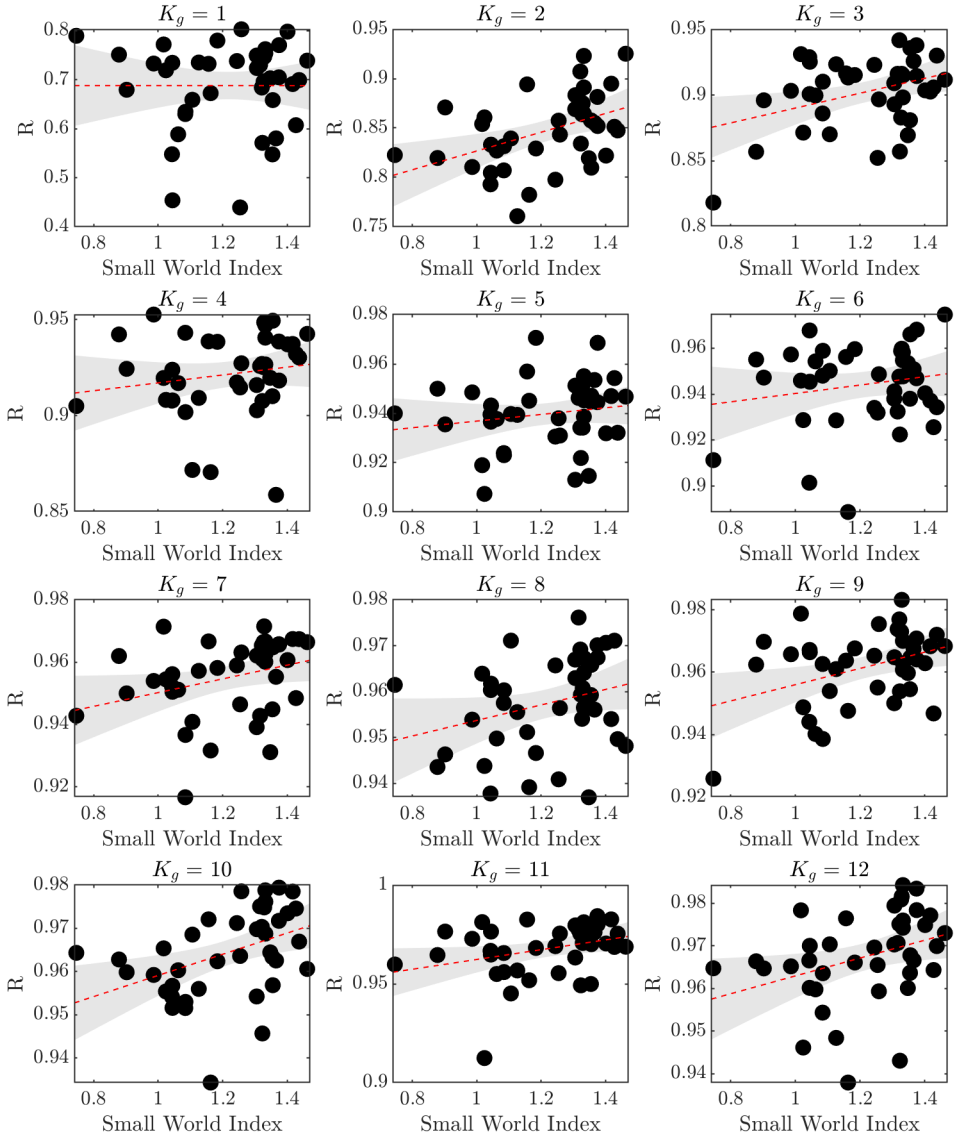


Figure 6.16: **Scatterplots Showing the Relationship Between Small World Index and R: Mean Node Degree Three.**

6.3.3 18 Node Networks: Mean Node Degree Four

The results of correlating the three synchronisation measures with the two graph metrics for $P = 18$ and $\langle k \rangle = 4$ are given below. Also, Figure 6.17 shows a significant relationship between trophic incoherence and small world index. Note that $K_g \leq 9$ due to eq 6.2.

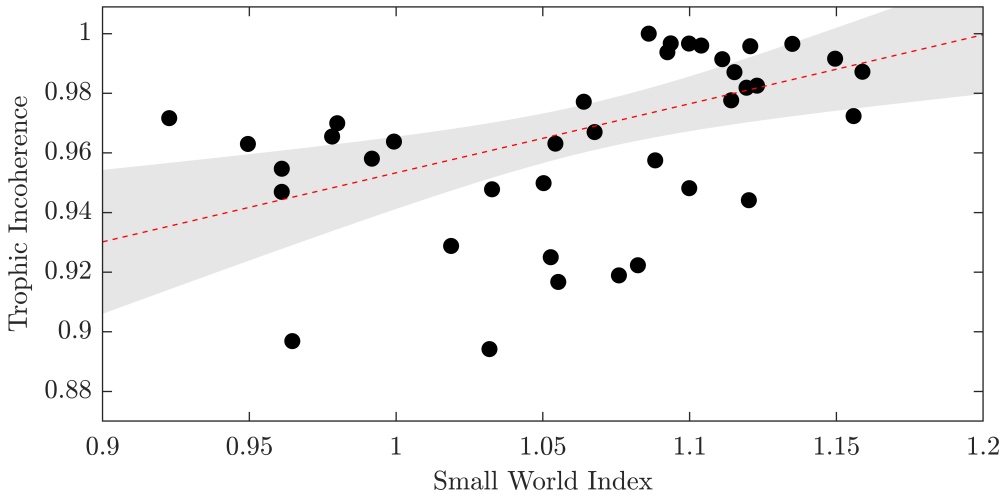


Figure 6.17: **Scatterplot Comparing Small World Index to Trophic Incoherence for 18 Node Networks: Mean Node Degree Four.** Under Pearson's correlation the two measures are significantly correlated, $r_{PC} = 0.4624$ and $p = 0.0014$.

6.3.3.1 Synchronisation Index

We see in Table 6.17 that across all the K_g values and the two graph metrics all Pearson's correlations were considered significant for trophic incoherence and that only $K_g = \{1, 2\}$ were non-significant for small world index. Both the correlation values and the p-values show very similar trends to the $\langle k \rangle = 3$ case. Also, similarly to the $\langle k \rangle = 3$ case (Table 6.14) the effect size for the small world index was $\sim$ 40% lower compared to trophic incoherence.

Also, the individual relationship between SI and trophic incoherence and small world index for each K_g value are displayed in Figures 6.18 and 6.19 respectively. Similar to Figure 6.11 we see an almost linear relation past $K_g = 4$ between trophic incoherence and SI. Also, within Figure 6.19 there were some networks which were far away from the

	Trophic Incoherence			Small World Index		
K_g	Correlation	p-value	Adjusted p-value	Correlation	p-value	Adjusted p-value
1	0.5169	0.0005	0.0011^*	0.1315	0.4123	0.4123
2	0.8131	< 0.0001	$< 0.0001^*$	0.2978	0.0587	0.0621
3	0.8732	< 0.0001	$< 0.0001^*$	0.4500	0.0032	0.0057^*
4	0.9600	< 0.0001	$< 0.0001^*$	0.4079	0.0081	0.0097^*
5	0.9926	< 0.0001	$< 0.0001^*$	0.4320	0.0048	0.0072^*
6	0.9878	< 0.0001	$< 0.0001^*$	0.4380	0.0042	0.0068^*
7	0.9789	< 0.0001	$< 0.0001^*$	0.4255	0.0056	0.0081^*
8	0.9776	< 0.0001	$< 0.0001^*$	0.4280	0.0052	0.0082^*
9	0.9598	< 0.0001	$< 0.0001^*$	0.3981	0.0099	0.0112^*

Table 6.17: **Pearson's Correlations Between SI with Small World Index and Trophic Incoherence: Mean Node Degree Four.** The Pearson's correlation, p-value and adjusted p-value when comparing SI for each global coupling strength to the small world index and trophic incoherence of the network. The p-values were corrected for the range of global coupling strengths and the two graph metrics using Benjamini-Hochberg method of correcting for FDR [78]. * denotes significance p-value < 0.05.

linear fit. Within Appendix C.5 we investigated if there was a consistency to which networks were further away from the linear fit across the graph metrics and synchronisation measures. Some networks, particularly those with $p_{ws} = 0.45$, were visually further away from the linear fit, however as seen in Appendix C.5 no networks were considered outliers.

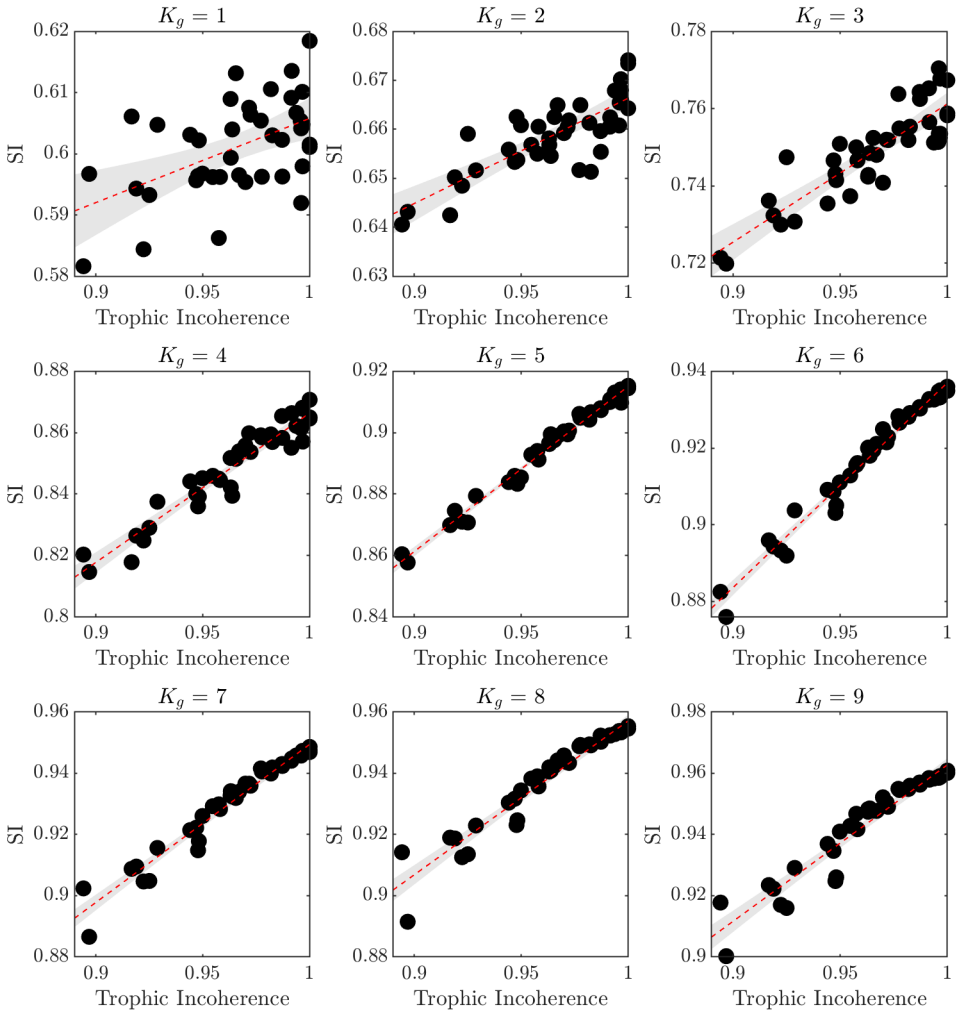


Figure 6.18: **Scatterplots Showing the Relationship Between Trophic Incoherence and SI: Mean Node Degree Four.**

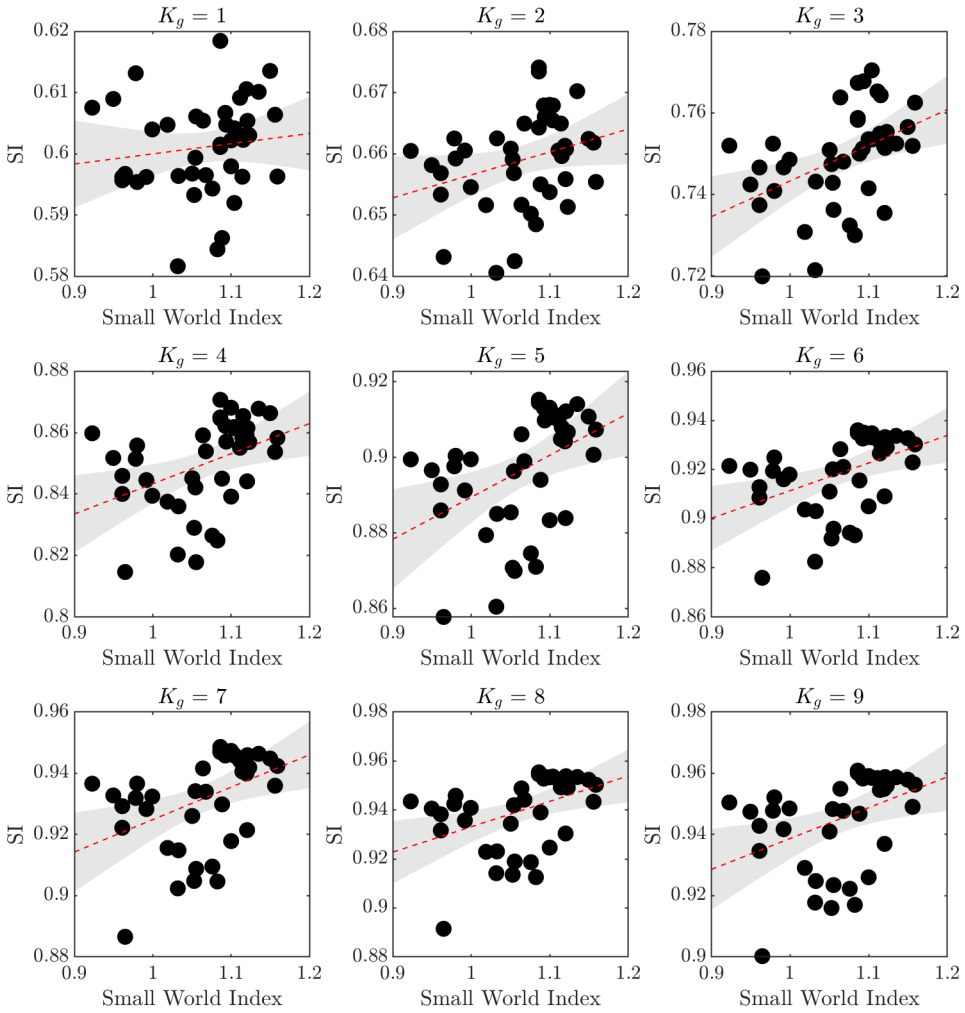


Figure 6.19: **Scatterplots Showing the Relationship Between Small World Index and SI: Mean Node Degree Four.**

6.3.3.2 Node Strength Index

Table 6.18 shows the results of correlating the two graph metrics with NSI for each K_g value. We see that trophic incoherence significantly correlates with NSI for all K_g except $K_g = 3$, which was similar to the results for the trophic coherence in the $\langle k \rangle = 3$ case, as seen in Table 6.15. However, the small world index did not significantly correlate with NSI for any global coupling strength, unlike the $\langle k \rangle = 3$ case. The Pearson's correlation was a lower magnitude compared to the $\langle k \rangle = 3$ case for the small world index, hindering a significant relationship.

	Trophic Incoherence			Small World Index		
K_g	Correlation	p-value	Adjusted p-value	Correlation	p-value	Adjusted p-value
1	0.4720	0.0018	0.0049*	0.0806	0.6164	0.6526
2	0.4279	0.0053	0.0120*	0.0914	0.5697	0.6409
3	0.1614	0.3135	0.3858	0.0037	0.9819	0.9819
4	0.7955	< 0.0001	< 0.0001*	0.2370	0.1357	0.1879
5	0.8351	< 0.0001	< 0.0001*	0.2495	0.1157	0.1879
6	0.8217	< 0.0001	< 0.0001*	0.2922	0.0637	0.1275
7	0.8118	< 0.0001	< 0.0001*	0.2494	0.1158	0.1879
8	0.7641	< 0.0001	< 0.0001*	0.2457	0.1215	0.1879
9	0.7084	< 0.0001	< 0.0001*	0.1836	0.2507	0.3223

Table 6.18: **Pearson's Correlations Between NSI with Small World Index and Trophic Incoherence: Mean Node Degree Four.** The Pearson's correlation, p-value and adjusted p-value when comparing SI for each global coupling strength to the small world index and trophic incoherence of the network. The p-values were corrected for the range of global coupling strengths as well as the two graph metrics using Benjamini-Hochberg method of correcting for FDR [78]. * denotes significance p-value < 0.05.

Furthermore, the relationships between NSI and trophic incoherence and small world index are displayed in Figures 6.20 and 6.21 respectively. For trophic incoherence most networks have a monotonic relationship with NSI, however for small world index this relationship is less clear.

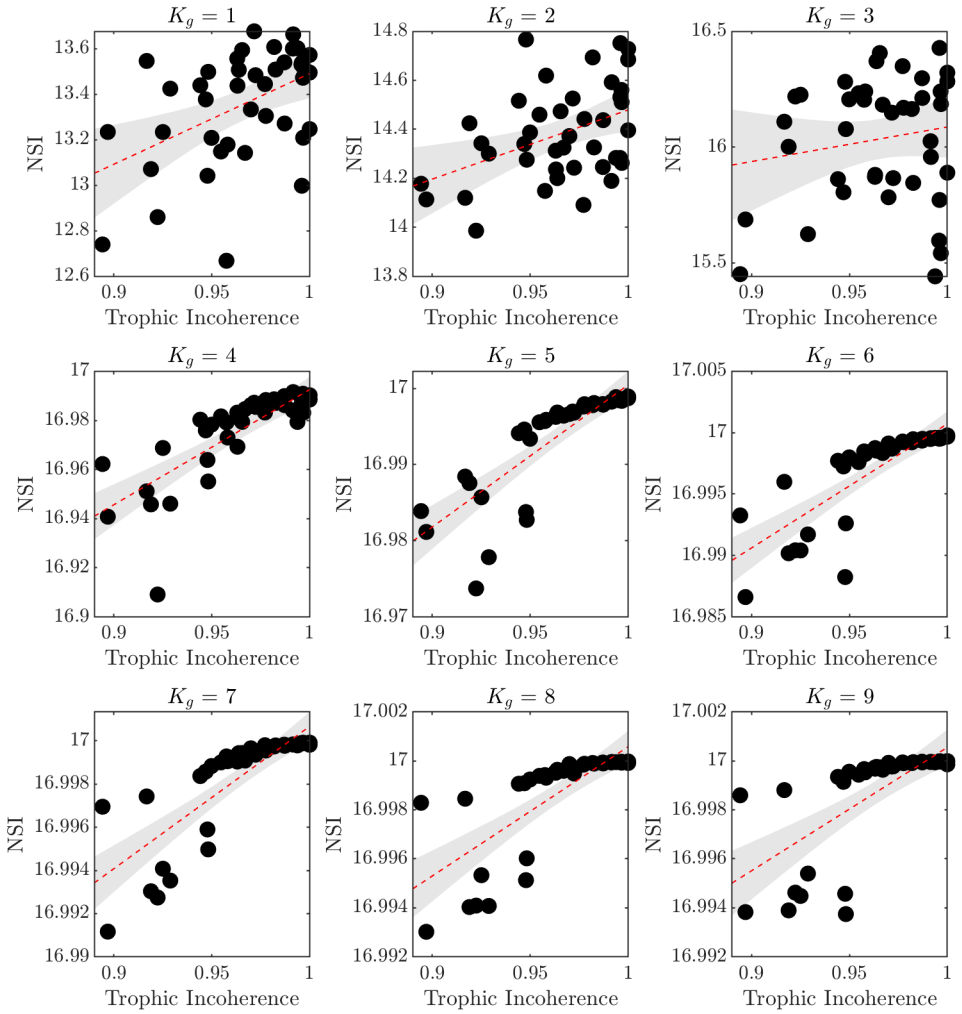


Figure 6.20: **Scatterplots Showing the Relationship Between Trophic Incoherence and SI: Mean Node Degree Four.**

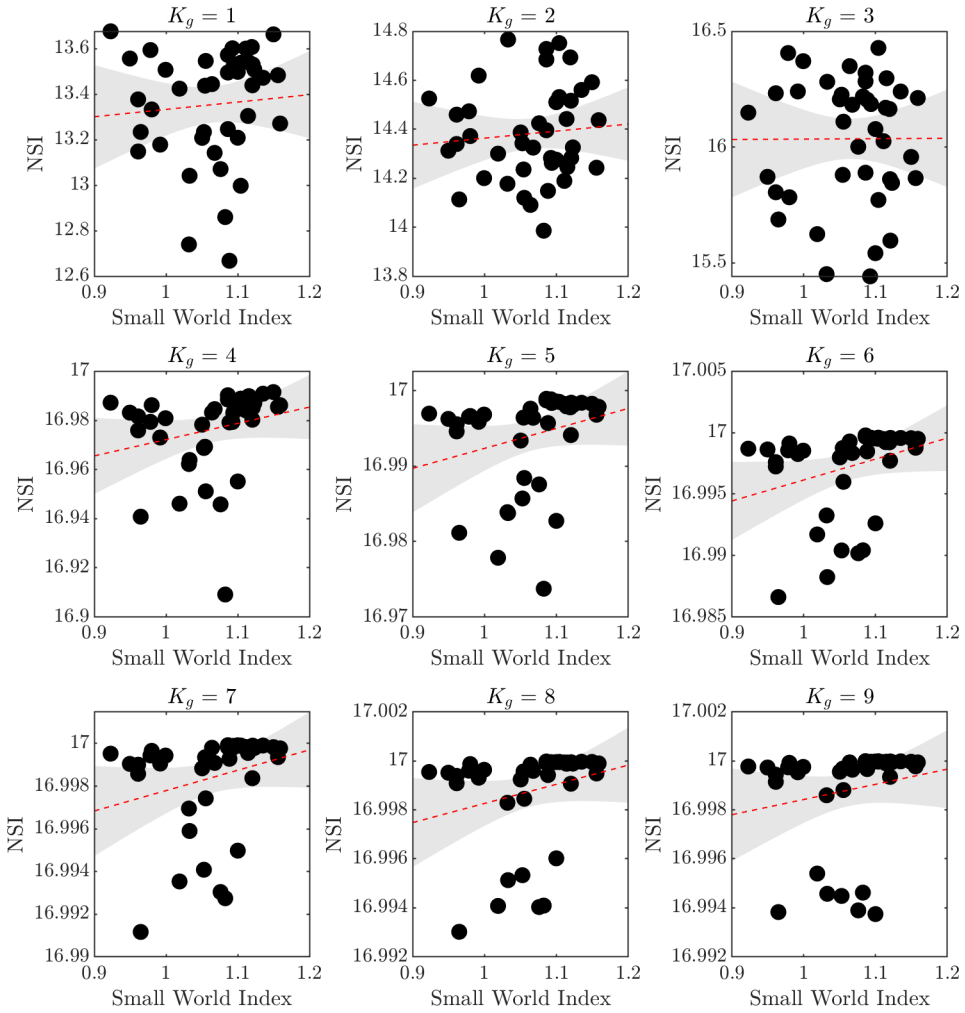


Figure 6.21: **Scatterplots Showing the Relationship Between Small World Index and SI: Mean Node Degree Four.**

6.3.3.3 Order Parameter Approach

The Pearson's correlation between R and trophic incoherence and small world index are given in Table 6.19. We see that for all $K_g \geq 4$ there was a significant correlation for trophic incoherence. This is more limited than the $\langle k \rangle = 3$ case, where significance occured for all K_g. Furthermore, no global coupling strengths had a significant correlation between small world index and R, unlike the $\langle k \rangle = 4$ case, although significance was restricted to high and low values of K_g in Table 6.16.

	Trophic Incoherence			Small World Index		
K_g	Correlation	p-value	Adjusted p-value	Correlation	p-value	Adjusted p-value
1	0.2843	0.0716	0.1516	0.2365	0.1365	0.2047
2	0.2730	0.0842	0.1516	0.1939	0.2244	0.3107
3	0.2796	0.0766	0.1516	0.1062	0.5088	0.5088
4	0.5441	0.0002	0.0014*	0.2648	0.0944	0.1544
5	0.5038	0.0008	0.0035*	0.1285	0.4233	0.4763
6	0.4356	0.0044	0.0133*	0.1069	0.5060	0.5088
7	0.6294	< 0.0001	0.0001*	0.2920	0.0639	0.1516
8	0.4421	0.0038	0.0133*	0.1453	0.3647	0.4376
9	0.6738	< 0.0001	< 0.0001*	0.1819	0.2551	0.3279

Table 6.19: **Pearson's Correlations Between R with Small World Index and Trophic Incoherence: Mean Node Degree Four.** The Pearson's correlation, p-value and adjusted p-value when comparing R for each global coupling strength to the small world index and trophic incoherence of the network. The p-values were corrected for the range of global coupling strengths as well as the two graph metrics using Benjamini-Hochberg method of correcting for FDR [78]. * denotes significance p-value < 0.05.

The relationship between R and trophic incoherence for each global coupling strength is displayed in Figure 6.22, while Figure 6.23 displays the relationships for small world index.

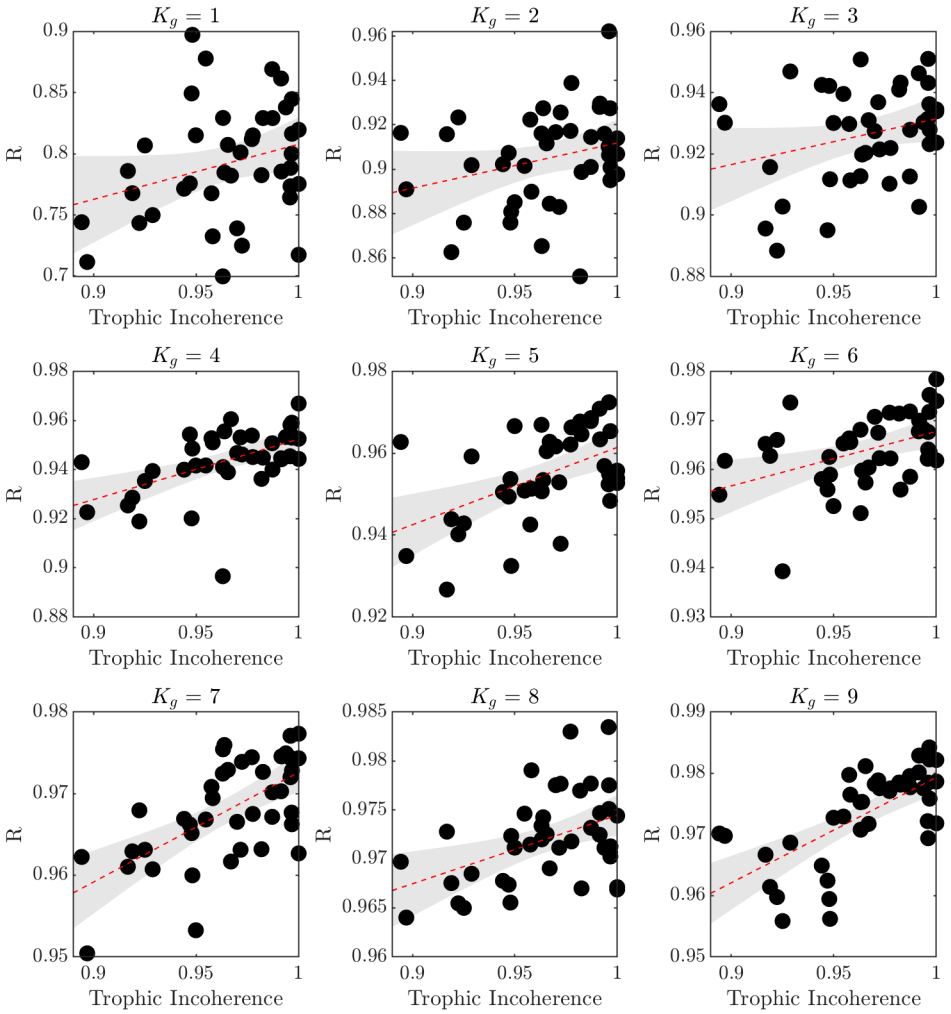


Figure 6.22: **Scatterplots Showing the Relationship Between Trophic Incoherence and R: Mean Node Degree Four.**

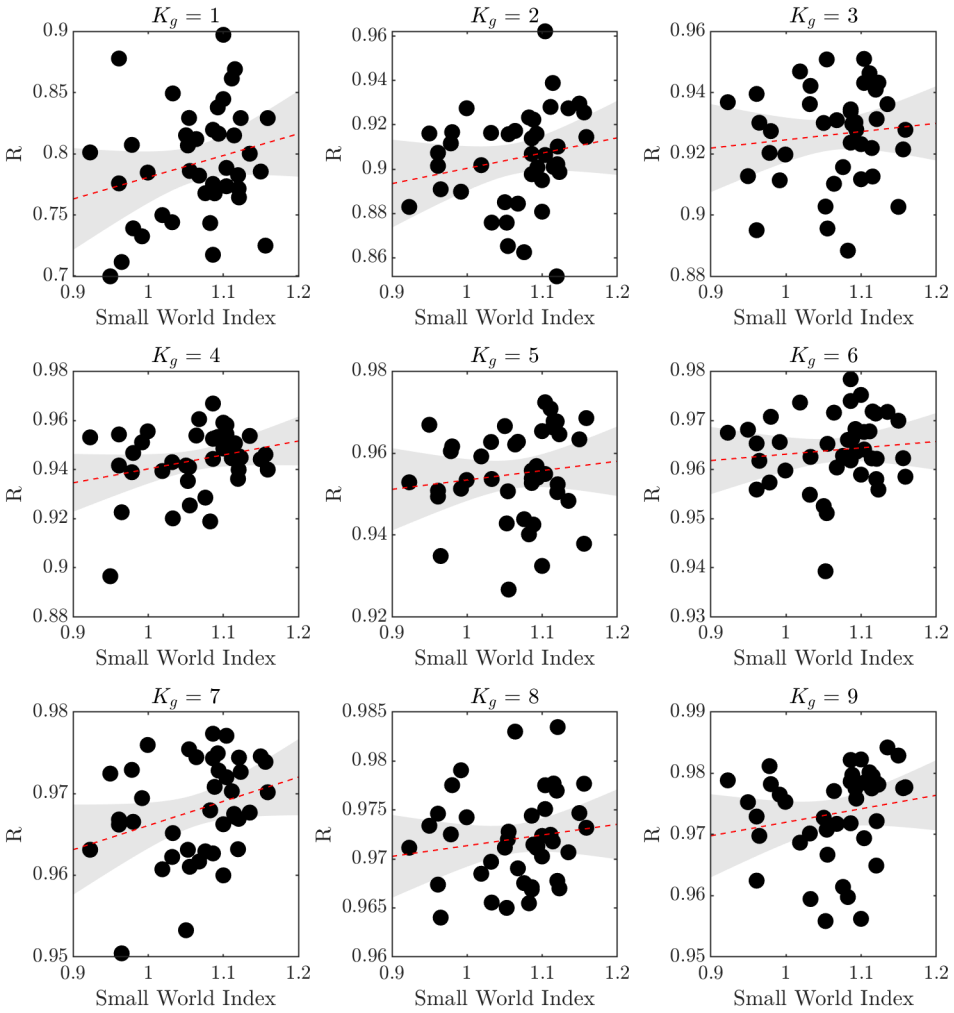


Figure 6.23: **Scatterplots Showing the Relationship Between Small World Index and R: Mean Node Degree Four.**

6.4 Discussion

Within this Chapter, we have used the Kuramoto model to increase our understanding of the link between network structure, synchronisation and sleep deprivation. The local coupling strength was used as a proxy for the effect of sleep deprivation and the global synchronisation of the network was assessed over a range of global coupling values using the Synchronisation Index, the Node Strength Index and the Order Parameter Approach. Both weakly connected and strongly connected networks were considered when $P = 3$ and the number of edges in each network was allowed to vary. When $P = 18$ only strongly connected networks with $\langle k \rangle = 3$ and $\langle k \rangle = 4$ were considered. Overall, we see evidence for FNs with higher mean node degree ($P = 3$) and trophic incoherence ($P = 18$) being more impacted by the simulated effect of sleep deprivation, especially when measured using SI.

In general, the significant correlations in Section 6.3.1 suggest that a higher baseline mean node degree will result in greater levels of global network synchronisation. Indeed, we see that for $P = 3$, the relationship between mean node degree and synchronisation was strongly correlated for SI (reaching a correlation of 98% when basal nodes were excluded) and to a lesser extent R, both with and without the inclusion of basal nodes. The higher mean node degree resulting in increased levels of synchronisation aligns with findings in epilepsy research, as network models of synchronisation can be used to represent epileptic brain activity [164] and epilepsy cohorts are known to have a higher mean node degree compared to healthy controls [35]. Combined this suggests that a higher mean node degree can contribute to an increased excitability in the brain's FN. The strong influence of mean node degree could be because there were only 9 networks considered and the number of edges in these networks ranged from 3 to 6 (maximally connected). Hence, one network had 100% more edges than others, ensuring a high disparity in the mean node degree between networks. This could explain why mean node degree affected synchronisation to such an extent, as the addition or removal of an edge on three nodes was a dominating factor in the topology of the network.

In addition, networks N_1^3 and N_4^3 both help to emphasise the effect of basal nodes on a network's synchronisation, as their inclusion reduced the effect size for the mean node degree for SI, NSI and R. Their effect was highlighted by the low level of synchronisation of these networks in Figures 6.7, 6.8 and 6.9. Indeed, increasing the level of K_g actually decreases the level of normalised synchronisation in all three measures; indeed, the raw values of NSI for $K_g \geq 2$ are actually lower than at $K_g = 0.5$. Therefore, despite high levels of global coupling strength, the basal nodes prevent global network synchronisation. Hence, networks with basal nodes may require additional analyses and should be considered on a case-by-case basis.

In Sections 6.3.2 and 6.3.3 for $P = 18$ there was a clear association between trophic incoherence and global synchronisation such that higher trophic incoherence led to greater global network synchronisation. This coincides with the idea that basal nodes, which can add directedness to the network and hence lower trophic incoherence, hinder synchronisation. Furthermore, Rodgers et al. [154] used a Kuramoto model on the *C.Elegans* connectome, with 20% of the edges removed. This was completed twice: once for random edges and once for the most 'backwards' edges - where backwards refers to edges going in the opposite direction to the overall network flow. Removing backward edges corresponds with increasing directionality and therefore decreasing trophic incoherence. When backward edges are removed synchronisation, as measured using the Kuramoto order parameter, is reduced compared to the removal of random edges and in this case the Kuramoto order parameter decreases more than in the random case. Again this reflects the notion that increased trophic incoherence supports global network synchronisation.

However, for $P = 3$ we see that across the synchronisation measures, trophic incoherence of the baseline network was not associated with the level of synchronisation as trophic incoherence never significantly correlated with any synchronisation measure. The lack of correlation between trophic incoherence and the synchronisation measures when $P = 3$ is unsurprising given that the mean node degree is not fixed. Indeed, the mean node degree had such a dominating relationship with synchronisation that it overwhelmed

the influence of other network characteristics, as indicated by the regression analysis in Section 6.3.1 as trophic incoherence is rarely significant as a singular variable. When we consider the amount of variance that is explained, through adjusted R-square, when the multiple regression is used compared to just mean node degree we see that for SI and NSI when basal nodes are included that a consistent increase in the explained variance occurs, especially for $K_g \leq 4$. The increase in the explained variance when basal nodes are included could be because trophic incoherence captures the presence of basal nodes whilst mean node degree did not. However, it is unclear why this occurs for SI and NSI and not R. Overall, the link between trophic incoherence and synchronisation suggests that less hierarchy in the network and therefore less directedness in the flow of the network [126] aids network synchronisation. This could be an indication that synchronisation is not occurring from singular drivers in the system but through constant synchronising with adjacent nodes.

Also, for $P = 18$, we see that the small world index significantly correlates with SI for nearly all K_g values and with NSI and R for a limited number of global coupling strengths. This suggests that a higher small world index is associated with greater levels of synchronisation under a fixed mean node degree. However, it should be noted that the correlation is $\sim 40\%$ lower than trophic coherence as seen in Tables 6.14-6.19.

Across the $\langle k \rangle = 3$ and $\langle k \rangle = 4$ cases we see that the two groups have a similar relationship for SI. Also, the global coupling values that have a significant relationship between NSI and trophic incoherence are similar across the groups. However, for R, the relationship with trophic incoherence is reduced as $K_g = \{1, 2, 3\}$ are not significant. Furthermore, neither NSI nor R sees a significant relationship with small world index for $\langle k \rangle = 4$. The lower number of significant relationships when $\langle k \rangle = 4$ for the small world index could be because the range of the small world index is lower for $\langle k \rangle = 4$ compared to $\langle k \rangle = 3$, see Figures 6.1 and 6.2. Alternatively, it could be related to the density of the network however as the three node networks indicate higher network density enables synchronisation the lower level of significance for $\langle k \rangle = 4$ indicates that other network

features are more important as the network complexity increases. Therefore, for trophic incoherence the level of synchronisation is relatively insensitive to the change in mean node degree and SI is the most robust measure however this is not true for the small world index.

The choice to fix the mean node degree greatly impacted the conclusion of how trophic incoherence relates to synchronisation. While many methodological choices could ensure that FNs created from a participant time-series have the same number of nodes it is much more restrictive to ensure that all networks have both the same number of nodes and mean node degree. While this is possible through proportional thresholding on binary networks, this may remove useful topological information about patient groups limiting the application of this method. For instance, a higher mean degree is a biomarker for epilepsy and proportional thresholding on a binary network would have prevented finding this feature [35]. In addition, the use of weighted FNs would also hinder each network from having the same mean node strength. Therefore, the choice to fix the mean node degree when $P = 18$ may not be fully representative of real networks. However, due to the vast number of minimally weakly connected networks that could be created on 18 nodes it was decided to add this restriction. This ensured that the density could no longer affect synchronisation and allowed some criteria for the creation of the networks to initially explore these relations in a controlled manner. Therefore, ranging the mean node degree could be a natural extension. Indeed, an investigation into the level of synchronisation in networks with differing mean node degree but the same trophic incoherence in the future could be of interest to further explore the relationship between mean node degree, trophic incoherence and synchronisation. However, another alternative may be to repeat this analysis on smaller network sizes where all networks could conceivably be simulated, such as $P = 4$. This may be more informative than considering another small subset of 18 node networks.

In addition, this analysis focused on only three graph metrics; while these all seem to be associated with synchronisation a simple extension would be to consider additional

graph metrics, such as assortativity or betweenness centrality, to assess how they relate to synchrony. However, with limited literature looking at the effect of network structure on synchronisation there is no obvious reason to select any additional graph metrics than popular use.

Furthermore, a possible extension to the work presented here would be the effect of changing the strength of local coupling at a population or regional level. For instance, frontal areas of the brain are thought to be more impacted by sleep deprivation [195]. Therefore, the local coupling strength could be higher in certain Kuramoto populations to represent this effect rather than using the same value of local coupling for all populations. This could allow more physiologically accurate effects of sleep deprivation to be modelled. An investigation into the local graph metric properties of the 'frontal' nodes could further our understanding of how network structure impacts synchronisation.

Within the simulations, the level of local synchronisation at a given global coupling strength was used as a proxy for excitability with the simulations replicating the effect of sleep deprivation through the value of the local coupling parameter changing over each set of 19 simulations (Figure 6.4c). Overall, we have seen that higher levels of mean node degree and trophic incoherence are strongly associated with higher levels of synchronisation, especially as measured using SI. This research provides valuable candidate markers for testing the susceptibility to sleep deprivation using real-life FNs. Indeed such features in a baseline EEG acquisition may be indicative of individuals who will be the most impacted by sleep deprivation, as their level of excitability would be predicted to increase the most. It is unclear how this would manifest as a behavioural response but this could correspond with worse performance on tests, which will be investigated in Chapter 7, or greater responsiveness to TMS [135].

CHAPTER 7

USING FUNCTIONAL NETWORKS TO PREDICT AND UNDERSTAND THE EFFECT OF SLEEP DEPRIVATION AS MEASURED USING PVT

7.1 Introduction

Sleep deprivation is a huge perturbation to the brain, which can manifest in its FN. While many people do not regularly experience the prolonged sleep deprivation that occurs from staying awake an entire night, the perturbations seen from total sleep deprivation experiments may provide a greater understanding of the mechanisms involved in the cognitive decline which accumulates due to daily sleep debt [52], as discussed in Section 2.3.1.

Studying participants during or before and after prolonged wakefulness is one way to monitor the effects of sleep deprivation. Participants can be monitored through their performance on tasks [37, 49, 133] as well as changes in metabolite concentration [77]. Indeed, as discussed in Section 2.3, the effect of sleep deprivation on task performance is considered by Van Dongen et al. [49] to be trait-like and therefore an individuals experience of sleep deprivation will be unique. If task performance under sleep deprivation is trait-like then it could possibly indicate that responses to sleep deprivation in that participant's FN would also be trait-like.

Using baseline information before sleep deprivation occurs to predict the effect of pro-

longed wakefulness is not a new concept, as discussed in Section 2.3. For instance, Floros et al. [67] used metadata to find that higher levels of inattention in an ADHD cohort predicted higher levels of cognitive conflict as measured using a Stroop test when participants were sleep deprived. In addition, Walsh et al. [198] used a mathematical model to predict people's performance on PVT tests using a model of fatigue [132] combined with a diffusion model to recreate PVT RTs. Furthermore, Chua et al. [37] extended the notion of trait-like vulnerability of participants to sleep deprivation, seen by Van Dongen et al. [49], by considering the link between PVT responses, ECG measures and spectral EEG power.

However, to the best of our knowledge, FNs have not been used to predict susceptibility to sleep deprivation despite many papers finding significant changes to the brains FN at whole brain [101, 110, 123, 137, 147, 172] and local [79, 167, 195, 202] levels, as highlighted in Section 2.3.

Overall, being able to predict someone's susceptibility to sleep deprivation without requiring them to be sleep deprived could offer vital insights into the work patterns suitable for employees. Also, in certain careers acute sleep deprivation and sleep debt are prone and even unavoidable. For example, the US Department of Health reported that only 33% of military service members reported sufficient sleep, defined as > 7 h for adults older than 22 and > 8 h for adults 21 and under, compared to 68% for the general population [134]. In addition, a report by the US Department of Health and Human Services stated that in Healthcare 40.1% of professionals did not get sufficient (> 7 h) sleep, meaning they have the 2^{nd} highest prevalence of short sleep duration, behind professions in production, which reported a prevalence of 42.9% [170]. It should be noted that people on active military duty were removed from the study due to the high extent sleep disruption during normal duty would occur.

With further development, a prediction of vulnerability to sleep deprivation could be used in a targeted manner within the employment process for certain professions. Such a test could help prioritise people for additional resources, mitigating their increased im-

pairment before any incidents occur. Therefore, we investigate if an individual's response to sleep deprivation can be predicted using information from the participant's FN measured before sleep deprivation. Indeed, we consider the ability to predict an individual's impairment and performance on a PVT using FNs created from two baseline acquisitions: the First EEG Acquisition After Awakening (B_{FA}) and the Acquisition 11 hours Before DLMO (B_{-11}). We create FNs and calculate how much mean node strength and trophic incoherence correlate with PVT impairment and performance. In addition, we correlate participant impairment and performance to sleep deprivation with the simulated effect of sleep deprivation measured using SI, which was introduced in Chapter 6. Furthermore, we use a stability analysis to try and understand why PVT impairment differs between individuals.

7.2 Methodology

The data used in this research has been provided by Dr Clare Anderson at the Monash Institute of Cognitive and Clinical Neuroscience. Information directly relevant to this study is provided, however for a full description of the CRP the reader is directed to McMahon et al. [133].

7.2.1 Ethical Approval

Ethical approval was provided by the Monash University Human Research Ethics Committee (CF14/2790 – 2014001546). Participants were required to give informed consent before involvement in the study. All provided data were already anonymised; therefore, no personal information could be associated with an individual.

7.2.2 Participants

Exclusion criteria were (1) no artificial disruption to normal sleep patterns prior to the study (no shift work which required 5 or more hours worked between $20:00$ and $07:00$ or transmeridian travel across three or more timezones) for at least the previous month (2) no prior diagnosis of medical, psychiatric or sleep disorders (3) no extreme chronotype. To ensure no extreme chronotypes were accepted sleep habits were monitored and all participants reported habitual bedtimes between $21:30$ and $01:00$ and habitual wake times of $05:30$ and $09:00$. This resulted in the study having a total of 22 participants with an average age of 25.53 ± 5.78 years (mean $\pm$ standard deviation) of which 4 were female.

After two days of acclimatisation within the laboratory, participants awoke on the third day to the CR wake conditions for 40 h within private, sound-attenuated, temperature and light controlled suites. Participants were closely monitored and all time-cues were removed. Light ($\sim 3 \pm 1$ lux (horizontal) and $\sim 1 \pm 3$ lux (vertical)) and temperature levels ($21^{\circ}C \pm 2^{\circ}C$) were kept constant. In addition, participants had to remain in a semi-recumbent position throughout - including having to use metal urinals and bedpans for urine voids and bowel movements. Finally, isocaloric snacks were provided hourly, following Australian Dietary Guidelines 2013 for macronutrients.

The experimental protocol ensured participants refrained from consuming alcohol and caffeine or using nicotine, supplements or prescription or non-prescription drugs for 3 weeks prior to the protocol beginning. This included women not using hormonal contraception or being pregnant. These measures were verified through a urine toxicology screen and a breathalyser test. In addition, for the three weeks prior to laboratory settings and the first two days in the clinic a strict 8:16 hours sleep:wake schedule was adhered to. Compliance was checked via actigraphy data collected from Actiwatch Spectrum (Philips Repironics, BMedical, QLD, Australia) and time-stamped call-in messages upon waking and when participants went to bed.

7.2.3 Dim Light Melatonin Onset Calculation

Melatonin levels were measured during the protocol for the calculation of DLMO ($21:11 \pm 00:52$) to provide a marker of circadian phase per individual. Participants' plasma melatonin levels were assessed through hourly blood samples starting approximately 1 h after starting CR. Values for hourly melatonin levels were then interpolated with DLMO times calculated as the first time plasma melatonin concentration exceeded 5 pg/mL. Where possible DLMO was calculated for both the first and second evening of the CRP. This led to 11 participants having DLMO correctly identified for both evenings and these times had a high correlation, $r_{PC} = 0.94$ [133]. DLMO was only established using melatonin concentrations from the second evening when a recording for the first evening was not possible. The circadian phase for each participant was then set, such that DLMO on the first day was 0. Participant data and EEG data acquisition were aligned by selecting the EEG acquisition closest to n hours before or after that participant's DLMO.

7.2.4 Psychomotor Vigilance Test

Every two hours each participant undertook a 10-minute PVT test on a computer screen that had been wheeled above them. Within this test, participants observed a white rectangle and had to respond with a thumb press once a stopwatch appeared and started counting upwards. The stimulus for each trial appeared at a random interval of 2 to 10 s after the previous trial.

A RT of $<$ 100 ms was considered to be an anticipatory error and was considered non-useable. Trials over 500 ms were considered useable but were labelled as lapses and any trial over $5,000$ ms produced an alerting noise [133] before the next trial started. The mean, median and standard deviation of RT (std_{RT}), and the percentage of lapses from useable trials for each 10-minute trial, were calculated.

Data for 9 participants were lost at the time of recording due to technical difficulties, resulting in PVT data for 13 participants, with an average age of 24.85 ± 4.26 years and

an average DLMO of $21:13 \pm 00:58$, of whom 2 were females. In addition, the results of certain testing sessions were not used in the analysis due to the test either not occurring or lasting less than the required 10 minutes. The available tests for each participant are given in Figure 7.1.

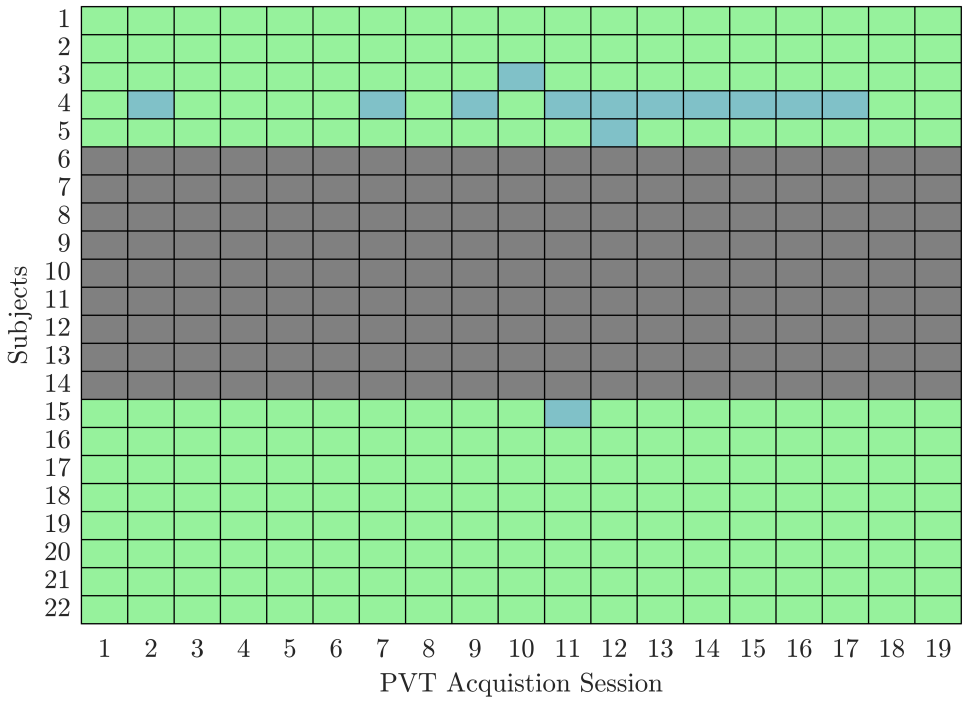


Figure 7.1: **PVT Acquisitions Available.** The available PVT acquisition sessions for each participant across the CRP. The colours represent a successful PVT acquisition, unable to record a PVT acquisition and PVT acquisitions for which the data were lost.

7.2.5 PVT Impairment and Performance

Performance was monitored throughout the CRP using PVT, where the mean, median and standard deviation of RT and percentage of lapses were recorded, figures displaying these time-series are given in Appendix D.1, note longer RT is considered worse. To calculate the level of impairment the participants faced due to sleep deprivation the percentage increase from the best session in the range $[\text{DLMO} - 11\text{ h}, \text{DLMO}]$, to the worst session in the range $[\text{DLMO} + 1\text{ h}, \text{DLMO} + 24\text{ h}]$ was calculated, for the mean, median and

standard deviation of RT. Hence 'performance' will refer to the recorded PVT measure at a specific timepoint and 'impairment' will refer to the percentage difference from the minimum PVT performance over the first 12 h to the worst PVT performance over the subsequent 24 h.

For almost all participants their lowest percentage of lapses during $[\text{DLMO}-11\text{ h}, \text{DLMO}]$ was 0%, preventing a percentage increase from being calculated. Therefore, impairment was represented by their worst percentage during $[\text{DLMO} + 1\text{ h}, \text{DLMO} + 24\text{ h}]$. These times were selected as the effect of sleep deprivation should have been minimal up to DLMO on the first day. The timings of the PVT tests with the minimum and maximum impairment are presented in Table 7.1.

The general slowing of RT is mainly captured by the mean and median RT and the percentage of lapses while std_{RT} captures the increased variability in RT, which is expected under the state instability hypothesis [53], as introduced in Section 2.3.

7.2.6 EEG Acquisition

EEG data were recorded using 18 scalp electrodes from the standard 10-10 system (Fp1, Fp2, F3, F4, Fz, C3, C4, Cz, P3, P4, Pz, P7, P8, Po3, Po4, O1, O2, Oz), alongside ECG recordings and monitoring of the eyes with mastoids used as a reference. The first 150 s recording occurred 2 h after waking and subsequent recordings occurred every 2 h for a total of 40 h awake. Participants had their eyes-closed during the acquisition. This resulted in up to 19 recordings per participant.

All EEG acquisitions were collected on a Compumedics Grael system with Profusion Sleep 4 software (Compumedics Ltd, Vic, Aus) with sampling rate 512 Hz, the data was notch filtered at 50 Hz, and low and high-band pass filters were used at 0.3 Hz and 30 Hz respectively.

For acquisitions where one or more electrode time-series were corrupted, the entire acquisition was removed, $n = 7$. This was to ensure all EEG networks contained the same base network of 18 nodes. Not only making each FN directly comparable but

Participant	Mean RT (ms)		Median RT (ms)		Standard Deviation of RT (ms)		Percentage of Lapses	
1	-1,0	17,18	-11	9,10	-3,-2	14,15	-	11,12
2	-2,-1	14,15	0	20,21	0	14,15	-	20,21
3	-2,-1	10,11	-2,-1	10,11	-2,-1	12,13	-	10,11
4	-4,-3	6,7	-4,-3	6,7	-4,-3	6,7	-	6,7
5	-11	20,21	-6,-5	20,21	0	20,21	-	20,21
15	-3,-2	9,10	-3,-2	6,7	-1,0	9,10	-	6,7
16	-9,-8	19,20	-9,-8	23,24	-9,-8	19,20	-	23,24
17	-10,-9	10,11	-11	10,11	-10,-9	10,11	-	10,11
18	-1,0	9,10	-1,0	17	-1,0	9,10	-	15,16
19	-2,-1	8,9	-2,-1	8,9	0	16,17	-	8,9
20	-7,-6	11,12	-7,-6	21,22	-7,-6	11,12	-	11,12
21	-9,-8	17,18	-9,-8	19,20	-9,-8	17,18	-	19,20
22	-2	10,11	-6,-5	10,11	-1,0	10,11	-	10,11

Table 7.1: **Timings of the Minimum and Maximum PVT Performance with Respect to DLMO.** For each of the four PVT performance measures the timing of the minimum mean RT, median RT, standard deviation of RT and percentage of lapses with respect to DLMO is given in the first column and the maximum is given in the second column. The timing for the minimum percentage of lapses is not provided as this is not used when assessing impairment.

also ensuring the properties of all networks closely align with the theoretical networks considered in Chapter 6. In addition, $n = 11$ EEG acquisitions were missing, due to technical issues with the recording devices or participants requiring medical attention or subject distress. Figure 7.2 shows the available EEG recordings for each participant.

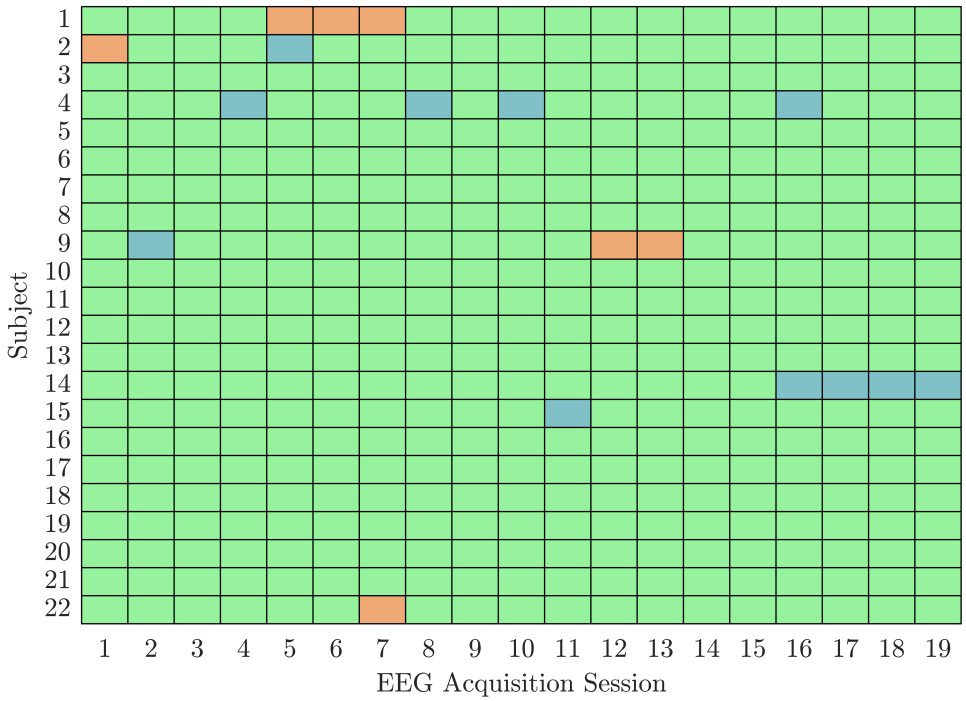


Figure 7.2: **EEG Acquisitions Available.** The available EEG acquisition sessions for each participant across the CRP. The colours represent a successful EEG acquisition, an EEG acquisition with at least one faulty electrode and unable to record an EEG acquisition.

7.2.7 EEG Preprocessing

For each 150 s recording the EEG was referenced to the common average. Then the EEG acquisition was bandstop filtered between 49-51 Hz to remove powerline interference and filtered into the broadband (1-70 Hz). An epoch was then selected before the epoch time-series was filtered into a specific frequency band. The frequency bands considered were $0.5 - 4$ Hz (delta), $4 - 8$ Hz (theta), $8 - 14$ Hz (alpha) and $14 - 30$ Hz (beta), chosen to ensure each frequency between $0.5 - 30$ Hz is included. Within each frequency band the

data were then normalised such that each channel had mean 0 and standard deviation 1 [171].

7.2.8 Epoch Selection

EEG epochs were selected in one of two ways. First, for stability, the entire 150 s acquisition was split into 30 s epochs each overlapping their neighbour by half the epoch size (15 s). This means all of the data was used and 9 epochs were created.

Otherwise, a single 30 s epoch was selected, from each baseline 150 s acquisition. The EEG data was collected under supervision within a strict protocol. Therefore, the artifacts were minimal and there were multiple 30 s epochs, which could have been selected. To provide an objective way to select an epoch a Resting State Epoch Selector Algorithm (RSESA) was used. The algorithm found an epoch by finding 30 s of the acquisition which maximised the peak alpha frequency in the occipital nodes O1 and O2, which is associated with expected eyes-closed restful EEG. Also, the algorithm minimised the variance of the power spectrum in the frequency band $1-48$ Hz and minimised instantaneous correlation (zero lag correlation) over all electrodes to eliminate major artifacts.

7.2.9 Functional Network Construction

For each epoch, the 18 channels of filtered and normalised EEG data were used to calculate FNs using steps introduced in Section 3.1.1. Here PLF as introduced in Section 6.2.6 was used to calculate the FC between nodes. Each frequency band filtered EEG time-series was considered an oscillator, with its position at time $t \in \{1, \ldots, L\}$ given by $z_i(t) = e^{i\theta_i(t)}$. The level of synchronisation between pairs of nodes was then summarised by how clustered the two oscillators were, which was determined by the similarity of their phases eq 6.7. This resulted in undirected weighted adjacency matrices $\rho \in \mathbb{R}$, each with a size 18×18 and edge weights in the range $[0, 1]$.

Surrogate analysis was then used to calculate the significance of each connection. Using

only the bandpass filtered time-series 100 surrogate time-series were created by altering the time-series using IAAFT - a Fourier-based method which ensures the autocorrelation and spectrum of the time-series were preserved [161]. The same methodology was used to create 100 surrogate PLF networks. Edges in the participant's original PLF network remained if their weight was significantly higher than the corresponding edge from the surrogate networks at a 95% significance level, whilst non-significant edges were replaced by 0. For more details about using surrogates to check the significance of an edge please refer to Schmidt et al. [164].

In addition, the lag (eq 6.8) between each pair of EEG times-series was calculated and this was used to make the surrogate-corrected PLF network directed by retaining edges with a positive lag, as explained in Section 6.2.6.

Finally, an order two edge reduction was used to remove connections where an alternative path via one or two additional nodes was stronger [164]. This process for creating FNs was chosen to reduce the impact of indirect connections.

7.2.10 Calculating Graph Metrics

Two graph metrics were then calculated for each alpha baseline PLF network calculated using RSESA. These are mean node strength and trophic incoherence, see Section 3.1.1.6 for more details. The graph metrics were calculated to try and understand the link between the properties of baseline FNs and the impairment due to sleep deprivation as measured using PVT.

These graph metrics were chosen due to the results of Chapter 6, which showed how both these metrics correlated with SI under the different circumstances of variable and fixed mean node degree. Also, only data filtered in the alpha band was chosen because Chua et al. [37] found the alpha frequency band to be the only band able to significantly explain intra-individual variance in task performance after sleep deprivation.

Trophic incoherence, calculated on directed networks, provides a value between 0 and 1 for the directedness of the network [126]. Networks with a clear direction have

a low incoherence (high coherence), while networks with no clear direction have a high incoherence (low coherence); for more detail refer to Section 3.1.1.6 and Figure 3.5.

7.2.11 Kuramoto Model and Synchronisation Index

The single RSESA alpha PLF network was used as the FN required by the Kuramoto model. The Kuramoto model was used to simulate the effect of sleep deprivation and the resultant level of synchronisation was calculated to try and understand any correlations between baseline FNs and the PVT impairment following sleep deprivation. For each network SI, as introduced in Section 6.2.5.1, was then calculated for a given global coupling strength, K_g, ranging from 1 to 20 while the local coupling strength, K_{cc}, varied from 0 to the K_{cc}^{max} in 19 increments. Then the simulations were run using a forward Euler scheme over $T = 1,000$ s with time-step $dt = 0.005$. Each population had $N = 100$ oscillators, which were equally spaced around their respective unit circles at time $t = 0$. The oscillator's frequency was selected from a Gaussian distribution 9 Hz $\pm$ 0.5 Hz. The choice of parameters matches those in Section 6.2.4, and SI was chosen due to the high number of significant correlations between SI and networks measures in Chapter 6.

7.2.12 Stability Analysis

As discussed in Section 2.3.1 performance on PVT has previously been linked to the state instability hypothesis [53]. To understand how stability in functional brain networks changes during sleep deprivation, a stability analysis was completed for all four frequency bands.

The stability of an individual's FN was defined to be the consistency of their PLF networks across all 9 epochs in a given acquisition, as measured using 2-D correlation. This is based on network stability as presented and used by both Shrey et al. [171] and Smith et al. [175].

Therefore, for each EEG acquisition, the 150 s were split into 9 epochs of 30 s, each

overlapping by 15 s. For each of the 9 epochs, a PLF network was calculated. The stability of each EEG acquisition was then quantified by 2-D correlation between each of the 9 epochs. Therefore, each epoch was correlated to the other 8 epochs, using MATLAB function *corr2*, resulting in 36 correlations. The median stability is then taken as representative of the stability of the FNs for that EEG acquisition.

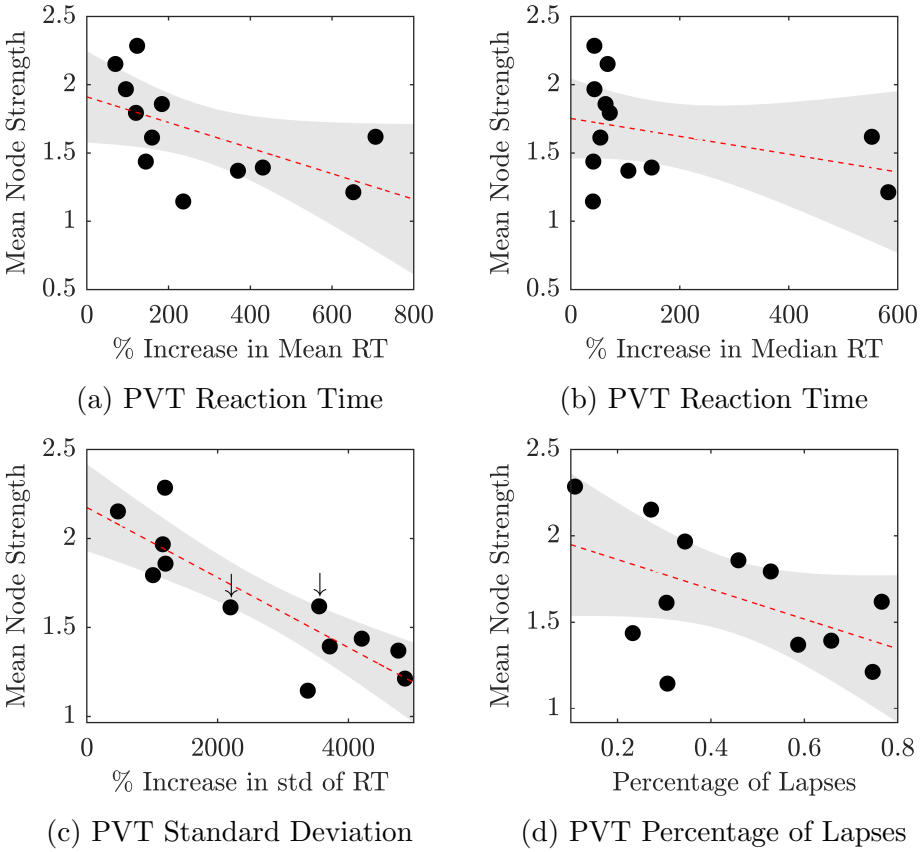
7.2.13 Statistical Analysis

After the graph metrics and SI were calculated from the baseline acquisitions, they were correlated to the level of PVT impairment using Pearson's correlation. In addition, the Pearson's correlation between the baseline predictors and PVT performance across the CRP was calculated. Plus, the time-series for stability at the group level was considered and the Spearman's rank between stability and PVT impairment at an individual level was calculated. Furthermore, a comparison between mean node strength and circadian strength is given in Appendix D.2. Also, linear regression analysis was completed to understand the contribution of mean node strength and trophic incoherence as independent variables and the variance explained when both independent variables were considered together.

7.3 Results

7.3.1 Predicting PVT Impairment Using Mean Node Strength

To assess if a baseline EEG acquisition provides information about the impairment of the participant under sleep deprivation the mean node strength of the baseline network was correlated to the level of impairment in each of the four PVT measures. The results for B_{FA} are seen in Figure 7.3 whilst the results for $B_{\text{-}11}$ are given in Figure 7.4. In addition, the Pearson's correlation and FDR adjusted p-value for the correlation between PVT impairment and mean node strength are presented in Table 7.2.



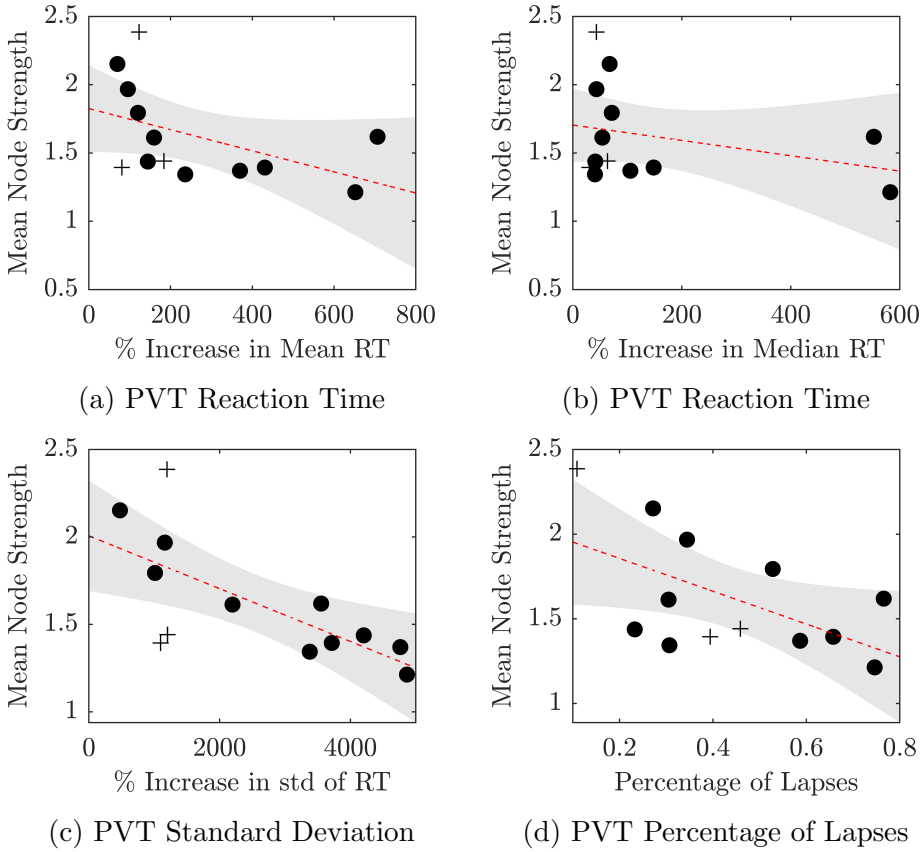
(a) PVT Reaction Time (b) PVT Reaction Time

(c) PVT Standard Deviation (d) PVT Percentage of Lapses

Figure 7.3: **Scatterplot Relating PVT Impairment to Mean Node Strength for the First Acquisition After Awakening.** Scatterplots relating the PVT impairment as measured using **(a)** mean RT **(b)** median RT **(c)** standard deviation of RT and **(d)** percentage of lapses to mean node strength for the first acquisition after awakening. For all plots, a black dot represents a participant, the red dashed line is the linear fit between the two variables and the grey patch represents the 95% confidence interval. The two ↓ signifies two participants with similar mean node strength and varying % increases in std of RT.

For all measures of PVT impairment and the two choices of baseline acquisition a negative correlation occurred when compared with mean node strength, as seen in Table 7.2. However, we see that only the correlation between std_{RT} and mean node strength had a significantly strong negative correlation. In particular, the strongest correlation was between mean node strength and std_{RT} for B_{FA}. Indeed, when considering Figure 7.4 the participants whose acquisition 11 hours before DLMO differed from the first acquisition after awakening showed the largest error for the linear fit for std_{RT}.

In general, we see that the lower the mean node strength in the baseline network the



(a) PVT Reaction Time (b) PVT Reaction Time

(c) PVT Standard Deviation (d) PVT Percentage of Lapses

Figure 7.4: **Scatterplot Relating PVT Impairment to Mean Node Strength for the Acquisition 11 Hours Before DLMO.** Scatterplots relating the PVT impairment as measured using **(a)** mean RT **(b)** median RT **(c)** standard deviation of RT and **(d)** percentage of lapses to mean node strength for the acquisition 11 hours before DLMO. Participants whose EEG acquisition 11 hours before DLMO is not their first recording are represented by + in all plots, while those whose first EEG acquisition is 11 hours before DLMO are denoted by •.

Correlations	Pearson's Correlation	p-value	Adjusted p-value
First Acquisition: Mean RT and Mean Node Strength	-0.5618	0.0573	0.1146
First Acquisition: Median RT and Mean Node Strength	-0.3538	0.2592	0.2962
First Acquisition: RT std and Mean Node Strength	-0.8667	0.0003	0.0021*
First Acquisition: Percentage of Lapses and Mean Node Strength	-0.5058	0.0934	0.1375
11 Hours Before DLMO: Mean RT and Mean Node Strength	-0.4724	0.1031	0.1375
11 Hours Before DLMO: Median RT and Mean Node Strength	-0.3053	0.3104	0.3104
11 Hours Before DLMO: RT std and Mean Node Strength	-0.6829	0.0101	0.0404*
11 Hours Before DLMO: Percentage of Lapses and Mean Node Strength	-0.5634	0.0450	0.1146

Table 7.2: **Table Showing the Pearson's Correlation and p-value for PVT impairment and Mean Node Strength.** The Pearson's correlation between the participant's PVT impairment and the mean node strength of their functional network was calculated from the first EEG acquisition after awakening and the EEG acquisition 11 hours before DLMO. The p-values in the table are corrected for multiple comparisons using the Benjimini-Hochberg correct for FDR [78]. * denotes significance p-value < 0.05.

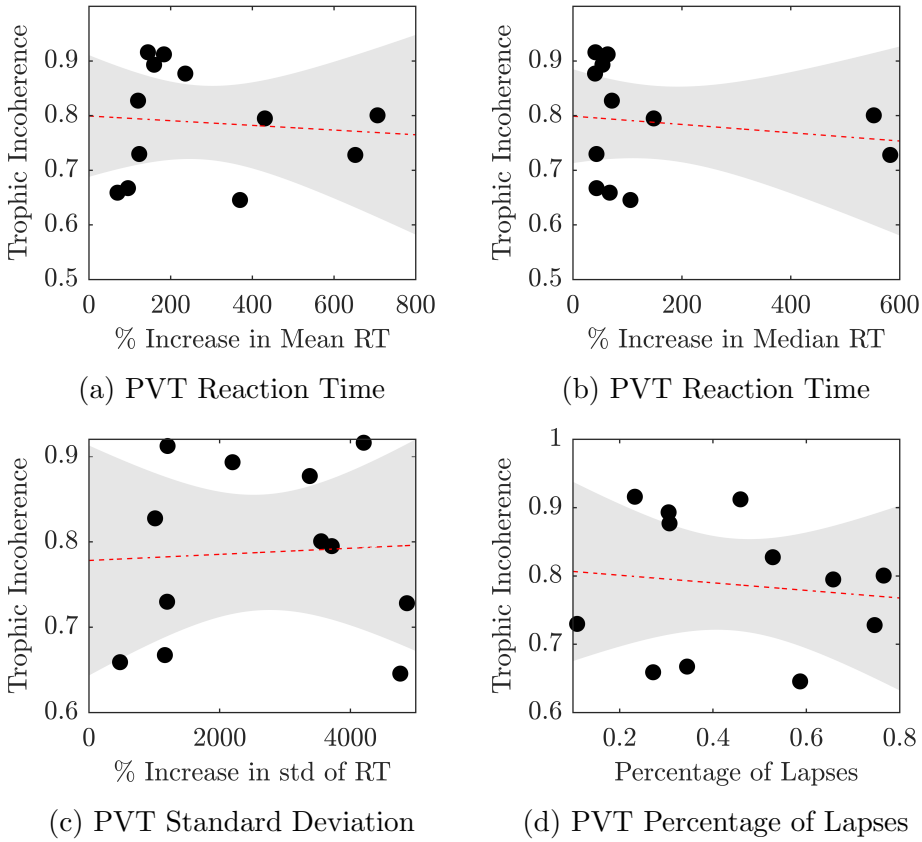
higher the std_{RT} impairment. However, within Figure 7.3c and 7.4c we see that some participants had an almost identical mean node strength despite their std_{RT} impairment level being quite variable. For instance, two participants (referenced by arrows in Figure 7.3c) had a percentage difference of 0.36% in mean node strength whilst their standard deviations had a percentage difference of 47.16%. This could indicate that a factor other than mean node strength was contributing to the impairment of participants.

It is worth noting that in Figures 7.3b and 7.4b and the corresponding figures in Sections 7.3.2, 7.3.3 and 7.3.6 the two participants with the highest % increase in median RT appear to be outliers. These participants were not three standard deviations from the mean, however they were further than 1.5 times the interquartile range away from the 75^{th} percentile. To ensure the results were not skewed by these participants, they were removed and the analysis for these sections was repeated. The full results are given in Appendix D.3, but the removal of these participants did not greatly change the correlations and did not lead to any significant relationships between % increase in median RT and any predictor.

7.3.2 Predicting PVT Impairment Using Trophic Incoherence

We now correlate the trophic incoherence of the baseline networks with PVT impairment. The results for B_{FA} are presented in Figure 7.5 and the results for $\text{B}_{\text{-11}}$ are presented in Figure 7.6.

Furthermore, the Pearson's correlation between impairment and trophic incoherence and the corresponding p-values are presented in Table 7.3. We see that none of the measures for either baseline acquisition had a significant correlation between impairment and trophic incoherence.



(a) PVT Reaction Time

(b) PVT Reaction Time

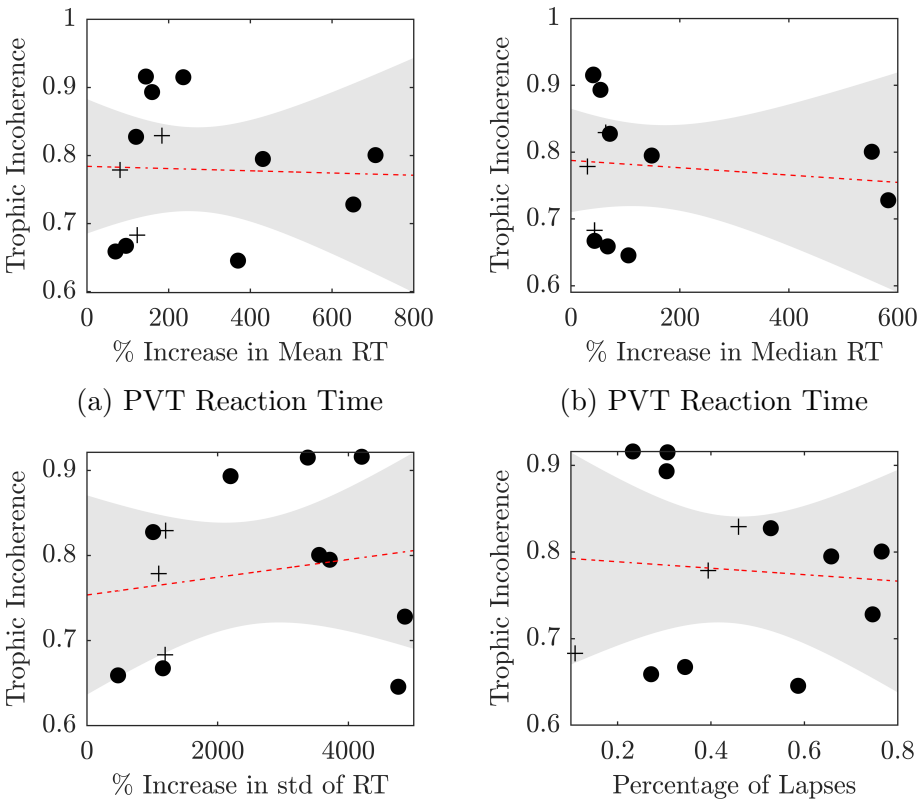
(c) PVT Standard Deviation

(d) PVT Percentage of Lapses

Figure 7.5: **Scatterplot Relating PVT Impairment to Trophic Incoherence for the First Acquisition After Awakening.** Scatterplots relating the PVT impairment as measured using **(a)** mean RT **(b)** median RT **(c)** standard deviation of RT and **(d)** percentage of lapses, to trophic incoherence for the first acquisition after awakening.

Correlations	Pearson's Correlation	p-value	Adjusted p-value
First Acquisition: Mean RT and Trophic Incoherence	-0.0932	0.7734	0.9062
First Acquisition: Median RT and Trophic Incoherence	-0.1486	0.6449	0.9062
First Acquisition: RT std and Trophic Incoherence	0.0573	0.8596	0.9062
First Acquisition: Percentage of Lapses and Trophic Incoherence	-0.1182	0.7145	0.9062
11 Hours Before DLMO: Mean RT and Trophic Incoherence	-0.0363	0.9062	0.9062
11 Hours Before DLMO: Median RT and Trophic Incoherence	-0.1084	0.7244	0.9062
11 Hours Before DLMO: RT std and Trophic Incoherence	0.1720	0.5741	0.9062
11 Hours Before DLMO: Percentage of Lapses and Trophic Incoherence	-0.0789	0.7978	0.9062

Table 7.3: **Table Showing the Pearson's Correlation and p-value for PVT impairment and Trophic Incoherence.** The Pearson's Correlation between the participants' PVT impairment and the trophic incoherence of their functional network calculated from the first recording after awakening and the recording 11 hours before DLMO. The p-values in the table are corrected for multiple comparisons using the Benjamini-Hochberg correction for FDR [78].



(a) PVT Reaction Time (b) PVT Reaction Time

(c) PVT Standard Deviation (d) PVT Percentage of Lapses

Figure 7.6: **Scatterplot Relating PVT Impairment to Trophic Incoherence.** Scatterplots relating the PVT impairment as measured using **(a)** mean RT **(b)** median RT **(c)** standard deviation of RT and **(d)** percentage of lapses to trophic incoherence for the acquisition 11 hours before DLMO.

7.3.3 Predicting PVT Impairment Using Synchronisation Index

The baseline EEG acquisitions were put through the pipeline outlined in Chapter 6 and Section 7.2.11 to assess their ability to predict PVT performance. Per K_g each participant's SI was correlated to the four measures of PVT impairment.

Scatterplots with the Pearson's correlation and corresponding p-values, FDR corrected across all K_g values and the four measures, for impairment as measured using std_{RT} impairment are presented in Figure 7.7 and Figure 7.8, for B_{FA} and $\text{B}_{\text{-11}}$ respectively. We see that after correcting for the multiple comparisons, K_g = { 1, 2, 3, 4, 5, 6, 7, 8, 9, 10, 11, 12, 19 } and K_g ={$1, 3, 4, 5, 6, 7, 8, 9, 10, 11, 12$} had significant correlations between std_{RT} impairment and SI for B_{FA} and $\text{B}_{\text{-11}}$ respectively. For all K_g values where both baseline EEG acquisitions are significant, the magnitude of the correlation was higher for the first acquisition after awakening.

Similar results for the other three impairment measures can be found in Appendix D.4, none of which had a significant correlation. It is worth noting that none of the other impairment measures had any significant correlations even when the p-values were uncorrected, therefore the lack of significance was not merely an effect of a high number of multiple comparisons.

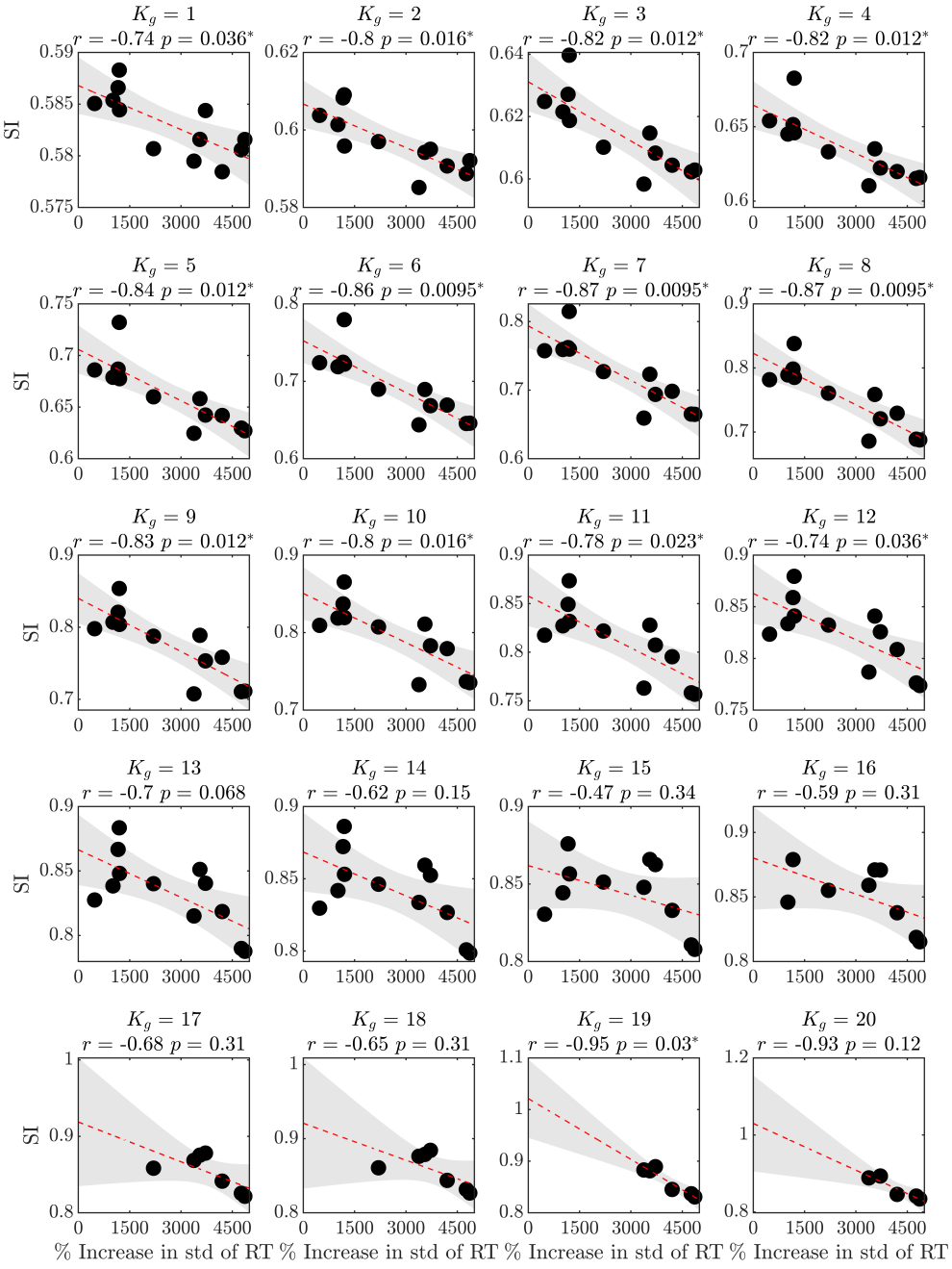


Figure 7.7: **Scatterplot Relating PVT Impairment to SI for the First Acquisition After Awakening.** Scatterplots relating the PVT impairment as measured using the standard deviation of RT to SI for K_g = 2 to K_g = 21 for the first EEG acquisition after awakening. The Pearson's r correlation and the p-value corrected for multiple comparisons using the Benjamnini-Hochberg method [78] for all K_g values and the four PVT measures are given above each diagram.* denotes significance p-value < 0.05. Uncorrected p-values are given in Appendix D.4.

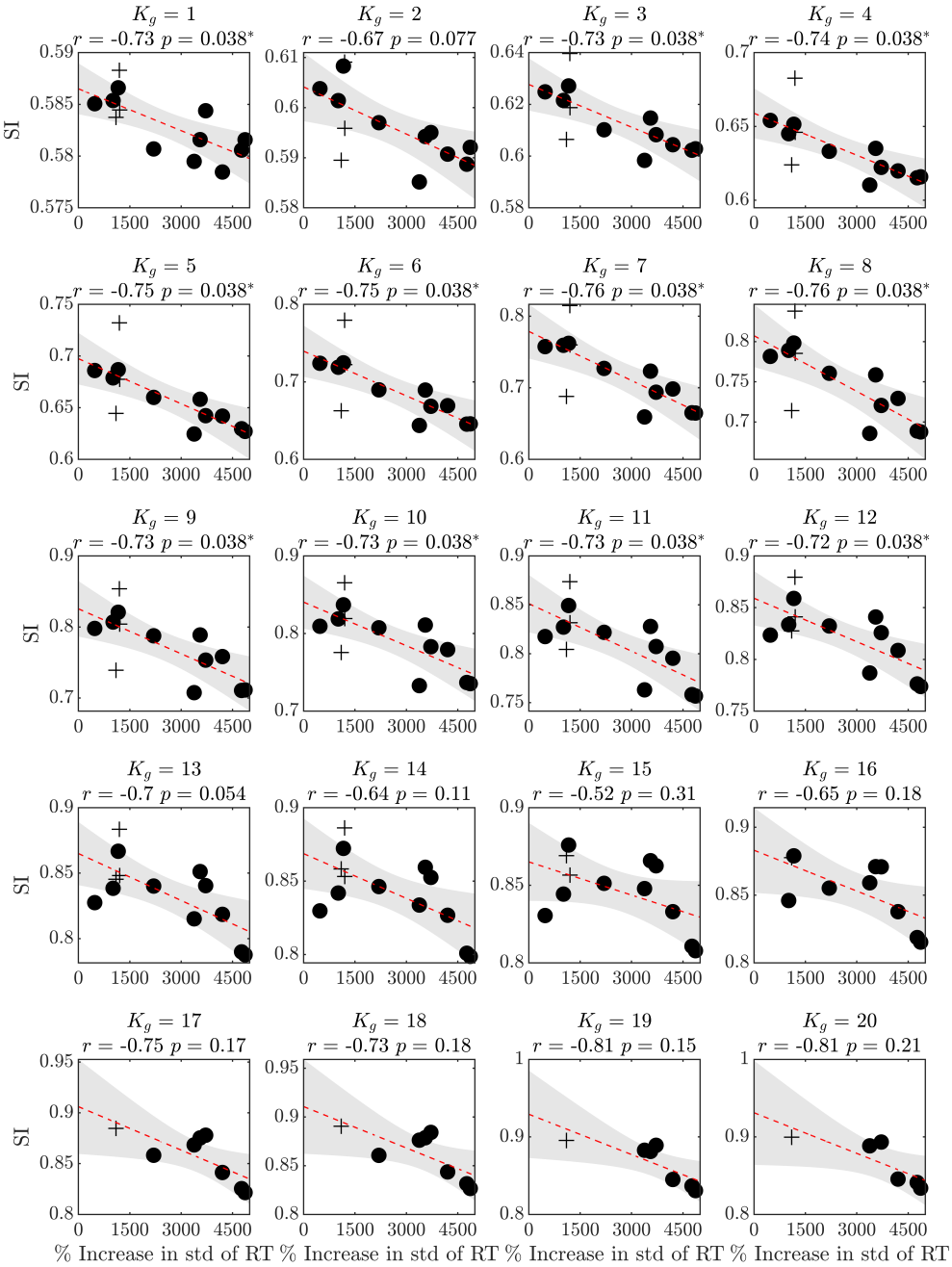


Figure 7.8: **Scatterplot Relating PVT Impairment to SI for the Acquisition 11 Hours Before DLMO.** Scatterplots relating the PVT impairment as measured using the standard deviation of RT to SI for K_g = 1 to K_g = 20 for the EEG recording 11 hours before DLMO. The Pearson's r correlation and the p-value corrected for multiple comparisons using the Benjamnini-Hochberg method [78] for all K_g values and the four PVT measures are given above each diagram. * denotes significance p-value < 0.05. Uncorrected p-values are given in Appendix D.4.

7.3.4 Trophic Incoherence Adds Value

In Section 7.3.2 we saw that the trophic incoherence of the baseline network did not significantly correlate with PVT impairment. This is similar to the results in Section 6.3.1 when correlating trophic incoherence with synchronisation measures. However, we saw evidence through regression analysis that trophic incoherence alongside mean node degree explained more variance in the simulated synchronisation measure than just mean node degree. Also, in Sections 6.3.2 and 6.3.3 we saw that when the mean node degree of the networks was fixed the trophic incoherence of the network highly correlated with synchronisation. To better understand the influence of trophic incoherence in larger networks, when the mean node strength of the participant's FNs varied between $[1.10, 2.29]$, a linear regression analysis was completed between std_{RT} impairment and trophic incoherence as well as mean node strength both individually and together. The results are given in Table 7.4 for B_{FA} and Figure 7.5 for $B_{\text{-11}}$.

Regression Parameters	SSE	R-square	Adj R-square	p-value	Adjusted p-value
RT std and Trophic Incoherence	2822	0.0033	-0.0964	0.8566	0.8566
RT std and Mean Node Strength	704	0.7511	0.7263	0.0006	0.0016*
RT std and Mean Node Strength and Trophic Incoherence	577	0.7962	0.7509	0.0011	0.0016 *

Table 7.4: **The Results of the Linear and Multiple Regression for the First Acquisition After Awakening.** The results of the two linear regressions and one multiple regression in terms of the Sum of Square Errors (SSE), R-square and Adjusted R-square for the first acquisition after awakening. * denotes significance p-value < 0.05, calculated using non-parametric permutation testing ($n = 10,000$). The p-values in the table are corrected for multiple comparisons using the Benjamini-Hochberg correction for FDR [78].

Regression Parameters	SSE	R-square	Adj R-square	p-value	Adjusted p-value
RT std and Trophic Incoherence	2962	0.0296	-0.0586	0.5639	0.5639
RT std and Mean Node Strength	1629	0.4664	0.4179	0.0258	0.0774
RT std and Mean Node Strength and Trophic Incoherence	1548	0.4928	0.3914	0.0569	0.0853

Table 7.5: **The Results of the Linear and Multiple Regression for the Acquisition 11 Hours Before DLMO.** The results of the two linear regressions and one multiple regression in terms of the Sum of Square Errors (SSE), R-square and Adjusted R-square for the first acquisition after awakening. * denotes significance p-value < 0.05, calculated using non-parametric permutation testing ($n = 10,000$). The p-values in the table are corrected for multiple comparisons using the Benjamini-Hochberg correction for FDR [78].

For B_{FA}, we see that the multiple regression has both the lowest SSE and the highest adjusted R-square, with the combined model explaining an additional ~ 4% variance. When using B_{FA} the explained variance was ~ 30% higher compared to B_{-11} when mean node strength was included in the regression. In addition, for B_{-11} the multiple regression did not have the highest R-square value when adjusted for the higher number of variables in that model.

In particular, there were two participants, highlighted by arrows in Figure 7.9, whose mean node strength differed by only 0.4% but have varying levels of PVT impairment and whose trophic incoherence differed by 11.6%. The regression analysis suggests that trophic incoherence could explain how networks of similar mean node strength differ so much in their PVT impairment.

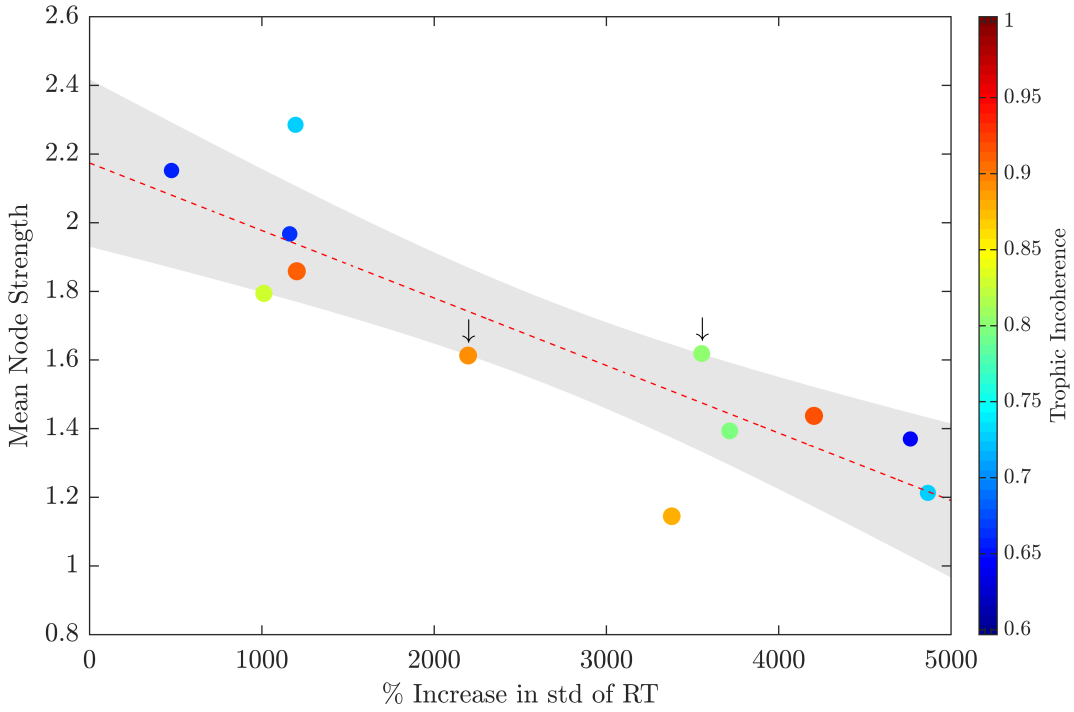


Figure 7.9: **Scatterplot Relating PVT Impairment to Mean Node Strength and Trophic Incoherence for the First Acquisition After Awakening.** Scatterplots relating the PVT impairment as measured using standard deviation of RT to mean node strength for the first acquisition after awakening with trophic incoherence depicted through node size and colour. The two ↓ signifies two participants with similar mean node strength and varying % increases in std of RT and the red dashed line is the linear fit between the two variables and the grey patch represents the 95% confidence interval.

Overall, this shows that while mean node strength was the dominant feature in explaining std_{RT} impairment, we also saw evidence that this effect was modulated by trophic incoherence and indeed more incoherent networks saw a lower level of impairment.

The other three impairment measures (mean RT, median RT and percentage of lapses) were not considered due to the lack of significance in Sections 7.3.1 - 7.3.3.

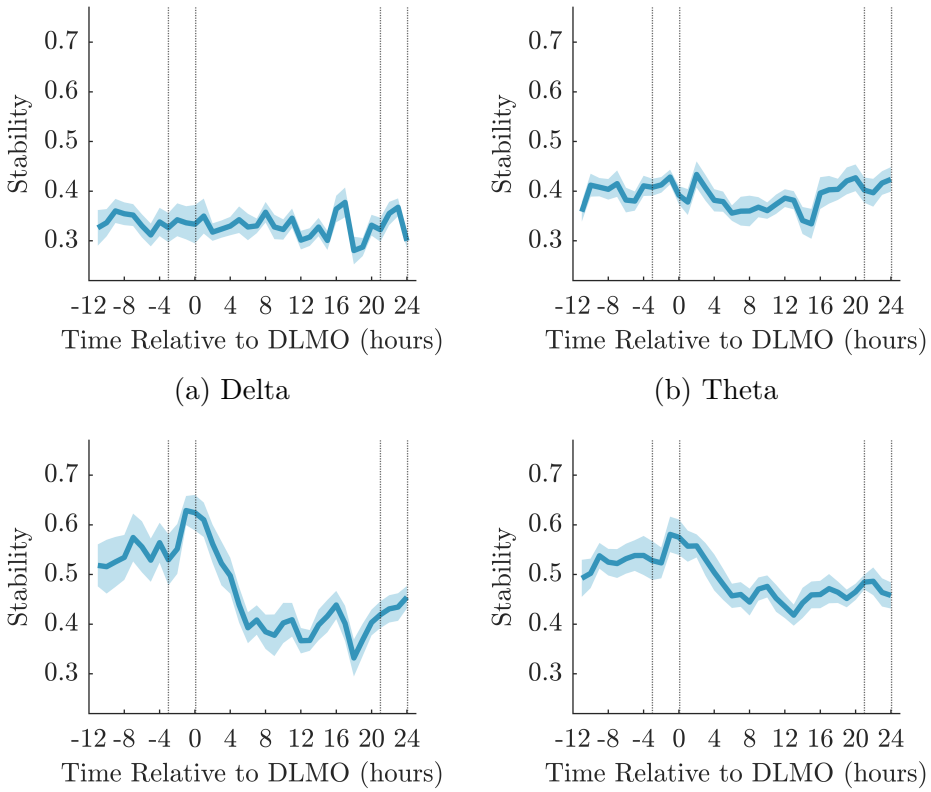
7.3.5 Stability

The stability of the FNs over the CRP was assessed at the whole group level. In addition, the participants were split into groups of high and low impairment as measured using their std_{RT}. Furthermore, each participant's individual stability and std_{RT} impairment was compared.

7.3.5.1 Group Level

The stability of each participant for a given EEG acquisition was calculated and Figure 7.10 shows the group-level stability across participants.

We see that the alpha and beta frequency bands both showed the same general pattern of a consistent level of stability during the day before peaking during the WMZ, as introduced in Section 2.2.3. However, when comparing the stability prior to and during the WMZ there were no significant differences as measured using permutation tests when corrected for the four frequency bands, as seen in Table 7.6. After the WMZ peak the stability started to decline from DLMO into the biological night before it reached a plateau with some variation, during the second day. The presence of a local maximum during the second WMZ was less clear. There was no clear visual trend for the delta and theta frequency bands.



(a) Delta (b) Theta

(c) Alpha (d) Beta

Figure 7.10: **Stability of Participant's Functional Networks.** The median stability, as measured from correlating the PLF networks from each all epochs for that participant from an EEG acquisition, across all participants for a given frequency band **(a)** Delta **(b)** Theta **(c)** Alpha and **(d)** Beta. The solid blue line is the mean across the participants median stability and the shaded area is the standard error of the mean. In all plots the dotted vertical lines indicate the times considered to be in the WMZ (3 hours before DLMO to 5 minutes after).

Frequency Band	Cohen's d	p-value	Adjusted p-value
Delta	0.4819	0.1682	0.2242
Theta	0.1915	0.4855	0.4855
Alpha	0.6953	0.0334	0.1337
Beta	0.3615	0.0815	0.1629

Table 7.6: **Stability Prior to and During the WMZ.** Cohen's d and associated p-values for t-tests. The associated p-values for t-test comparing all the participants 5 hours before DLMO to their maximum stability during the WMZ. Both p-values and adjusted p-values corrected for multiple comparisons using the Benjamini-Hochberg method are given [78]. Also, Cohen's d effect size is given for each frequency band.

7.3.5.2 PVT Groups

Due to the consistent significant p-values for std_{RT} impairment in Section 7.3.1 - 7.3.3 we split the participants into the two groups of low and high impairment using std_{RT} impairment. Therefore, the 13 participants were split into the 6 lowest and 6 highest impaired participants, as measured using std_{RT} impairment, with 1 participant not included. The median participant was removed to allow greater differentiation between the high and low impairment groups and ensure equal group sizes.

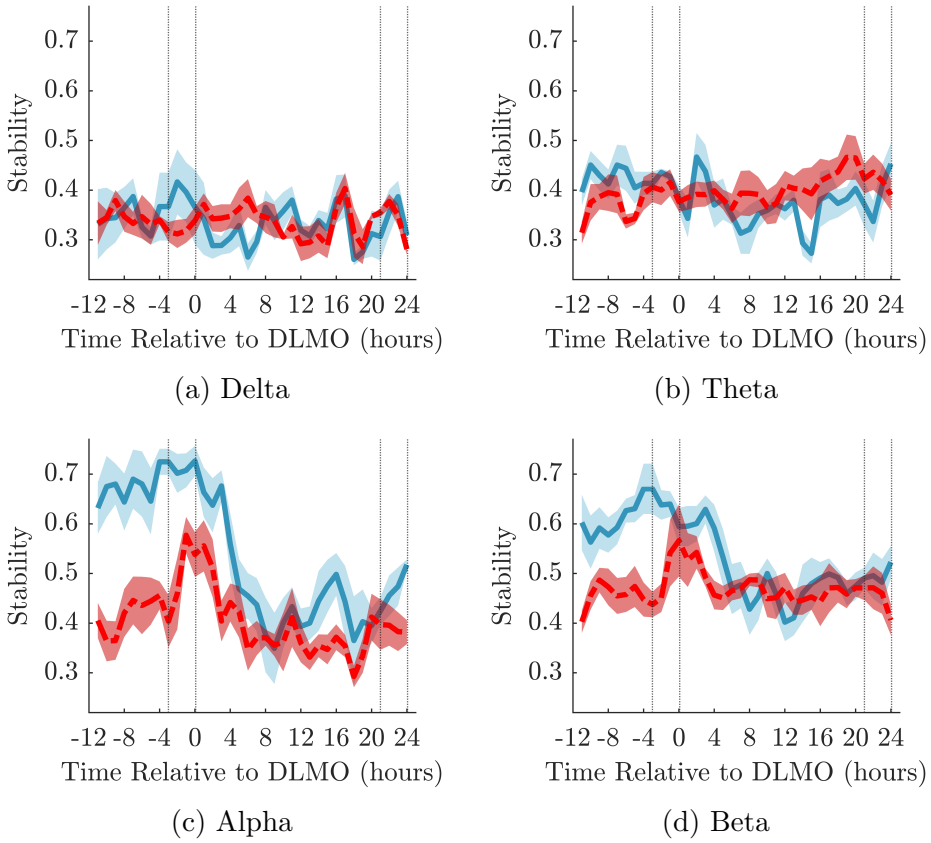


Figure 7.11: **Stability of Participant's Functional Networks with Low and High Impairment.** The median stability, as measured from correlating the PLF networks from each all epochs for that participant from an EEG acquisition, across the participant with the lowest PVT impairment and the highest PVT impairment as measured using the percentage increase in standard deviation. The solid blue line (——) is the mean across the median stability of the 6 participants with the lowest impairment and the dashed red line (- - - - -) is the mean across the median stability of the 6 participants with the highest impairment. The shaded error represents the standard error of the mean. Results are given for **(a)** Delta **(b)** Theta **(c)** Alpha and **(d)** Beta frequency bands.

As seen in Figure 7.11 and Table 7.7 when the participants were split in this way the

Frequency Band	DLMO-11h	DLMO+1h - DLMO+12h	DLMO+13h - DLMO+24h
Delta	0.1093 (0.0911)	0.1215 (0.1114)	0.4912 (0.4912)
Theta	0.0003^{*} (0.0001)	0.1093 (0.0861)	0.0007^{*} (0.0003)
Alpha	$< 0.0001^{*}$ (< 0.0001)	0.0032^{*} (0.0016)	$< 0.0001^{*}$ (< 0.0001)
Beta	$< 0.0001^{*}$ (< 0.0001)	0.0597 (0.0348)	0.0738 (0.0492)

Table 7.7: **Table Showing the *p*-values for Permutation Tests Comparing Stability with Participants Grouped by Standard Deviation of RT.** Results for Permutation Tests ($n = 10,000$) comparing the mean value of the low and high impairment groups over adjacent 12 hour periods. The p-values have been corrected using the Benjamini-Hochberg method of correcting for FDR [78]. * denotes significance p-value < 0.05. Uncorrected p-values are given in brackets.

	Low Impairment			High Impairment		
Frequency Band	Cohen's d	p-value	Adjusted p-value	Cohen's d	p-value	Adjusted p-value
Delta	1.3094	0.0116	0.0465^{*}	0.0245	0.9356	0.9356
Theta	0.2883	0.6329	0.7233	1.2013	0.0624	0.1664
Alpha	0.3595	0.5476	0.7233	1.0730	0.0070	0.0465^{*}
Beta	0.2979	0.4224	0.6758	0.4880	0.2325	0.4650

Table 7.8: **Stability Prior to and During the WMZ for Groups of High and Low Impairment.** Cohen's d and the associated p-values for t-tests comparing participants with either high or low impairment, as measured using standard deviation of RT, 5 hours before DLMO to their maximum stability during the WMZ. Both uncorrected p-values and p-values corrected for multiple comparisons using the Benjamini-Hochberg method [78].* denotes significance p-value < 0.05

groups were significantly different as measured using a permutation test during the first 12 h in the theta, alpha and beta band, the middle 12 h in only the alpha band and the final 12 h in the theta and alpha bands. Indeed, in the alpha band, the low impairment group consistently had higher stability.

It is interesting to note the different levels of stability during the first 12 h in the alpha and beta bands despite this being a time when neither group should have been experiencing the effects of sleep deprivation. Also, peak levels of stability are clearly seen during the WMZ for the high impairment group in both the alpha and beta frequency bands (Figure 7.11). However, when comparing the stability prior to and during the WMZ there was only a significant increase in the alpha band for the high impairment group, as seen in Table 7.8. This could be because the centre of the peak was towards the end and partially after the WMZ.

7.3.5.3 Individuals

To directly understand the relation between std_{RT} over the CR and the stability of the participant's network these time-series were also compared. Across all participants the std_{RT} and the stability were normalised to have a mean of 0 and a standard deviation of 1, to ensure comparable scales. This is displayed in Figure 7.12.

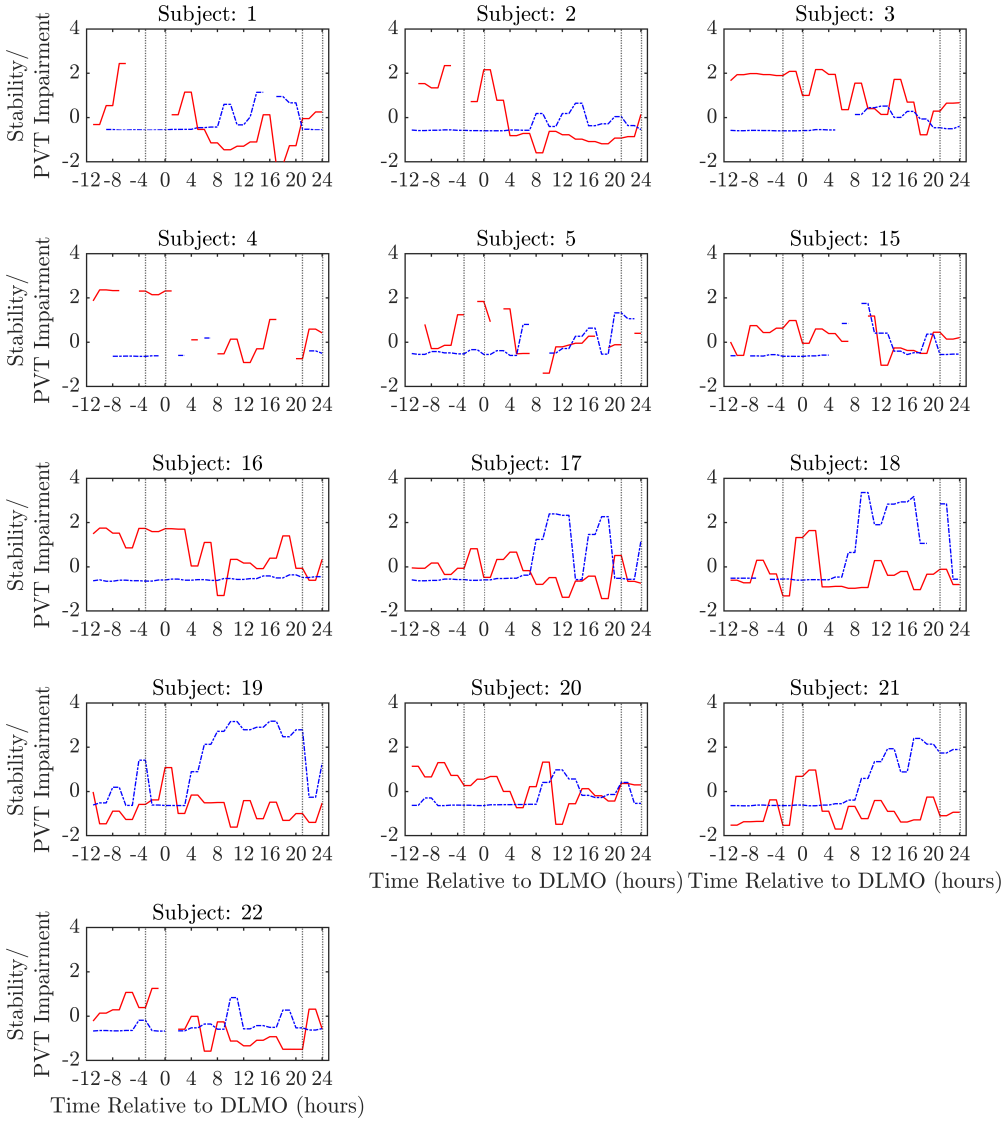


Figure 7.12: **Individual Stability and Standard Deviation on PVT.** The individual time-series for the standard deviation of RT on the PVT (-·-·-) and the stability of the functional networks (—). The dotted vertical lines indicate the times considered to be in the WMZ (3 hours before DLMO to 5 minutes after).

The general trend of the two time-series was that the PVT performance worsened

over time and the stability decreased. This trend was seen through the Spearman rank correlations for each participant between the two time-series as displayed in Table 7.9.

Particpant	Spearman's Rank Correlation	p-value	Adjusted p-value
1	-0.8139	< 0.0001	$< 0.0001^*$
2	-0.7527	< 0.0001	$< 0.0001^*$
3	-0.6603	< 0.0001	0.0001^*
4	-0.8261	0.0032	0.0052^*
5	-0.2064	0.2920	0.3796
15	-0.3327	0.0628	0.0907
16	-0.5418	0.0006	0.0017^*
17	-0.5055	0.0017	0.0036^*
18	-0.1653	0.3501	0.4137
19	-0.1363	0.4279	0.4318
20	-0.4923	0.0023	0.0043^*
21	0.1352	0.4318	0.4318
22	-0.5602	0.0006	0.0017^*

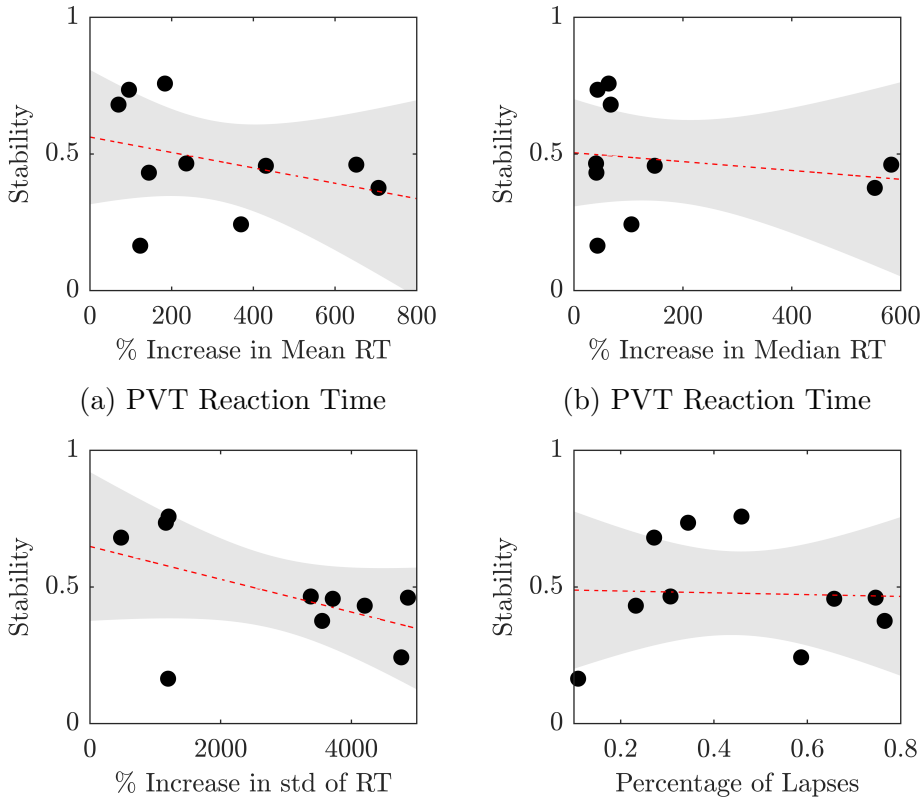
Table 7.9: **Spearman's Rank Correlation Between std RT and Stability for Individuals.** The Spearman's rank correlation and associated p-value for the correlation between the participants standard deviation of RT and the stability of their FNs over the CRP. The p-values have been corrected using the Benjamini-Hochberg method of correcting for FDR [78]. * denotes significance p-value < 0.05.

Indeed, all but one participant has a negative correlation between the two measures and for 8 out of the 13 participants this negative correlation was significant. For instance, Subject 17 exhibited a clear inverse relationship between the stability of the network and std_{RT}. This is because there were two peaks when the std_{RT} reached the level of worst performance with a brief period of recovery in between, which closely resembled the two dips in stability at almost the same time.

However, this was not true for all participants. For example, Subject 21 had a positive, albeit non-significant, correlation between the two measures. They had an increasingly impaired PVT performance, which was consistent with other participants but their stability saw no noticeable drop below the first acquisition, unlike the other participants.

7.3.6 Predicting PVT Impairment Using Stability

To understand how baseline stability can be used to predict PVT performance the median stability across each baseline acquisition was correlated to the PVT impairment. The results for B_{FA} are given in Figure 7.13 whilst the results for B_{-11} are given in Figure 7.14. In addition, the Pearson's correlation values and corresponding p-values are given in Table 7.10.

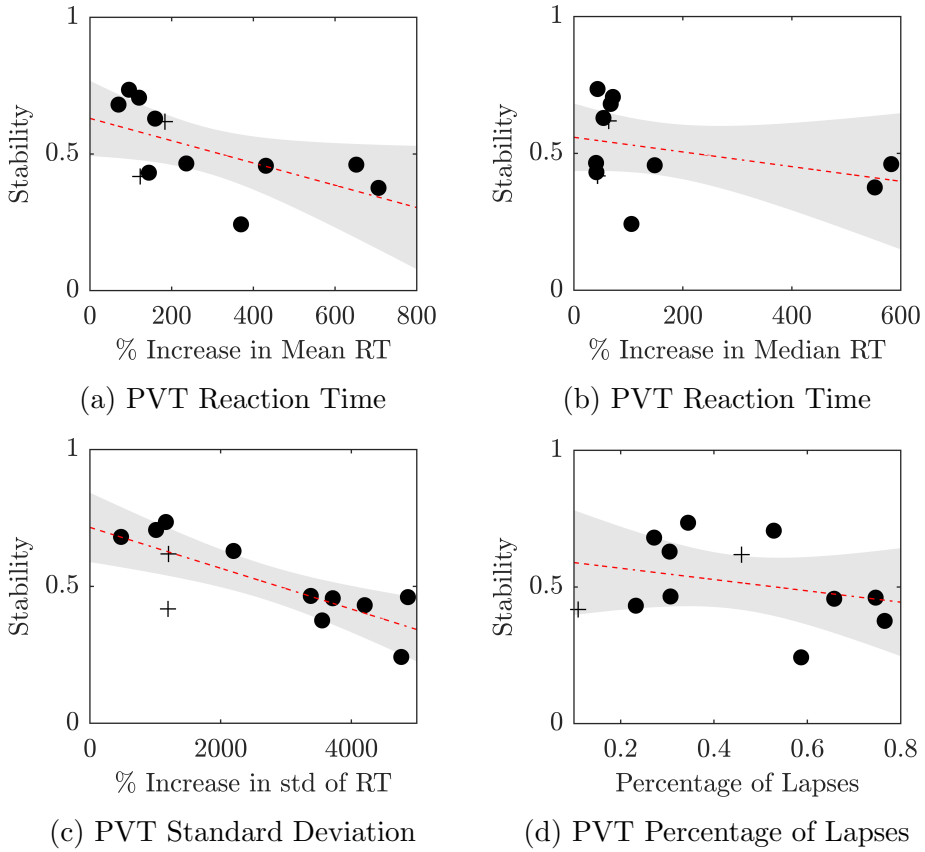


(a) PVT Reaction Time (b) PVT Reaction Time

(c) PVT Standard Deviation (d) PVT Percentage of Lapses

Figure 7.13: **Scatterplot Relating PVT Impairment to Stability for the First Acquisition After Awakening.** Scatterplots relating the PVT impairment as measured using **(a)** mean RT **(b)** median RT **(c)** standard deviation of RT and **(d)** percentage of lapses to stability for the first acquisition after awakening.

In all cases, Pearson's correlation was negative; however only B_{-11} when correlating std_{RT} and stability produced a significant p-value. Also, across all the PVT measures B_{-11} had a stronger magnitude of correlation compared to the corresponding comparison for B_{FA}.



(a) PVT Reaction Time (b) PVT Reaction Time

(c) PVT Standard Deviation (d) PVT Percentage of Lapses

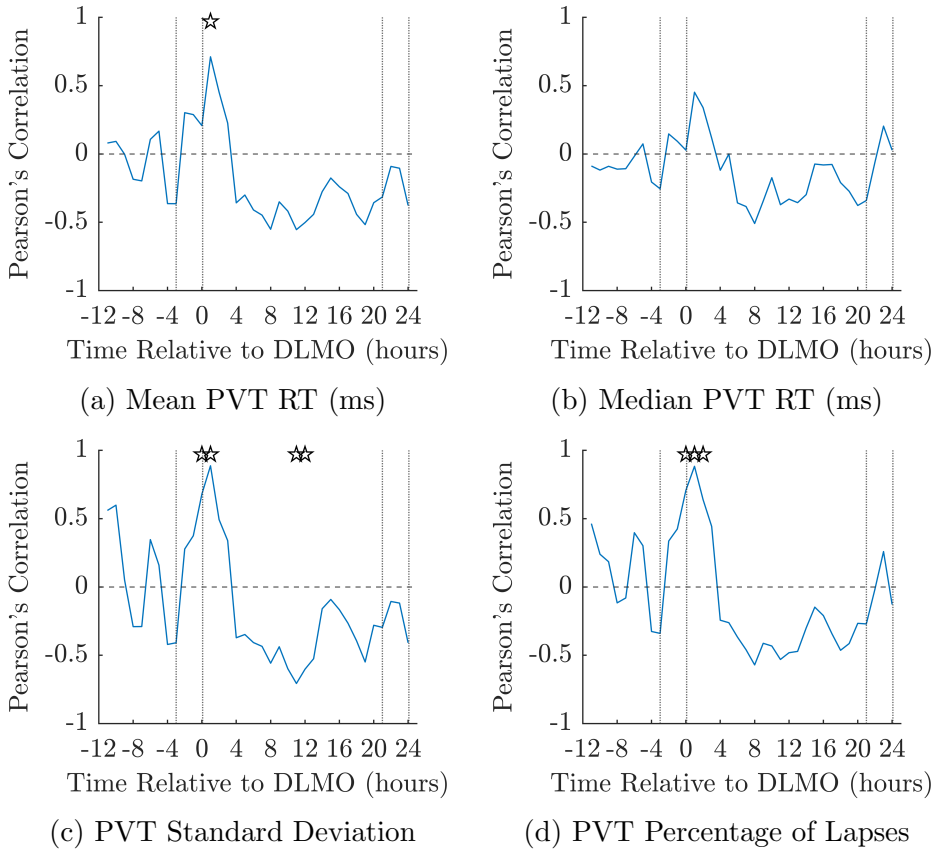
Figure 7.14: **Scatterplot Relating PVT Impairment to Stability for the Acquisition 11 Hours Before DLMO.** Scatterplots relating the PVT impairment as measured using **(a)** mean RT **(b)** median RT **(c)** standard deviation of RT and **(d)** percentage of lapses to stability for the acquisition 11 hours before DLMO.

Correlations	Pearson's Correlation	p-value	Adjusted p-value
First Acquisition: Mean RT and Stability	-0.3282	0.3545	0.4795
First Acquisition: Median RT and Stability	-0.1743	0.6302	0.7202
First Acquisition: RT std and Stability	-0.5056	0.1360	0.3627
First Acquisition: Percentage of Lapses and Stability	-0.0385	0.9160	0.9160
11 Hours Before DLMO: Mean RT and Stability	-0.5843	0.0460	0.1842
11 Hours Before DLMO: Median RT and Stability	-0.3465	0.2699	0.4795
11 Hours Before DLMO: RT std and Stability	-0.7854	0.0025	0.0197*
11 Hours Before DLMO: Percentage of Lapses and Stability	-0.2905	0.3596	0.4795

Table 7.10: **Table Showing the Pearson's Correlation and p-value for PVT impairment and Stability.** The Pearson's correlation between the participant's PVT impairment and the stability of their functional network was calculated from the first recording after awakening and the recording 11 hours before DLMO. The p-values in the table are corrected for multiple comparisons using the Benjamini-Hochberg correction for FDR [78].* denotes significance p-value < 0.05

7.3.7 Predicting PVT Performance Over the Constant Routine Protocol Using Mean Node Strength

Within this Section we use the mean node strength of the baseline EEG acquisitions to predict PVT performance over the CRP. Note that here performance values across the CRP were predicted rather than the single value of PVT impairment, which was predicted above. Across the PVT measures the timepoint that consistently had the highest amplitude Pearson's correlation was DLMO + 1 h with the std_{RT} and percentage of lapses reaching correlations of 0.89 and 0.88, respectively (Figure 7.17). Across the pe-



(a) Mean PVT RT (ms)

(b) Median PVT RT (ms)

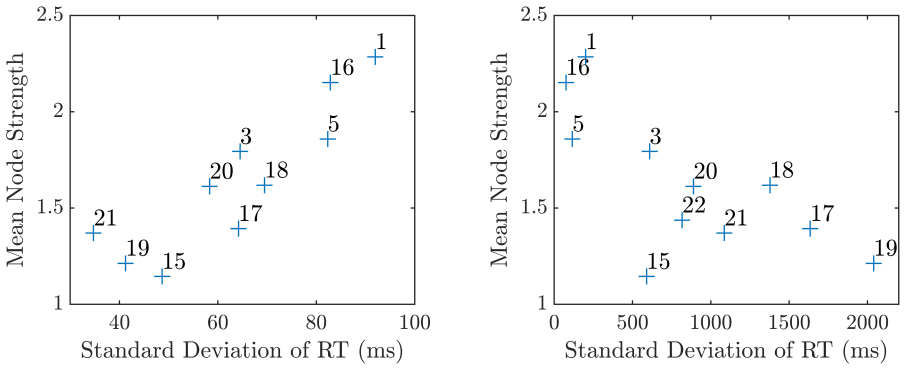
(c) PVT Standard Deviation

(d) PVT Percentage of Lapses

Figure 7.15: **Correlation Between Baseline Mean Node Strength for the First Acquisition and PVT Performance Over Time.** How the Pearson's correlation coefficient between the baseline mean node strength for the first acquisition after awakening and the PVT performance as measured using **(a)** mean RT **(b)** median RT **(c)** standard deviation and **(d)** percentage of lapses changes over the CRP. In all plots the ☆ indicates where the p-value associated with the correlation is significant $p < 0.05$ (uncorrected) and the dotted vertical lines indicate the times considered to be in the WMZ (3 hours before DLMO to 5 minutes after). Also, note that correlations are with RT, where higher PVT RT indicate worse performance.

riod [DLMO + 8 h, DLMO + 13 h] there was also a fairly consistent negative correlation across the four measures reaching -0.55 (mean RT), -0.51 (median RT), -0.71 (std_{RT}) and -0.57 (percentage of lapses) respectively. There were 6 comparisons that had significant ($p < 0.05$) p-values when uncorrected for multiple comparisons, which were clustered around DLMO, covering all PVT measures except median RT. Also, significant correlations occurred at DLMO + 11 h and DLMO + 12 h for std_{RT}. However, no significance remained after correcting for multiple comparisons using the Benjamini-Hochberg method of correcting for FDR. Although this was not surprising given the number of comparisons.

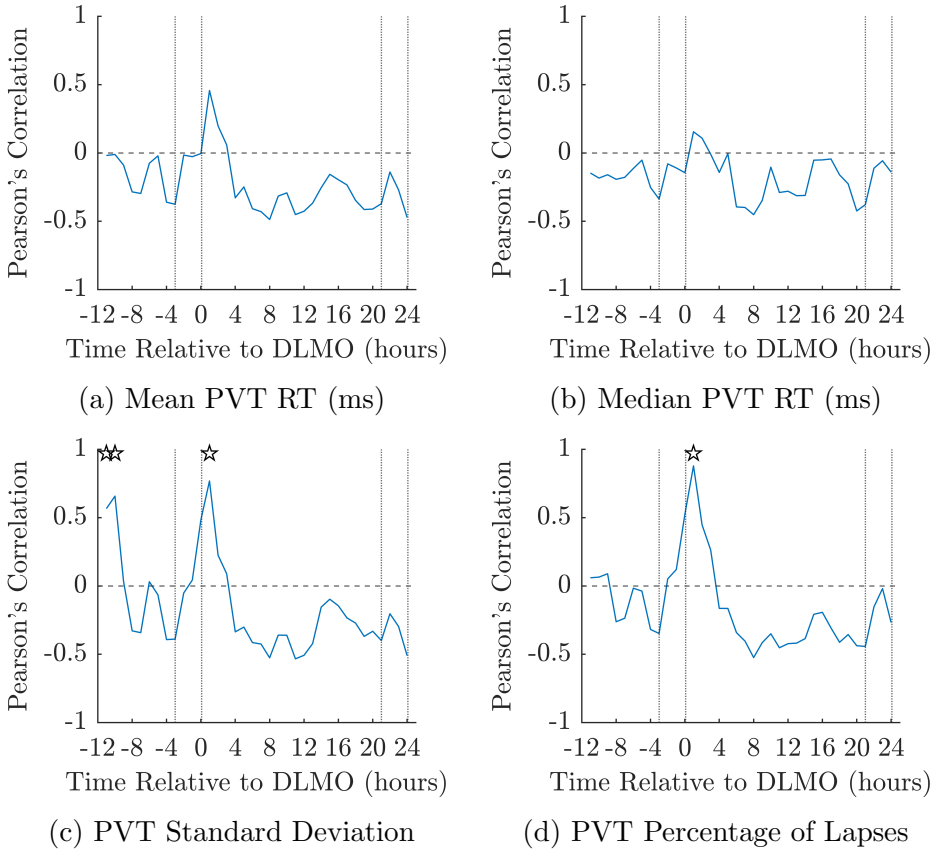
To understand the change in correlation sign that occurs between DLMO + 1 h and DLMO + 11 h scatterplots for these two times are given in Figure 7.16.



(a) DLMO + 1 h (b) DLMO + 11 h

Figure 7.16: **Scatterplots Relating Mean Node Strength to Standard Deviation of RT for the First Acquisition.** The relationship between mean node strength and standard deviation of RT at **(a)** DLMO + 1 h and **(b)** DLMO + 11 h where participants are individually labelled.

For $\text{B}_{\text{-11}}$ in Figure 7.17 the general trend of the correlation was similar to B_{FA}, however, the amplitude of the correlation was generally damped, except for DLMO−11 h and DLMO−10 h for std_{RT}. For instance, the peak at DLMO + 1 h reached correlations of 0.77 and 0.88 for std_{RT} and percentage of lapses. Also, the minimum correlation reached -0.49 (mean RT), -0.45 (median RT), -0.53 (std_{RT}) and -0.52 (percentage of lapses), respectively. Unlike B_{FA} no negative correlations were significant when uncorrected. None of the four p-values, which were significant when uncorrected, survived correcting for multiple comparisons using the Benjamini-Hochberg method of correcting for FDR.



(a) Mean PVT RT (ms)

(b) Median PVT RT (ms)

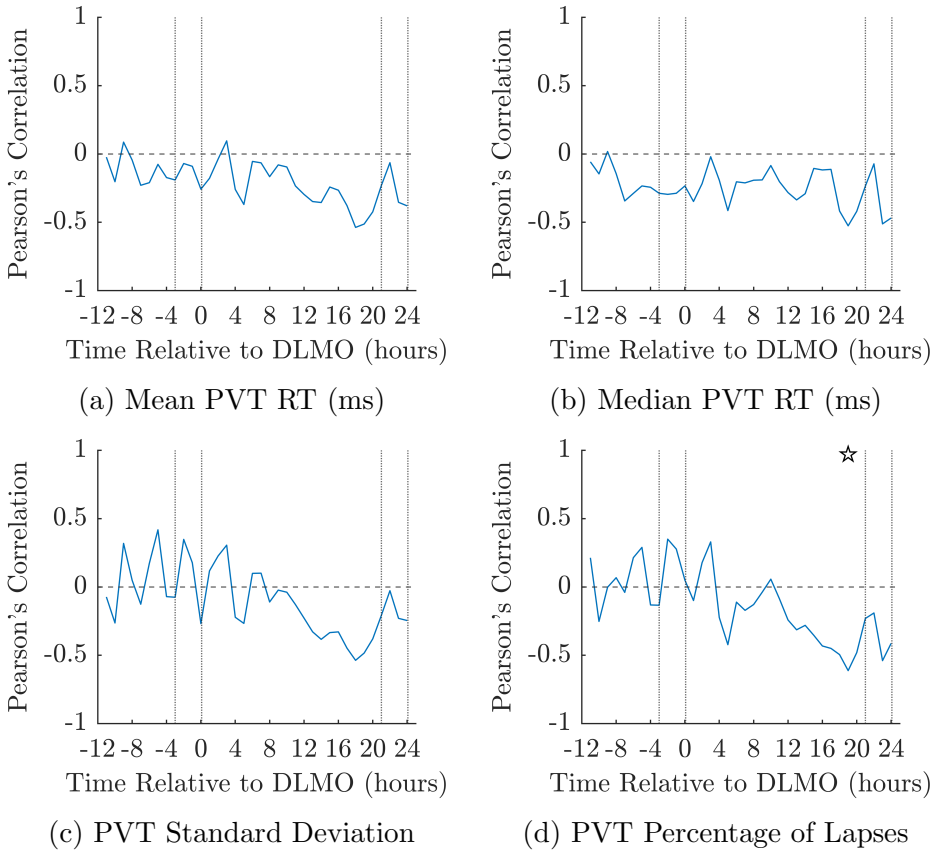
(c) PVT Standard Deviation

(d) PVT Percentage of Lapses

Figure 7.17: **Correlation Between Baseline Mean Node Strength for the Acquisition 11 hours before DLMO and PVT Performance Over Time.** How the Pearson's correlation coefficient between the baseline mean node strength for the acquisition 11 hours before DLMO and the PVT performance as measured using **(a)** mean RT **(b)** median RT **(c)** standard deviation and **(d)** percentage of lapses changes over the CRP.

7.3.8 Predicting PVT Performance Over the Constant Routine Protocol Using Trophic Incoherence

The Pearson's correlation between the trophic incoherence of the two baseline acquisitions and PVT performance over the CRP was rarely above zero for the mean and median RT as seen in Figures 7.18 and 7.19. However, a negative correlation ~ -0.5 was reached near DLMO + 18 h for std_{RT} and the percentage of lapses for both baseline acquisitions. Also, the Pearson's correlation between trophic incoherence and std_{RT} and percentage of lapses for B_{FA} to PVT performance for $[\text{DLMO} - 11\text{ h}, \text{DLMO} + 3\text{ h}]$ showed high variability between $\sim -10\%$ and $\sim 30\%$. Overall, the greatest magnitude reached was -0.61 ($p = 0.03$, uncorrected) for the percentage of lapses at DLMO + 19 h.



(a) Mean PVT RT (ms)

(b) Median PVT RT (ms)

(c) PVT Standard Deviation

(d) PVT Percentage of Lapses

Figure 7.18: **Correlation Between Baseline Trophic Incoherence for the First Acquisition and PVT Performance Over Time.** How the Pearson's correlation coefficient between the baseline trophic incoherence for the first acquisition after awakening and the PVT performance as measured using **(a)** mean RT **(b)** median RT **(c)** standard deviation and **(d)** percentage of lapses changes over the CRP.

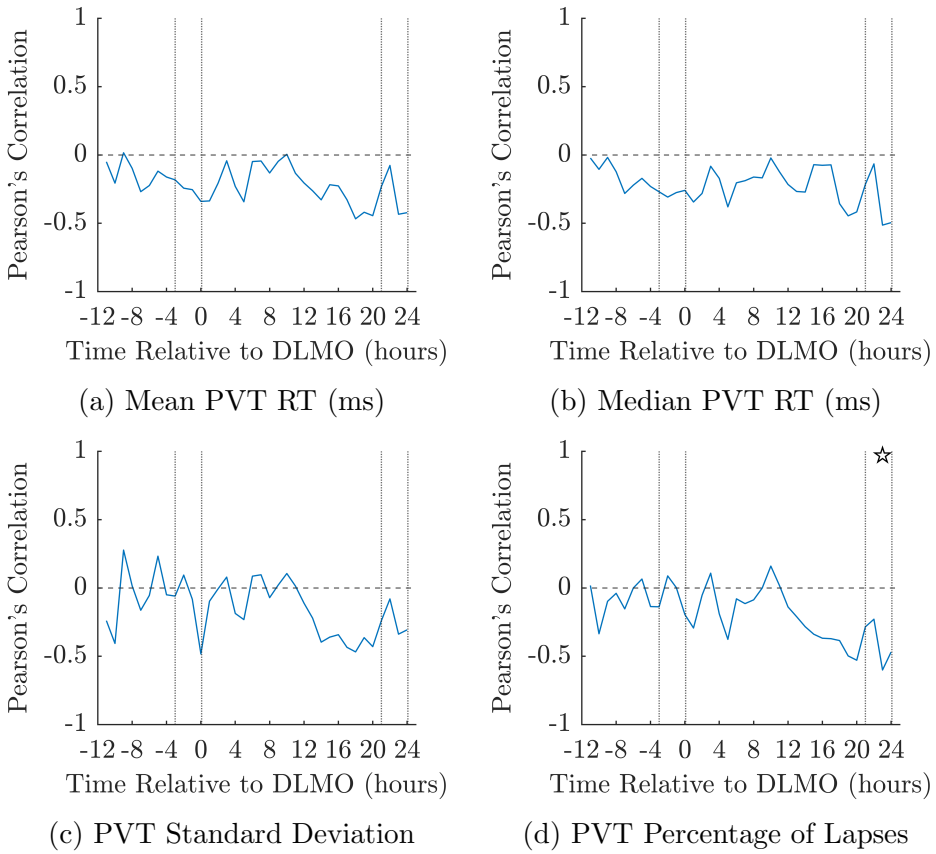


Figure 7.19: **Correlation Between Baseline Trophic Incoherence for the Acquisition 11 hours before DLMO and PVT Performance Over Time.** How the Pearson's correlation coefficient between the baseline trophic incoherence for the acquisition 11 hours before DLMO and the PVT performance as measured using **(a)** mean RT **(b)** median RT **(c)** standard deviation and **(d)** percentage of lapses changes over the CRP.

7.3.9 Predicting PVT Performance Over the Constant Routine Protocol Using Synchronisation Index

The correlations between SI at each K_g and PVT performance showed similar trends to mean node strength above and stability below. The full results for std_{RT} across all K_g are seen in Figures 7.20 and 7.21, corresponding results for the other PVT measures are given in Appendix D.5. For ease of comparison with the other sections the results for B_{FA} when K_g = 6 as an example are also plotted in Figure 7.22.

We see a spike of high correlations across a large range of K_g occurred for std_{RT} (Figures 7.20 and 7.21) and the percentage of lapses (Figures D.13 and D.14) for both baseline acquisitions at DLMO + 1 h. In addition, negative correlations were seen at DLMO + 11 h and DLMO + 19 h, however this is reduced for $\text{B}_{\text{-11}}$.

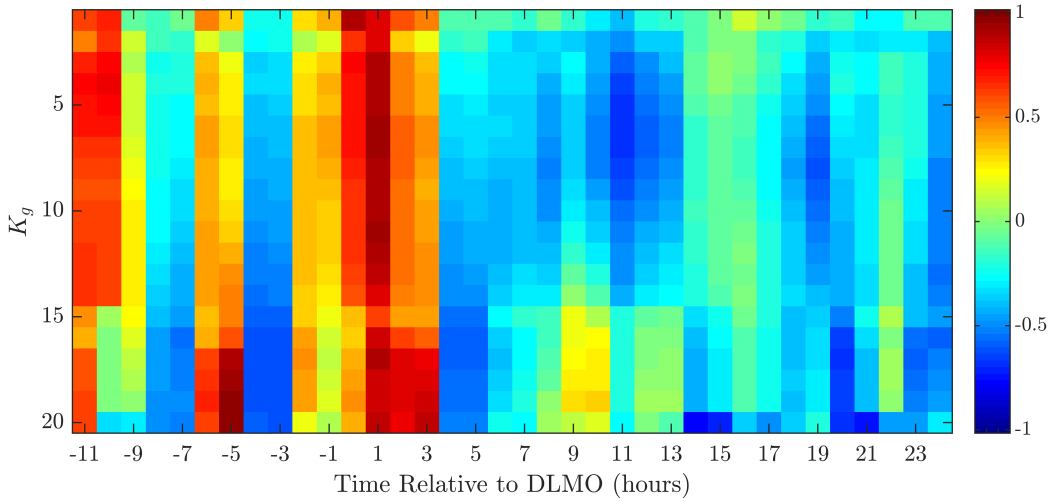


Figure 7.20: **Colorplots Showing the Correlation Between the SI for the First Acquisition after Awakening and PVT Standard Deviation RT.** The Pearson's correlation between SI for the first acquisition after awakening at a given K_g and PVT performance measured using the standard deviation of RT at a specific timepoint.

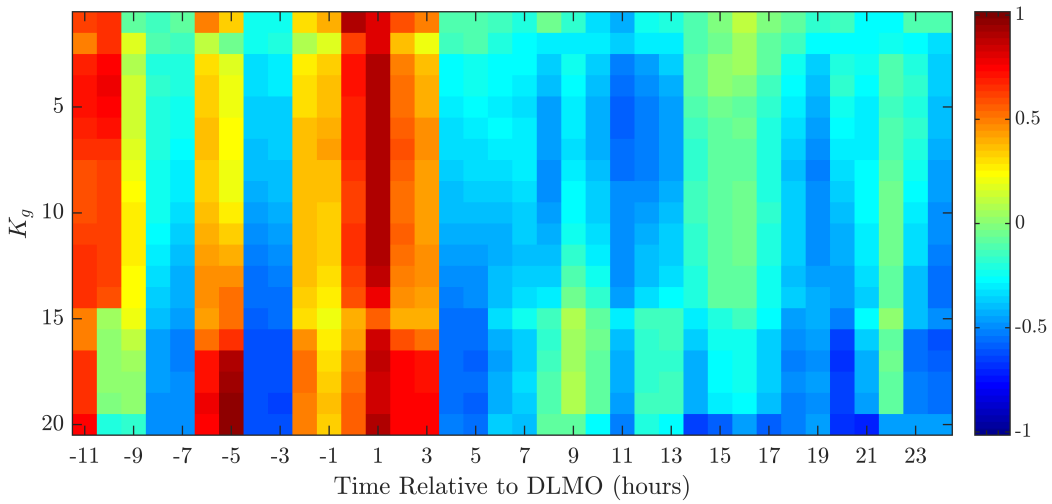


Figure 7.21: **Colorplots Showing the Correlation Between the SI for the Acquisition 11 hours before DLMO and PVT Standard Deviation RT.** The Pearson's correlation between SI for the acquisition 11 hours before DLMO at a given K_g and PVT performance measured using the standard deviation of RT at a specific timepoint.

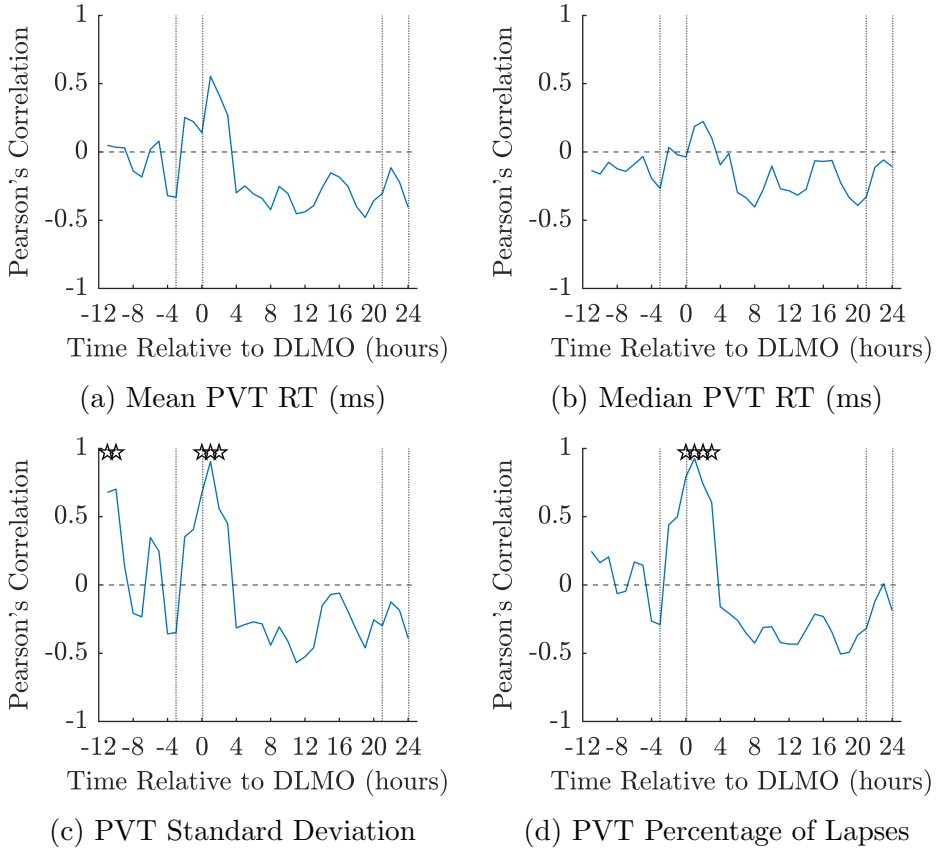
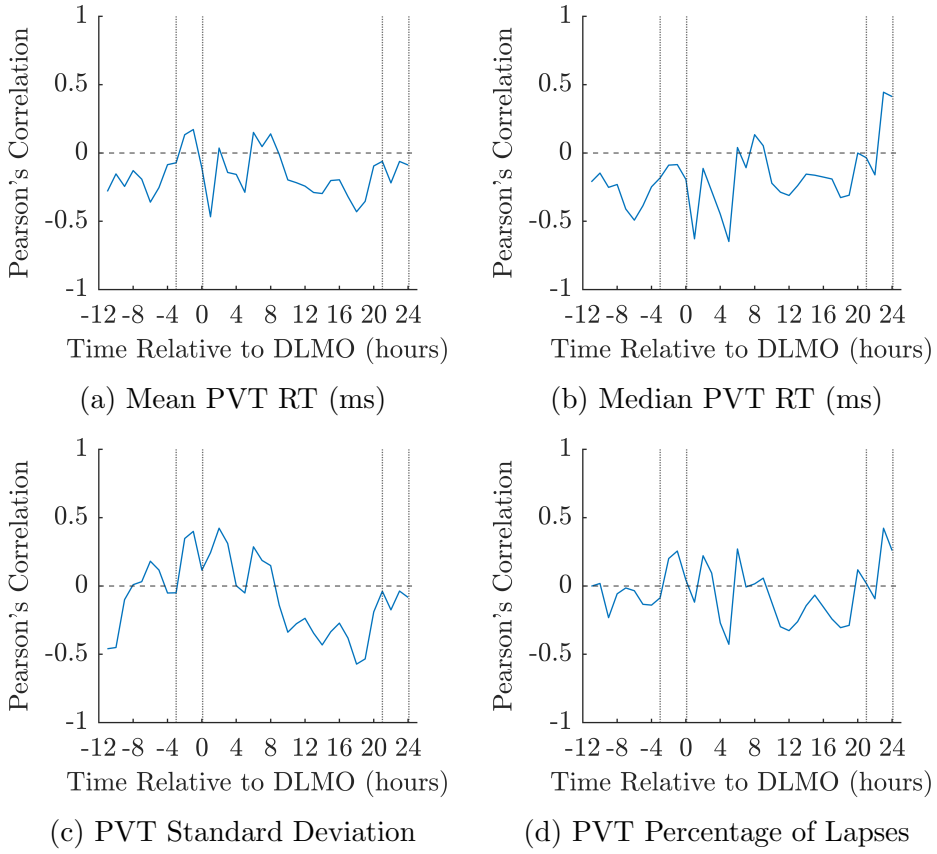


Figure 7.22: **Correlations Between the SI for the First Acquisition and PVT Performance Over Time.** How the Pearson's correlation coefficient between the baseline SI at K_g = 6 for the first acquisition after awakening and the PVT performance as measured using **(a)** mean RT **(b)** median RT **(c)** standard deviation and **(d)** percentage of lapses changes over the CRP.

7.3.10 Predicting PVT Performance Over the Constant Routine Protocol Using Stability

For B_{FA}, as seen in Figure 7.23, even without correcting for multiple comparisons there were no significant p-values. Overall, the general trend was similar to that seen for trophic incoherence however during the second WMZ there was a positive correlation reaching 0.44 for the median RT and percentage of lapses.



(a) Mean PVT RT (ms)

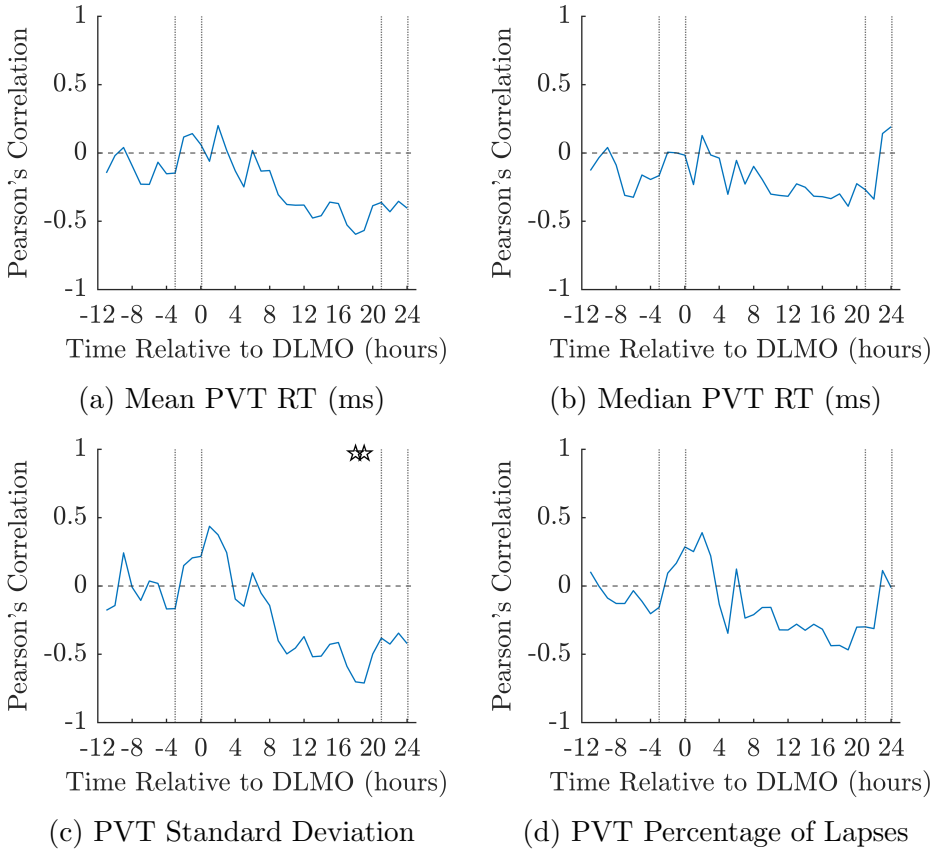
(b) Median PVT RT (ms)

(c) PVT Standard Deviation

(d) PVT Percentage of Lapses

Figure 7.23: **Correlation Between Baseline Stability for the First Acquisition and PVT Performance Over Time.** How the Pearson's correlation coefficient between the baseline stability for the first acquisition after awakening and the PVT performance as measured using **(a)** mean RT **(b)** median RT **(c)** standard deviation and **(d)** percentage of lapses changes over the CRP. Note that $p > 0.05$ (uncorrected) for all correlations.

For $B_{\text{-}11}$, as displayed in Figure 7.24, the only significant correlations before correcting for multiple comparisons occurred for std_{RT} at DLMO + 18 h and DLMO + 19 h with Pearson's correlation ~ -0.7. A similar spike in positive correlation to mean node strength was seen at DLMO + 1 h for std_{RT} and percentage of lapses, however with a reduced



(a) Mean PVT RT (ms)

(b) Median PVT RT (ms)

(c) PVT Standard Deviation

(d) PVT Percentage of Lapses

Figure 7.24: **Correlation Between Baseline Stability for the Acquisition 11 hours before DLMO and PVT Performance Over Time.** How the Pearson's correlation coefficient between the baseline stability for the acquisition 11 hours before DLMO and the PVT performance as measured using **(a)** mean RT **(b)** median RT **(c)** standard deviation and **(d)** percentage of lapses changes over the CRP.

amplitude.

7.4 Discussion

Within this Chapter, we have sought to understand the relationship between sleep deprivation and FNs. In particular, we used only information from baseline EEG acquisitions to try and predict to what extent an individual participant is impacted by sleep deprivation. The level of impairment was calculated by their performance on bi-hourly PVT tests over a 40 h CRP, as measured using the mean, median and standard deviation of RT and percentage of lapses. Graph metrics and synchronisation from a baseline EEG acquisition were used as predictors. Initially, an investigation into predicting the highest percentage increase in PVT performance over the CRP, known as impairment, was completed. High mean node strength, high stability and high SI at baseline significantly correlated with lower levels of impairment as measured using PVT. A natural extension was to consider if information from baseline EEG acquisitions could predict PVT performance across the CRP. This analysis showed that high mean node strength, high stability and high SI at baseline, are not only associated with more resilience to sleep deprivation during the second day of the CRP but are more strongly associated with reduced performance at DLMO + 1 h - when the drive to sleep starts to increase. This means that in general the performance of the group still decreased with time awake but within the group the ranking of the participants changed such that the individuals with the worst performance at DLMO + 1 h where among the best performers at DLMO + 11 h as seen in Figure 7.16.

In particular, mean node strength could predict the greatest amount of variability in the level of impairment, reaching correlations of -0.87 (Table 7.2) for std_{RT}. However, we see an even stronger positive correlation, 0.89, between mean node strength and std_{RT} at DLMO + 1 h, see Figure 7.15. Therefore, indicating that individuals with high mean node strength at baseline will be the worst performers within a group at DLMO + 1 h and the best performers within the group at DLMO + 11 h. However, the overall performance of the group will be reduced at DLMO + 11 h as reaction times become longer and more variable, see Figure D.1. There is very limited literature available that uses FC to predict performance under the influence of sleep deprivation. One such paper is by Mu et al. [139]

who found using fMRI that low baseline (09 : 00 local time) global brain levels, measured as the number of activated voxels after correcting for multiple comparisons, correlated with vulnerability to sleep deprivation (30 h) on a working memory task. In addition, Caldwell [31] found that levels of cortical activation from fMRI in fighter pilots were significantly correlated with resilience to sleep deprivation as measures using performance in a flight simulator. These studies differs in many ways, such as using fMRI rather than EEG, no CRP and use of a memory task and real-world simulator rather than sustained attention. However, global brain activation can be seen as analogous to mean node strength and therefore the results at least align after extended sleep deprivation.

The result for SI (Sections 7.3.3 and 7.3.9) and stability (Sections 7.3.6 and 7.3.10) are both similar to those of mean node strength, albeit the magnitude of the correlations are generally diminished. A common feature is a positive correlation occurring at DLMO + 1 h, indicating high mean node strength, high SI and stability are associated with worse performance at DLMO + 1 h, when the bodies natural drive towards sleep increases.

Also, near DLMO + 11 h we see a negative correlation between PVT performance and baseline markers. The negative correlations at DLMO + 11 h are consistent with the results in Sections 7.3.1, 7.3.3 and 7.3.6 when predicting impairment, however the magnitude is lower. This reduction could be due to both inter-individual differences in the periods of circadian rhythms and the data being aligned to DLMO. For instance, if the periods differ then timepoints closer to the phase-locking time of DLMO, such as DLMO + 1 h, will be more consistently phase locked across participants. Whereas at DLMO + 11 h phases may be more misaligned. Also, Table 7.1 shows high variability in the timing of the worst performance, which could explain the reduced predictive capacity over the CRP when considering a specific timepoint.

Therefore, across the CRP the EEG derived predictors correlate with PVT performance measures both positively and negatively. This indicates that while sleep deprivation has a general negative effect on a population's performance, it may be the individual's own circadian rhythm that dictates the magnitude of the effect at a given time. Indeed

the EEG derived marker may indicate greater susceptibility to the perturbation of sleep deprivation and in particular the influence of the circadian rhythm. This is because if the monotonically increasing homeostatic process, as introduced in Section 3.3, was the only influence, then the order of sleep deprivation susceptibility within the group would have no reason to reverse. However, a stronger circadian strength that pushes individuals more towards sleep at night but also more towards alertness in the day could explain the change in correlation sign. Indeed, if circadian strength reflects performance, then a higher circadian amplitude could force better and worse performance at the trough and peak respectively, compared to an individual with reduced circadian amplitude. Indeed if total sleep deprivation is unavoidable, then the best individual for a task at DLMO + 1 h would actually be among the worst to complete the task at DLMO + 11 h. Therefore, an investigation into whether the FN predictors could be related to circadian strength, as measured using core body temperature, was completed in Appendix D.2. However, no significant relationship between circadian strength and any of the baseline markers were found. There is a potential that circadian strength as measured using core body temperature is not related enough to circadian strength within the brain. Therefore, circadian strength measured from brain temperature using new non-invasive magnetic resonance spectroscopy in the future may be more informative. Especially as brain temperature is known to relate to neurological conditions including epilepsy and mood disorders [199] and circadian changes in brain temperature have been found to be predictive of survival after brain injury, with the absence of circadian changes indicative of lower survival rate [162].

In addition, throughout the analysis, B_{FA} saw a consistently higher magnitude of correlation compared to $B_{\text{-}11}$, when significance occurred, for all metrics other than stability. Indeed, when correlating mean node strength with std_{RT} impairment B_{FA} could explain $\sim 20\%$ more variance than $B_{\text{-}11}$. However, for stability only $B_{\text{-}11}$ could explain a significant amount of the variance and in this case $\sim 17 - 25\%$ more variance was explained. Similar changes in predicting PVT performance across the two baseline acquisitions are seen

when correlating over the CRP. With only 13 participants, it is difficult to understand how much of this effect is actually due to the time of the acquisition or because of the relatively small sample size, but it does seem to indicate that while $B_{\text{-}11}$ has some predictive power B_{FA} is more successful. It is unclear exactly why the first acquisition after awakening generally performs better but it could be linked to sleep inertia. For instance, the three process model [68] uses a sleep inertia term to correct levels of alertness for three hours after awakening, which is within the timeframe of the first acquisition after awakening. However, the acquisition closest to DLMO $-$ 11 h was recorded ~4 hours after awakening for some participants. Alternatively, the timelocking across the participants is more consistent for B_{FA} compared to $B_{\text{-}11}$. Indeed for B_{FA} the acquisitions took place 2.53 ± 0.09 h after awakening, whilst the acquisitions for $B_{\text{-}11}$ took place 11.02 ± 0.61 h before DLMO. This increase in variability could have hindered the ability to predict PVT performance.

Unlike the other metrics, trophic incoherence was unable to significantly predict PVT impairment in either baseline acquisition for any of the four PVT measures (Table 7.3). When predicting PVT performance across the CRP the correlation magnitude increased, however trophic incoherence showed high levels of variability during the first 24 h of the protocol for std_{RT} and percentage of lapses (Figures 7.18 and 7.19). More consistent negative correlations were seen when correlating trophic incoherence with PVT performance towards the end of the CRP across both baseline acquisitions. Indeed significance when uncorrected occurs for the percentage of lapses. This provides limited evidence that increased trophic incoherence at baseline is associated with impairment from sleep deprivation.

Within Chapter 6 trophic incoherence was seen to correlate highly with SI in Sections 6.3.2.1 and 6.3.3.1 when mean node degree was fixed and did not correlate when mean node degree differed between networks (Section 6.3.1.1). Here weighted networks were used and mean node strength varied between individual FNs. Therefore, the lack of correlation between trophic incoherence and PVT impairment and performance is not surprising.

Ultimately, we see trophic incoherence is not able to explain the main variability in the PVT impairment but linear and multiple regressions were completed in Section 7.3.4 to better understand the contribution of trophic incoherence for predicting std_{RT} impairment. When comparing the performance of the linear regression with just mean node strength to the performance of the linear regression with both mean node strength and trophic incoherence, we see that the multiple regression can explain some additional variability in the participant's level of impairment. Especially for B_{FA}, where trophic incoherence explained an additional 4% of the variance, as seen in Table 7.4, which is broadly in line with the results of multiple regressions seen in Chapter 6, as seen in Tables 6.4 and 6.5 .

A more in-depth comparison between the results of Chapter 6 and Chapter 7 is given in the Discussion in Section 8.2.

Across both the impairment and performance analysis, the ability to predict std_{RT} was consistently high. This could be because the measure encompasses both the sporadic good RTs and the lapses, that are consistent with the state instability hypothesis [53]. Indeed, Van Dongen et al. [51] suggests that state instability could be due to parts or even the whole brain falling asleep for brief periods of time, neighboured by periods of normal wakefulness - note that within this protocol of total sleep deprivation only regional sleep could occur. Also, this could explain why the median consistently has the weakest correlation as it, by the nature of the metric, removes the effect of these extremes so the variability seen when sleep deprived will be damped.

Furthermore, motivated by the instability hypothesis [53] the stability of the FNs across the CRP was calculated, using the 2-D correlation between each possible pair of EEG epochs in a given acquisition for an individual to try and understand how the brain reacts to sleep deprivation both in the long term over the protocol and the short term within an EEG acquisition. The stability across all participants in the alpha and beta frequency bands (Figure 7.10) shows a relation to the PVT measures. Importantly, the stability of the FNs shows peaks and local maxima during the WMZ, highlighting the effect of the circadian rhythm, while the drop in stability during the biological night

shows the influence of the homeostatic pressure. This corresponds to the steep decrease in PVT performance during the biological night ~ 5 hours after DLMO before a marked improvement during the WMZ, as seen in Figure D.1. This relation could provide evidence for the state instability hypothesis [53], which suggests that brief returns to baseline levels occur alongside a general decrease in performance creating more variability. Indeed, instability and std_{RT} both increase with sleep deprivation reflecting increased variability in both FNs and behavioural performance, respectively.

The drop in stability in the alpha frequency band could be due to the drop in alpha spectral power that is found to occur during sleep deprivation [209]. However, the spectral power of theta is known to increase with time awake [29] and this does not coincide with an increased stability in the theta band. This motivates future research into how spectral power affects the properties of FNs and in particular the effect on stability.

When the participants are split into groups based on std_{RT} impairment, we see a stark difference in the stability of the two groups in the alpha and beta bands during the first 12 hours. Indeed, the stability significantly differs in both frequency bands and theta, as seen in Table 7.7, despite the fact neither group should be influenced by sleep deprivation during this time and the PVT performance of the two groups does not significantly differ in the mean, median or standard deviation of RT as seen in Table D.1. It is worth noting that the high impairment group does have a significantly higher percentage of lapses during the first 12 hours. Therefore, this could suggest that the percentage of lapses can reflect stability better than the other measures. However, as the percentage of lapses is unable to predict impairment, see Figures 7.13 and 7.14, it is difficult to assess how informative this measure is. If instead we consider the lack of significant difference in the other three PVT measures paired with the significant differences in stability this could suggest that the level of impairment a participant faces when sleep deprived is due to a mechanism that is present during the day, but only affects performance when sleep debt accumulates. Interestingly it is through sleep deprivation that the stability of the groups becomes more similar in the alpha and beta bands. Indeed, the beta frequency band no

longer significantly differs. This occurs due to the low impairment group decreasing their level of stability closer to the high impairment group, rather than any marked change in the high impairment group. However, the PVT performances start to differ significantly across all four measures, Table D.1. This could suggest that the stability in the alpha band is the most informative and most closely linked to PVT performance.

It was shown by Ly et al. [125] that the amplitude of a TMS response significantly decreased from prior to the WMZ to the WMZ. Here, we see a visual increase in stability in the alpha and beta frequency bands as we enter the WMZ (Figure 7.10) - especially in the high impairment group, which sees a significant increase (Figure 7.11) - suggesting a reduction in cortical excitability. Also, the general pattern of stability in this study decreases with sleep deprivation in the alpha and beta bands, especially for the low impairment group whilst excitability is known to increase with sleep deprivation [125, 135]. Therefore, this suggests that high stability can be interpreted as less excitability and vice versa. Although, this relationship seems to be more obvious in the two impairment groups at different times of the CRP. As the high impairment group have similar levels of stability throughout the protocol aside from during the WMZ; while the low impairment group sees a general decline.

When considering stability at the level of the individual the general trend over the participants is an inverse relationship between std_{RT} on the PVT and the stability of their FNs. Indeed as their std_{RT} increases their stability decreases. This is true for all but one participant and this trend is significant for 8 out of the 13 participants, as measured using Spearman's rank correlation, Table 7.9. This provides additional evidence for the association between PVT performance and the stability of the network. The variability in the strength between the correlation of the two measures is to be expected given the trait-like vulnerability to sleep-deprivation found by Chua et al. and Van Dongen et al. [37, 49]. Across both measures the variability between acquisitions is quite high, especially for stability. Dynamic changes to sleep deprivation are to be expected given the epochs cover 150 s and the instability hypothesis suggests sporadic returns to baseline, such

changes could differ in frequency between testing sessions. However, despite the significant correlations for certain participants, it is unlikely that stability is the only factor driving PVT performance. Indeed, if stability was the only factor then the high impairment group would see poor PVT performance during the first day. Therefore, stability may only be a factor when sleep deprivation occurs and a compensatory mechanism may be present during the day to counteract the low stability, which is no longer effective under constant wakefulness. For instance, prolonged wakefulness is known to affect the concentrations of neurotransmitters through increasing excitatory neurotransmitters [143]. Future research could investigate if there is an underlying link between neurotransmitters and the stability of FNs or alternatively PVT performance.

A fundamental limitation of this study is the availability of only 13 participants' PVT data out of the possible 22. However, as significant correlations and differences have been found, this Chapter still motivates further studies with a greater number of participants to understand how generalisable the results are to the population. Although the long and complex nature of the studies protocol and the large amount of data required, may hinder much larger levels of recruitment.

Furthermore, as there are only two PVT datasets from females, we were unable to investigate if sex differences affect predictive power. For instance, Santhi et al. [163] have already shown that sex $\times$ time awake interactions are significant when participants are kept awake for 19 h and Blatter et al. [16] have shown that women have significantly slower RTs than men. This suggests sex differences may contribute to a person's vulnerability to sleep deprivation and the ability to predict this vulnerability, should be considered in future studies through a higher recruitment of females. In addition, the participants in this study were younger adults (25.53 ± 5.78 years), therefore repeating the dataset on older adults to understand if the findings are similar would be of future interest, especially as older adults while worse when rested were found to be less impacted by sleep deprivation, as measures using PVT, compared to younger adults [16]. Furthermore, only ICPs have been considered in the study. Since the higher correlations were found when considering

B_{FA} rather than B_{-11} it may be that for restful extreme chronotypes the conclusions are the same. However, Facer-Childs et al. [57] found that PVT performance profiles do differ between extreme chronotypes and are significantly different at 08 : 00, which is similar to the time of both baseline acquisitions. Also, when constrained to the societal day the sleep debt that LCPs are prone to face may alter predictive ability. Indeed, predicting susceptibility to sleep deprivation in the context of sustained sleep restriction rather than prolonged deprivation could be an interesting extension of this research across the chronotype spectrum.

In addition, throughout the predictive analysis at most two EEG acquisitions were considered per person. It is reasonable that other EEG acquisitions over the 40 h CRP would have some predictive power; however, no other acquisitions were used. For instance, Chua et al. [37] used data collected every 2 h across the first 16 h of wakefulness to create one predictor. However, we choose not to use additional samples as sampling across multiple hours reduces practicality and considering additional timepoints could create problems that could arise from multiple comparisons. Indeed the analysis in this chapter could be seen as streamlining the approach of Chua et al. [37] as high predictive power (Pearson's correlation of 0.89) from a singular EEG acquisition increases the practicality for real-world applications in the future. In addition, this analysis has expanded upon the work completed by Chua et al. [37] by correlating susceptibility to sleep deprivation using the properties of FNs rather than just EEG spectral power, which explained a maximum of 66% of the trait-like variance between participants.

Throughout this analysis the predictions were calculated using FNs created using the alpha frequency band. The alpha band was chosen due to the literature which shows the alpha band has the highest spectral content during the baseline acquisitions [109]. Also, Chua et al. [37] found that only the alpha power spectrum could explain significant amounts of the variance between participants when they were sleep deprived. However, checking the predictive capacity of the other frequency bands is a possible extension. In addition, the predictive capacity of individual electrodes could be considered in the

future. For instance, Verweij et al. [195] found that only scalp electrodes placed above the prefrontal and frontal brain regions were significantly impacted by sleep deprivation, therefore a focus on these electrodes could offer more predictive capacity.

In addition, within this study impairment was assessed using the results from PVT. PVT has been used in many sleep deprivation studies to assess the impact on performance. The requirement of sustained attention for high PVT performance is thought to reflect some real-world scenarios - especially tasks which require quick response times [9]. Also, a lack of sustained attention is likely to have negative downstream impacts on other cognitive tasks. For example, PVT performance has been linked to performance in other tasks such as memory [42], lane position and speed variability in a simulated driving scenario [99] as well as mathematical fluency and reading comprehension in children [74]. Therefore, while PVT provides a basis for results with real-world implications this study still motivates future research into how well the markers of sleep deprivation in this Chapter are predictive of performance in other tasks and the link between PVT and other cognitive tasks in general.

Overall, we have approached the problem of sleep deprivation from two different angles: how can baseline networks be used to predict the effect of sleep deprivation using FNs and how does the stability of the networks help to understand the effect of sleep deprivation? We have seen that within a group lower mean node strength, lower SI, less stability and slightly more coherent networks are all features associated with greater levels of impairment after a night of sleep deprivation, as measured using std_{RT}. However, these same features are associated with improved performance at DLMO + 1 h. Therefore, whilst the performance is generally decreased throughout the CRP the ranking of the participant's performance almost reversed, suggesting the optimum person to complete a task at DLMO + 1 h is actually amongst the worst at DLMO + 11 h. Hence, indicating high mean node strength, high SI and high stability make performance more susceptible to the perturbations of sleep deprivation. Also, the stability of the network may help to explain why some participants are more resistant to the effects of sleep deprivation and

why PVT performance generally decreases with wakefulness. This research could help to better tailor roles within high-risk situations to ensure the task is not completed by the same individual for an entire shift but instead is given to a more optimum employee for that timepoint. The practicality of such a suggestion may be outweighed by the benefits of ensuring sleep deprivation does not occur. However, in unavoidable situations, it would provide employers with a greater chance of mitigating accidents associated with fatigue. Furthermore, individuals could have greater awareness about the level of risk associated with their actions such as whether they should be driving at a given time.

CHAPTER 8

DISCUSSION

This thesis considered the effect of sleep and circadian rhythms from two different perspectives using two datasets. Initially, an investigation into how rs-fMRI derived FNs differed between extreme chronotypes was undertaken. This naturally led to an investigation into how the properties of FNs (theoretical and those derived from EEG data) are associated with the effects of sleep deprivation.

The underlying theme of the Results Chapters was the drive of the circadian rhythm and the association with FNs. For example, it is the phase difference between the endogenous circadian rhythms of extreme chronotypes which defined the ECPs and LCPs in Chapters 4 and 5. Also, within the theoretical simulation in Chapter 6 and the sleep deprivation protocol in Chapter 7 both synchronisation and the performance of the participants over time are affected by both the endogenous circadian rhythm and the homeostatic pressure to sleep.

Furthermore, the main mathematical tool used throughout the thesis to investigate chronotypes and sleep deprivation was graph metrics and network analysis. Whilst the behavioural [59], cognitive [57] and medical effects [95, 122] of chronotype are well understood, only limited research has considered the link between chronotype and FNs. Using the graph metrics from ECPs and LCPs, classifiers were trained and it was found that the FNs of extreme chronotypes held sufficient information that participants could be differentially labelled with high accuracy.

By contrast, the effect of sleep deprivation on FNs has been thoroughly studied in the literature. However, despite finding evidence for trait-like differences between the behavioural outcomes of individuals [49], there has been more limited research investigating potential mechanisms underlying such differences [37]. This motivated, within Chapter 6 an initial study using a theoretical approach based on Kuramoto oscillators. This approach was inherently reliant upon an adjacency matrix to define the influence of each population on the others and enabled an investigation into how network structure can impact synchronisation, leading to the discovery of potential biomarkers for sleep deprivation susceptibility. This naturally led to Chapter 7 where the conclusions from Chapter 6 were fully investigated through a comparison with PVT data from a CRP. Indeed, it appears that the circadian rhythm may be driving the inter-individual differences in participants at a given time.

The main findings of the thesis, as well as future work inspired by this analysis, will be discussed in more detail below.

8.1 NBS is an Important Alternative to Graph Metrics

The aim of Chapters 4 and 5 was to investigate if the FNs of extreme chronotypes differ. This was assessed through the framework of training classifiers and establishing classification accuracy. Initially, a graph metric approach was utilised - a common approach when analysing FNs because of their ability to quantitatively summarise features of complex networks, providing a basis for testing differentiation. The graph metrics were then used to train logistic regression classifiers with the aim of classifying the test subject as an ECP or LCP. Across these classifiers, a maximum accuracy of 76% was achieved when looking at the local properties of the PCC in the Afternoon scanning session. The importance of the PCC in chronobiological research had previously been established [57], and it is therefore sensible it should contribute to differentiating between extreme chronotypes.

However, the importance of the Afternoon scan compared to the Morning or Evening is harder to justify. Given neither group should be adversely affected by the clock time - either by ECPs wanting to sleep in the evening or LCPs experiencing lack of sleep in the morning - it was even hypothesised that the Afternoon scan would be the most similar.

However, overall the accuracy in Chapter 4 was low, and while it is feasible the differences between ECPs and LCPs are limited both temporally to the afternoon and spatially to the PCC, another investigation was completed using a different classification framework. Indeed, it was theorised that differences between extreme chronotypes occur more broadly across the FN but the effect is more subtle than can be discerned by quite coarse-grained graph metric analysis. Therefore, a classification framework based on NBS was utilised, which focused on the group level differences per edge across FNs rather than per graph metric. Through this framework parameters were found such that the classifier achieved high classification accuracy ($\sim$ 90%) for each of the three scanning sessions - under one contrast. While issues of multiple comparisons in Section 5.3.2 prevent the defining of parameters for future datasets, the results do suggest that differentiable information about chronotype exists in rs-fMRI data across the day and that the ROIs involved also change over time. For instance, in the Evening scan the effect is widespread, incorporating all 70 ROIs. However, the number of ROIs decreased in the Morning and Afternoon; indeed only 7 ROIs were required for high accuracy in the Afternoon (Table 5.3). To the best of my knowledge, no other study has found significant differences between the FNs of extreme chronotypes nor trained a classifier to produce such high accuracy. Although, as scanning times were aligned by clock time rather than internal time, it is difficult to separate the effect of circadian and homeostatic pressures on FNs from those driven purely by chronotype.

Whilst the calculation of graph metrics is a typical step in the analysis of FNs, the results of Chapter 4 and 5 suggest that NBS, and classification frameworks based upon NBS may be an important alternative, or possibly complementary, methodology in analysis pipelines. While the use of NBS may be more important when considering two

non-clinical cohorts, such as extreme chronotypes, the approach may also offer insights into the existence of differential information that would otherwise be missing if only graph metrics were considered.

The results and conclusions of Chapters 4 and 5 are based on methodological pipelines using FNs calculated with Tikhonov partial correlation. This FC was chosen due to the research into the effects of regularisation techniques for partial correlation completed by Pervazi et al. [146] and the optimal performance of partial correlation seen in the literature [127, 128, 177, 200, 201]. However, despite papers investigating the effect of different types of FC, no gold standard pipeline exists for creating FNs. Therefore, to further understand the results, the methodology could be repeated with FC calculated using Pearson's correlation instead - the most popular form of FC for analysing fMRI data [65]. This could help with understanding the influence of Tikhonov partial correlation on the successful differentiation of the ECPs and LCPs. Hence, this could either enable the generalisability of the pipeline, as many researchers will already have FNs calculated using Pearson's correlation, or provide additional evidence for supporting alternatives to Pearson's correlation.

8.2 Susceptibility to Sleep Deprivation is Associated with FN Properties

Within Chapters 6 and 7 the area of interest switches from chronotype to total sleep deprivation and in particular investigating how the properties and topology of a baseline FN may affect susceptibility to sleep deprivation. Within Chapter 6 this was investigated using the Kuramoto model alongside Total Drive to simulate the effect of sleep deprivation. The synchronisation of oscillators was calculated to understand how network topology affected levels of global excitability. The results suggest that networks with a high mean node degree and high trophic incoherence will have higher levels of global synchronisation across time. Therefore, it was hypothesised that networks with these graphical features

are more likely to be adversely affected by sleep deprivation.

This research was extended further in Chapter 7, which considered comparisons between real behavioural data and EEG data collected from participants undergoing a 40 h CRP to test the hypothesis from Chapter 6 as well as investigate the link between FN topology and the effect of sleep deprivation further. The results showed, through high correlation magnitudes (70% or higher), that high mean node strength, high SI and high stability during a baseline EEG acquisition were associated with high susceptibility to the perturbation of sleep deprivation and in particular the circadian rhythm. This is because at DLMO + 1 h and DLMO + 11 h the correlation between the mean node strength of baseline networks and $\mathrm{std}_{\mathrm{RT}}$ changed from 89% to -71% for B_{FA}. Hence those participants whose performance was most adversely affected within the group at DLMO + 1 h actually performed the best within the group at DLMO + 11 h, albeit the performance of the group saw an overall decrease. To the best of my knowledge, this is the first study to find associations between baseline EEG FNs and susceptibility to sleep deprivation as measured using PVT. Whilst validation on larger and more diverse cohorts is needed to fully understand these associations in the general population these results indicate a simple way to assess vulnerability to sleep deprivation without requiring the individual to endure sleep deprivation. This could have huge implications in many professions where sleep deprivation commonly occurs such as the military and healthcare [134, 170]. In addition, this could influence best-practice for shift work professions, which are commonly associated with acute and chronic sleep deprivation [80].

The complicated relationship that internal homeostatic and circadian drives may have on behavioural outcomes as sleep deprivation occurs could be a reason for the differences between the two Chapters. Indeed, due to the way that the Total Drive function is defined in Chapter 6 the influence of circadian and homeostatic pressure is always proportional to the ease at which the network synchronises as dictated by eq 6.3. However, the proportional contribution of homeostatic and circadian drives within the individuals in Chapter 7 are unlikely to be so closely associated to the network structure of the baseline FN.

For instance, inter-individual differences in circadian strength could influence these proportions within the participants, which is not accounted for in the theoretical networks. Indeed, it would be interesting to understand the influence of homeostatic and circadian pressure on network synchronisation by investigating how different proportions of the two pressures affect synchronisation when the network structure is fixed. This may offer an insight into how differences in the circadian strength of individuals manifest under sleep deprivation and is discussed in more detail in Section 8.3.3 below.

8.3 Future Research

8.3.1 Greater Separation of Chronotype and Fatigue

The results of Chapter 5 show promise that rs-fMRI data in the form of FNs contains differentiable information about extreme chronotypes. However, while differences in FNs were found with a high degree of accuracy, it is difficult to disentangle if the classifier is identifying differences directly driven by chronotype, or if the differences are indirect. For instance, the levels of fatigue the two groups faced over the three scanning sessions differed [59]; such that ECPs were more fatigued during the evening as the drive to sleep increased, whilst LCPs were more fatigued during the morning due to artificially ending their sleep early. Given that many ECPs and LCPs are usually constrained by times similar to the scanning session due to professional and societal pressures, this may accurately reflect the differences in the FNs of extreme chronotypes on a day-to-day basis. However, to truly investigate the differences between extreme chronotypes it may be necessary to repeat the experiment while controlling for differences in fatigue. One possible way to do this could be to align all scans to the individual's internal circadian rhythm. For instance, all 'Evening' scans could occur at DLMO + 1 h. If participants again follow their normal schedule for two weeks before scanning, such that they do not artificially end their sleep early, then this may control for differences in fatigue levels. Hence, high accuracy would

be more clearly associated with chronotype.

8.3.2 Additional Studies and the Inclusion of Extreme Chronotypes as Study Cohorts

The high correlations in Chapter 7 are very interesting, with properties of baseline FNs from EEG being strongly associated with susceptibility to sleep deprivation. However, the generalisability of these conclusions are hindered by the small sample size, low recruitment of females, limited age range, the exclusion of extreme chronotypes and CR conditions. These findings provide strong preliminary evidence to support conducting a much more detailed study that accounts for many of these limitations or a complementary study where participants are under more naturalistic conditions.

For example, given the findings in Chapter 5, the sleep deprivation analysis in Chapter 7 could be repeated for two cohorts of ECPs and LCPs. It may be that if the acquisitions are aligned to DLMO and the participants are well rested, then chronotype may have a limited effect on the correlations since no significant differences were found between the mean node strength of ECPs and LCPs in Chapter 4 - however this was on fMRI networks rather than EEG and the link between the modalities is not always clear given the spatial and temporal differences of the two modalities. If fatigue is not accounted for, such as by waking LCPs early for the start of the CRP, then it is likely that their brain excitability level will be higher during their baseline acquisition, which may inflate their mean node strength, as indicated by the contrast ECP<LCP being more informative in the Morning scanning session in Section 5.3.2. Currently, this is indicative that LCPs would be more susceptible to the influence of the circadian rhythm. However, as the FNs of different chronotypes were shown to differ in Chapter 5 it would be important not to simply extrapolate the findings of ICPs to ECPs or LCPs across neurological recording devices.

Furthermore, another way to expand the research could be by making the protocol more applicable to everyday life. For instance, while prolonged sleep deprivation can

occur infrequently, chronic sleep deprivation through restricting the period of sleep is very common [34]. Such sleep restriction can occur, in LCPs when they are forced to awaken early for work or in ECPs when they are pressured into staying awake late into the night [158]. In addition, lack of sleep is common in combination with shift work when sleeping during the day is harder due to the circadian drive and in particular the WMZ [179]. Therefore, an investigation into how the properties of a baseline FN are associated with PVT performance when participants undertake sleep restriction of 2 h, 4 h or even 6 h per night over a period of 2 weeks, similar to Van Dongen et al. [52], could be undertaken. If less sleep has occurred, it would be interesting if the properties of the first acquisition after awakening would still be informative when the effect of sleep inertia would likely be increased. Such an experiment could be undertaken in CR conditions initially to get an understanding of the data and trends in 'cleaner' data before being repeated under more realistic settings with participants working or sleeping at their house.

8.3.3 Circadian Strength Should Receive More Focus

There is an increasing awareness of chronotypes within research, which is typically accounted for through the exclusion of extreme chronotypes or the measuring and aligning of results to an individual's circadian phase. However, while internal clock time is important and indeed has been shown to be associated with differences in FNs, as seen in Chapter 5, this thesis also motivates the measuring of circadian strength. This is because it is sensible to conclude that the change in ranking that occurs in Chapter 7 is driven by differences in the circadian strength of individuals. Indeed, if the only influence was the monotonic rise of homeostatic pressure then it would be unclear how the ranking could reverse. However, sinusoids with the same period but differing amplitudes would see the waves with the highest value at the crest subsequently have the lowest value at the trough, which could explain this reverse in the ranking of PVT performance. Circadian strength is a relatively new research area with a very limited number of studies [136]. Current studies use a range of methods for assessing circadian strength including amplitude of

core body temperature (Chapter 7), magnetic resonance spectroscopy [162] and questionnaires [136]; therefore standardisation of these measures and additional research into the links between these methodologies and their relative effect on research studies, especially the link to FNs, is needed. For instance, it is possible, since we do not understand the magnitude to which circadian strength can influence behavioural outcomes and FNs, that this has a confounding effect on current research without currently being accounted for.

One possible way to investigate this would be through an extension of the Kuramoto framework used within Chapter 6. Within this thesis the ratio between homeostatic pressure and circadian rhythm was fixed to be proportional to the theoretical values of local and global coupling required for full synchronisation while letting the network structure differ. However, by fixing the network structure and changing the proportion of homeostatic and circadian processes while monitoring how synchronisation changes over the 19 simulations a direct analysis of circadian strength could be completed. To fully understand the results of such an analysis it may be necessary to use different metrics rather than SI, NSI or R. This is because these measures average over all simulations and hence the influence of a stronger circadian amplitude may be overlooked if averages over all simulations are considered as in Chapter 6. It may be necessary to consider the synchronisation per simulation m i.e. $\langle s^m \rangle$ or R^m. Alternatively, a completely different metric may be more informative such as the difference between the minimum and maximum synchronisation measure across the 19 simulations, which would create a metric more similar to how PVT impairment was measured.

While further research would be needed to validate the influence of circadian strength both in general and in the context of sleep deprivation as in Chapter 7, it appears that this could be an important factor within sleep and performance research, which is currently unaccounted for. Indeed, research into the effect of the amplitude of the circadian rhythm could see a similar rise in awareness and publications that research into chronotype, which considers the phase of the circadian rhythm, saw a decade or so ago [152].

8.4 Concluding Remarks

The main findings of this thesis are:

1. Graph metrics are unable to train a highly accurate classifier for differentiating extreme chronotypes.

2. A NBS framework can be used to train a highly accurate classifier for differentiating extreme chronotypes.

3. Higher mean node degree and trophic incoherence are associated with higher levels of synchronisation when using theoretical networks within the Kuramoto model.

4. Higher mean node strength, stability and SI in a baseline EEG derived FN are associated with less vulnerability to the effect of total sleep deprivation as measured using PVT impairment.

5. Higher mean node strength, stability and SI in a baseline EEG derived FN are associated with more vulnerability to the effect of sleep pressure 1 h post DLMO as measured using PVT performance.

6. Findings (4) and (5) suggest that circadian strength could be modulating performance.

Overall, we have used network analysis, machine learning and the Kuramoto model to gain insight into how circadian rhythms interact with FNs. The NBS classification framework presents evidence that the FNs of extreme chronotypes are sufficiently different at three different scanning session to enable accurate classification. In addition, biomarkers derived from EEG FNs provide a potential method for predicting an individual's susceptibility to sleep deprivation compared to a group. To the best of our knowledge, these are the first investigations to present such findings. This highlights the requirement to control for extreme chronotypes in future FN studies as chronotype could have a confounding effect on FC. Also, the potential implications of a sleep deprivation biomarker

are widespread influencing not only the economy but individual safety by providing information about the most efficient timing of tasks. These results present significant findings for the field of chronobiology and sleep deprivation and motivate a greater link between the two areas as well as an extension of circadian research to include circadian amplitude.

APPENDIX A

KURAMOTO DERIVATION

Mean field approximations use the assumption of an infinite number of oscillators to enable the use of the continuity equation. Therefore, enabling analysis into steady-state solutions for the system of coupled ODEs representing multiple populations of Kuramoto oscillators.

A.1 Mean-field Limit

For multiple Kuramoto populations we use eq 3.15 and eq 3.18, to form an alternative version of the oscillator dynamics in terms of the local order parameter,

$$\begin{aligned}
\frac{d\theta_j^c}{dt} &= \omega_j^c + \sum_{\gamma=1}^{P} \eta_\gamma \frac{K_{c\gamma}}{N_\gamma} \sum_{k=1}^{N_\gamma} \frac{1}{2i} \left(e^{i(\theta_k^\gamma - \theta_j^c)} - e^{-i(\theta_k^\gamma - \theta_j^c)} \right) \\
&= \omega_j^c + \sum_{\gamma=1}^{P} \eta_\gamma \frac{K_{c\gamma}}{2i} \left(\frac{e^{-i\theta_j^c}}{N_\gamma} \sum_{k=1}^{N_\gamma} e^{i\theta_k^\gamma} - \frac{e^{i\theta_j^c}}{N_\gamma} \sum_{k=1}^{N_\gamma} e^{-i\theta_k^\gamma} \right) \\
&= \omega_j^c + \sum_{\gamma=1}^{P} \eta_\gamma \frac{K_{c\gamma}}{2i} \left(z_\gamma e^{-i\theta_j^c} - \bar{z_\gamma} e^{i\theta_j^c} \right).
\end{aligned}$$

We now consider the mean field limit by letting $N_c \to \infty$ and $N \to \infty$ such that η_c remains a constant. Therefore, we define the distribution of the oscillators in population

c with the natural frequency ω at time t by the continuous distribution function,

$$f_c(\theta, \omega, t), \tag{A.1}$$

therefore,

$$f_c(\theta, \omega, t) d\theta d\omega,$$

is the fraction of oscillators with phase θ and natural frequency ω, between θ and $\theta + d\theta$ and ω and $\omega + d\omega$. Then the evolution of an individual oscillator from population c with natural frequency ω, is governed by:

$$\frac{d\theta_j}{dt} = \omega_j + \frac{1}{2i} \sum_{\gamma=1}^{P} \eta_\gamma K_{c\gamma} \left(z_\gamma e^{-i\theta_j} - \bar{z_\gamma} e^{i\theta_j} \right).$$

Now using eq A.1 we can define the continuous version of the order parameter as:

$$z_c(t) = \int_{\omega=-\infty}^{\omega=\infty} \int_{\theta=0}^{\theta=2\pi} f_c(\theta, \omega, t) e^{i\theta} d\theta d\omega. \tag{A.2}$$

When considering the mean-field limit the continuity equation holds since the number of oscillators in every population is conserved over time.

A.1.1 The Continuity Equation

The rate of change with respect to time, t, of the fraction of oscillators between θ_1 and θ_2 is equal to the fraction of oscillators entering and leaving the interval $0 \leq \theta_1 \leq \theta \leq \theta_2 \leq 2\pi$. Let $F(\theta, \omega, t)$ be the function for the fraction of oscillators crossing the angle location θ at time t with natural frequency ω given by:

$$F(\theta, \omega, t) = f_c \left[\omega_j + \frac{1}{2i} \sum_{\gamma=1}^{P} \eta_\gamma K_{c\gamma} \left(z_\gamma e^{-i\theta_j} - \bar{z_\gamma} e^{i\theta_j} \right) \right]. \tag{A.3}$$

Then, we have,

$$\begin{aligned}
&\frac{d}{dt}\left\{\int_{\theta=\theta_1}^{\theta_2} f_c(\theta,\omega,t)d\theta\right\} = \left[F(\theta,\omega,t)\right]_{\theta_2}^{\theta_1} \\
\Rightarrow &\int_{\theta_1}^{\theta_2} \frac{\partial f_c(\theta,\omega,t)}{\partial t}d\theta = \int_{\theta_2}^{\theta_1} \frac{\partial F(\theta,\omega,t)}{\partial \theta} \\
\Rightarrow &\int_{\theta_1}^{\theta_2} \frac{\partial f_c(\theta,\omega,t)}{\partial t}d\theta + \int_{\theta_1}^{\theta_2} \frac{\partial F(\theta,\omega,t)}{\partial \theta} = 0 \\
\Rightarrow &\int_{\theta_1}^{\theta_2} \frac{\partial f_c(\theta,\omega,t)}{\partial t} + \frac{\partial F(\theta,\omega,t)}{\partial \theta}d\theta = 0 \\
\Rightarrow &\frac{\partial f_c(\theta,\omega,t)}{\partial t} + \frac{\partial F(\theta,\omega,t)}{\partial \theta} = 0.
\end{aligned}$$

The Ott-Antonsen ansatz is built around the assumption that f_c can be expressed as a Fourier series with coefficients $\alpha_c(\omega,t)^n$:

$$f_c(\theta,\omega,t) = \frac{g_c(\omega)}{2\pi}\left\{1 + \sum_{n=1}^{\infty} \alpha_c^n(\omega,t)e^{in\theta} + \sum_{n=1}^{\infty} \bar{\alpha}_c^n(\omega,t)e^{-in\theta}\right\} \tag{A.4}$$

where $|\alpha_c(\omega,t)| < 1$, to ensure absolute convergence, and $\alpha_c(\omega,t) : \mathbb{R}\times\mathbb{R}_{\leq 0} \mapsto \mathbb{C}$. We can now substitute eq A.4 into the first term of the continuity equation,

$$\begin{aligned}
\frac{\partial f_c}{\partial t} &= \frac{\partial}{\partial t}\left\{\frac{g_c(\omega)}{2\pi} + \frac{g_c(\omega)}{2\pi}\sum_{n=1}^{\infty} \alpha_c^n(\omega,t)e^{in\theta} + \frac{g_c(\omega)}{2\pi}\sum_{n=1}^{\infty} \bar{\alpha}_c^n(\omega,t)e^{-in\theta}\right\} \\
&= \frac{g_c(\omega)}{2\pi}\frac{\partial}{\partial t}\left(\sum_{n=1}^{\infty} \alpha_c^n(\omega,t)e^{in\theta}\right) + \frac{g_c(\omega)}{2\pi}\frac{\partial}{\partial t}\left(\sum_{n=1}^{\infty} \bar{\alpha}_c^n(\omega,t)e^{-in\theta}\right) \\
&= \frac{g_c(\omega)}{2\pi}\left[\sum_{n=1}^{\infty} n\alpha_c^{n-1}(\omega,t)e^{in\theta}\right]\frac{\partial \alpha_c}{\partial t} + \frac{g_c(\omega)}{2\pi}\left[\sum_{n=1}^{\infty} n\bar{\alpha}_c^{n-1}(\omega,t)e^{-in\theta}\right]\frac{\partial \bar{\alpha}_c}{\partial t}.
\end{aligned}$$

Now we can substitute eq A.3 as well as eq A.4 into the second term of the continuity equation:

$$\frac{\partial F}{\partial \theta} = \frac{\partial}{\partial \theta}\left\{\left(\frac{g_c(\omega)}{2\pi} + \frac{g_c(\omega)}{2\pi}\sum_{n=1}^{\infty} \alpha_c^n(\omega,t)e^{in\theta} + c.c\right)\left(\omega_j + \frac{1}{2i}\sum_{\gamma=1}^{P} \eta_\gamma K_{c\gamma}\left(z_\gamma e^{-i\theta_j} - \bar{z_\gamma}e^{i\theta_j}\right)\right)\right\},$$

where $c.c$ stands for the complex conjugate resulting in,

$$\frac{\partial F}{\partial \theta} = \frac{g_c(\omega)}{2\pi}\left(i\omega\alpha_c\sum_{n=1}^{\infty}\alpha_c^{n-1}ne^{in\theta} - \frac{1}{2}\sum_{\gamma=1}^{P}\eta_\gamma K_{c\gamma}z_\gamma e^{-i\theta} - \frac{1}{2}\sum_{\gamma=1}^{P}\eta_\gamma K_{c\gamma}\bar{z}_\gamma e^{i\theta}\right) + \frac{1}{2}\sum_{n=1}^{\infty}\alpha_c^{n}(n-1)e^{i\theta(n-1)}\sum_{\gamma=1}^{P}\eta_\gamma K_{c\gamma}z_\alpha - \frac{1}{2}\sum_{n=1}^{\infty}\alpha_c^{n}(n+1)e^{i\theta(n+1)}\sum_{\gamma=1}^{P}\eta_\gamma K_{c\gamma}\bar{z}_\alpha$$

Now using a change of indices we have,

$$\frac{\partial F}{\partial \theta} = \frac{g_c(\omega)}{2\pi}\left(i\omega\alpha_c\sum_{n=1}^{\infty}\alpha_c^{n-1}ne^{in\theta} - \frac{1}{2}\sum_{\gamma=1}^{P}\eta_\gamma K_{c\gamma}\bar{z}_\alpha e^{i\theta} + \frac{1}{2}\sum_{n=1}^{\infty}\alpha_c^{n+1}ne^{i\theta n}\sum_{\gamma=1}^{P}\eta_\gamma K_{c\gamma}z_\gamma - \frac{1}{2i}\left(\sum_{n=1}^{\infty}\alpha_c^{n-1}ne^{in\theta} - e^{i\theta}\right)\sum_{\gamma=1}^{P}\eta_\gamma K_{c\gamma}\bar{z}_\gamma + c.c\right),$$

which can simplify to,

$$\frac{\partial F}{\partial \theta} = \frac{g_c(\omega)}{2\pi}\left(\sum_{n=1}^{\infty}\alpha_c^{n-1}ne^{in\theta}\right)\left(i\omega\alpha_c - \frac{1}{2}\sum_{\gamma=1}^{P}\eta_\gamma K_{c\gamma}\bar{z}_\gamma + \frac{\alpha_c^2}{2}\sum_{\gamma=1}^{P}\eta_\gamma K_{c\gamma}z_\gamma\right) + c.c.$$

Therefore, the continuity equation can be written in full as,

$$\frac{g_c(\omega)}{2\pi}\frac{\partial\bar{\alpha}_c}{\partial t}\sum_{n=1}^{\infty}\alpha_c^{n-1}ne^{in\theta} + \frac{g_c(\omega)}{2\pi}\left(\sum_{n=1}^{\infty}\alpha_c^{n-1}ne^{in\theta}\right).\left[i\omega\alpha_c - \frac{1}{2}\sum_{\gamma=1}^{P}\eta_\gamma K_{c\gamma}\bar{z}_\gamma + \frac{\alpha_c^2}{2}\sum_{\gamma=1}^{P}\eta_\gamma K_{c\gamma}z_\gamma\right] + c.c = 0,$$

which can be simplified to,

$$\frac{g_c(\omega)}{2\pi}\left(\sum_{n=1}^{\infty}\alpha_c^{n-1}ne^{in\theta}\right)\left(\frac{\partial\alpha_c}{\partial t} + i\omega\alpha_c - \frac{1}{2}\sum_{\gamma=1}^{P}\eta_\gamma K_{c\gamma}\bar{z}_\gamma + \frac{\alpha_c^2}{2}\sum_{\gamma=1}^{P}\eta_\gamma K_{c\gamma}z_\gamma\right) + c.c = 0.$$

Note that,

$$\sum_{n=1}^{\infty}\alpha_c^{n-1}ne^{in\theta} = \frac{e^{i\theta}}{(1-\alpha_c e^{i\theta})^2} \neq 0.$$

Therefore,

$$\frac{\partial\alpha_c}{\partial t} + i\omega\alpha_c - \frac{1}{2}\sum_{\gamma=1}^{P}\eta_\gamma K_{c\gamma}\bar{z}_\gamma + \frac{\alpha_c^2}{2}\sum_{\gamma=1}^{P}\eta_\gamma K_{c\gamma}z_\gamma = 0. \tag{A.5}$$

A.2 Deriving K_g

This system of equations is independent of θ and if we assume that the frequencies ω are independent and identically distributed with density $g_c(\omega)$, then using eq A.2 the order parameter is,

$$z_c(t) = \int_{\omega=-\infty}^{\omega=\infty} \int_{\theta=0}^{\theta=2\pi} \frac{g_c(\omega)}{2\pi} \left\{ e^{i\theta} + \sum_{n=1}^{\infty} \alpha_c^n(\omega,t) e^{i(n+1)\theta} + \sum_{n=1}^{\infty} \bar{\alpha}_c^n(\omega,t) e^{-i(n-1)\theta} \right\} d\theta d\omega. \quad \text{(A.6)}$$

When integrating eq A.6 we note that $|\bar{\alpha}c^n| < 1$ and converges absolutely therefore we have,

$$z_c(t) = \int_{\omega=-\infty}^{\omega=\infty} \int_{\theta=0}^{\theta=2\pi} \frac{g_c(\omega)}{2\pi} \bar{\alpha}_c d\theta d\omega = \int_{\omega=-\infty}^{\omega=\infty} g_c(\omega) \bar{\alpha}_c d\omega.$$

Let $g_c(\omega)$ be the Cauchy distribution:

$$\begin{aligned}
g_c(\omega) =& \frac{1}{\Delta\pi} \left[\frac{1}{1 + \left(\frac{\omega-\omega_0}{\Delta}\right)^2} \right] \\
=& \frac{1}{\pi} \left[\frac{\Delta}{\Delta^2 + (\omega-\omega_0)^2} \right] \\
=& \frac{1}{2\pi i} \left[\frac{2i\Delta}{-(i)^2\Delta^2 + (\omega-\omega_0)^2} \right] \\
=& \frac{1}{2\pi i} \left[\frac{2i\Delta}{(\omega-\omega_0)^2 - (i\Delta)^2} \right] \\
=& \frac{1}{2\pi i} \left[\frac{1}{\omega-\omega_0-i\Delta} - \frac{1}{\omega-\omega_0+i\Delta} \right]
\end{aligned}$$

then we have

$$z_c(t) = \int_{\omega=-\infty}^{\omega=\infty} \frac{\bar{\alpha}_c}{2\pi i} \left[\frac{1}{\omega-\omega_0-i\Delta} - \frac{1}{\omega-\omega_0+i\Delta} \right] d\omega.$$

Let $w_0 = 0$ and $\Delta = 1$ then,

$$z_c(t) = \frac{1}{2\pi i} \int_{\omega=-\infty}^{\omega=\infty} \frac{\bar{\alpha}_c(\omega,t)}{\omega - i} - \frac{1}{2\pi i} \int_{\omega=-\infty}^{\omega=\infty} \frac{\bar{\alpha}_c(\omega,t)}{\omega + i} d\omega. \quad \text{(A.7)}$$

If we let Γ be the semi-circle with infinite radius in the lower half-plane then there are two singularities at $w = i$ and $w = -i$ with only the latter inside of the domain Γ. Therefore,

using Cauchys integral formula,

$$z_c(t) = \bar{\alpha}_c(-i,t) \text{ and also } \bar{z}_c(t) = \alpha_c(-i,t).$$

Now we recall eq 3.18 and eq A.5 and using $\omega = -i$ we have,

$$\frac{d}{dt}(r_c e^{-i\phi_c}) + r_c e^{-i\phi_c} + \frac{1}{2}\sum_{\gamma=1}^{P} \eta_\gamma K_{c\gamma} \left(r_c^2 e^{-2i\phi_c} r_\gamma e^{i\phi_\gamma} - r_\gamma e^{-i\phi_\gamma} \right) = 0.$$

By differentiating we then have,

$$e^{-i\phi_c}\left(\frac{d}{dt}(r_c) - i r_c \frac{d}{dt}(\phi_c) + r_c + \frac{1}{2}\sum_{\gamma=1}^{P} \eta_\gamma K_{c\gamma} r_\gamma \left(r_c^2 e^{i(\phi_\gamma - \phi_c)} - e^{-i(\phi_\gamma - \phi_c)} \right) \right) = 0.$$

Dividing through by $e^{-i\phi_c}$ and collecting real and imaginary variable we have:

$$0 = \frac{dr_c}{dt} + r_c + \frac{r_c^2 - 1}{2}\sum_{\gamma=1}^{P} \eta_\gamma K_{c\gamma} r_\gamma \cos\big(\phi_\gamma - \phi_c\big)$$
$$0 = -r_c \frac{d\phi_c}{dt} + \frac{r_c^2 + 1}{2}\sum_{\gamma=1}^{P} \eta_\gamma K_{c\gamma} r_\gamma \sin\big(\phi_\gamma - \phi_c\big).$$

Finally, resulting in $2P$ coupled non-linear ODEs:

$$\frac{dr_c}{dt} = -r_c + \frac{1 - r_c^2}{2}\sum_{\gamma=1}^{P} \eta_\gamma K_{c\gamma} r_\gamma \cos\big(\phi_\gamma - \phi_c\big)$$
$$\frac{d\phi_c}{dt} = \frac{1 + r_c^2}{2r_c}\sum_{\gamma=1}^{P} \eta_\gamma K_{c\gamma} r_\gamma \sin\big(\phi_\gamma - \phi_c\big).$$

Where we can define the global phase coherence:

$$r_g = \left| \frac{1}{P}\sum_{\gamma=1}^{P} r_c e^{i\phi_c} \right|.$$

Note that if we assume a rotating frame of reference then $\phi_\gamma - \phi_c \to 0$, in addition if we linearise eq A.5 then we have

$$\frac{dr_c}{dt} = -r_c + \frac{1}{2}\sum_{\gamma=1}^{P} \eta_\gamma K_{c\gamma} r_\gamma$$
$$\frac{d\phi_c}{dt} = 0.$$

Therefore, steady-state solutions occur for the linear problem when,

$$0 = -r_c + \frac{1}{2}\sum_{\gamma=1}^{P} \eta_\gamma K_{c\gamma} r_\gamma. \tag{A.8}$$

Substituting eq 3.17 into eq A.8 we have:

$$0 = -r_c + \frac{1}{2}\sum_{\gamma=1}^{P} \eta_\gamma (K_g A_{c\gamma} + K_{cc} I_{c\gamma}) r_\gamma.$$

Therefore, we have,

$$0 = -r_c + \frac{\eta_c K_{cc}}{2} r_c + \frac{K_g}{2}\sum_{\gamma=1}^{P} \eta_\gamma A_{c\gamma} r_\gamma$$
$$0 = r_c\left(-1 + \frac{\eta_c K_{cc}}{2}\right) + \frac{K_g}{2}\sum_{\gamma=1}^{P} \eta_\gamma A_{c\gamma} r_\gamma.$$

Rearranging we have,

$$\frac{K_g}{2}\sum_{\gamma=1}^{P} \eta_\gamma A_{c\gamma} r_\gamma = r_c\left(1 - \frac{\eta_c K_{cc}}{2}\right),$$
$$\sum_{\gamma=1}^{P} \eta_\gamma A_{c\gamma} r_\gamma = r_c\left(\frac{2 - \eta_c K_{cc}}{K_g}\right).$$

If every population has the same number of oscillators then $\eta_c = \frac{1}{P}$. Resulting in,

$$\sum_{\gamma=1}^{P} A_{c\gamma} r_\gamma = r_c\left(\frac{2P - K_{cc}}{K_g}\right).$$

Therefore, the problem becomes finding the solution of the eigenvalue problem,

$$\mathbf{Ar} = \left(\frac{2P - K_{cc}}{K_g} \right) \mathbf{r}.$$

It is sufficient to compute the absolute value of the largest eigenvalue, $\lambda_{\max}$. Consequently, the critical value for global coupling can be determined by:

$$K_g = \frac{2P - K_{cc}}{|\lambda_{\max}|}.$$

APPENDIX B

CHAPTER 5

B.1 Main Steps of the Classifier

A summary of the main steps of the methodological pipeline for the NBS classifier are given below, starting with the creation of functional networks:

1. For each participant a 70×70 functional network is calculated where each ROI is a node in the network and Tikhonov Partial Correlation is the functional connectivity measure used to calculate the pairwise connection between ROIs.

2. A single test subject m is selected and initially labelled an ECP.

   (a) Similar to NBS a 70×70 t-statistic matrix is then calculated, such that each element is the result of a t-test comparing edge weights for the two groups with Subject m considered an ECP.

   (b) The t-statistic matrix is then thresholded such that a minimum connected component is created i.e. all 70 ROIs are still connected but a higher threshold will remove at least 1 ROI. The threshold is denoted t_E^m and the suprathreshold network is called a dysconnected network, denoted $E_{t_E}^m$ and via the approach in NBS the dysconnected network will have an associated FWE corrected p-value.

3. Test subject m is then labelled an LCP.

(a) As in NBS a 70×70 t-statistic matrix is then calculated, such that each element is the result of a t-test comparing edge weights for the two groups with Subject m considered an LCP.

(b) The t-statistic matrix is then thresholded such that a minimum connected component is created i.e. all 70 ROIs are still connected but a higher threshold will remove at least 1 ROI. The threshold is denoted t_L^m and the suprathreshold network is called a dysconnected network, denoted $L_{t_L}^m$, and via the approach in NBS the dysconnected network will have an associated FWE corrected p-value.

4. Step 1: If neither $E_{t_E}^m$ or $L_{t_L}^m$ are significant the test subject is labelled unclear. If $E_{t_E}^m$ is significant and $L_{t_L}^m$ is not significant the test subject is labelled an ECP. If $L_{t_L}^m$ is significant and $E_{t_E}^m$ is not significant the test subject is labelled an LCP. If both are deemed to have a significant size compared to a null distribution, then further steps are needed.

5. Step 2 if required:

   (a) Similarly to above the dysconnected networks $E_{t_L}^m$ and $L_{t_E}^m$ are created by labelling test subject m an ECP and using threshold t_L^m and by labelling test subject m an LCP and using threshold t_E^m respectively.

   (b) If neither $E_{t_L}^m$ or $L_{t_E}^m$ are significant the test subject is labelled unclear. If $E_{t_L}^m$ is significant and $L_{t_E}^m$ is not significant the test subject is labelled an ECP. If $L_{t_E}^m$ is significant and $E_{t_L}^m$ is not significant the test subject is labelled an LCP. If both are deemed to have a significant size compared to a null distribution, then further steps are needed.

6. Step 3 if required: If all four dysconnected networks are significant then the label is determined by considering the number of edges in each dysconnected network, with more edges taken as an indication of correct labelling, see Figure 5.1 for all possible comparisons.

B.2 NBS Predict

We present the results of classifying the extreme chronotypes using NBS Predict for each of the three scanning sessions and two contrasts. The result for each classification is given as the accuracy under a LOOCV analysis, where p=0.05. There are three classification types included in NBS Predict [166], logistic regression, Support Vector Machine classification, and Linear Discriminant Analysis, each of which are considered in Tables B.1 - B.3 respectively.

Scanning Session	Contrast	Accuracy	Sensitivity	Specificity	Balanced Accuracy
Afternoon	[ECP > LCP]	0.5946	0	1	0.5000
Afternoon	[ECP < LCP]	0.5946	0	1	0.5000
Evening	[ECP > LCP]	0.5263	0	0.9091	0.4546
Evening	[ECP < LCP]	0.5789	0	1	0.5000
Morning	[ECP > LCP]	0.5526	0	0.9545	0.4773
Morning	[ECP < LCP]	0.5789	0	1	0.5000

Table B.1: **NBS Predict: Logistic Regression.** Table giving the results for each scanning session and contrast when using logistic regression in NBS Predict.

Scanning Session	Contrast	Accuracy	Sensitivity	Specificity	Balanced Accuracy
Afternoon	[ECP > LCP]	0.5946	0	1	0.5000
Afternoon	[ECP < LCP]	0.5946	0	1	0.5000
Evening	[ECP > LCP]	0.5000	0	0.8636	0.4318
Evening	[ECP < LCP]	0.5789	0	1	0.5000
Morning	[ECP > LCP]	0.5526	0	0.9545	0.4773
Morning	[ECP < LCP]	0.5789	0	1	0.5000

Table B.2: **NBS Predict: Support Vector Machine.** Table giving the results for each scanning session and contrast when using support vector machine NBS Predict.

Scanning Session	Contrast	Accuracy	Sensitivity	Specificity	Balanced Accuracy
Afternoon	[ECP > LCP]	0.5135	0.1333	0.7727	0.4530
Afternoon	[ECP < LCP]	0.7838	0.5333	0.9545	0.7439
Evening	[ECP > LCP]	0.2632	0.0625	0.4091	0.2358
Evening	[ECP < LCP]	0.3421	0.0625	0.5455	0.3040
Morning	[ECP > LCP]	0.3947	0.1875	0.5455	0.3665
Morning	[ECP < LCP]	0.3158	0.1250	0.4545	0.2898

Table B.3: **NBS Predict: Linear Discriminant Analysis.** Table giving the results for each scanning session and contrast when using Linear Discriminant Analysis NBS Predict.

We see from Table B.1 and Table B.2, that for two of the models in NBS Predict all of the ECPs are incorrectly labelled as LCPs. Indeed, for at least one contrast in each scanning session all the subjects are labelled as LCPs.

When using Linear Discriminant Analysis in NBS Predict we see a general decrease in the accuracy across 5 of the scanning sessions and contrasts; this is because the classifier has a lower tendency to label every subject an LCP. However, for Afternoon [ECP < LCP] the accuracy is higher reaching 78% due to 8 ECPs and all but 1 LCP being correctly labelled. This shows that 1 out of the 18 cases has a balanced accuracy greater than 50% and highlights a bias in the labelling of test subjects as LCP across the classifiers, scanning sessions and contrasts. Unfortunately, NBS Predict is unable to provide information on which subjects were incorrectly labelled, preventing comparison at the individual level.

Similar to the results in the Section 5.3.1 this indicates that a time of day effect is present, as the high accuracy occurred in only one scanning session for one contrast. However, while in Section 5.3.1 the high accuracy was restricted to Evening [ECP > LCP] when using NBS Predict the high accuracy was restricted to Afternoon [ECP < LCP], which is similar to the results of Chapter 4.

Overall, we see that NBS Predict is highly reliant on the choice of classification method and classification is heavily weighted towards the correct classification of LCPs. Also, if only NBS Predict has been used then this would have given the false impression that neither the Evening nor the Morning scan had any differential information.

B.3 Participant's Metadata

All the participants were screened as ECPs or LCPs through a combination of actigraphy data, DLMO and CAR concentrations as well as their midpoint of sleep on free days (MSF) when corrected for sleep debt (MSF_{SC}). Therefore, subject metadata was considered to see if this offers an explanation for why the classifier is sensitive to certain subjects.

The metadata does seem to offer some explanation for why the classifier is so sensitive to the removal of certain subjects, especially in the case of ECPs as the MSF and DLMO appear to be lower for the subjects who were incorrectly labelled in the Afternoon and Evening scan. However, when corrected for multiple comparisons using Benjamini-Hochberg test no significance remains.

Therefore, across the three scanning sessions there was no significant information to support that the metadata of subjects provides explains the sensitivity of the classifier to a subjects removal especially. This is further supported because, across the scanning sessions there is no consistency in the subjects whose removal has the biggest effect. Indeed, across all 3 scanning sessions the removal of 21 subjects leads to a high difference in the accuracy. Therefore, over half of the subjects cannot be considered outliers according to the metadata or the data would be fundamentally flawed.

It is worth noting that for 12 of the Subjects their Evening scanning session took place during their WMZ. However, these subjects did not align with those whose removal leads to large differences in accuracy and it is therefore not thought to be a confounding factor.

APPENDIX C

CHAPTER 6

C.1 Examplar Simulated Time-series

To provide an idea of the properties of the simulated time-series, the time-series for two examplar three node networks (N_1^3 and N_9^3) at a given global coupling value are given below in Figures C.1 and C.2. Note that each simulation differs due to the local coupling parameter changing according to the Total Drive (see Figure 6.4c). Hence an oscillation in the synchronisation of the network is to be expected as the simulation number increases.

We see that for some simulations, despite not reaching full synchronisation, the relative amplitude is still informative. For instance, simulation 12 in Figure C.1 shows that node 1 and node 2 have relatively stable amplitudes below the maximum. However, node 3, which is a basal node, has only transient local synchronisation seen through the small temporally isolated rises in amplitude. Whereas in Figure C.2 if we consider simulation 12 again we see that all the nodes have a higher amplitude and there is more consistency across the nodes, which is to be expected on a fully connected network.

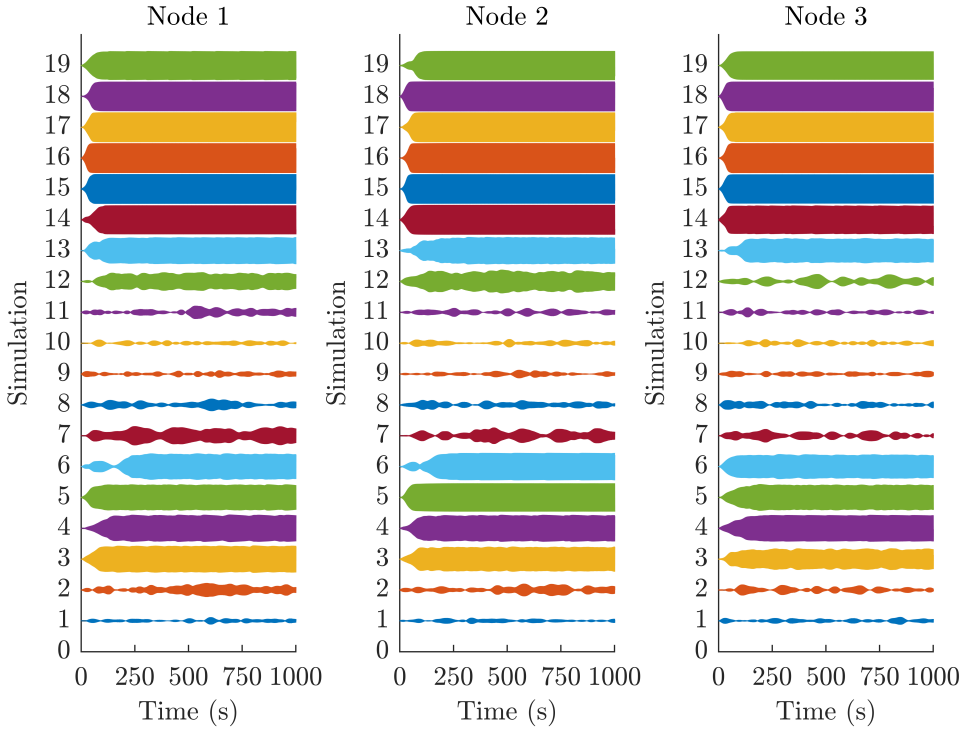


Figure C.1: **Time-series for N_1^3 Across the 19 Simulations.** For each of the 19 simulations and 3 nodes the simulated time-series is plotted for $K_g = 0.5$. Here the amplitude of the signal provides information about the local synchronisation of the node.

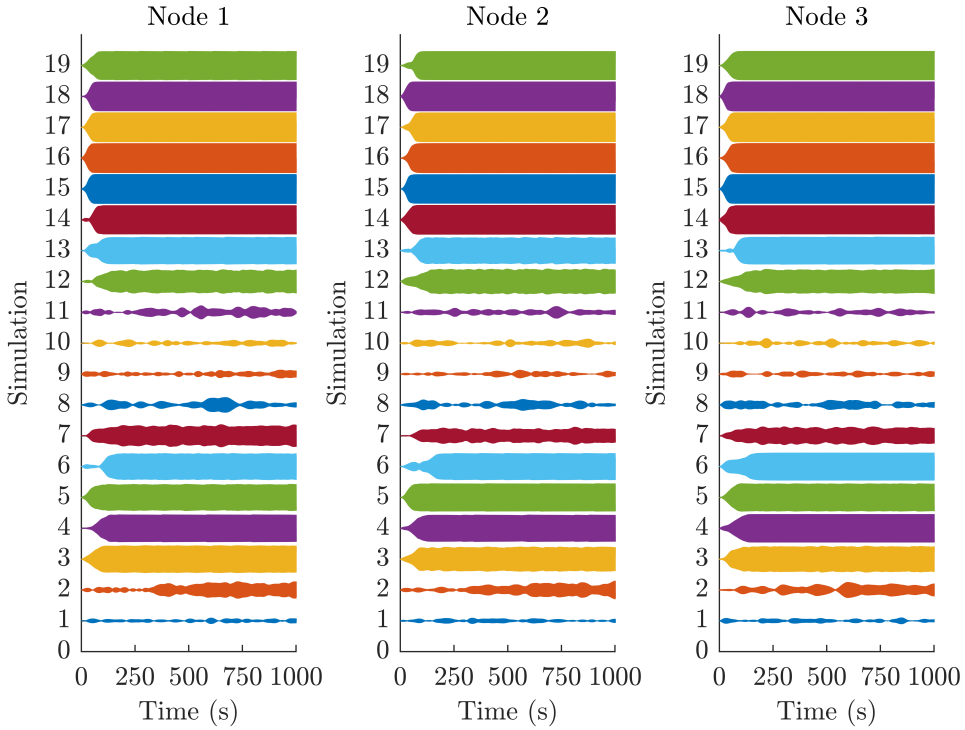


Figure C.2: **Time-series for N_9^3 Across the 19 Simulations.** For each of the 19 simulations and 3 nodes the simulated timeseries is plotted for $K_g = 0.5$. Here the amplitude of the signal provides information about the local synchronisation of the node.

C.2 Synchronisation Using $N_c = 1,000$

To understand how the choice of $N_c = 100$ affects the synchronisation and subsequently the correlation with graph metrics the analysis for the three node networks was repeated with $N_c = 1,000$. Tables C.1 and C.2 have the correlations for SI, with and without basal node networks. Similarly Tables C.3 and C.4 have the results for NSI while Tables C.5 and C.6 have the results for R.

	Trophic Incoherence			Mean Node Degree		
K_g	Correlation	p-value	Adjusted p-value	Correlation	p-value	Adjusted p-value
0.5	0.3537	0.3504	0.6007	0.8321	0.0054	0.0432*
1	0.5287	0.1434	0.3441	0.8532	0.0034	0.0432*
1.5	0.6335	0.0670	0.2298	0.8360	0.0050	0.0432*
2	0.6337	0.0669	0.2298	0.7140	0.0307	0.1843
2.5	0.6356	0.0658	0.2298	0.5662	0.1120	0.2987
3	0.5959	0.0904	0.2712	0.4484	0.2260	0.4520
3.5	0.5277	0.1789	0.3903	0.2730	0.5130	0.7449
4	0.4926	0.2614	0.4826	0.1107	0.8132	0.9316
4.5	0.4388	0.3840	0.6145	0.0163	0.9755	0.9847
5	0.3542	0.5587	0.7449	-0.1457	0.8151	0.9316
5.5	0.3560	0.5565	0.7449	-0.1479	0.8124	0.9316
6	-0.0161	0.9839	0.9847	0.0153	0.9847	0.9847

Table C.1: **Correlating SI with Mean Node Degree and Trophic Incoherence Using $N_c = 1,000$.** The Pearson's correlation, p-value and adjusted p-value when comparing SI for each global coupling strength to the mean node degree and trophic incoherence of the network. Here $N_c = 1,000$ rather than $N_c = 100$ was used. The p-values were corrected for the range of global coupling strengths as well as the two graph metrics using Benjamini-Hochberg method of correcting for FDR [78]. * denotes significance p-value < 0.05.

	Trophic Incoherence			Mean Node Degree		
K_g	Correlation	p-value	Adjusted p-value	Correlation	p-value	Adjusted p-value
0.5	0.5000	0.2532	0.4402	0.9725	0.0002	0.0011*
1	0.4222	0.3454	0.5181	0.9751	0.0002	0.0011*
1.5	0.4439	0.3185	0.5095	0.9791	0.0001	0.0010*
2	0.4990	0.2543	0.4402	0.9450	0.0013	0.0053*
2.5	0.3837	0.3955	0.5273	0.9814	0.0001	0.0010*
3	0.2744	0.5514	0.6302	0.9976	< 0.0001	< 0.0001*
3.5	-0.2142	0.6836	0.7457	0.9378	0.0057	0.0151*
4	-0.7079	0.1809	0.4343	0.6278	0.2568	0.4402
4.5	-0.7810	0.2190	0.4402	0.6177	0.3823	0.5273
5	-0.7604	0.4500	0.5400	1.0000	0.0044	0.0151*
5.5	-0.7617	0.4487	0.5400	1.0000	0.0057	0.0151*
6	-1.0000	NaN	NaN	1.0000	NaN	NaN

Table C.2: **Correlating SI with Mean Node Degree and Trophic Incoherence Using $N_c = 1,000$ - No Basal Node Networks.** The Pearson's correlation, p-value and adjusted p-value when comparing SI for each global coupling strength to the mean node degree and trophic incoherence of the network. Here $N_c = 1,000$ rather than $N_c = 100$ was used. The p-values were corrected for the range of global coupling strengths as well as the two graph metrics using Benjamini-Hochberg method of correcting for FDR [78]. * denotes significance p-value < 0.05.

	Trophic Incoherence			Mean Node Degree		
K_g	Correlation	p-value	Adjusted p-value	Correlation	p-value	Adjusted p-value
0.5	0.5905	0.0941	0.3589	0.5174	0.1537	0.4085
1	0.5565	0.1196	0.3589	0.8047	0.0089	0.2137
1.5	0.6359	0.0656	0.3589	0.5711	0.1082	0.3589
2	0.5572	0.1191	0.3589	0.3679	0.3300	0.6601
2.5	0.5654	0.1126	0.3589	0.2840	0.4589	0.7384
3	0.5681	0.1105	0.3589	0.2824	0.4615	0.7384
3.5	0.5367	0.1702	0.4085	0.2168	0.6061	0.8081
4	0.5127	0.2394	0.5223	0.0809	0.8632	0.9865
4.5	0.4493	0.3714	0.6857	0.0085	0.9872	0.9973
5	0.3677	0.5426	0.7669	-0.1582	0.7994	0.9593
5.5	0.3672	0.5432	0.7669	-0.1772	0.7755	0.9593
6	-0.0248	0.9752	0.9973	-0.0027	0.9973	0.9973

Table C.3: **Correlating NSI with Mean Node Degree and Trophic Incoherence Using $N_c = 1,000$.** The Pearson's correlation, p-value and adjusted p-value when comparing NSI for each global coupling strength to the mean node degree and trophic incoherence of the network. Here $N_c = 1,000$ rather than $N_c = 100$ was used. The p-values were corrected for the range of global coupling strengths as well as the two graph metrics using Benjamini-Hochberg method of correcting for FDR [78]. * denotes significance p-value < 0.05.

	Trophic Incoherence			Mean Node Degree		
K_g	Correlation	p-value	Adjusted p-value	Correlation	p-value	Adjusted p-value
0.5	0.3909	0.3859	0.7387	0.6423	0.1198	0.3595
1	0.3843	0.3947	0.7387	0.9802	0.0001	0.0025 *
1.5	0.2967	0.5183	0.7640	0.8695	0.0110	0.0880 *
2	0.0511	0.9134	0.9964	0.6855	0.0891	0.3056
2.5	0.2603	0.5730	0.7640	0.8304	0.0207	0.1242
3	0.1303	0.7807	0.8922	0.9284	0.0025	0.0304 *
3.5	-0.1802	0.7326	0.8791	0.8181	0.0466	0.1959
4	-0.3529	0.5602	0.7640	0.3934	0.5123	0.7640
4.5	-0.5999	0.4001	0.7387	0.6853	0.3147	0.7387
5	-0.4098	0.7312	0.8791	0.9069	0.2768	0.7382
5.5	-0.7034	0.5033	0.7640	0.9970	0.0490	0.1959
6	-1.0000	NaN	NaN	1.0000	NaN	NaN

Table C.4: **Correlating NSI with Mean Node Degree and Trophic Incoherence Using $N_c = 1,000$ - No Basal Node Networks.** The Pearson's correlation, p-value and adjusted p-value when comparing NSI for each global coupling strength to the mean node degree and trophic incoherence of the network. Here $N_c = 1,000$ rather than $N_c = 100$ was used. The p-values were corrected for the range of global coupling strengths as well as the two graph metrics using Benjamini-Hochberg method of correcting for FDR [78]. * denotes significance p-value < 0.05.

	Trophic Incoherence			Mean Node Degree		
K_g	Correlation	p-value	Adjusted p-value	Correlation	p-value	Adjusted p-value
0.5	0.3485	0.3581	0.6004	0.6819	0.0430	0.4112
1	0.3754	0.3195	0.5898	0.6633	0.0514	0.4112
1.5	0.4470	0.2277	0.5831	0.6300	0.0690	0.4112
2	0.4342	0.2429	0.5831	0.6029	0.0857	0.4112
2.5	0.6326	0.0675	0.4112	0.4806	0.1904	0.5831
3	0.5470	0.1275	0.5098	0.3778	0.3162	0.5898
3.5	0.4956	0.2117	0.5831	0.3027	0.4661	0.6991
4	0.4842	0.2709	0.5898	0.1901	0.6830	0.8627
4.5	0.4461	0.3752	0.6004	0.0270	0.9596	0.9596
5	0.3503	0.5633	0.7511	-0.1502	0.8095	0.9515
5.5	0.3514	0.5620	0.7511	-0.1319	0.8325	0.9515
6	-0.0488	0.9512	0.9596	0.0422	0.9578	0.9596

Table C.5: **Correlating R with Mean Node Degree and Trophic Incoherence Using $N_c = 1,000$.** The Pearson's correlation, p-value and adjusted p-value when comparing R for each global coupling strength to the mean node degree and trophic incoherence of the network. Here $N_c = 1,000$ rather than $N_c = 100$ was used. The p-values were corrected for the range of global coupling strengths as well as the two graph metrics using Benjamini-Hochberg method of correcting for FDR [78]. * denotes significance p-value < 0.05.

	Trophic Incoherence			Mean Node Degree		
K_g	Correlation	p-value	Adjusted p-value	Correlation	p-value	Adjusted p-value
0.5	0.1732	0.7104	0.9471	0.7599	0.0475	0.2057
1	0.2006	0.6663	0.9471	0.7782	0.0393	0.2057
1.5	0.2155	0.6427	0.9471	0.7807	0.0383	0.2057
2	0.2236	0.6298	0.9471	0.7811	0.0381	0.2057
2.5	0.2235	0.6300	0.9471	0.7714	0.0422	0.2057
3	0.2090	0.6529	0.9471	0.7515	0.0514	0.2057
3.5	-0.0643	0.9037	~ 1	0.3954	0.4378	0.9471
4	-0.1329	0.8313	~ 1	0.2313	0.7082	0.9471
4.5	0.3132	0.6868	0.9471	0.7489	0.2511	0.8609
5	0.0914	0.9417	~ 1	0.5828	0.6039	0.9471
5.5	0.1435	0.9083	~ 1	0.5394	0.6373	0.9471
6	-1.0000	NaN	NaN	1.0000	NaN	NaN

Table C.6: **Correlating R with Mean Node Degree and Trophic Incoherence Using $N_c = 1,000$ - No Basal Node Networks.** The Pearson's correlation, p-value and adjusted p-value when comparing R for each global coupling strength to the mean node degree and trophic incoherence of the network. Here $N_c = 1,000$ rather than $N_c = 100$ was used. The p-values were corrected for the range of global coupling strengths as well as the two graph metrics using Benjamini-Hochberg method of correcting for FDR [78]. * denotes significance p-value < 0.05.

C.3 NSI calculated with 30 s

To understand how the choice of selecting the final 20 s of the simulation was effecting the correlation between NSI and the graph metrics, NSI was recalculated using the final 30 s for the three node networks. Tables C.7 and C.8 display the results when basal node networks are included and excluded respectively.

	Trophic Incoherence			Mean Node Degree		
K_g	Correlation	p-value	Adjusted p-value	Correlation	p-value	Adjusted p-value
0.5	0.5905	0.0941	0.3589	0.7079	0.0329	0.3589
1	0.5565	0.1196	0.3589	0.6599	0.0531	0.3589
1.5	0.6359	0.0656	0.3589	0.4412	0.2345	0.5223
2	0.5572	0.1191	0.3589	0.3234	0.3960	0.7310
2.5	0.5654	0.1126	0.3589	0.2830	0.4606	0.7526
3	0.5681	0.1105	0.3589	0.2771	0.4704	0.7526
3.5	0.5367	0.1702	0.4539	0.2249	0.5922	0.7896
4	0.5127	0.2394	0.5223	0.0939	0.8414	0.9616
4.5	0.4493	0.3714	0.7310	0.0227	0.9659	0.9752
5	0.3677	0.5426	0.7669	-0.1556	0.8027	0.9616
5.5	0.3672	0.5432	0.7669	-0.1545	0.8041	0.9616
6	-0.0248	0.9752	0.9752	0.0248	0.9752	0.9752

Table C.7: **Correlating NSI with Mean Node Degree and Trophic Incoherence Using 30 s.** The Pearson's correlation, p-value and adjusted p-value when comparing NSI for each global coupling strength to the mean node degree and trophic incoherence of the network. Here the NSI value has been calculated using the final 30 s of the simulation rather than 20 s. The p-values were corrected for the range of global coupling strengths as well as the two graph metrics using Benjamini-Hochberg method of correcting for FDR [78].

	Trophic Incoherence			Mean Node Degree		
K_g	Correlation	p-value	Adjusted p-value	Correlation	p-value	Adjusted p-value
0.5	0.3177	0.4874	0.7219	0.8256	0.0222	0.1389
1	0.1621	0.7283	0.8740	0.9087	0.0046	0.0553
1.5	0.4999	0.2533	0.5069	0.8224	0.0232	0.1389
2	0.5822	0.1702	0.4086	0.7477	0.0533	0.2132
2.5	0.7627	0.0461	0.2132	0.6847	0.0897	0.2559
3	0.3013	0.5114	0.7219	0.9490	0.0011	0.0264*
3.5	-0.2025	0.7005	0.8740	0.7351	0.0960	0.2559
4	-0.4418	0.4564	0.7219	-0.0465	0.9408	~ 1
4.5	-0.6388	0.3612	0.6546	0.2180	0.7820	0.8937
5	-0.4430	0.7078	0.8740	0.9218	0.2535	0.5069
5.5	-0.9935	0.0725	0.2487	0.8255	0.3818	0.6546
6	-1.0000	NaN	NaN	1.0000	NaN	NaN

Table C.8: **Correlating NSI with Mean Node Degree and Trophic Incoherence Using 30 s - No Basal Node Networks.** The Pearson's correlation, p-value and adjusted p-value when comparing NSI for each global coupling strength to the mean node degree and trophic incoherence of all networks without a basal node. Here the NSI value has been calculated using the final 30 s of the simulation rather than 20 s. The p-values were corrected for the range of global coupling strengths as well as the two graph metrics using Benjamini-Hochberg method of correcting for FDR [78]. * denotes significance p-value < 0.05.

C.4 Scatterplots for $P = 3$

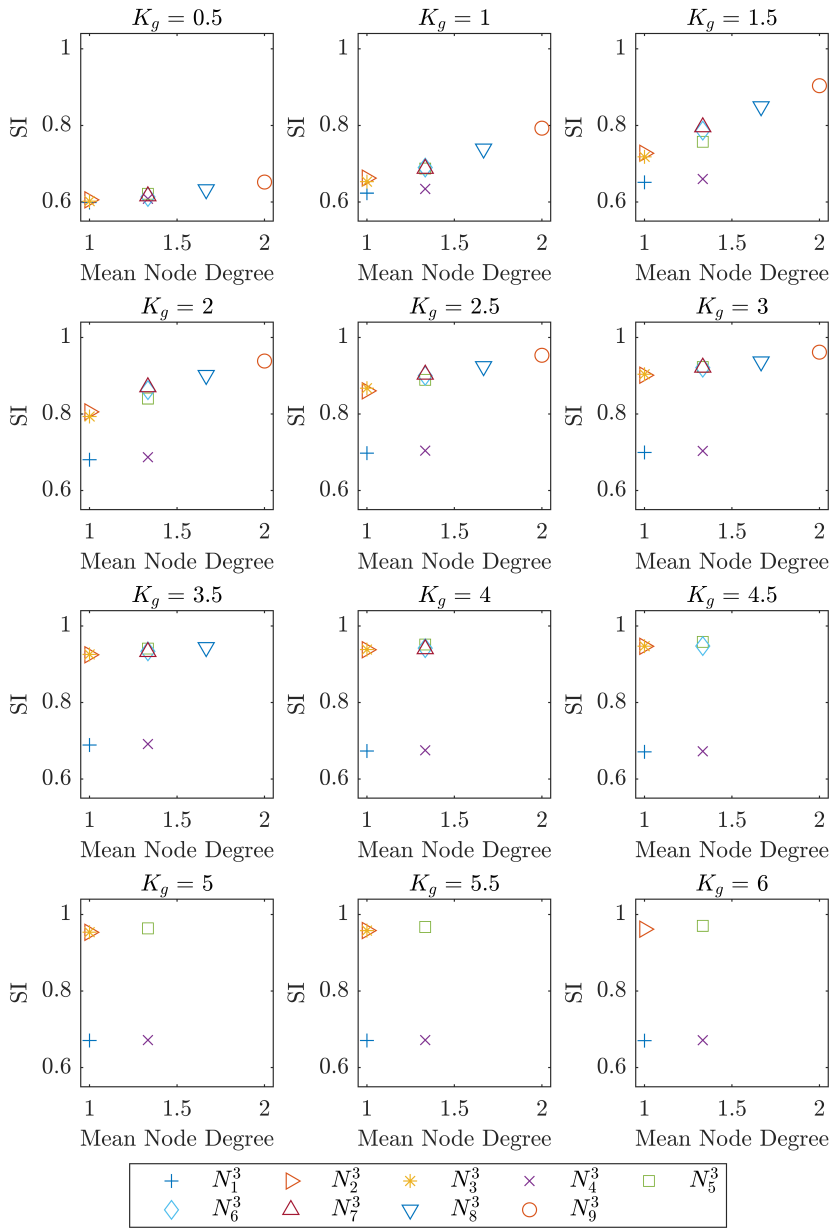


Figure C.3: **Scatterplot Comparing Mean Node Strength With SI for Three Node Networks.**

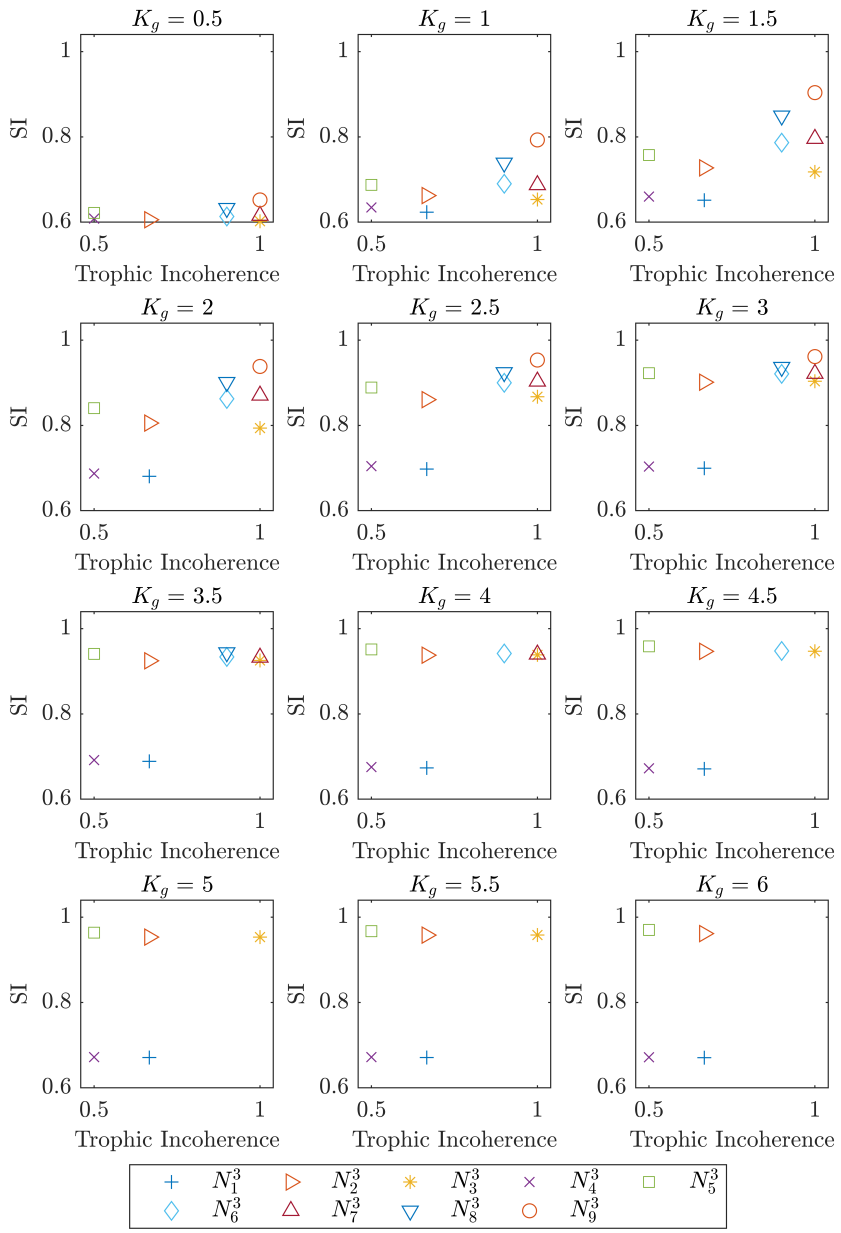


Figure C.4: **Scatterplot Comparing Trophic Incoherence With SI for Three Node Networks.**

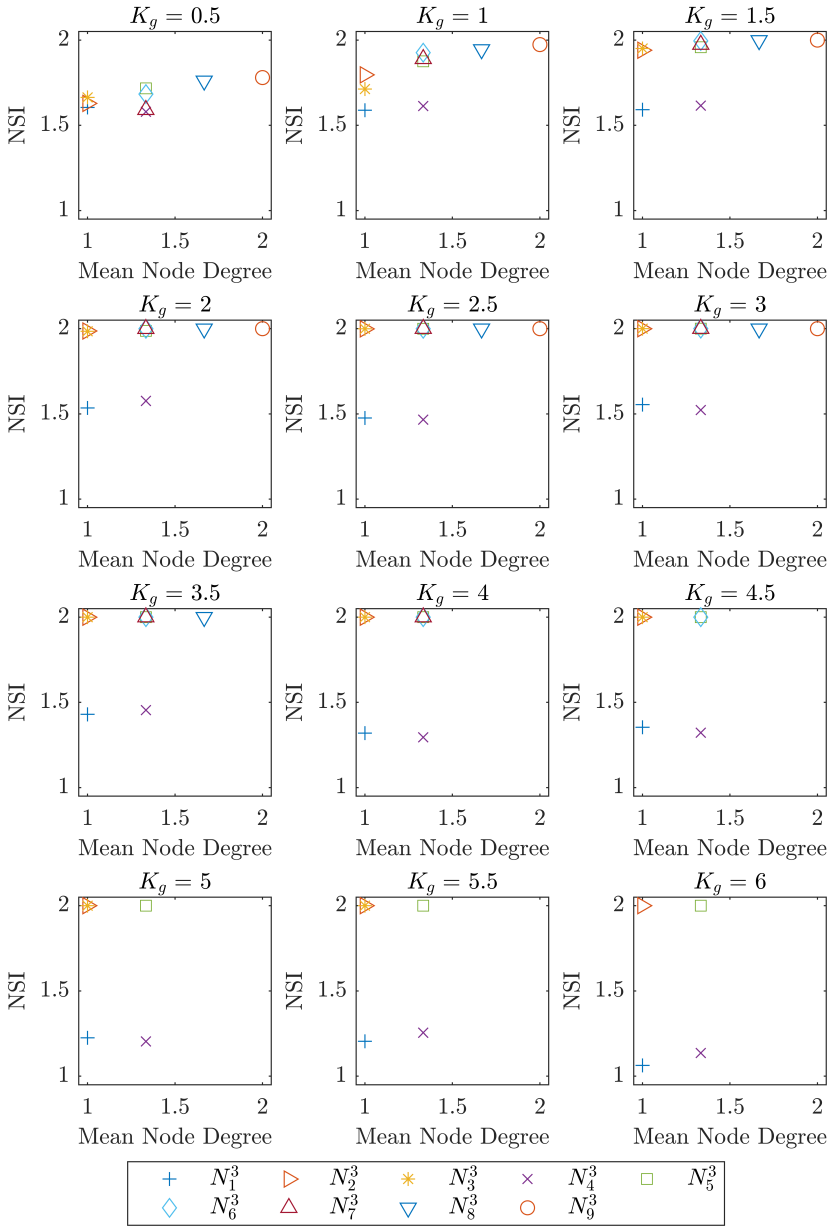


Figure C.5: **Scatterplot Comparing Mean Node Strength With NSI for Three Node Networks.**

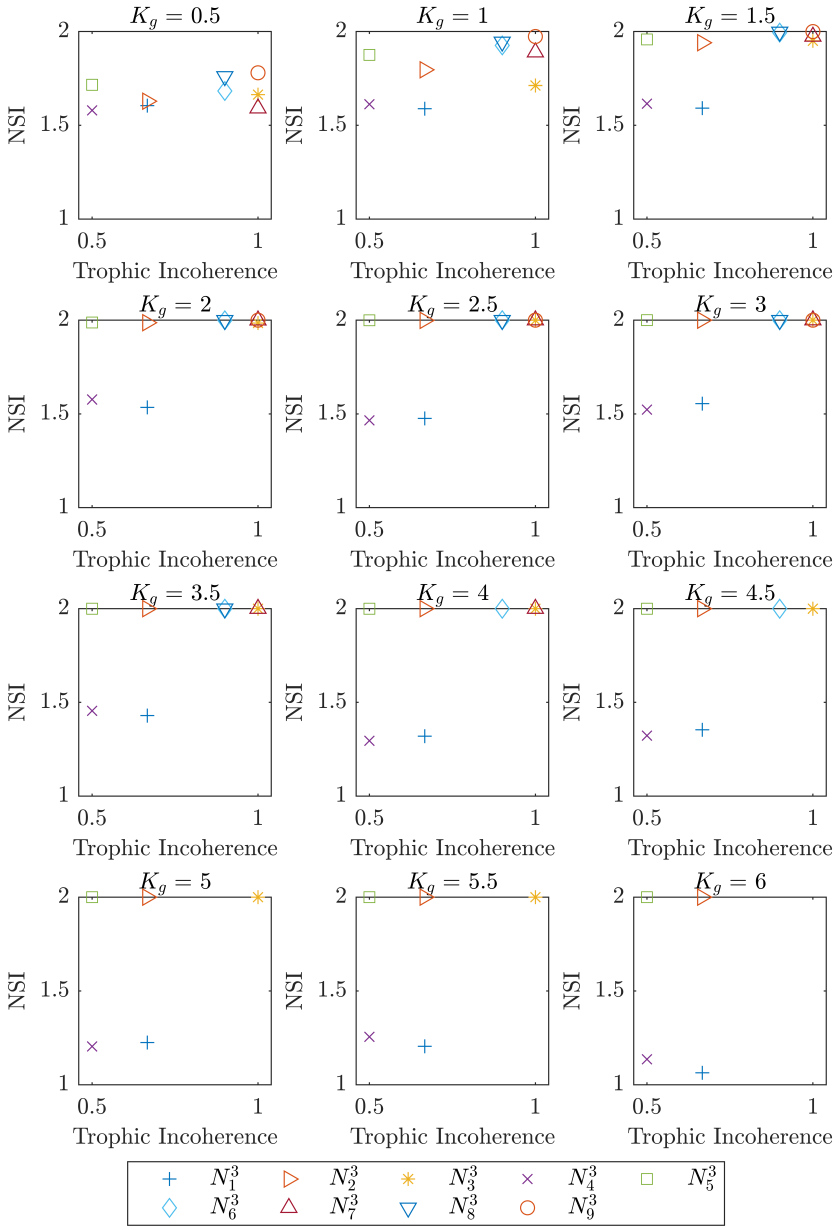


Figure C.6: **Scatterplot Comparing Trophic Incoherence With NSI for Three Node Networks.**

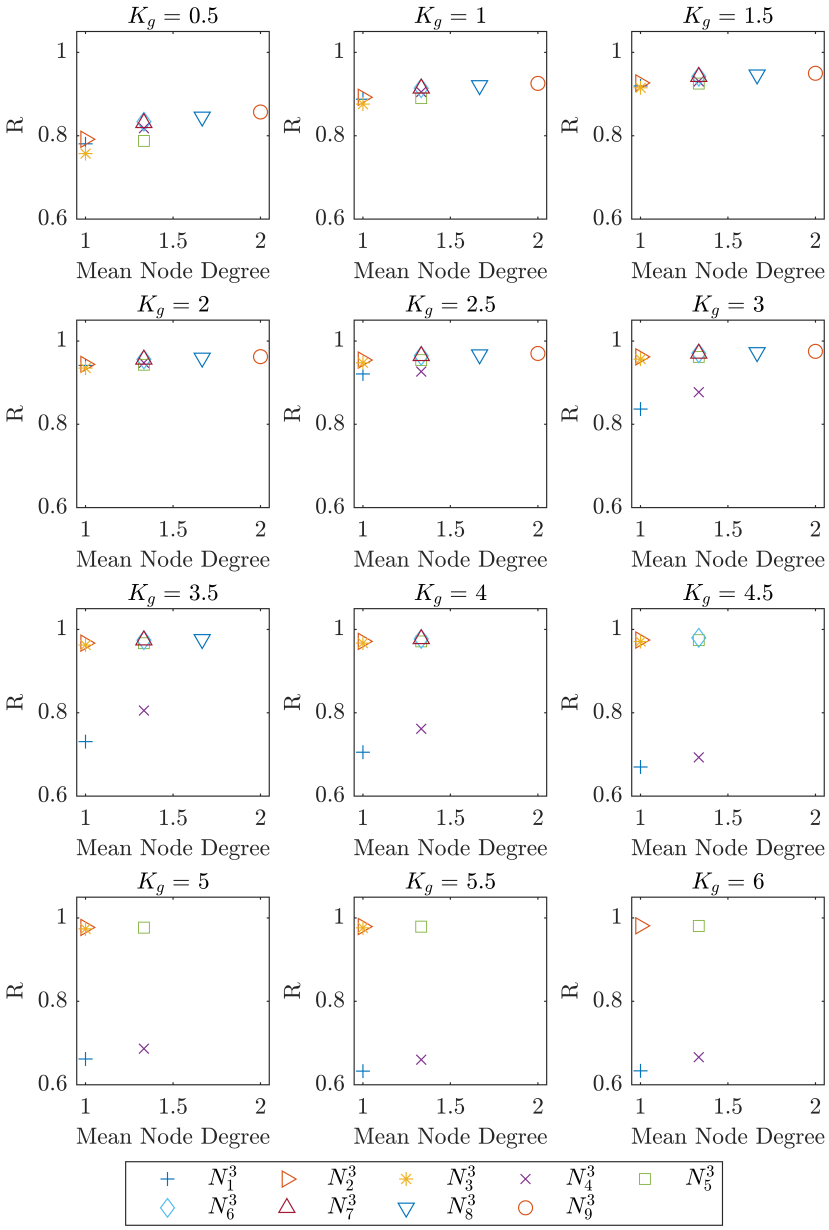


Figure C.7: **Scatterplot Comparing Mean Node Strength With R for Three Node Networks.**

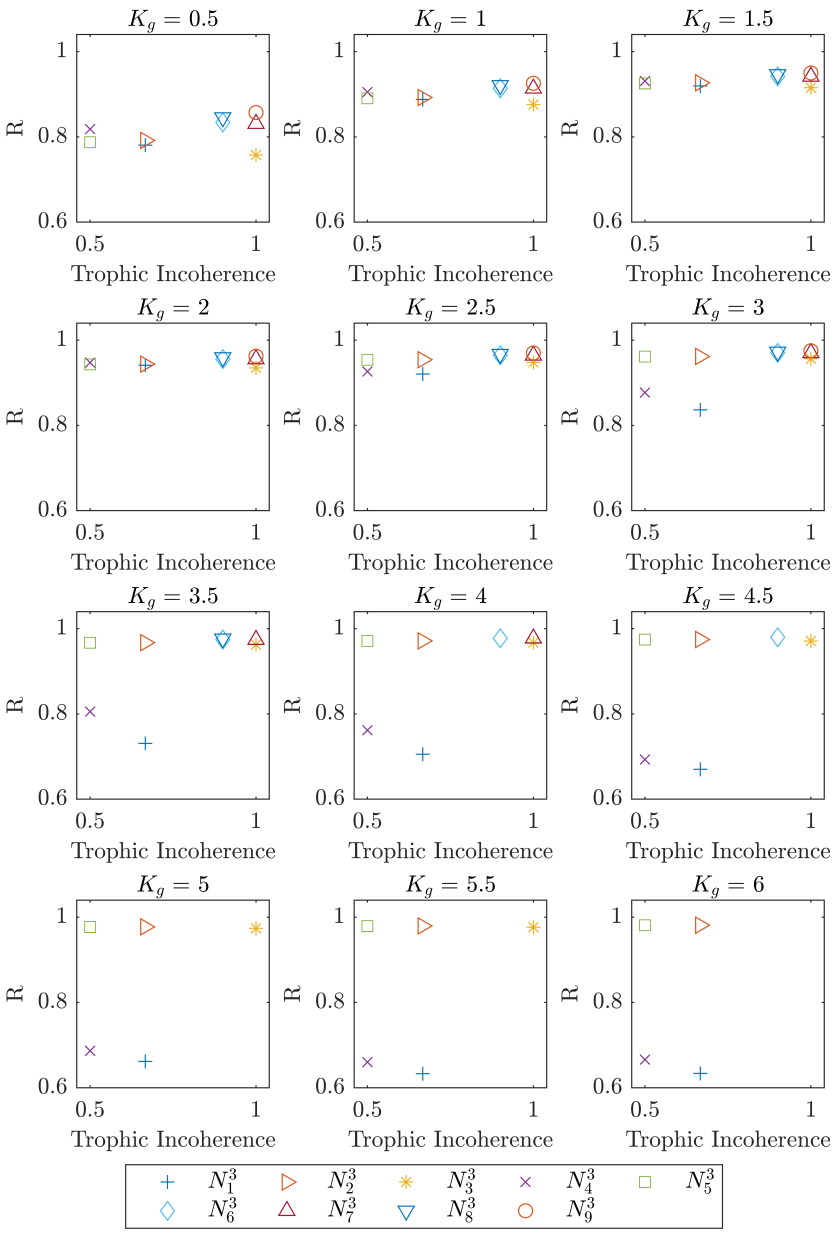


Figure C.8: **Scatterplot Comparing Trophic Incoherence With R for Three Node Networks.**

C.5 Consistency of Outliers

For all three synchronisation measures and the two graph metrics (trophic incoherence and small world index) the percentage difference between the simulated synchrony measure and the predicted synchronisation level from the linear fit was evaluated. Then the summations of the percentage difference across the six combinations and all K_g was calculated.

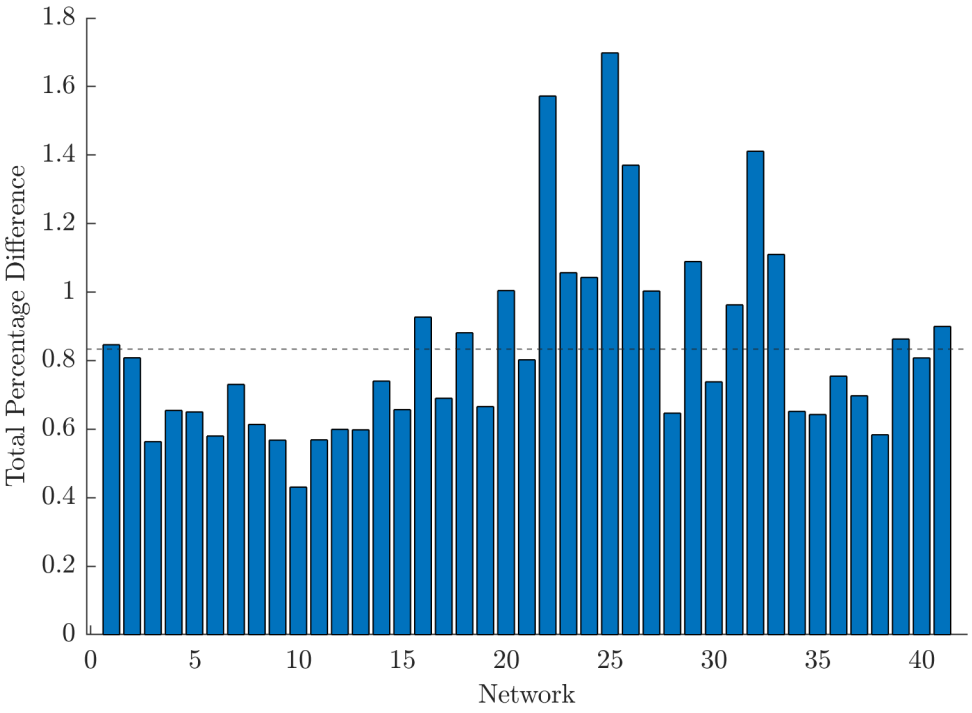


Figure C.9: **Barchart Showing the Total Percentage Difference Between the Simulation and Linear Fit: Mean Degree Three.** The dashed black line is the average total percentage difference across the networks.

We see that there are some networks in particular 22, 25, 26 and 32 for $\langle k \rangle = 3$ and 18, 26, 34 and 36 for $\langle k \rangle = 4$ where they have larger percentage differences from the predicted linear regression compared to the average across the networks. Generally, these networks have a higher p_{ws} with the differences seeing consistently greater than average differences for $p_{ws} \geq 0.15$ for $\langle k \rangle = 3$ and $p_{ws} \geq 0.25$ for $\langle k \rangle = 4$. However, only network 25 ($p_{ws} = 0.25$) for $\langle k \rangle = 3$ had a total percentage difference that was greater than 3 standard deviations away from the mean.

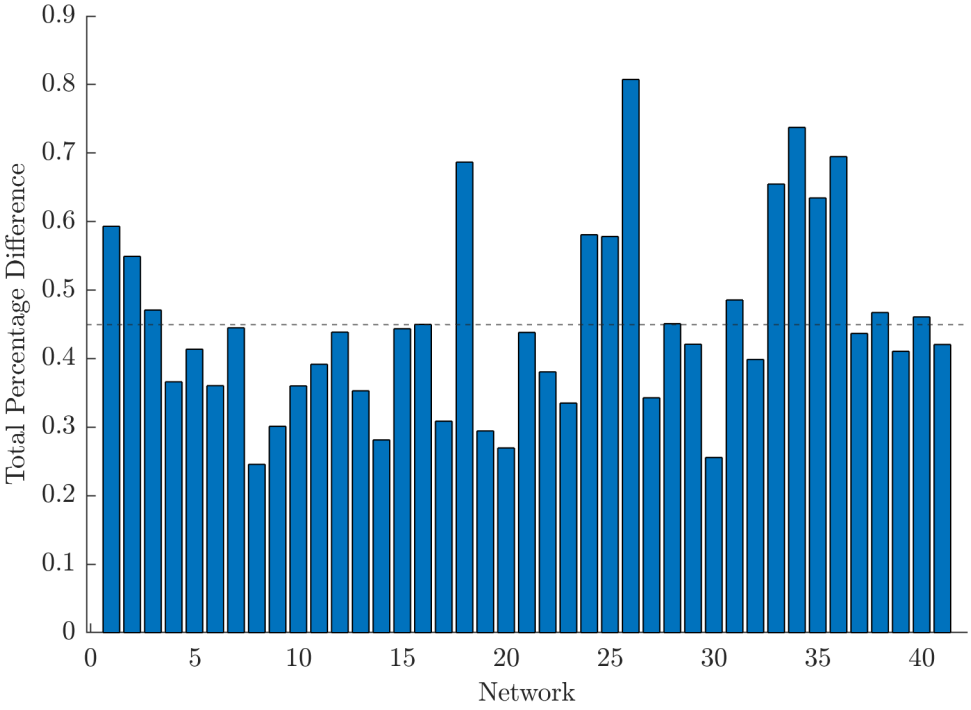


Figure C.10: **Barchart Showing the Total Percentage Difference Between the Simulation and Linear Fit: Mean Degree Four.** The dashed black line is the average total percentage difference across the networks.

APPENDIX D

CHAPTER 7

D.1 Psychomotor Vigilance Test

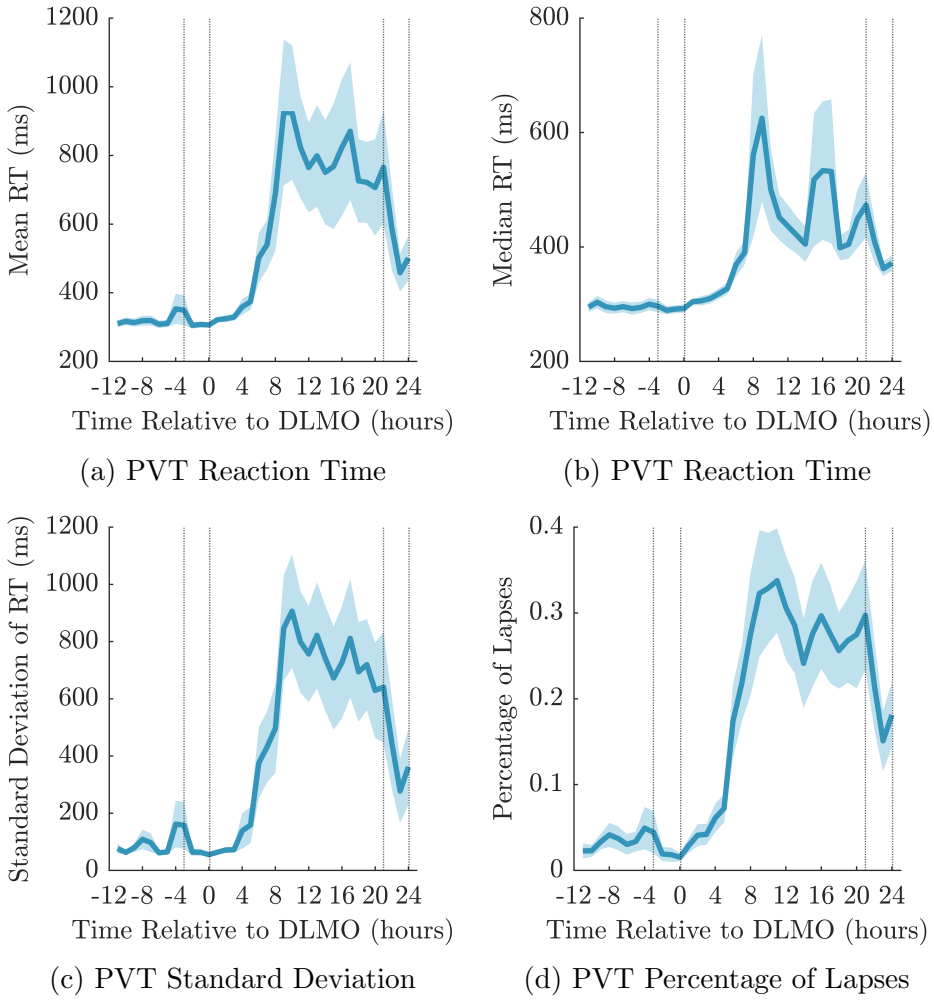
D.1.1 Group Level

At the group level the trend across all subjects for the mean, median and standard deviation of RT as well as the percentage of lapses is given in Figure D.1. The general trend for all subjects was that the measure was stable until ~ DLMO + 5 h when the PVT measures increase, reflecting both an increase in the RT and greater variability in RT. Finally, a decrease in all measures was seen around DLMO + 21 h, with a local minimum occurring during the second WMZ leading to ~ 50% reduction in the mean RT, std_{RT} and percentage of lapses.

D.1.2 PVT Groups

In addition, the PVT performance was also considered when the 13 subjects were split into the 6 lowest and 6 highest impaired subjects, with 1 subject not included. The median subject was removed to allow greater differentiation between the high and low impairment groups and ensure equal group sizes. The subjects were split by the level of impairment for each measure. This is presented in Figure D.2.

In addition, a permutation test with ($n = 10,000$) permutations was calculated to



(a) PVT Reaction Time

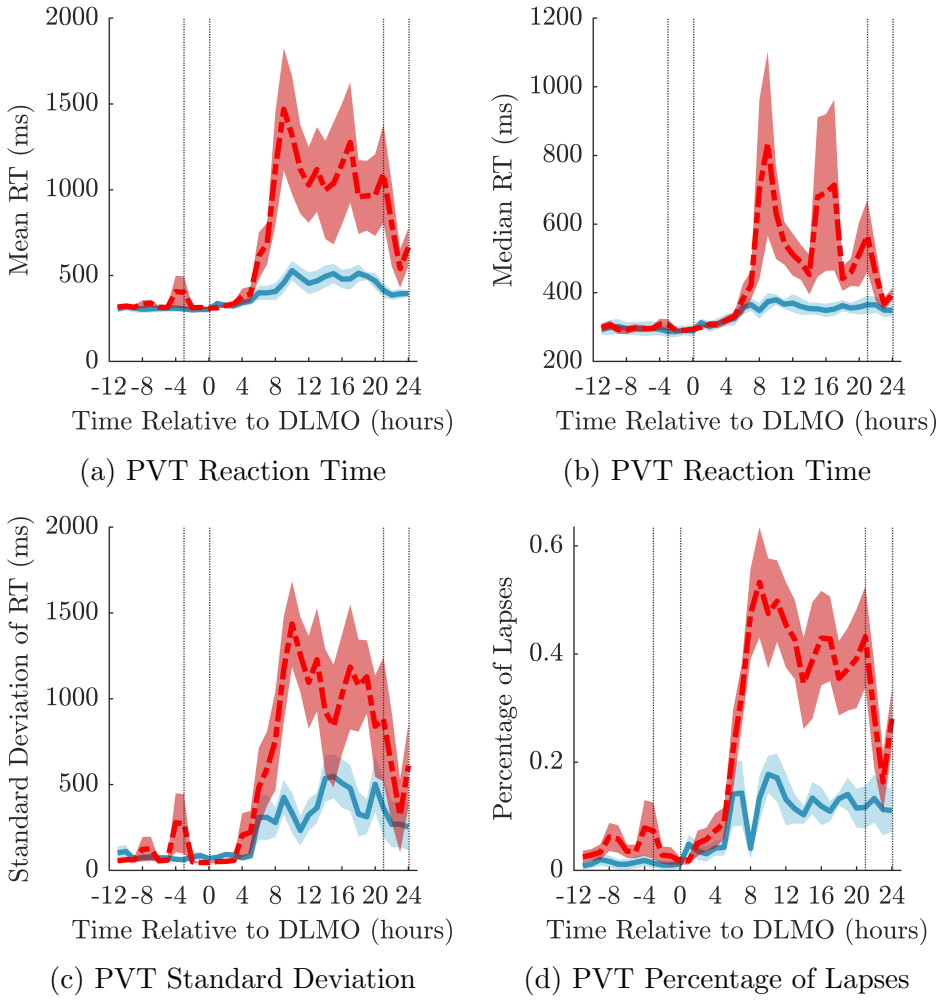
(b) PVT Reaction Time

(c) PVT Standard Deviation

(d) PVT Percentage of Lapses

Figure D.1: **Psychomotor Vigilance Test Performance.** The performance of all subjects in the PVT as measured using mean RT, median RT, standard deviation of RT and percentage of lapses at each PVT session, relative to DLMO. The solid blue line is the mean across the subjects and the shaded area is the standard error of the mean. The dotted vertical lines indicate the times considered to be in the WMZ (3 hours before DLMO to 5 minutes after).

find a p-value for the difference between the mean of the two groups for each measure over the three ranges: $[\text{DLMO} - 11\text{ h}, \text{DLMO}]$, $[\text{DLMO} + 1\text{ h}, \text{DLMO} + 12\text{ h}]$ and $[\text{DLMO} + 13\text{ h}, \text{DLMO} + 24\text{ h}]$. Grouping the timeslots into three ranges was chosen to avoid problems that may arise from multiple comparisons if each timepoint was considered for each of the four measures. Table D.1 shows the resulting p-values, which are adjusted for multiple comparisons using the Benjamini-Hochberg method of correcting for multiple comparisons [78].



(a) PVT Reaction Time

(b) PVT Reaction Time

(c) PVT Standard Deviation

(d) PVT Percentage of Lapses

Figure D.2: **Psychomotor Vigilance Test Performance Split into Groups Based on High and Low Impairment.** The subjects are split into two groups based on the level of impairment in that measure. The solid blue line (—) and dashed red line (- - - - -) are the mean across the 6 lowest and 6 highest impaired subjects and highest value, respectively. The corresponding shaded area is the standard error of the mean. The dotted vertical lines indicate the times considered to be in the WMZ (3 hours before DLMO to 5 minutes after).

PVT Measure	$[\text{DLMO} - 11h, \text{DLMO}]$	$[\text{DLMO} + 1h, \text{DLMO} + 12h]$	$[\text{DLMO} + 13h, \text{DLMO} + 24h]$
Mean RT	0.0139 (0.0116)	$< 0.0001^*$ (< 0.0001)	$< 0.0001^*$ (< 0.0001)
Median RT	0.2715 (0.2715)	0.0001^* (0.0001)	$< 0.0001^*$ (< 0.0001)
Standard Deviation of RT	0.1435 (0.1315)	$< 0.0001^*$ (< 0.0001)	$< 0.0001^*$ (< 0.0001)
Percentage of Lapses	$< 0.0001^*$ (< 0.0001)	0.0001^* (0.0001)	$< 0.0001^*$ (< 0.0001)

Table D.1: **Table Showing the *p*-values for Permutation Tests Comparing the PVT Performance with Subjects Grouped by PVT Performance.** Results for Permutation Tests ($n = 10,000$) comparing the mean value of the low and high impairment groups over adjacent 12-hour periods. The p-values have been corrected using the Benjamini-Hochberg method of correcting for the false discovery rate [78]. Uncorrected p-values are given in brackets. * denotes significance p-value < 0.05.

D.2 Circadian Strength

D.2.1 Calculating Circadian Strength

The amplitude of the core body temperature was used as a proxy for circadian strength. The core body temperature was recorded throughout the CRP. The data was cleaned by removing the first 5 hours before an order two harmonic function was fitted. The amplitude of the fitted function was then used to determine circadian strength [1]. Therefore, greater fluctuations in core body temperature, a known marker of circadian rhythm [205], will equate to higher values for circadian strength.

D.2.2 Investigating Circadian Strength

When predicting the level of impairment at different timepoints the sign of the relationship changes over time, typically peaking at the highest positive value at DLMO + 1 h and reaching the most negative point around DLMO + 11 h. Therefore, those participants in the group who performed the best at DLMO+1 h performed the worst at DLMO+11 h and vice versa. This suggests that these subjects are either receiving a greater perturbation to the system or their baseline network could be more susceptible to perturbations. In particular, this perturbation could be the cumulative drive of circadian and homeostatic processes. To investigate this we initially considered if the baseline metrics were related to circadian strength, as measured using the amplitude of core body temperature. Therefore, we correlated circadian strength with baseline mean node strength, trophic incoherence, stability and SI for K_g strength. However, none of the p-values associated with these correlations were significant (even when uncorrected for multiple comparisons). This could mean that mean node strength is not a marker of circadian strength, however it could also mean that core body temperature does not accurately reflect the circadian perturbation in the brain and a more direct measurement such as brain temperature

[1] The precise details of the protocol will be available in a publication in preparation [4]

could be more informative, as these two measures are not identical [162].

D.3 Removal of Outliers

The results for Sections 7.3.2, 7.3.3 and 7.3.6 repeated when the two participants who are visually outliers in Figure 7.3b are removed.

Correlations	Pearson's Correlation	p-value	Adjusted p-value
First Acquisition: Mean RT and Mean Node Strength	-0.6784	0.0310	0.0466*
First Acquisition: Median RT and Mean Node Strength	-0.3051	0.3914	0.9460
First Acquisition: RT std and Mean Node Strength	-0.8524	0.0017	0.0466*
First Acquisition: Percentage of Lapses and Mean Node Strength	-0.4484	0.1937	0.2214
11 Hours Before DLMO: Mean RT and Mean Node Strength	-0.5494	0.0800	0.0510
11 Hours Before DLMO: Median RT and Mean Node Strength	-0.2490	0.4603	0.9460
11 Hours Before DLMO: RT std and Mean Node Strength	-0.6410	0.0335	0.0510
11 Hours Before DLMO: Percentage of Lapses and Mean Node Strength	-0.5693	0.0676	0.1711

Table D.2: **Table Showing the Pearson's Correlation and p-value for PVT impairment and Mean Node Strength with Outliers Removed.** The Pearson's Correlation between the PVT impairment of the subject and the mean node strength of their functional network was calculated from the first EEG acquisition after awakening and the EEG acquisition 11 hours before DLMO, when the two potential outliers were removed. The p-values in the table are corrected for multiple comparisons using the Benjimini-Hochberg correct for FDR [78]. * denotes significance p-value < 0.05.

Correlations	Pearson's Correlation	p-value	Adjusted p-value
First Acquisition: Mean RT and Mean Node Strength	-0.0154	0.9662	0.6076
First Acquisition: Median RT and Mean Node Strength	-0.2361	0.5115	0.6076
First Acquisition: RT std and Mean Node Strength	0.1556	0.6677	0.6076
First Acquisition: Percentage of Lapses and Mean Node Strength	-0.0658	0.8567	0.6076
11 Hours Before DLMO: Mean RT and Mean Node Strength	0.0352	0.9181	0.6076
11 Hours Before DLMO: Median RT and Mean Node Strength	-0.2040	0.5474	0.6076
11 Hours Before DLMO: RT std and Mean Node Strength	0.2704	0.4213	0.6076
11 Hours Before DLMO: Percentage of Lapses and Mean Node Strength	-0.0460	0.8932	0.6076

Table D.3: **Table Showing the Pearson's Correlation and p-value for PVT impairment and Trophic Incoherence with Outliers Removed.** The Pearson's Correlation between the PVT impairment of the subject and the trophic incoherence of their functional network was calculated from the first EEG acquisition after awakening and the EEG acquisition 11 hours before DLMO, when the two potential outliers were removed. The p-values in the table are corrected for multiple comparisons using the Benjamini-Hochberg correct for FDR [78]. * denotes significance p-value < 0.05.

Correlations	Pearson's Correlation	p-value	Adjusted p-value
First Acquisition: Mean RT and Mean Node Strength	-0.3815	0.3511	0.8583
First Acquisition: Median RT and Mean Node Strength	-0.1493	0.7242	0.9457
First Acquisition: RT std and Mean Node Strength	-0.5266	0.1800	0.5765
First Acquisition: Percentage of Lapses and Mean Node Strength	0.1060	0.8027	0.8583
11 Hours Before DLMO: Mean RT and Mean Node Strength	-0.6677	0.0349	0.2410
11 Hours Before DLMO: Median RT and Mean Node Strength	-0.3183	0.3701	0.9457
11 Hours Before DLMO: RT std and Mean Node Strength	-0.8086	0.0046	0.1274
11 Hours Before DLMO: Percentage of Lapses and Mean Node Strength	-0.1138	0.7542	0.9457

Table D.4: **Table Showing the Pearson's Correlation and *p*-value for PVT impairment and Stability with Outliers Removed.** The Pearson's Correlation between the PVT impairment of the subject and the stability of their functional network was calculated from the first EEG acquisition after awakening and the EEG acquisition 11 hours before DLMO, when the two potential outliers were removed. The p-values in the table are corrected for multiple comparisons using the Benjamini-Hochberg correct for FDR [78]. * denotes significance p-value < 0.05.

K_g	Pearson's Correlation	p-value	Adjusted p-value
1	-0.3259	0.3281	0.3977
2	-0.5338	0.0908	0.1676
3	-0.5977	0.0521	0.1545
4	-0.6116	0.0456	0.1402
5	-0.6524	0.0296	0.0986
6	-0.6692	0.0243	0.0884
7	-0.6946	0.0177	0.0811
8	-0.7226	0.0120	0.0686
9	-0.7162	0.0132	0.0703
10	-0.6951	0.0176	0.0811
11	-0.6798	0.0214	0.0849
12	-0.6588	0.0275	0.0956
13	-0.6391	0.0343	0.1096
14	-0.5916	0.0552	0.1577
15	-0.5030	0.1383	0.2128
16	-0.5358	0.1711	0.2428
17	-0.3944	0.4391	0.5019
18	-0.3463	0.5013	0.5570
19	-0.2938	0.6314	0.6735
20	-0.2684	0.6624	0.6818

Table D.5: **Table Showing the Pearson's Correlation and *p*-value for % Increase in Mean RT and SI with Outliers Removed.** The Pearson's Correlation between the % increase in Mean RT of the subject and SI, which was calculated from the first EEG acquisition after awakening, when the two potential outliers were removed. The p-values in the table are corrected for multiple comparisons using the Benjamini-Hochberg correct for FDR [78]. * denotes significance p-value < 0.05.

K_g	Pearson's Correlation	p-value	Adjusted p-value
1	-0.1535	0.6522	0.6818
2	-0.2470	0.4640	0.5229
3	-0.3446	0.2994	0.3743
4	-0.3603	0.2764	0.3566
5	-0.4119	0.2081	0.2822
6	-0.4246	0.1931	0.2663
7	-0.4424	0.1730	0.2428
8	-0.4694	0.1453	0.2152
9	-0.4770	0.1379	0.2128
10	-0.4828	0.1325	0.2120
11	-0.5010	0.1165	0.1983
12	-0.5167	0.1037	0.1803
13	-0.5479	0.0810	0.1581
14	-0.5521	0.0782	0.1581
15	-0.5572	0.0943	0.1676
16	-0.5679	0.1420	0.2143
17	-0.5363	0.2727	0.3566
18	-0.5134	0.2975	0.3743
19	-0.4865	0.4060	0.4776
20	-0.4741	0.4198	0.4868

Table D.6: **Table Showing the Pearson's Correlation and *p*-value for % Increase in Median RT and SI with Outliers Removed.** The Pearson's Correlation between the % increase in Median RT of the subject and SI, which was calculated from the first EEG acquisition after awakening, when the two potential outliers were removed. The p-values in the table are corrected for multiple comparisons using the Benjamini-Hochberg correct for FDR [78]. * denotes significance p-value < 0.05.

K_g	Pearson's Correlation	p-value	Adjusted p-value
1	-0.7369	0.0097	0.0595
2	-0.7970	0.0033	0.0249
3	-0.8381	0.0013	0.0141
4	-0.8342	0.0014	0.0141
5	-0.8434	0.0011	0.0141
6	-0.8669	0.0006	0.0110
7	-0.8842	0.0003	0.0110
8	-0.8894	0.0002	0.0110
9	-0.8683	0.0005	0.0110
10	-0.8439	0.0011	0.0141
11	-0.8255	0.0017	0.0156
12	-0.7953	0.0034	0.0249
13	-0.7560	0.0071	0.0474
14	-0.6880	0.0193	0.0811
15	-0.5599	0.0924	0.1676
16	-0.6603	0.0747	0.1581
17	-0.6988	0.1224	0.2040
18	-0.6560	0.1572	0.2286
19	-0.9380	0.0184	0.0811
20	-0.9294	0.0223	0.0849

Table D.7: **Table Showing the Pearson's Correlation and *p*-value for % Increase in std of RT and SI with Outliers Removed.** The Pearson's Correlation between the % increase in std of RT of the subject and SI, which was calculated from the first EEG acquisition after awakening, when the two potential outliers were removed. The p-values in the table are corrected for multiple comparisons using the Benjamini-Hochberg correct for FDR [78]. * denotes significance p-value < 0.05.

K_g	Pearson's Correlation	p-value	Adjusted p-value
1	-0.1477	0.6648	0.6818
2	-0.3953	0.2288	0.3051
3	-0.4903	0.1257	0.2052
4	-0.5515	0.0786	0.1581
5	-0.5785	0.0622	0.1581
6	-0.5654	0.0699	0.1581
7	-0.5500	0.0796	0.1581
8	-0.5622	0.0718	0.1581
9	-0.5573	0.0749	0.1581
10	-0.5439	0.0837	0.1595
11	-0.5482	0.0808	0.1581
12	-0.5482	0.0808	0.1581
13	-0.5662	0.0694	0.1581
14	-0.5537	0.0772	0.1581
15	-0.3306	0.3508	0.4189
16	-0.4159	0.3055	0.3760
17	-0.3097	0.5503	0.6030
18	-0.2634	0.6140	0.6638
19	-0.2029	0.7434	0.7528
20	-0.1766	0.7764	0.7764

Table D.8: **Table Showing the Pearson's Correlation and *p*-value for the Percentage of Lapses and SI with Outliers Removed.** The Pearson's Correlation between the % increase in Mean RT of the subject and SI, which was calculated from the first EEG acquisition after awakening, when the two potential outliers were removed. The p-values in the table are corrected for multiple comparisons using the Benjamini-Hochberg correct for FDR [78]. * denotes significance p-value < 0.05.

K_g	Pearson's Correlation	p-value	Adjusted p-value
1	-0.3284	0.2973	0.3472
2	-0.4259	0.1674	0.2435
3	-0.5223	0.0815	0.1387
4	-0.5430	0.0681	0.1316
5	-0.5822	0.0470	0.1300
6	-0.5799	0.0481	0.1300
7	-0.6049	0.0372	0.1240
8	-0.6299	0.0281	0.1125
9	-0.6249	0.0298	0.1136
10	-0.6373	0.0258	0.1125
11	-0.6475	0.0228	0.1087
12	-0.6496	0.0222	0.1087
13	-0.6465	0.0231	0.1087
14	-0.6116	0.0346	0.1202
15	-0.5505	0.0793	0.1379
16	-0.5995	0.0879	0.1436
17	-0.5479	0.2029	0.2732
18	-0.5120	0.2401	0.3001
19	-0.5074	0.3042	0.3472
20	-0.4860	0.3283	0.3648

Table D.9: **Table Showing the Pearson's Correlation and *p*-value for Mean RT and SI with Outliers Removed: Acquisition 11 hours before DLMO.** The Pearson's Correlation between the % increase in Mean RT of the subject and SI, which was calculated from the EEG acquisition 11 hours before DLMO, when the two potential outliers were removed. The p-values in the table are corrected for multiple comparisons using the Benjamini-Hochberg correct for FDR [78]. * denotes significance p-value < 0.05.

K_g	Pearson's Correlation	p-value	Adjusted p-value
1	-0.1599	0.6196	0.6275
2	-0.1899	0.5544	0.5836
3	-0.3053	0.3346	0.3667
4	-0.3252	0.3024	0.3472
5	-0.3756	0.2289	0.2954
6	-0.3762	0.2281	0.2954
7	-0.3941	0.2049	0.2732
8	-0.4192	0.1750	0.2500
9	-0.4272	0.1660	0.2435
10	-0.4541	0.1381	0.2085
11	-0.4880	0.1075	0.1687
12	-0.5175	0.0848	0.1414
13	-0.5572	0.0598	0.1316
14	-0.5659	0.0551	0.1316
15	-0.5741	0.0647	0.1316
16	-0.5889	0.0952	0.1523
17	-0.5725	0.1792	0.2516
18	-0.5540	0.1970	0.2717
19	-0.5501	0.2581	0.3128
20	-0.5401	0.2686	0.3207

Table D.10: **Table Showing the Pearson's Correlation and p-value for % Increase in Median RT and SI with Outliers Removed: Acquisition 11 hours before DLMO.** The Pearson's Correlation between the % increase in median RT of the subject and SI, which was calculated from the EEG acquisition 11 hours before DLMO, when the two potential outliers were removed. The p-values in the table are corrected for multiple comparisons using the Benjamini-Hochberg correct for FDR [78]. * denotes significance p-value < 0.05.

K_g	Pearson's Correlation	p-value	Adjusted p-value
1	-0.7247	0.0077	0.0511
2	-0.6675	0.0177	0.1011
3	-0.7486	0.0051	0.0371
4	-0.7533	0.0047	0.0371
5	-0.7623	0.0039	0.0371
6	-0.7642	0.0038	0.0371
7	-0.7817	0.0027	0.0371
8	-0.7849	0.0025	0.0371
9	-0.7662	0.0037	0.0371
10	-0.7782	0.0029	0.0371
11	-0.7868	0.0024	0.0371
12	-0.7805	0.0027	0.0371
13	-0.7582	0.0043	0.0371
14	-0.7032	0.0107	0.0661
15	-0.6048	0.0487	0.1300
16	-0.7221	0.0280	0.1125
17	-0.7940	0.0330	0.1200
18	-0.7698	0.0430	0.1300
19	-0.8227	0.0443	0.1300
20	-0.8138	0.0488	0.1300

Table D.11: **Table Showing the Pearson's Correlation and *p*-value for % Increase in std of RT and SI with Outliers Removed: Acquisition 11 hours before DLMO.** The Pearson's Correlation between the % increase in std of RT of the subject and SI, which was calculated from the EEG acquisition 11 hours before DLMO, when the two potential outliers were removed. The p-values in the table are corrected for multiple comparisons using the Benjamini-Hochberg correct for FDR [78]. * denotes significance p-value < 0.05.

K_g	Pearson's Correlation	p-value	Adjusted p-value
1	-0.1490	0.6440	0.6440
2	-0.3713	0.2348	0.2981
3	-0.4764	0.1174	0.1806
4	-0.5391	0.0705	0.1316
5	-0.5659	0.0551	0.1316
6	-0.5462	0.0662	0.1316
7	-0.5315	0.0753	0.1339
8	-0.5429	0.0681	0.1316
9	-0.5385	0.0709	0.1316
10	-0.5361	0.0724	0.1316
11	-0.5464	0.0660	0.1316
12	-0.5488	0.0647	0.1316
13	-0.5649	0.0557	0.1316
14	-0.5480	0.0651	0.1316
15	-0.3388	0.3081	0.3472
16	-0.4283	0.2501	0.3078
17	-0.3378	0.4587	0.4959
18	-0.2993	0.5143	0.5486
19	-0.2869	0.5815	0.6042
20	-0.2643	0.6128	0.6275

Table D.12: **Table Showing the Pearson's Correlation and p-value for the Percentage of Lapses and SI with Outliers Removed: Acquisition 11 hours before DLMO.** The Pearson's Correlation between the percentage of lapses of the subject and SI, which was calculated from the EEG acquisition 11 hours before DLMO, when the two potential outliers were removed. The p-values in the table are corrected for multiple comparisons using the Benjamini-Hochberg correct for FDR [78]. * denotes significance p-value < 0.05.

D.4 Figures for SI Impairment and Uncorrected *p*-values

Tables displaying the uncorrected p-values when correlating PVT impairment to SI across the different K_g values are given below in Tables D.13 and D.14 for reference. These uncorrected p-values correspond to the Figures D.3-D.8 and Figures 7.7 and 7.8.

K_g	% Increase in Mean RT	% Increase in Median RT	% Increase in std of RT	Percentage of Lapses
1	0.2717	0.5072	0.0056	0.5338
2	0.1133	0.4206	0.0018	0.2021
3	0.1304	0.4155	0.0010	0.1656
4	0.1100	0.3712	0.0010	0.1054
5	0.0741	0.2787	0.0007	0.0784
6	0.0689	0.2719	0.0004	0.0891
7	0.0669	0.2769	0.0002	0.1096
8	0.0713	0.2905	0.0003	0.1195
9	0.0977	0.3335	0.0007	0.1475
10	0.1293	0.3607	0.0017	0.1774
11	0.1586	0.3668	0.0029	0.1887
12	0.1972	0.3766	0.0059	0.2055
13	0.2359	0.3611	0.0120	0.2006
14	0.3131	0.3833	0.0303	0.2307
15	0.6207	0.5626	0.1449	0.7517
16	0.6339	0.5998	0.0959	0.6552
17	0.9822	0.7928	0.0930	0.9408
18	0.9981	0.7806	0.1167	0.9727
19	0.9644	0.7972	0.0041	0.9831
20	0.6624	0.4198	0.0223	0.7764

Table D.13: **Uncorrected *p*-values when Correlating PVT Impairment to SI for the First Acquisition After Awakening.**

K_g	% Increase in Mean RT	% Increase in Median RT	% Increase in std of RT	Percentage of Lapses
1	0.2411	0.4696	0.0044	0.5056
2	0.1981	0.5207	0.0125	0.2227
3	0.1827	0.4727	0.0046	0.1673
4	0.1494	0.4149	0.0039	0.1031
5	0.1046	0.3139	0.0030	0.0760
6	0.1128	0.3266	0.0030	0.0927
7	0.1099	0.3320	0.0024	0.1137
8	0.1182	0.3502	0.0027	0.1250
9	0.1538	0.3981	0.0049	0.1541
10	0.1611	0.3904	0.0045	0.1709
11	0.1673	0.3674	0.0043	0.1726
12	0.1798	0.3493	0.0053	0.1817
13	0.1938	0.3135	0.0081	0.1737
14	0.2434	0.3193	0.0187	0.2013
15	0.4502	0.4439	0.0822	0.6619
16	0.4238	0.4550	0.0403	0.5398
17	0.5998	0.5732	0.0332	0.7725
18	0.6091	0.5599	0.0392	0.7995
19	0.6057	0.5562	0.0289	0.7964
20	0.3283	0.2686	0.0488	0.6128

Table D.14: **Uncorrected *p*-values when Correlating PVT Impairment to SI for the Acquisition 11 Hours Before DLMO.**

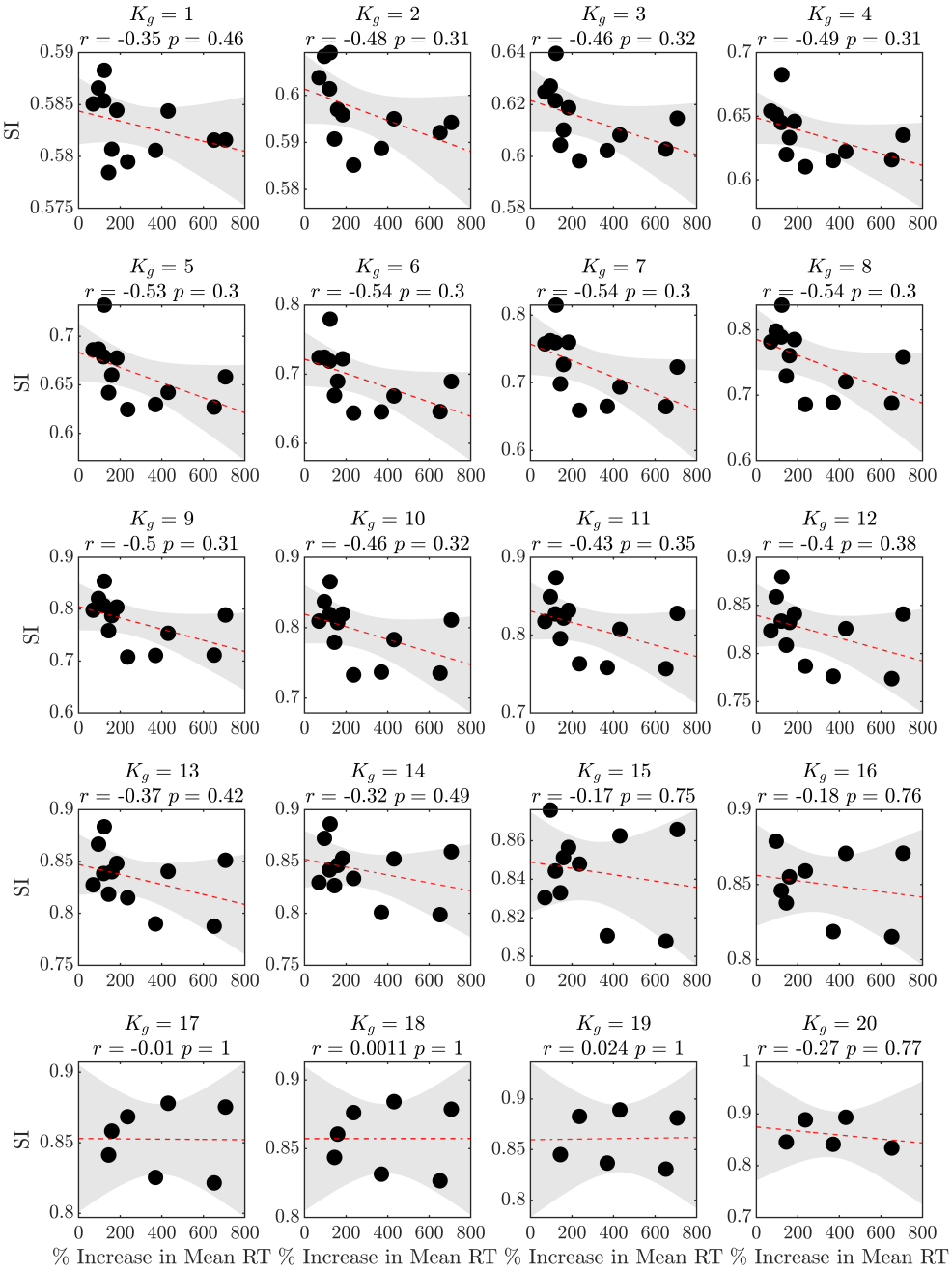


Figure D.3: **Scatterplot Relating PVT Impairment to SI Using Mean RT for the First Acquisition After Awakening.** Scatterplots relating the PVT impairment as measured using mean RT to SI for K_g = 2 to K_g = 21 for the first scan after awakening. In all plots a black dot represents a participant, the red dashed line is the linear fit between the two variables and the grey patch represents the 95% confidence interval. The Pearson's r correlation and the p-value corrected for multiple comparisons using the Benjamnini-Hochberg method for all K_g values and the four PVT measures are given above each diagram.

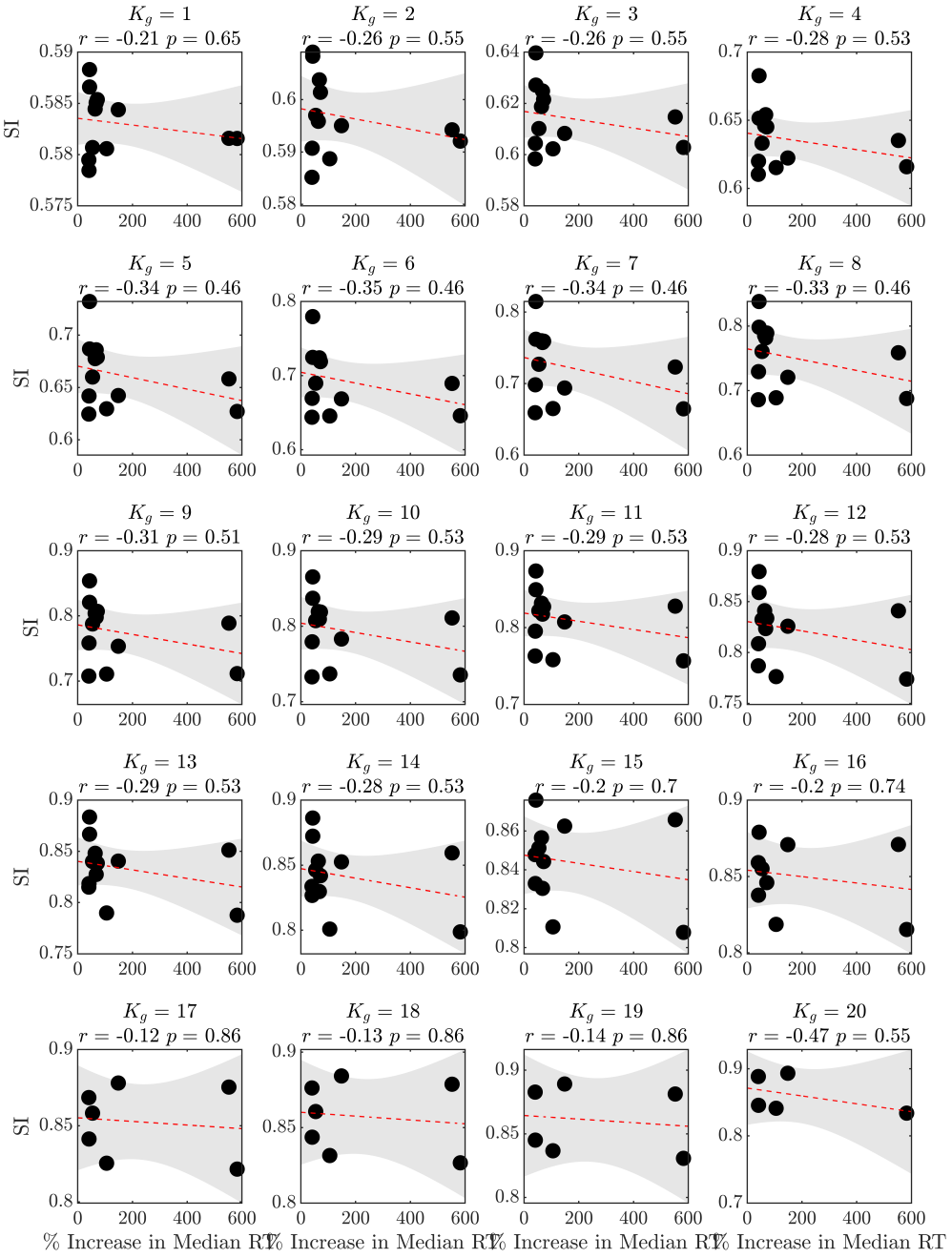


Figure D.4: **Scatterplot Relating PVT Impairment to SI Using Median RT for the First Acquisition After Awakening.** Scatterplots relating the PVT impairment as measured using mean RT to SI for K_g = 2 to K_g = 21 for the first scan after awakening. The Pearson's r correlation and the p-value corrected for multiple comparisons using the Benjamnini-Hochberg method for all K_g values and the four PVT measures are given above each diagram.

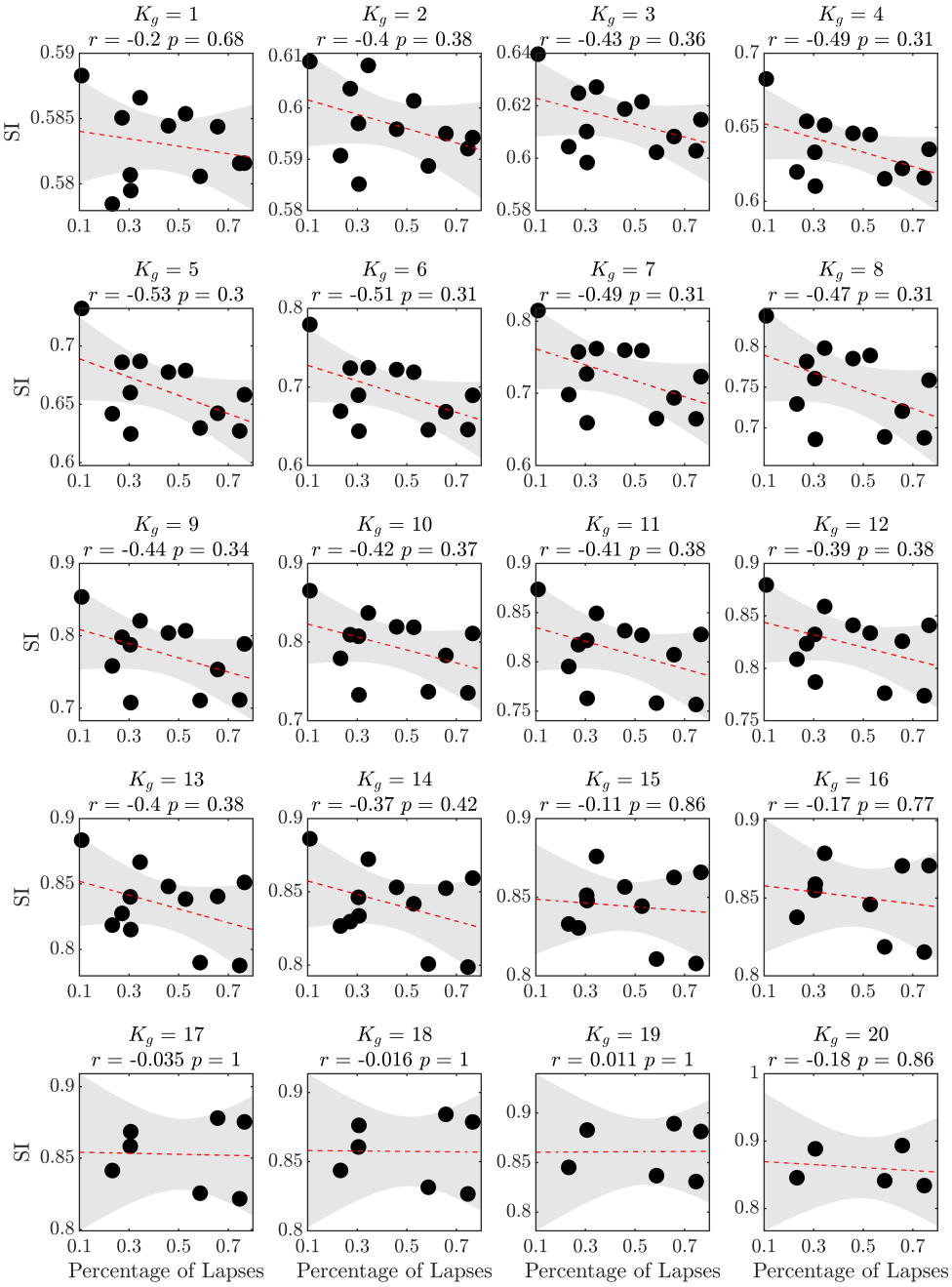


Figure D.5: **Scatterplot Relating PVT Impairment to SI Using Percentage of Lapses for the First Acquisition After Awakening.** Scatterplots relating the PVT impairment as measured using percentage of lapses of RT to SI for K_g = 2 to K_g = 21 for the first scan after awakening. The Pearson's r correlation and the p-value corrected for multiple comparisons using the Benjamnini-Hochberg method for all K_g values and the four PVT measures are given above each diagram.

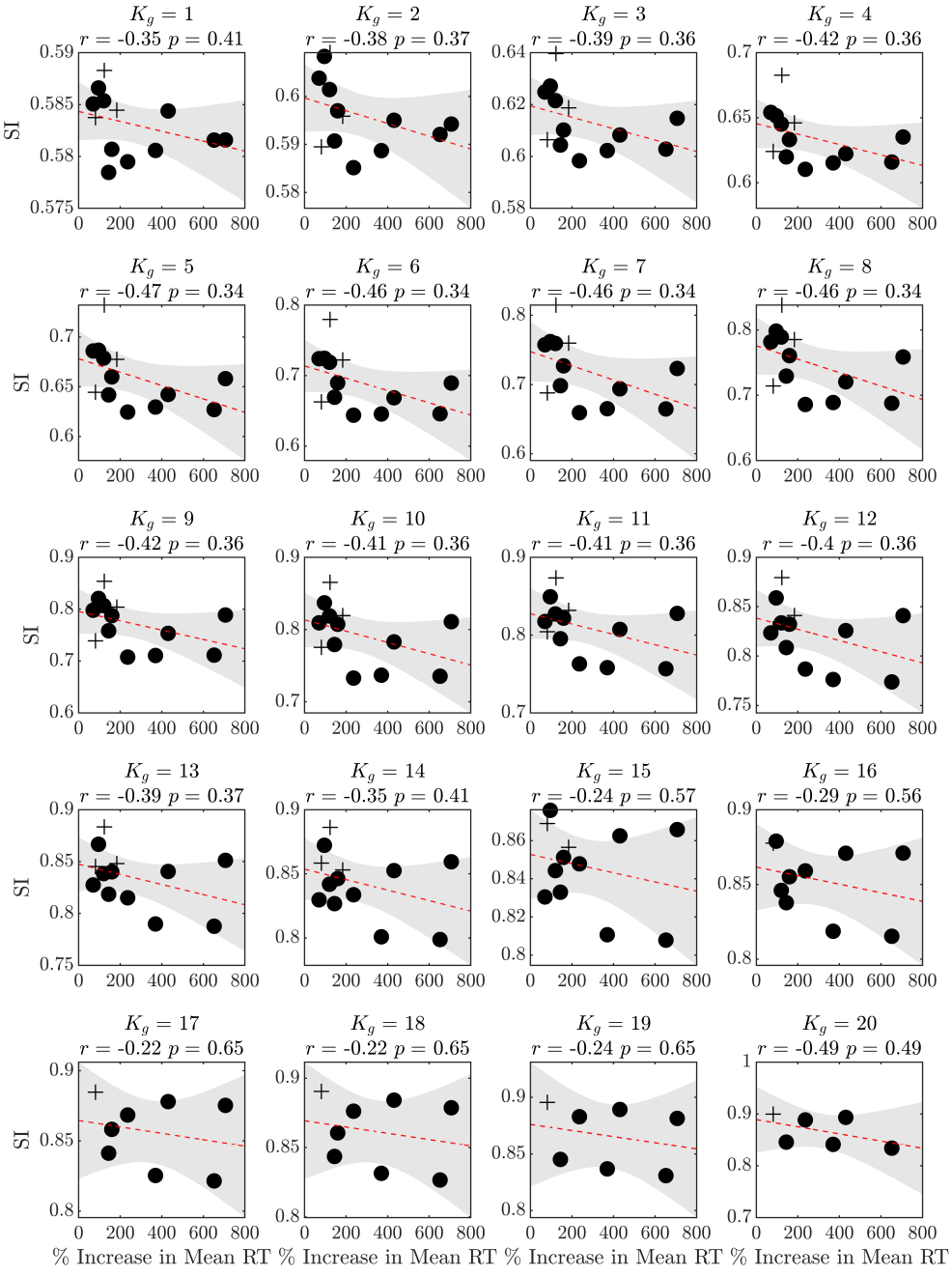


Figure D.6: **Scatterplot Relating PVT Impairment to SI Using Mean RT for the Acquisition 11 Hours Before DLMO.** Scatterplots relating the PVT impairment as measured using mean RT to SI for K_g = 2 to K_g = 21 for scan 11 hours before DLMO. Participants whose scan 11 hours before DLMO is not their first EEG acquisition are represented by + in all plots, while those whose first EEG acquisition is 11 hours before DLMO are denoted by •. The Pearson's r correlation and the p-value corrected for multiple comparisons using the Benjamnini-Hochberg method for all K_g values and the four PVT measures are given above each diagram.

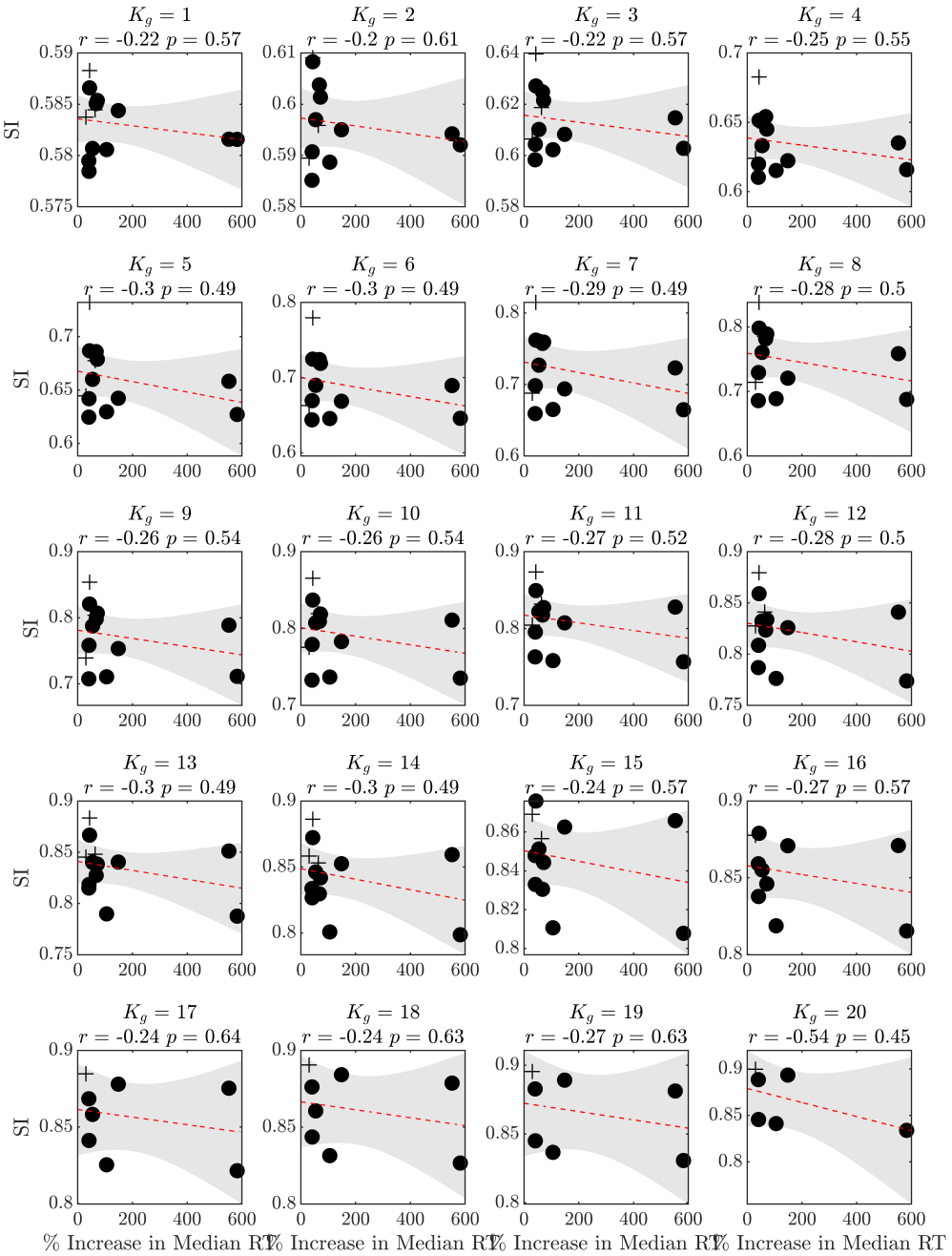


Figure D.7: **Scatterplot Relating PVT Impairment to SI Using Median RT for the Acquisition 11 Hours Before DLMO.** Scatterplots relating the PVT impairment as measured using median RT to SI for K_g = 2 to K_g = 21 for scan 11 hours before DLMO. The Pearson's r correlation and the p-value corrected for multiple comparisons using the Benjamnini-Hochberg method for all K_g values and the four PVT measures are given above each diagram.

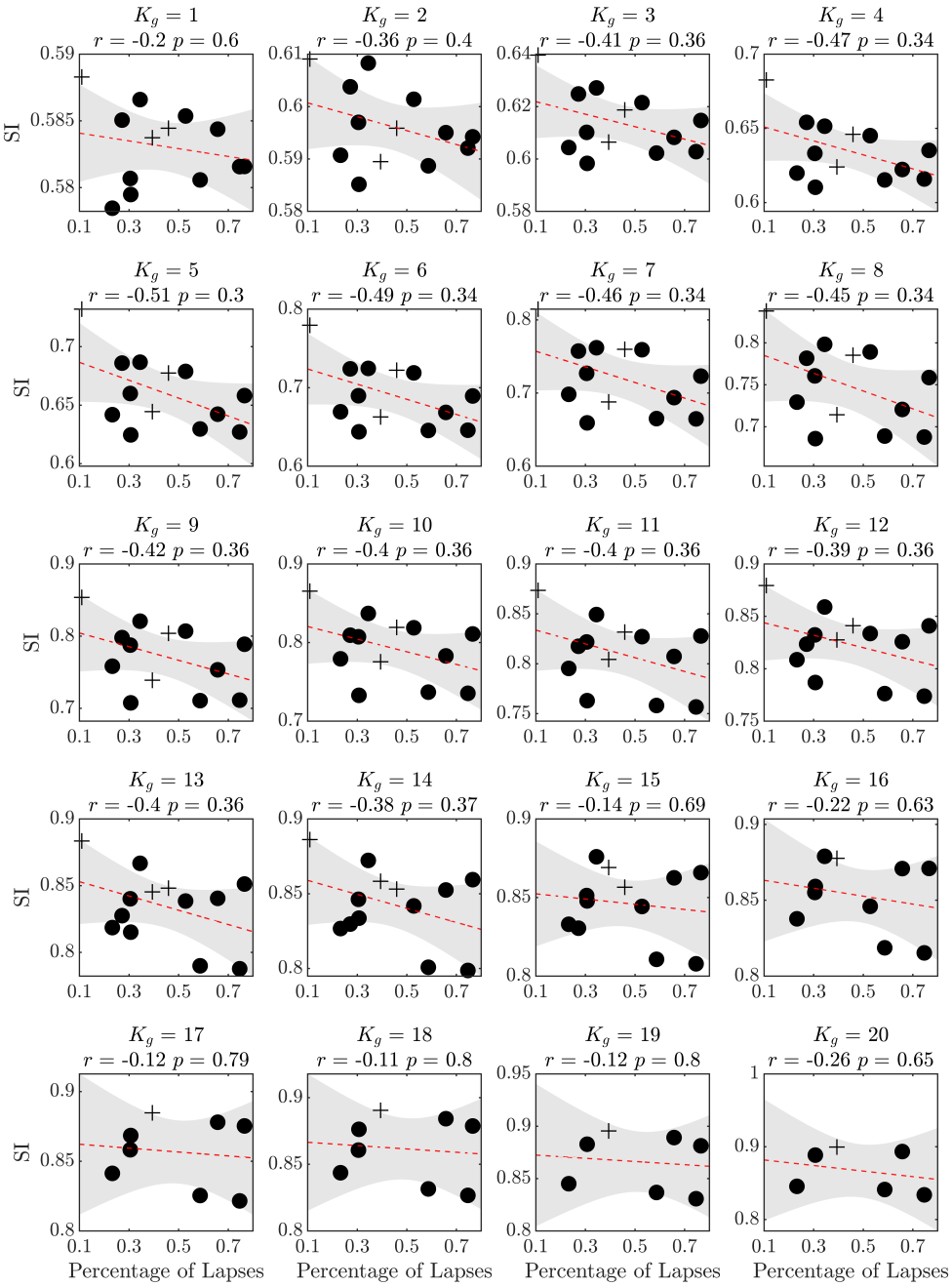


Figure D.8: **Scatterplot Relating PVT Impairment to SI Using Percentage of Lapses for the Acquisition 11 Hours Before DLMO.** Scatterplots relating the PVT impairment as measured using percentage of lapses to SI for K_g = 2 to K_g = 21 for scan 11 hours before DLMO. The Pearson's r correlation and the p-value corrected for multiple comparisons using the Benjamnini-Hochberg method for all K_g values and the four PVT measures are given above each diagram.

D.5 Predicting Performance using Synchronisation Index

The remaining colorplots displaying the correlations between the value of SI calculated from a baseline acquisition at a specific value of K_g and the PVT performance across the CRP protocol are given below for the mean RT (Figures D.9 and D.10), median RT (Figures D.11 and D.12) and percentage of lapses (Figures D.13 and D.14).

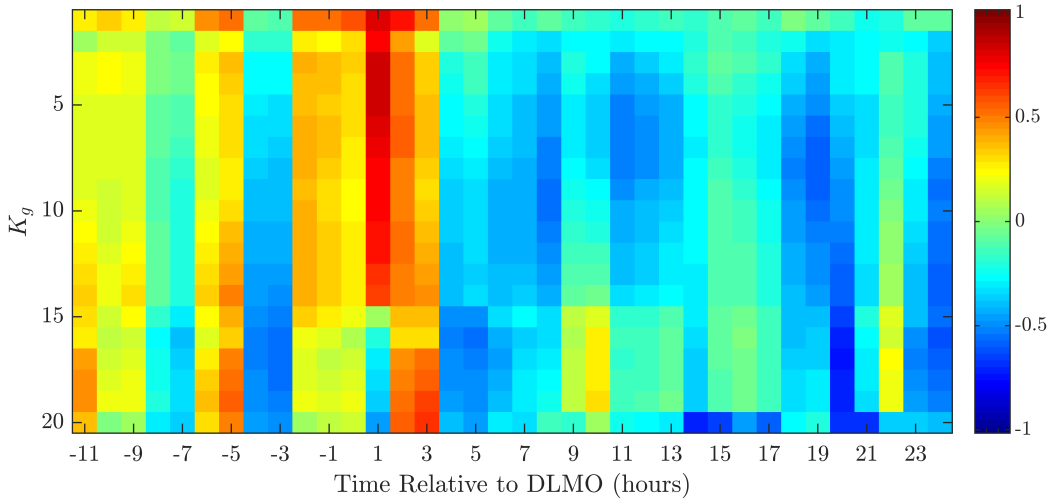


Figure D.9: **Colorplots Showing the Correlation Between the SI for the First Acquisition after Awakening and PVT Mean RT.** The Pearson's correlation between SI for the first acquisition after awakening at a given K_g and PVT performance measured using mean RT at a specific timepoint.

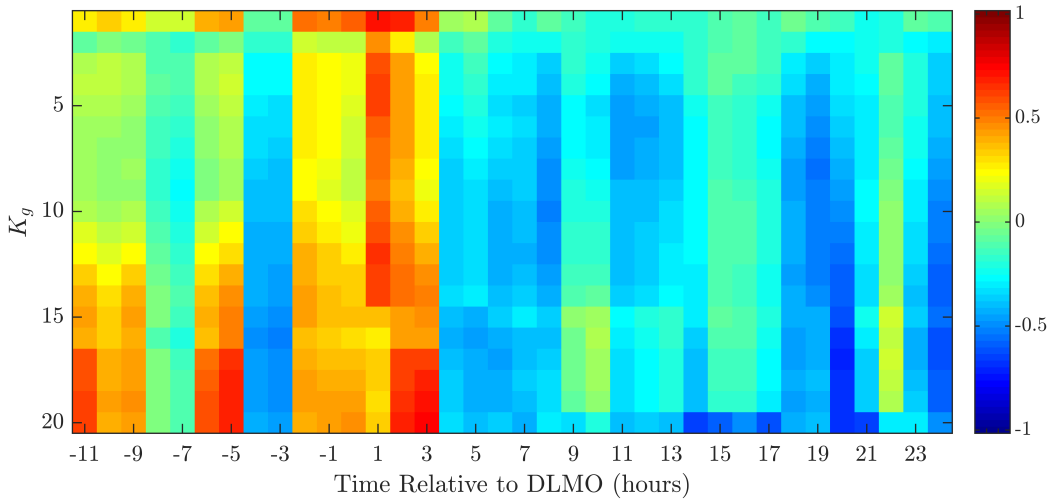


Figure D.10: **Colorplots Showing the Correlation Between the SI for the Acquisition 11 hours before DLMO and PVT Mean RT.** The Pearson's correlation between SI for the acquisition 11 hours before DLMO at a given K_g and PVT performance measured using mean RT at a specific timepoint.

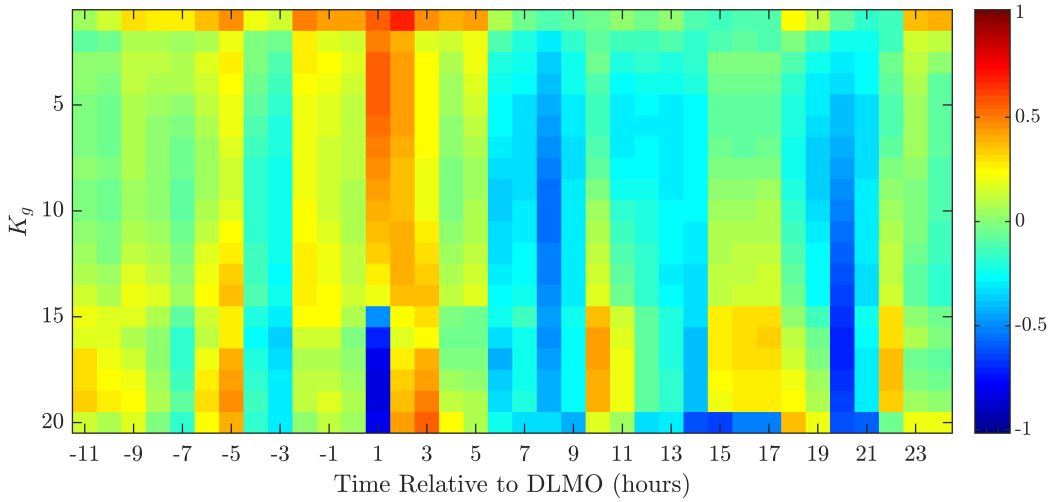


Figure D.11: **Colorplots Showing the Correlation Between the SI for the First Acquisition after Awakening and PVT Median RT.** The Pearson's correlation between SI for the first acquisition after awakening at a given K_g and PVT performance measured using median RT at a specific timepoint.

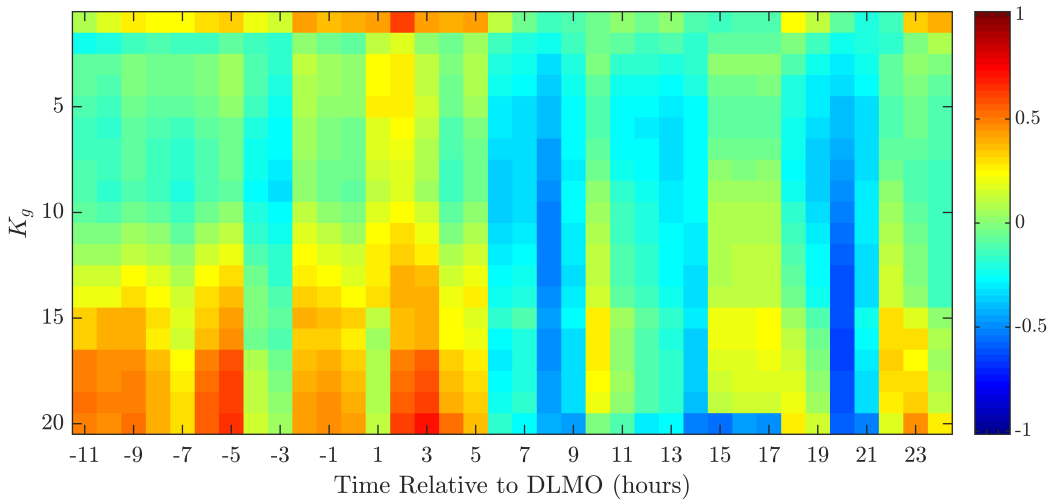


Figure D.12: **Colorplots Showing the Correlation Between the SI for the Acquisition 11 hours before DLMO and PVT Median RT.** The Pearson's correlation between SI for the acquisition 11 hours before DLMO at a given K_g and PVT performance measured using median RT at a specific timepoint.

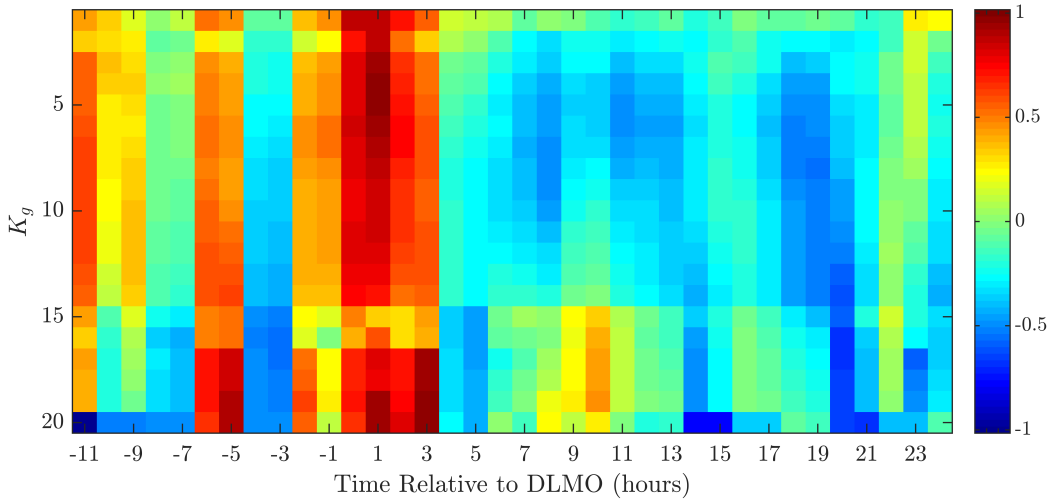


Figure D.13: **Colorplots Showing the Correlation Between the SI for the First Acquisition after Awakening and Percentage of Lapses.** The Pearson's correlation between SI for the first acquisition after awakening at a given K_g and PVT performance measured using the percentage of lapses at a specific timepoint.

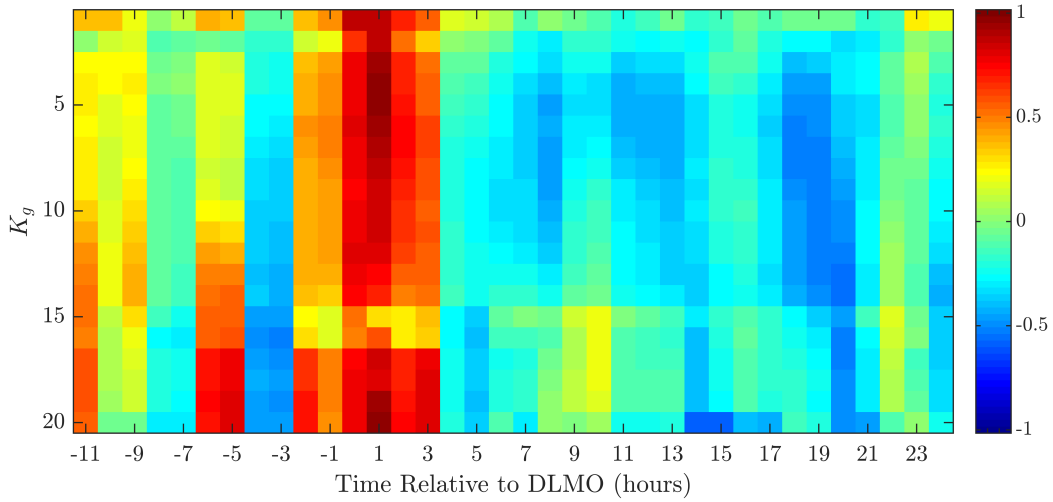


Figure D.14: **Colorplots Showing the Correlation Between the SI for the Acquisition 11 hours before DLMO and Percentage of Lapses.** The Pearson's correlation between SI for the acquisition 11 hours before DLMO at a given K_g and PVT performance measured using the percentage of lapses at a specific timepoint.

LIST OF REFERENCES

[1] J. H. Abel, K. Lecamwasam, M. A. S. Hilaire, and E. B. Klerman. Recent advances in modeling sleep: from the clinic to society and disease. *Current Opinion in Physiology*, 15:37–46, 6 2020.

[2] J. A. Acebrón, L. L. Bonilla, C. J. P. Vicente, F. Ritort, and R. Spigler. The kuramoto model: A simple paradigm for synchronization phenomena. *Reviews of Modern Physics*, 77:137–185, 1 2005.

[3] A. Aertsen and H. Preißl. Dynamics of activity and connectivity in physiological neuronal networks. In H. G. Schuster, editor, *Nonlinear Dynamics and Neuronal Networks*, pages 281–302. VCH publishers, New York, 1991.

[4] C. Anderson, 2023. Manuscript in Preparation.

[5] A. Andronache, C. Rosazza, D. Sattin, M. Leonardi, L. D'Incerti, and L. Minati. Impact of functional mri data preprocessing pipeline on default-mode network detectability in patients with disorders of consciousness. *Frontiers in Neuroinformatics*, 7:1–13, 8 2013.

[6] P. Antràs, D. Chor, T. Fally, and R. Hillberry. Measuring the upstreamness of production and trade flows. *American Economic Review*, 102:412–416, 2012.

[7] J. Axelsson, M. Sallinen, T. Sundelin, and G. Kecklund. Sleep and shift work. volume 2, pages 179–188. Oxford University Press, 2 edition, 8 2018.

[8] E. Barreto, B. Hunt, E. Ott, and P. So. Synchronization in networks of networks: The onset of coherent collective behavior in systems of interacting populations of heterogeneous oscillators. *Physical Review E*, 77:036107, 2008.

[9] M. Basner and D. F. Dinges. Maximizing sensitivity of the psychomotor vigilance test (pvt) to sleep loss. *Sleep*, 34:581–591, 2011.

[10] C. F. Beckmann and S. M. Smith. Probabilistic independent component analysis for functional magnetic resonance imaging. *IEEE Transactions on Medical Imaging*, 23:137–152, 2 2004.

[11] Y. Benjamini and Y. Hochberg. Controlling the false discovery rate: A practical and powerful approach to multiple testing. *Royal Statistical Society. Series B (Methodological)*, 57:289–300, 1995.

[12] S. Benloucif, H. J. Burgess, E. B. Klerman, A. J. Lewy, B. Middleton, P. J. Murphy, B. L. Parry, V. L. Revell, and B. Cross. Measuring melatonin in humans. *Journal of Clinical Sleep Medicine*, 4:66–69, 2008.

[13] A. Berger. How does it work? magnetic resonance imaging. *British Medical Journal*, 324:35, 1 2002.

[14] C. Bick, M. Goodfellow, C. R. Laing, and E. A. Martens. Understanding the dynamics of biological and neural oscillator networks through exact mean-field reductions: a review. *Journal of Mathematical Neuroscience*, 10:1–43, 12 2020.

[15] A. Blackwelder, M. Hoskins, and L. Huber. Effect of inadequate sleep on frequent mental distress. *Preventing Chronic Disease*, 18:1–9, 2021.

[16] K. Blatter, P. Graw, M. Münch, V. Knoblauch, A. Wirz-Justice, and C. Cajochen. Gender and age differences in psychomotor vigilance performance under differential sleep pressure conditions. *Behavioural Brain Research*, 168:312–317, 4 2006.

[17] J. Blautzik, C. Vetter, I. Peres, E. Gutyrchik, D. Keeser, A. Berman, V. Kirsch, S. Mueller, E. Pöppel, M. Reiser, T. Roenneberg, and T. Meindl. Classifying fmri-derived resting-state connectivity patterns according to their daily rhythmicity. *NeuroImage*, 71:298–306, 5 2013.

[18] Y. Bo, E. kiong Yeoh, C. Guo, Z. Zhang, T. Tam, T. C. Chan, L. yun Chang, and X. Q. Lao. Sleep and the risk of chronic kidney disease: A cohort study. *Journal of Clinical Sleep Medicine*, 15:393–400, 2019.

[19] A. A. Borbély. Sleep regulation: Circadian rhythm and homeostasis. In D. Ganten and D. Pfaff, editors, *Sleep Clinical and Experimental Aspects*, volume 1 of *Current Topics in Neuroendocrinology*, pages 83–103. Springer-Verlag, Germany, 1 edition, 1982.

[20] A. A. Borbély and P. Achermann. Sleep homeostasis and models of sleep regulation. *Journal of Biological Rhythms*, 14:559–568, 1999.

[21] A. A. Borbély, S. Daan, A. Wirz-Justice, and T. Deboer. The two-process model of sleep regulation: A reappraisal. *Journal of Sleep Research*, 25:131–143, 4 2016.

[22] M. Breakspear, S. Heitmann, and A. Daffertshofer. Generative models of cortical oscillations: neurobiological implications of the kuramoto model. *Frontiers in Human Neuroscience*, 4:1–14, 2010.

[23] J. Britton, L. Frey, J. Hopp, P. Korb, M. Koubeissi, W. Lievens, and E. Pestana-Knight. Brief history and background. In *Electroencephalography (EEG): An Introductory Text and Atlas of Normal and Abnormal Findings in Adults, Children, and Infants*. American Epilepsy Society, Chicago, 2016.

[24] C. R. Buchanan, M. E. Bastin, S. J. Ritchie, D. C. Liewald, J. W. Madole, E. M. Tucker-Drob, I. J. Deary, and S. R. Cox. The effect of network thresholding and weighting on structural brain networks in the uk biobank. *NeuroImage*, 211:1–14, 5 2020.

[25] C. Büchel and K. J. Friston. Effective connectivity and neuroimaging. `https://www.fil.ion.ucl.ac.uk/spm/doc/books/hbf1/Ch6.pdf`, 1997. unpublished draft.

[26] E. Bullmore and O. Sporns. Complex brain networks: graph theoretical analysis of structural and functional systems. *Nature Reviews*, 10:186–198, 2 2009.

[27] T. M. Burke, F. A. Scheer, J. M. Ronda, C. A. Czeisler, and K. P. Wright. Sleep inertia, sleep homeostatic and circadian influences on higher-order cognitive functions. *Journal of Sleep Research*, 24:364–371, 8 2015.

[28] L. Burns, B. Mcallister, and W. Dement. The boy who stayed awake for eleven days. Radio: BBC Sounds: Witness `https://www.bbc.co.uk/sounds/play/w3csvtts`,History, Jan 2018. accessed: 29/09/2021.

[29] C. Cajochen, R. Foy, and D.-J. Dijk. Frontal predominance of a relative increase in sleep delta and theta eeg activity after sleep loss in humans. *Sleep Research Online*, 2:65–69, 1999.

[30] C. Cajochen, S. S. B. Khalsa, J. K. Wyatt, C. A. Czeisler, and D. jan Dijk. Eeg and ocular correlates of circadian melatonin phase and human performance decrements during sleep loss. *American Journal of Physiology*, 277:640–649, 1999.

[31] J. A. Caldwell, J. K. Smith, J. L. Caldwell, D. L. Brown, Q. Mu, A. Mishory, G. Peters, and M. S. George. Are individual differences in fatigue vulnerability related to baseline differences in cortical activation? *Behavioral Neuroscience*, 119:694–707, 6 2005.

[32] V. D. Calhoun, J. Liu, and T. Adali. A review of group ica for fmri data and ica for joint inference of imaging, genetic, and erp data. *NeuroImage*, 45:163–172, 2009.

[33] Centers for Disease Control and Prevention. 1 in 3 adults don't get enough sleep. `https://www.cdc.gov/media/releases/2016/p0215-enough-sleep.html`, 2016. Accessed: 01/02/2022.

[34] V. K. Chattu, M. D. Manzar, S. Kumary, D. Burman, D. W. Spence, and S. R. Pandi-Perumal. The global problem of insufficient sleep and its serious public health implications. *Healthcare*, 7:1–16, 3 2019.

[35] F. A. Chowdhury, W. Woldman, T. H. FitzGerald, R. D. Elwes, L. Nashef, J. R. Terry, and M. P. Richardson. Revealing a brain network endophenotype in families with idiopathic generalised epilepsy. *PLOS ONE*, 9:110136, 10 2014.

[36] C. J. Chu. High density eeg-what do we have to lose? *Clinical Neurophysiology*, 126:433–434, 3 2015.

[37] E. C. P. Chua, S. C. Yeo, I. T. G. Lee, L. C. Tan, P. Lau, S. S. Tan, I. H. Mien, and J. J. Gooley. Individual differences in physiologic measures are stable across repeated exposures to total sleep deprivation. *Physiological Reports*, 2:12129, 2014.

[38] M. X. Cohen. Where does eeg come from and what does it mean? *Trends in Neurosciences*, 40:208–218, 4 2017.

[39] N. E. Cross, F. B. Pomares, A. Nguyen, A. A. Perrault, A. Jegou, M. Uji, K. Lee, F. Razavipour, O. B. K. Ali, U. Aydin, H. Benali, C. Grova, and T. T. Dang-Vu. An altered balance of integrated and segregated brain activity is a marker of cognitive deficits following sleep deprivation. *PLOS Biology*, 19:1–22, 11 2021.

[40] C. A. Czeisler, J. F. Duffy, T. L. Shanahan, E. N. Brown, J. F. Mitchell, D. W. Rimmer, J. M. Ronda, E. J. Silva, J. S. Allan, J. S. Emens, D.-J. Dijk, and R. E. Kronauer. Stability, precision, and near–24-hour period of the human circadian pacemaker. *Science*, 61:2177–2181, 1998.

[41] S. Daan, D. G. M. Beersma, and A. A. Borbély. Timing of human sleep: recovery process gated by a circadian pacemaker. *American Physiological Society*, 246:161–183, 1984.

[42] M. T. de Bettencourt, K. A. Norman, and N. B. Turk-Browne. Forgetting from lapses of sustained attention. *Psychonomic Bulletin and Review*, 25:605–611, 4 2018.

[43] B. M. de Campos, A. C. Coan, C. L. Yasuda, R. F. Casseb, and F. Cendes. Large-scale brain networks are distinctly affected in right and left mesial temporal lobe epilepsy. *Human Brain Mapping*, 37:3137–3152, 9 2016.

[44] J. A. de Havas, S. Parimal, C. S. Soon, and M. W. Chee. Sleep deprivation reduces default mode network connectivity and anti-correlation during rest and task performance. *NeuroImage*, 59:1745–1751, 1 2012.

[45] F. de Vico Fallani, J. Richiardi, M. Chavez, and S. Achard. Graph analysis of functional brain networks: Practical issues in translational neuroscience. *Philosophical Transactions of the Royal Society B*, 369:1–27, 10 2014.

[46] J. de Zeeuw, S. Wisniewski, A. Papakonstantinou, F. Bes, A. Wahnschaffe, M. Zaleska, D. Kunz, and M. Münch. The alerting effect of the wake maintenance zone during 40 hours of sleep deprivation. *Scientific Reports*, 8:11012, 12 2018.

[47] D. J. Dijk and H. P. Landolt. Circadian rhythmicity: Sleep and waking performance. In *Sleep Physiology, Circadian Rhythms, Waking Performance and the Development of Sleep-Wake Therapeutics*, volume 253, pages 441–481. Springer New York LLC, 2019.

[48] H. P. A. V. Dongen. Circadian rhythms and fatigue risk managment. São Paulo School of Advanced Science on Ecology of Human Sleep and Biological Rhythms `https://espcachrono.wixsite.com/school-of-advanced`, 2022.

[49] H. P. A. V. Dongen, M. D. Baynard, G. Maislin, and D. F. Dinges. Systematic interindividual differences in neurobehavioral impairment from sleep loss: Evidence of trait-like differential vulnerability. *Sleep*, 27:423–433, 2004.

[50] H. P. A. V. Dongen and G. Belenky. Individual differences in vulnerability to sleep loss in the work environment. *Industrial Health*, 47:518–526, 2009.

[51] H. P. A. V. Dongen and S. R. Hursh. Fatigue, performance, errors, and accidents. volume 2, pages 753–759. Elsevier, 5 edition, 2011.

[52] H. P. A. V. Dongen, G. Maislin, J. M. Mullington, and D. F. Dinges. The cumulative cost of additional wakefulness: Dose-response effects on neurobehavioral functions and sleep physiology from chronic sleep restrictionand total sleep deprivation. *Sleep*, 26:117–126, 2003.

[53] S. Doran, H. P. A. V. Dongen, and D. Dinges. Sustained attention performance during sleep deprivation: Evidence of state instability. *Archives Italiennes de Biologie*, 139:253–267, 2001.

[54] J. F. Duffy and D.-J. Dijk. Getting through to circadian oscillators: Why use constant routines? *Journal of Biological Rhythms*, 17:4–13, 2002.

[55] R. R. Edelman. The history of MR imaging as seen through the pages of radiology. *Radiology*, 273(2S):S181–S200, Nov. 2014.

[56] E. R. Facer-Childs. *"Citius, Altius, Fortius" the impact of circadian phenotype and sleep on the brain's intrinsic functional architecture, well-being & performance.* PhD thesis, University of Birmingham, 2018. `https://etheses.bham.ac.uk/id/eprint/8300/`.

[57] E. R. Facer-Childs, B. M. de Campos, B. Middleton, D. J. Skene, and A. P. Bagshaw. Circadian phenotype impacts the brain's resting-state functional connectivity, attentional performance, and sleepiness. *Sleep*, 42:1–12, 5 2019.

[58] E. R. Facer-Childs, B. M. de Campos, B. Middleton, D. J. Skene, and A. P. Bagshaw. Temporal organisation of the brain's intrinsic motor network: The relationship with circadian phenotype and motor performance. *NeuroImage*, 232:1–8, 5 2021.

[59] E. R. Facer-Childs, B. Middleton, A. P. Bagshaw, and D. J. Skene. Human circadian phenotyping and diurnal performance testing in the real world. *Journal of Visualized Experiments*, 2020:e60448, 4 2020.

[60] M. Fafrowicz, B. Bohaterewicz, A. Ceglarek, M. Cichocka, K. Lewandowska, B. Sikora-Wachowicz, H. Oginska, A. Beres, J. Olszewska, and T. Marek. Beyond

the low frequency fluctuations: Morning and evening differences in human brain. *Frontiers in Human Neuroscience*, 13:1–6, 8 2019.

[61] G. Fagiolo. Clustering in complex directed networks. *Physical Review E*, 76:1–8, 8 2007.

[62] F. V. Farahani, M. Fafrowicz, W. Karwowski, B. Bohaterewicz, A. M. Sobczak, A. Ceglarek, A. Zyrkowska, M. Ostrogorska, B. Sikora-Wachowicz, K. Lewandowska, H. Oginska, A. Beres, M. Hubalewska-Mazgaj, and T. Marek. Identifying diurnal variability of brain connectivity patterns using graph theory. *Brain Sciences*, 11:1–20, 1 2021.

[63] F. V. Farahani, M. Fafrowicz, W. Karwowski, P. K. Douglas, A. Domagalik, E. Beldzik, H. Oginska, and T. Marek. Effects of chronic sleep restriction on the brain functional network, as revealed by graph theory. *Frontiers in Neuroscience*, 13:1–15, 2019.

[64] F. V. Farahani, W. Karwowski, M. D'Esposito, R. F. Betzel, P. K. Douglas, A. M. Sobczak, B. Bohaterewicz, T. Marek, and M. Fafrowicz. Diurnal variations of resting-state fmri data: A graph-based analysis. *NeuroImage*, 256:1–25, 8 2022.

[65] F. V. Farahani, W. Karwowski, and N. R. Lighthall. Application of graph theory for identifying connectivity patterns in human brain networks: A systematic review. *Frontiers in Neuroscience*, 13:1–27, 2019.

[66] D. Fischer, D. A. Lombardi, H. Marucci-Wellman, and T. Roenneberg. Chronotypes in the US – influence of age and sex. *PLOS ONE*, 12:1–17, 6 2017.

[67] O. Floros, J. Axelsson, R. Almeida, L. Tigerström, M. Lekander, T. Sundelin, and P. Petrovic. Vulnerability in executive functions to sleep deprivation is predicted by subclinical attention-deficit/hyperactivity disorder symptoms. *Biological Psychiatry: Cognitive Neuroscience and Neuroimaging*, 6:290–298, 3 2021.

[68] S. Folkard. Towards a model for the prediction of alertness and/or fatigue on different sleep/wake schedules. *Contemporary Advances in Shiftwork Research*, 1:231–240, 1987.

[69] A. Fornito, A. Zalesky, and M. Breakspear. Graph analysis of the human connectome: Promise, progress, and pitfalls. *NeuroImage*, 80:426–444, 10 2013.

[70] A. Fornito, A. Zalesky, and M. Breakspear. The connectomics of brain disorders. *Nature Reviews Neuroscience*, 16:159–172, 2 2015.

[71] A. Fornito, A. Zalesky, and E. T. Bullmore. Chapter 4 - node degree and strength. In *Fundamentals of Brain Network Analysis*, pages 115–136. Academic Press, Amsterdam and Boston and Heidelberg, 2016.

[72] K. J. Friston. Functional and effective connectivity: A review. *Brain Connectivity*, 1:13–36, 2011.

[73] B. D. Fulcher, A. J. Phillips, and P. A. Robinson. Quantitative physiologically based modeling of subjective fatigue during sleep deprivation. *Journal of Theoretical Biology*, 264:407–419, 5 2010.

[74] C. L. Gallen, S. Schaerlaeken, J. W. Younger, J. W. Younger, K. D. O'Laughlin, J. A. Anguera, S. A. Bunge, E. E. Ferrer, F. Hoeft, B. D. McCandliss, J. Mishra, M. Rosenberg-Lee, A. Gazzaley, M. R. Uncapher, J. A. Anguera, and A. Gazzaley. Contribution of sustained attention abilities to real-world academic skills in children. *Scientific Reports*, 13:1–11, 12 2023.

[75] D. Galvis. random_graph. unpublished, 2023.

[76] G. H. Glover. Overview of functional magnetic resonance imaging. *Neurosurgery Clinics of North America*, 22:133–139, 4 2011.

[77] L. K. Grant, S. Ftouni, B. Nijagal, D. P. D. Souza, D. Tull, M. J. McConville, S. M. Rajaratnam, S. W. Lockley, and C. Anderson. Circadian and wake-dependent changes in human plasma polar metabolites during prolonged wakefulness: A preliminary analysis. *Scientific Reports*, 9:1–14, 12 2019.

[78] D. M. Groppe. *fdr_bh*. MATLAB Central File Exchange, 2023. `https://www.mathworks.com/matlabcentral/fileexchange/27418-fdr_bh`.

[79] N. Gujar, S.-S. Yoo, P. Hu, and M. P. Walker. The unrested resting brain: Sleep deprivation alters activity within the default-mode network. *Journal of Cognitive Neuroscience*, 22:1637–1648, 2009.

[80] I. Gurubhagavatula, L. K. Barger, C. M. Barnes, M. Basner, D. B. Boivin, D. Dawson, C. L. Drake, E. E. Flynn-Evans, V. Mysliwiec, P. D. Patterson, K. J. Reid, C. Samuels, N. L. Shattuck, U. Kazmi, G. Carandang, J. L. Heald, and H. P. A. V.

Dongen. Guiding principles for determining work shift duration and addressing the effects of work shift duration on performance, safety, and health: guidance from the american academy of sleep medicine and the sleep research society. *Journal of Clinical Sleep Medicine*, 17:2283–2306, 11 2021.

[81] M. Hafner, M. Stepanek, J. Taylor, W. M. Troxel, and C. V. Stolk. *Why Sleep Matters - the economic costs of insufficient sleep: A cross-country compartative analysis*. RAND Corporation, Santa Monica, CA, 2016. Ebook `https://www.rand.org/pubs/research_reports/RR1791.html`.

[82] M. H. Hagenauer and T. M. Lee. Adolescent sleep patterns in humans and laboratory animals. *Hormones and Behavior*, 64:270–279, 7 2013.

[83] M. N. Hallquist and F. G. Hillary. Graph theory approaches to functional network organization in brain disorders: A critique for a brave new small-world. *Network Neuroscience*, 3:1–26, 1 2018.

[84] H. K. Hausman, A. O'Shea, J. N. Kraft, E. M. Boutzoukas, N. D. Evangelista, E. J. V. Etten, P. K. Bharadwaj, S. G. Smith, E. Porges, G. A. Hishaw, S. Wu, S. DeKosky, G. E. Alexander, M. Marsiske, R. Cohen, and A. J. Woods. The role of resting-state network functional connectivity in cognitive aging. *Frontiers in Aging Neuroscience*, 12:1–10, 6 2020.

[85] H. He and Y. Ma, editors. *Imbalanced Learning: Foundations, Algorithms, and Applications*. Wiley, June 2013.

[86] S. Herculano-Houzel. The remarkable, yet not extraordinary, human brain as a scaled-up primate brain and its associated cost. *Proceedings of the National Academy of Sciences of the United States of America*, 109:10661–10668, 6 2012.

[87] M. A. S. Hilaire, J. J. Gooley, S. B. S. Khalsa, R. E. Kronauer, C. A. Czeisler, and S. W. Lockley. Human phase response curve to a 1 h pulse of bright white light. *Journal of Physiology*, 590:3035–3045, 7 2012.

[88] D. Hillman, S. Mitchell, J. Streatfeild, C. Burns, D. Bruck, and L. Pezzullo. The economic cost of inadequate sleep. *Sleep*, 41:1–13, 8 2018.

[89] A. Hjelmfelt and J. Ross. Pattern recognition, chaos, and multiplicity in neural networks of excitable systems. *Proceedings of the National Academy of Sciences of the United States of America*, 91:63–67, 1994.

[90] A. L. Hodgkin and A. F. Huxley. A quantitative description of membrane current and its application to conduction and excitation in nerve. *Journal of Physiology*, 117:500–544, 1952.

[91] K. A. Honn, H. P. A. V. Dongen, and D. Dawson. Working time society consensus statements: Prescriptive rule sets and risk management-based approaches for the management of fatigue-related risk in working time arrangements. *Industrial Health*, 57:264–280, 2019.

[92] C. M. Horne and R. Norbury. Altered resting-state connectivity within default mode network associated with late chronotype. *Journal of Psychiatric Research*, 102:223–229, 7 2018.

[93] B. Hu, C. Liu, T. Mou, F. Luo, T. Lv, C. Qian, J. Zhang, M. Ye, and Z. Liu. Meta-analysis of sleep deprivation effects on patients with depression. *Frontiers in Psychiatry*, 12:1–9, 11 2021.

[94] R. Huber, H. Mäki, M. Rosanova, S. Casarotto, P. Canali, A. G. Casali, G. Tononi, and M. Massimini. Human cortical excitability increases with time awake. *Cerebral Cortex*, 23:332–338, 2 2013.

[95] E. Hug, K. Winzeler, M. Pfaltz, C. Cajochen, and K. Bader. Later chronotype is associated with higher alcohol consumption and more adverse childhood experiences in young healthy women. *Clocks & Sleep*, 1:126–139, 2 2019.

[96] M. D. Humphries and K. Gurney. Network 'small-world-ness': A quantitative method for determining canonical network equivalence. *PLOS ONE*, 3:e0002051, 4 2008.

[97] S. R. Hursh and T. Raslear. Analysis of the relationship between operator effectiveness measures and economic impacts of rail accidents, 2011.

[98] L. E. Ismail and W. Karwowski. A graph theory-based modeling of functional brain connectivity based on eeg: A systematic review in the context of neuroergonomics. *IEEE Access*, 8:155103–155135, 2020.

[99] M. L. Jackson, R. J. Croft, G. A. Kennedy, K. Owens, and M. E. Howard. Cognitive components of simulated driving performance: Sleep loss effects and predictors. *Accident Analysis and Prevention*, 50:438–444, 1 2013.

[100] S. Johnson, V. Domínguez-García, L. Donetti, and M. A. Muñoz. Trophic coherence determines food-web stability. *PNAS*, 111:17923–17928, 12 2014.

[101] S. Kar and A. Routray. Effect of sleep deprivation on functional connectivity of eeg channels. *IEEE Transactions on Systems, Man, and Cybernetics Part A:Systems and Humans*, 43:666–672, 2013.

[102] L. Kasper, S. Bollmann, A. O. Diaconescu, C. Hutton, J. Heinzle, S. Iglesias, T. U. Hauser, M. Sebold, Z. M. Manjaly, K. P. Pruessmann, and K. E. Stephan. The physio toolbox for modeling physiological noise in fmri data. *Journal of Neuroscience Methods*, 276:56–72, 1 2017.

[103] R. Keogh, J. Bergmann, and J. Pearson. Cortical excitability controls the strength of mental imagery. *eLife*, 9:1–33, 5 2020.

[104] J. R. Kercher and H. H. Shugart. Trophic structure, effective trophic position, and connectivity in food webs. *American Society of Naturalist*, 109:191–206, 1975.

[105] F. W. King. Introduction. In *Hilbert Transforms Volume 1*, volume 1, pages 1–10. Cambridge University Press, 1 edition, 4 2009.

[106] F. W. King. Review of some background mathematics. In *Hilbert Transforms Volume 1*, volume 1, pages 11–82. Cambridge University Press, 1 edition, 5 2009.

[107] J. Klaise and S. Johnson. From neurons to epidemics: How trophic coherence affects spreading processes. *Chaos*, 26:1–8, 6 2016.

[108] N. Kleitman. Periodicity. In G. Fleming, editor, *Sleep and Wakefulness*, pages 178–179. University of Chicago Press, 1963. Ebook.

[109] W. Klimesch. Alpha-band oscillations, attention, and controlled access to stored information. *Trends in Cognitive Sciences*, 16:606–617, 12 2012.

[110] M. M. Koenis, N. Romeijn, G. Piantoni, I. Verweij, Y. D. V. D. Werf, E. J. V. Someren, and C. J. Stam. Does sleep restore the topology of functional brain networks? *Human Brain Mapping*, 34:487–500, 2 2013.

[111] A. A. Kondratova and R. V. Kondratov. The circadian clock and pathology of the ageing brain. *Nature Reviews*, 13:325–335, 3 2012.

[112] O. Korhonen, H. Saarimäki, E. Glerean, M. Sams, and J. Saramäki. Consistency of regions of interest as nodes of fmri functional brain networks. *Network Neuroscience*, 1:254–274, 10 2017.

[113] O. Korhonen, M. Zanin, and D. Papo. Principles and open questions in functional brain network reconstruction. *Human Brain Mapping*, 42:3680–3711, 8 2021.

[114] A. Krishnamoorthy and D. Menon. Matrix inversion using cholesky decomposition. pages 70–72, 9 2013.

[115] M. O. Kuismin and M. J. Sillanpää. Estimation of covariance and precision matrix, network structure, and a view toward systems biology. *Wiley Interdisciplinary Reviews: Computational Statistics*, 9:1–13, 11 2017.

[116] Y. Kuramoto. *Chemical Oscillations, Waves, and Turbulence*. Springer Berlin Heidelberg, 1984.

[117] C. P. Kyriacou and M. H. Hastings. Circadian clocks: genes, sleep, and cognition. *Trends in Cognitive Sciences*, 14:259–267, 6 2010.

[118] J. P. Lachaux, E. Rodriguez, J. Martinerie, and F. J. Varela. Measuring phase synchrony in brain signals. *Human Brain Mapping*, 8:194–208, 1999.

[119] V. Latora and M. Marchiori. Efficient behavior of small-world networks. *American Physical Society*, 87:1–4, 2017.

[120] M. H. Lee, C. D. Smyser, and J. S. Shimony. Resting-state fmri: A review of methods and clinical applications. *American Journal of Neuroradiology*, 34:1866–1872, 10 2013.

[121] C. C. Leung and H. F. Chau. Weighted assortative and disassortative networks model. *Physica A*, 378:591–602, 5 2007.

[122] R. Levandovski, G. Dantas, L. C. Fernandes, W. Caumo, I. Torres, T. Roenneberg, M. P. L. Hidalgo, and K. V. Allebrandt. Depression scores associate with chronotype and social jetlag in a rural population. *Chronobiology International*, 28:771–778, 11 2011.

[123] H. Liu, H. Li, Y. Wang, and X. Lei. Enhanced brain small-worldness after sleep deprivation: A compensatory effect. *Journal of Sleep Research*, 23:554–563, 10 2014.

[124] Y. Liu, Y. Chen, X. Liang, D. Li, Y. Zheng, H. Zhang, Y. Cui, J. Chen, J. Liu, and S. Qiu. Altered resting-state functional connectivity of multiple networks and disrupted correlation with executive function in major depressive disorder. *Frontiers in Neurology*, 11:1–11, 4 2020.

[125] J. Q. Ly, G. Gaggioni, S. L. Chellappa, S. Papachilleos, A. Brzozowski, C. Borsu, M. Rosanova, S. Sarasso, B. Middleton, A. Luxen, S. N. Archer, C. Phillips, D. J. Dijk, P. Maquet, M. Massimini, and G. Vandewalle. Circadian regulation of human cortical excitability. *Nature Communications*, 7:1–10, 6 2016.

[126] R. S. Mackay, S. Johnson, and B. Sansom. How directed is a directed network? *Royal Society Open Science*, 7:1–24, 9 2020.

[127] G. Marrelec, J. Kim, J. Doyon, and B. Horwitz. Large-scale neural model validation of partial correlation analysis for effective connectivity investigation in functional mri. *Human Brain Mapping*, 30:941–950, 3 2009.

[128] G. Marrelec, A. Krainik, H. Duffau, M. Pélégrini-Issac, S. Lehéricy, J. Doyon, and H. Benali. Partial correlation for functional brain interactivity investigation in functional mri. *NeuroImage*, 32:228–237, 2006.

[129] E. A. Martens, E. Barreto, S. H. Strogatz, E. Ott, P. So, and T. M. Antonsen. Exact results for the kuramoto model with a bimodal frequency distribution. *American Physical Society*, 79:026204, 2 2009.

[130] S. L. Mason, L. Junges, W. Woldman, E. R. Facer-Childs, B. M. de Campos, A. P. Bagshaw, and J. R. Terry. Classification of human chronotype based on fmri network-based statistics. *Frontiers in Neuroscience*, 17:1–22, 6 2023.

[131] H. Matsuura, K. Tateno, and S. Aou. Dynamical properties of the two-process model for sleep-wake cycles in infantile autism. *Cognitive Neurodynamics*, 2:221–228, 9 2008.

[132] P. McCauley, L. V. Kalachev, D. J. Mollicone, S. Banks, D. F. Dinges, and H. P. A. V. Dongen. Dynamic circadian modulation in a biomathematical model for the effects of sleep and sleep loss on waking neurobehavioral performance. *Sleep*, 36:1987–1997, 12 2013.

[133] W. R. McMahon, S. Ftouni, S. P. Drummond, P. Maruff, S. W. Lockley, S. M. Rajaratnam, and C. Anderson. The wake maintenance zone shows task dependent

changes in cognitive function following one night without sleep. *Sleep*, 41:1–12, 10 2018.

[134] S. O. Meadows, C. C. Engel, R. L. Collins, R. L. Beckman, J. Breslau, E. L. Bloom, M. S. Dunbar, M. L. Gilbert, D. Grant, J. Hawes-Dawson, S. B. Holliday, S. Maccarthy, E. R. Pedersen, M. W. Robbins, A. J. Rose, J. Ryan, T. L. Schell, and M. M. Simmons. 2018 department of defense health related behaviors survey (hrbs): Results for the active component, 2018.

[135] C. Meisel, A. Schulze-Bonhage, D. Freestone, M. J. Cook, P. Achermann, and D. Plenz. Intrinsic excitability measures track antiepileptic drug action and uncover increasing/decreasing excitability over the wake/sleep cycle. *Proceedings of the National Academy of Sciences of the United States of America*, 112:14694–14699, 11 2015.

[136] L. D. Milia and S. Folkard. More than morningness: The effect of circadian rhythm amplitude and stability on resilience, coping, and sleep duration. *Frontiers in Psychology*, 12:1–7, 11 2021.

[137] F. Miraglia, C. Tomino, F. Vecchio, M. Gorgoni, L. D. Gennaro, and P. M. Rossini. The brain network organization during sleep onset after deprivation. *Clinical Neurophysiology*, 132:36–44, 1 2021.

[138] M. Moore-Ede and C. Czeisler. Circadian gating of human sleep-wake cycles. In M. Moore-Ede and C. Czeisler, editors, *Mathematical Models of the Circadian Sleep-Wake Cycle*, volume 1, pages 129–158. Raven Press, 1 edition, 1984.

[139] Q. Mu, A. Mishory, K. A. Johnson, Z. Nahas, F. A. Kozel, K. Yamanaka, D. E. Bohning, and M. S. George. Decreased brain activation during a working memory task at rested baseline is associated with vulnerability to sleep deprivation. *Sleep*, 28:433–446, 2005.

[140] M. Nagai, S. Hoshide, and K. Kario. Sleep duration as a risk factor for cardiovascular disease-a review of the recent literature. *Current Cardiology Reviews*, 6:54–61, 2010.

[141] J. J. Newson and T. C. Thiagarajan. Eeg frequency bands in psychiatric disorders: A review of resting state studies. *Frontiers in Human Neuroscience*, 12:1–24, 1 2019.

[142] J. A. Owens, R. Au, M. Carskadon, R. Millman, and A. Wolfson. School start times for adolescents. *American Academy of Pediatrics*, 134:642–649, 9 2014.

[143] P. Parameswari, N. Chethan, and S. B. Chidambaram. Neurochemicals and behavioural alterations in sleep deprivation: A revisit. *Journal of Dementia*, 1(1):1000104, 2017.

[144] D. A. Paranjpe and V. K. Sharma. Evolution of temporal order in living organisms. *Journal of Circadian Rhythms*, 3:1–13, 5 2005.

[145] W. Penny, K. Friston, J. Ashburner, S. Kiebel, and T. Nichols. *Statistical Parametric Mapping: The Analysis of Functional Brain Images*. Academic Press, London, 2007.

[146] U. Pervaiz, D. Vidaurre, M. W. Woolrich, and S. M. Smith. Optimising network modelling methods for fmri. *NeuroImage*, 211:116604, 5 2020.

[147] M. Pesoli, R. Rucco, M. Liparoti, A. Lardone, G. D'Aurizio, R. Minino, E. T. Lopez, A. Paccone, C. Granata, G. Curcio, G. Sorrentino, L. Mandolesi, and P. Sorrentino. A night of sleep deprivation alters brain connectivity and affects specific executive functions. *Neurological Sciences*, 43:1025–1034, 2 2022.

[148] S. E. Petersen and O. Sporns. Brain networks and cognitive architectures. *Neuron*, 88:207–219, 10 2015.

[149] G. Petkov, M. Goodfellow, M. P. Richardson, and J. R. Terry. A critical role for network structure in seizure onset: A computational modeling approach. *Frontiers in Neurology*, 5:1–7, 2014.

[150] S. Prashad, E. S. Dedrick, and F. M. Filbey. Cannabis users exhibit increased cortical activation during resting state compared to non-users. *NeuroImage*, 179:176–186, 10 2018.

[151] P. Proserpio, D. Arnaldi, F. Nobili, and L. Nobili. Integrating sleep and alzheimer's disease pathophysiology: Hints for sleep disorders management. *Journal of Alzheimer's Disease*, 63(3):871–886, May 2018.

[152] PubMed. `https://tinyurl.com/PubmedChronotypePublications`. Accessed: 30/06/2023.

[153] K. A. Robbins, J. Touryan, T. Mullen, C. Kothe, and N. Bigdely-Shamlo. How sensitive are eeg results to preprocessing methods: A benchmarking study. *IEEE Transactions on Neural Systems and Rehabilitation Engineering*, 28:1081–1090, 5 2020.

[154] N. Rodgers, P. I. Tiňo, and S. Johnson. Strong connectivity in real directed networks. *PNAS*, 120:e2215752120, 2023.

[155] T. Roenneberg, K. V. Allebrandt, M. Merrow, and C. Vetter. Social jetlag and obesity. *Current Biology*, 22:939–943, 5 2012.

[156] T. Roenneberg, L. K. Keller, D. Fischer, J. L. Matera, C. Vetter, and E. C. Winnebeck. Human activity and rest in situ. volume 552, pages 257–283. Academic Press Inc., 2015.

[157] T. Roenneberg, T. Kuehnle, M. Juda, T. Kantermann, K. Allebrandt, M. Gordijn, and M. Merrow. Epidemiology of the human circadian clock. *Sleep Medicine Reviews*, 11:429–438, 12 2007.

[158] T. Roenneberg, A. Wirz-Justice, and M. Merrow. Life between clocks: Daily temporal patterns of human chronotypes. *Journal of Biological Rhythms*, 18:80–90, 2 2003.

[159] Y. Rosen, L. Kirsch, and Y. Louzoun. Optimal network modification for spectral radius dependent phase transitions. *New Journal of Physics*, 18(9):093039, Sept. 2016.

[160] M. Rubinov and O. Sporns. Complex network measures of brain connectivity: Uses and interpretations. *NeuroImage*, 52:1059–1069, 9 2010.

[161] C. Rummel, E. Abela, M. Müller, M. Hauf, O. Scheidegger, R. Wiest, and K. Schindler. Uniform approach to linear and nonlinear interrelation patterns in multivariate time series. *Physical Review E*, 83:066215, 6 2011.

[162] N. M. Rzechorzek, M. J. Thrippleton, F. M. Chappell, G. Mair, A. Ercole, M. Cabeleira, J. Rhodes, I. Marshall, and J. S. O'neill. A daily temperature rhythm in the human brain predicts survival after brain injury. *Brain*, 145:2031–2048, 6 2022.

[163] N. Santhi, A. S. Lazar, P. J. McCabe, J. C. Lo, J. A. Groeger, and D. J. Dijk. Sex differences in the circadian regulation of sleep and waking cognition in humans. *Proceedings of the National Academy of Sciences of the United States of America*, 113:2730–2739, 5 2016.

[164] H. Schmidt, G. Petkov, M. P. Richardson, and J. R. Terry. Dynamics on networks: The role of local dynamics and global networks on the emergence of hypersynchronous neural activity. *PLOS Computional Biology*, 10:e1003947, 2014.

[165] H. Schmidt, W. Woldman, M. Goodfellow, F. A. Chowdhury, M. Koutroumanidis, S. Jewell, M. P. Richardson, and J. R. Terry. A computational biomarker of idiopathic generalized epilepsy from resting state eeg. *Epilepsia*, 57:e200–e204, 10 2016.

[166] E. Serin, A. Zalesky, A. Matory, H. Walter, and J. D. Kruschwitz. Nbs-predict: A prediction-based extension of the network-based statistic. *NeuroImage*, 244:1–15, 12 2021.

[167] Y. Shao, L. Wang, E. Ye, X. Jin, W. Ni, Y. Yang, B. Wen, D. Hu, and Z. Yang. Decreased thalamocortical functional connectivity after 36 hours of total sleep deprivation: Evidence from resting state fmri. *PLOS ONE*, 8:e78830, 10 2013.

[168] J. A. Shekleton, S. M. Rajaratnam, J. J. Gooley, E. V. Reen, C. A. Czeisler, and S. W. Lockley. Improved neurobehavioral performance during the wake maintenance zone. *Journal of Clinical Sleep Medicine*, 9:353–362, 2013.

[169] W. R. Shirer, S. Ryali, E. Rykhlevskaia, V. Menon, and M. D. Greicius. Decoding subject-driven cognitive states with whole-brain connectivity patterns. *Cerebral Cortex*, 22:158–165, 1 2012.

[170] T. M. Shockey and A. G. Wheaton. Short sleep duration by occupation group-29 states, 2013-2014. *US Department of Health and Human Services/Centers for Disease Control and Prevention*, 66:207–213, 2017.

[171] D. W. Shrey, O. K. McManus, R. Rajaraman, H. Ombao, S. A. Hussain, and B. A. Lopour. Strength and stability of eeg functional connectivity predict treatment response in infants with epileptic spasms. *Clinical Neurophysiology*, 129:2137–2148, 10 2018.

[172] E. B. Simon, A. Maron-Katz, N. Lahav, R. Shamir, and T. Hendler. Tired and misconnected: A breakdown of brain modularity following sleep deprivation. *Human Brain Mapping*, 38:3300–3314, 6 2017.

[173] P. S. Skardal and J. G. Restrepo. Synchronization of kuramoto oscillators in networks of networks. pages 171–174, 10 2012.

[174] A. C. Skeldon, D. J. Dijk, and G. Derks. Mathematical models for sleep-wake dynamics: Comparison of the two-process model and a mutual inhibition neuronal model. *PLOS ONE*, 9:e103877, 8 2014.

[175] R. J. Smith, E. Alipourjeddi, C. Garner, A. L. Maser, D. W. Shrey, and B. A. Lopour. Infant functional networks are modulated by state of consciousness and circadian rhythm. *Network Neuroscience*, 5:614–630, 5 2021.

[176] S. M. Smith, P. T. Fox, K. L. Miller, D. C. Glahn, P. M. Fox, C. E. Mackay, N. Filippini, K. E. Watkins, R. Toro, A. R. Laird, and C. F. Beckmann. Correspondence of the brain's functional architecture during activation and rest. *PNAS*, 106:13040–13045, 2009.

[177] S. M. Smith, K. L. Miller, G. Salimi-Khorshidi, M. Webster, C. F. Beckmann, T. E. Nichols, J. D. Ramsey, and M. W. Woolrich. Network modelling methods for fmri. *NeuroImage*, 54:875–891, 1 2011.

[178] X. Song, L. P. Panych, and N.-K. Chen. Data-driven and predefined roi-based quantification of long-term resting-state fmri reproducibility. *Brain Connectivity*, 6:136–151, 3 2016.

[179] A. R. Sparrow, D. J. Mollicone, K. Kan, R. Bartels, B. C. Satterfield, S. M. Riedy, A. Unice, and H. P. A. V. Dongen. Naturalistic field study of the restart break in US commercial motor vehicle drivers: Truck driving, sleep, and fatigue. *Accident Analysis and Prevention*, 93:55–64, 8 2016.

[180] C. Stam and B. V. Dijk. Synchronization likelihood: an unbiased measure of generalized synchronization in multivariate data sets. *Physica D*, 163:236–251, 2002.

[181] C. J. Stam, G. Nolte, and A. Daffertshofer. Phase lag index: Assessment of functional connectivity from multi channel eeg and meg with diminished bias from common sources. *Human Brain Mapping*, 28:1178–1193, 11 2007.

[182] A. Steptoe and B. Serwinski. Chapter 34 - cortisol awakening response. In G. Fink, editor, *Stress: Concepts, Cognition, Emotion, and Behavior*, pages 277–283. Academic Press, San Diego, 2016.

[183] S. H. Strogatz. From kuramoto to crawford: exploring the onset of synchronization in populations of coupled oscillators. *Physica D*, 143:1–20, 2000.

[184] E. Suni. Sleep deprivation what it is, its causes, symptoms, and long-term effects on physical, mental, and emotional health, 2021.

[185] Q. K. Telesford, K. E. Joyce, S. Hayasaka, J. H. Burdette, and P. J. Laurienti. The ubiquity of small-world networks. *Brain Connectivity*, 1:367–375, 12 2011.

[186] J. R. Terry, C. Anderson, and J. A. Horne. Nonlinear analysis of eeg during nrem sleep reveals changes in functional connectivity due to natural aging. *Human Brain Mapping*, 23:73–84, 10 2004.

[187] G. Thedchanamoorthy, M. Piraveenan, D. Kasthuriratna, and U. Senanayake. Node assortativity in complex networks: An alternative approach. *Procedia Computer Science*, 29:2449–2461, 2014.

[188] B. Thirion, G. Varoquaux, E. Dohmatob, and J.-B. Poline. Which fmri clustering gives good brain parcellations? *Frontiers in Neuroscience*, 8:1–13, 2014.

[189] L. Tonetti, A. Conca, G. Giupponi, M. Filardi, and V. Natale. Circadian activity rhythm in adult attention-deficit hyperactivity disorder. *Journal of Psychiatric Research*, 103:1–4, 8 2018.

[190] G. Tononi and C. Cirelli. Sleep function and synaptic homeostasis. *Sleep Medicine Reviews*, 10:49–62, 2 2006.

[191] R. Toro, M. Perron, B. Pike, L. Richer, S. Veillette, Z. Pausova, and T. Paus. Brain size and folding of the human cerebral cortex. *Cerebral Cortex*, 18:2352–2357, 10 2008.

[192] L. Torsvall and T. Åkerstedt. A diurnal type scale. construction, consistency and validation in shift work. *Scandinavian Journal of Work, Environment & Health*, 6:283–290, 1980.

[193] M. P. van den Heuvel, S. C. de Lange, A. Zalesky, C. Seguin, B. T. Yeo, and R. Schmidt. Proportional thresholding in resting-state fmri functional connectivity networks and consequences for patient-control connectome studies: Issues and recommendations. *NeuroImage*, 152:437–449, 5 2017.

[194] P. van Mierlo, O. Lie, W. Staljanssens, A. Coito, and S. Vulliémoz. Influence of time-series normalization, number of nodes, connectivity and graph measure selection on seizure-onset zone localization from intracranial eeg. *Brain Topography*, 31:753–766, 9 2018.

[195] I. M. Verweij, N. Romeijn, D. J. Smit, G. Piantoni, E. J. V. Someren, and Y. D. van der Werf. Sleep deprivation leads to a loss of functional connectivity in frontal brain regions. *BioMed Central Neuroscience*, 15:1–10, 7 2014.

[196] C. Vetter, D. Fischer, J. L. Matera, and T. Roenneberg. Aligning work and circadian time in shift workers improves sleep and reduces circadian disruption. *Current Biology*, 25:907–911, 2015.

[197] R. Vijayalakshmi, D. Nandagopal, N. Dasari, B. Cocks, N. Dahal, and M. Thilaga. Minimum connected component - a novel approach to detection of cognitive load induced changes in functional brain networks. *Neurocomputing*, 170:15–31, 12 2015.

[198] M. M. Walsh, G. Gunzelmann, and H. P. A. V. Dongen. Computational cognitive modeling of the temporal dynamics of fatigue from sleep loss. *Psychonomic Bulletin and Review*, 24:1785–1807, 12 2017.

[199] H. Wang, B. Wang, K. P. Normoyle, K. Jackson, K. Spitler, M. Sharrock, C. M. Miller, C. Best, D. Llano, and R. Du. Brain temperature and its fundamental properties: A review for clinical neuroscientists. *Frontiers in Neuroscience*, 8:1–17, 2014.

[200] H. E. Wang, C. G. Bénar, P. P. Quilichini, K. J. Friston, V. K. Jirsa, and C. Bernard. A systematic framework for functional connectivity measures. *Frontiers in Neuroscience*, 8:1–22, 12 2014.

[201] Y. Wang, J. Kang, P. B. Kemmer, and Y. Guo. An efficient and reliable statistical method for estimating functional connectivity in large scale brain networks using partial correlation. *Frontiers in Neuroscience*, 10:1–17, 3 2016.

[202] Y. Wang, H. Liu, G. Hitchman, and X. Lei. Module number of default mode network: Inter-subject variability and effects of sleep deprivation. *Brain Research*, 1596:69–78, 1 2015.

[203] D. J. Watts and S. H. Strogatz. Collective dynamics of 'small-world' networks. *Nature*, 393:440–442, 1998.

[204] T. B. Weng, G. L. Pierce, W. G. Darling, D. Falk, V. A. Magnotta, and M. W. Voss. The acute effects of aerobic exercise on the functional connectivity of human brain networks. *Brain Plasticity*, 2:171–190, 10 2016.

[205] A. Wirz-Justice. How to measure circadian rhythms in humans. *Medicographia*, 29:84–90, 2007.

[206] M. Wittmann, J. Dinich, M. Merrow, and T. Roenneberg. Social jetlag: Misalignment of biological and social time. *Chronobiology International*, 23:497–509, 2006.

[207] W. Woldman, H. Schmidt, E. Abela, F. A. Chowdhury, A. D. Pawley, S. Jewell, M. P. Richardson, and J. R. Terry. Dynamic network properties of the interictal brain determine whether seizures appear focal or generalised. *Scientific Reports*, 10:1–11, 12 2020.

[208] E. Wolf, M. Kuhn, C. Norman, F. Mainberger, J. G. Maier, S. Maywald, A. Bredl, S. Klöppel, K. Biber, D. van Calker, D. Riemann, A. Sterr, and C. Nissen. Synaptic plasticity model of therapeutic sleep deprivation in major depression. *Sleep Medicine Reviews*, 30:53–62, 12 2016.

[209] J. Wu, Q. Zhou, J. Li, Y. Chen, S. Shao, and Y. Xiao. Decreased resting-state alpha-band activation and functional connectivity after sleep deprivation. *Scientific Reports*, 11:1–10, 12 2021.

[210] M. Xia, J. Wang, and Y. He. Brainnet viewer: A network visualization tool for human brain connectomics. *PLOS ONE*, 8:e68910, 7 2013.

[211] S. D. Youngstedt, E. E. Goff, A. M. Reynolds, D. F. Kripke, M. R. Irwin, R. R. Bootzin, N. Khan, and G. Jean-Louis. Has adult sleep duration declined over the last 50+ years? *Sleep Medicine Reviews*, 28:69–85, 8 2016.

[212] A. Zalesky, A. Fornito, and E. T. Bullmore. Network-based statistic: Identifying differences in brain networks. *NeuroImage*, 53:1197–1207, 12 2010.

[213] A. Zalesky, A. Fornito, L. Cocchi, L. L. Gollo, M. P. V. D. Heuvel, and M. Breakspear. Connectome sensitivity or specificity: which is more important? *NeuroImage*, 142:407–420, 2016.

[214] A. Zalesky, A. Fornito, and B. ET. Nbs connectome reference manual for nbs connectome (v1.2), 2012.

[215] D. A. Zappalà, M. Barreiro, and C. Masoller. Global atmospheric dynamics investigated by using hilbert frequency analysis. *Entropy*, 18:1–11, 11 2016.